The deployment of power-to-fuels systems as a carbon mitigation and energy storage strategy

SAMUEL SOGBESAN

A thesis presented for the degree of

DOCTOR OF PHILOSOPHY

Birmingham Centre for Fuel Cell and Hydrogen Research

School of Chemical Engineering

College of Engineering and Physical Sciences

University of Birmingham

Submitted on the 8th of August 2023

Abstract

One of the critical challenges faced in the fight to mitigate the effects of climate change lies in the uncertainty of the successful deployment of any proposed means in light of an ever-dynamic socio-economic world. This study seeks to examine one of the means of climate change mitigation within the context of road transport via the deployment of electrofuels. The body of this thesis aims to explore gaps in the analysis of the potential of fuels that could be made available for future vehicles that rely on carbon-based fuels. The methodology takes a conservative yet realistic approach - if near-term climate change targets remain unmet.

Using the United Kingdom as a case study, this study assessed the potential of carbon dioxide that is readily available to be captured and valorised into electrofuels. The fuels discussed were considered based on their immediate adaptability with the current infrastructure. Process models were developed for the solid oxide electrolysers and various fuel synthesis processes.

The techno-economic performance of producing each fuel in terms of their profitability. The results showed that the economic viability of producing these fuels is highly dependent on the source and, consequently, the price of electricity. Using the net present value as a key economic indicator, profitability is achieved when the electricity prices are below £17.4 per MWh. A fuel performance analysis is carried out to understand how these fuels perform energetically and environmentally in today's vehicles. A well-to-wheel analysis showed that internal combustion engine vehicles achieve efficiencies between 11.3% to 19.8%.

A discussion on the prospects and barriers to deploying electrofuels concludes this study's assessment. The current infrastructure and limitations are highlighted at the close of this work. The significance of this study is to inform stakeholders of the opportunities and consequences of deploying electrofuels as a climate mitigation option and as a transitionary and enabling technology towards long-term climate strategies. Figure 1 and Figure 2 summarises the analysis in this work.

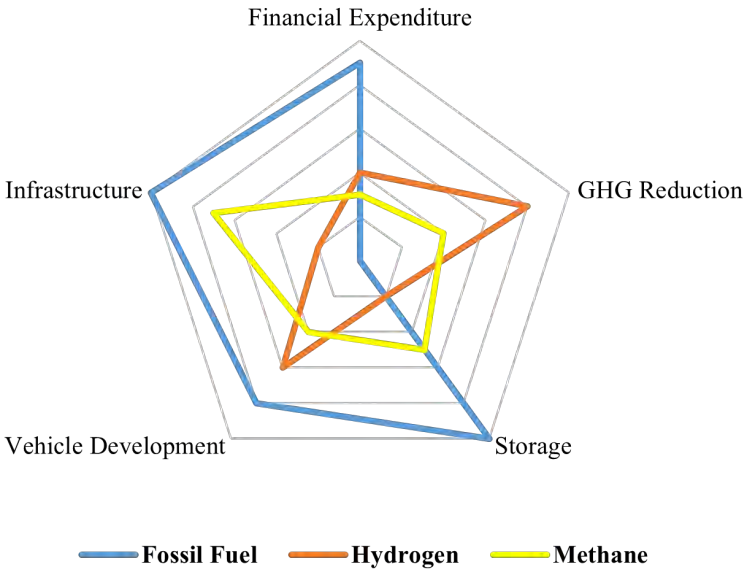

(a) *Methane.*

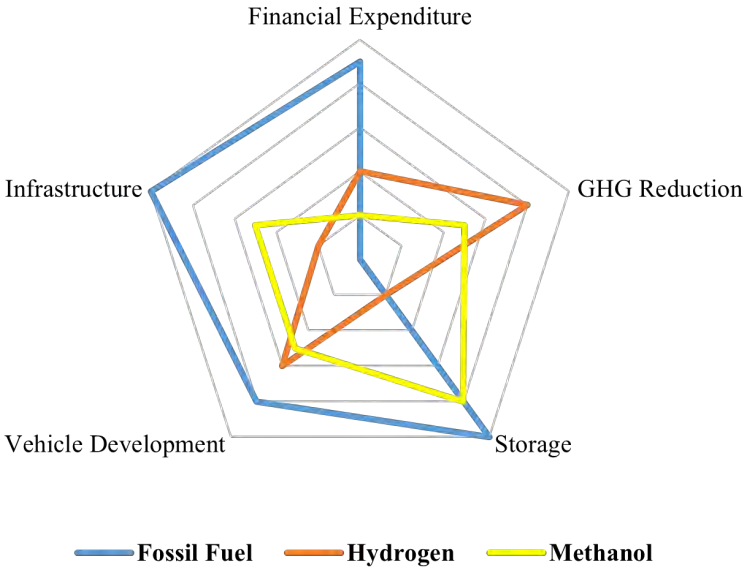

(b) *Methanol.*

Figure 1: *Overview of comparative features of the synthetic fuels analysed in this work. Fossil fuels and hydrogen are added for relative comparison.*

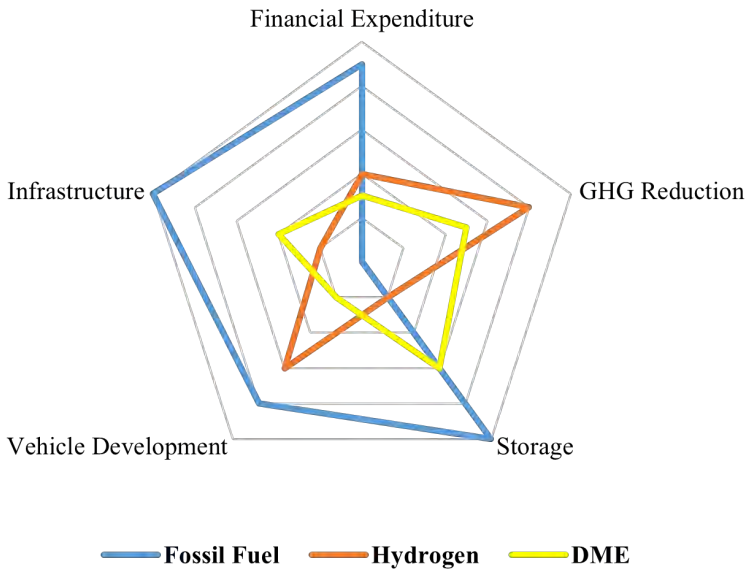

(a) *Dimethyl Ether.*

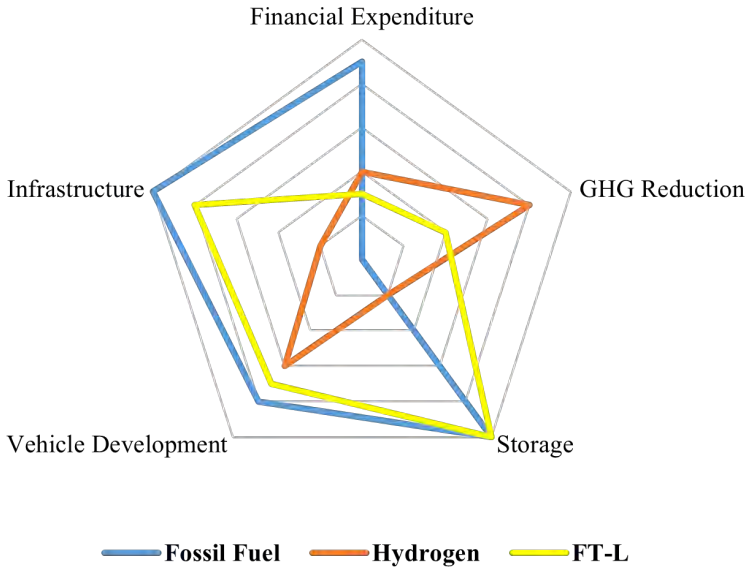

(b) *Fischer-tropsh Diesel.*

Figure 2: *Overview of comparative features of the synthetic fuels analysed in this work. Fossil fuels and hydrogen are added for relative comparison.*

Dedication

In loving memory of my parents and baby

Acknowledgements

Firstly, I would like to thank my supervisors, Prof. Robert Steinberger-Wilckens and Dr Grant Wilson, for their generous guidance and supervision, in particular, for their encouragement, enthusiasm and support throughout this work.

I want to express my gratitude to Dr El-kharouf, Dr Al-sagheer, Mr John Hooper and other colleagues and administrative staff members of the Centre for Fuel Cell and Hydrogen Research in the School of Chemical Engineering at the University of Birmingham, during the term of my postgraduate study.

The financial support received Engineering and Physical Sciences Research Council (EPSRC) and the Centre of Doctoral Training (CDT) is acknowledged gratefully.

To my siblings, Isaac and Victoria, for all their support.

Finally, to Oyewumi Sogbesan, my wife and best friend, for standing by my side through much hardship —thank you!

Contents

List of Figures

List of Tables

Nomenclature

The next list describes unfamiliar abbreviations that will be later used within the body of the document

Abbreviations

$CAPEX$ Capital Expenditures

CCS Carbon Capture and Storage

CCU Carbon Capture Utilisation

$CCUS$ Carbon Capture Utilisation and Storage

CN Cetane Number

DME Mimethyl Ether

FT Fischer Tropsch

GHG Greenhouse Gas

$MeOH$ Methanol

NPV Net Present Value

ON Octane Number

PtX Power-to-X

RES Renewable Energy Sources

$SOEL$ Solid Oxide Electrolyser

TEA Technoeconomic Analysis

Chapter 1

INTRODUCTION

This opening chapter introduces the motivation and research questions from the study concerning global discussions on climate change and energy sustainability. This chapter presents the then[1] current status of the current climate issue and proceeds with a proposed resolution. Finally, the research questions to be considered across the duration of the study are addressed in this thesis.

[1] c. 2019 and Pre-COVID

1.1 Background

The global population has increased by more than 400% over the 20th century. It is projected to continually increase with the population momentum owing to relatively higher fertility rates and a higher life expectancy — due to ever-developing global industrialisation [1]. In parallel, the global energy demand required to sustain an increased living standard and propel civilisation forward will continue to grow [2]. Adversely, the environment has been progressively areas impacted by industrialisation. These environmental areas include the geosphere, hydrosphere, and the atmosphere —, with the impacts becoming increasingly pernicious due to greenhouse gases (GHG) released by the intensive use of nitrogenous fertilizers and fossil fuels.

Carbon dioxide (CO_2) constitutes 64.3% by the concentration of all GHG — a compound gas that absorbs and re-emits infrared (thermal) radiation in the atmosphere [3]. This heat-trapping phenomenon initiated by the absorption of part of the electromagnetic spectrum is known as the greenhouse effect, which induces global warming – the gradual increase in the combined surface air and sea surface temperatures average over the earth and over a period (usually expressed as relative to the 1850 to 1900 period, an approximation of pre-industrial temperatures). Methane (CH_4), nitrous oxide (N_2O) and fluorinated gases (HFCs, PFCs, SF_6, NF_3) constitute the rest of the primary GHG that directly contribute to climate change owing to their positive radiative forcing effect. Others include oxides of sulphur (SOx) and non-methane volatile organic compounds (NMVOC) [4].

Climate-related hazards augmented by anthropogenic global warming (estimated at 1.30 °C above pre-industrial levels as of 2022) other than rising temperatures, include changes to rainfall patterns, rising sea levels, increasing ocean acidification and extreme weather events, such as droughts, heat waves and floods have been found to have direct adverse effects to the limits of human thermoregulation [5].

The adverse effects of climate change extend to the human system in

instances where climate-sensitive biophysical environments and socio-economic and political limitations on adaptive capabilities compound to prompt highly vulnerable situations. Globally, heavy precipitation affects the availability and quality of fresh water, inundations leading to the loss of coastal ecosystems and infrastructure, posing a risk to livelihood. The IPCC report published in 2014 by Arent et al. [6] indicates that the thermal efficiencies of power generation technologies show a reduction due to the availability of cooling water, induced by increasing global temperatures, consequently impacting energy systems directly related to the gross domestic product (GDP). It has been estimated that the economic loss resulting from an adverse climate change in the United States is equivalent to 1.20% cost of GDP per year per 1.00 °C increase in the average global temperature [7].

The issue of climate change is now apparent and poses a potentially irremediable threat to humanity. In recognition of this, and a commitment to secure the future of the next generations, 197 delegates representing their respective countries signed an international treaty, the Paris Agreement, in 2015 [8]. The universal commitment put forward during the COP21[2] (United Nations Framework Convention on Climate Change in 2015) set out to increase efforts to accelerate the objective of limiting the global temperature increase to 1.50 °C above the pre-industrial levels. In addition to the Paris Agreement, public policies relating to global warming and climate change are constantly developed at national, regional and local levels. These policies can be categorised as follows:

1. **Mitigation** – These policies and actions focus on the attenuation of the rate of global warming. The proposed strategies aim to reduce atmospheric GHG either by reducing the sources of the pollutant; or by enhancing sinks that accumulate and store more of these gases. Tree cover programs like reforestation could achieve a global carbon storage potential of up to 205 Gt across its lifetime [9].

[2]COP26 is the latest edition held in Glasgow, UK, in 2021. Outcomes included increased financing towards net zero amidst concern of reaching the 1.50 °C target

2. **Adaptation** – Initiatives and measures to reduce the susceptibility of natural and human systems to the present and/or anticipated detrimental effects of climate change are the main goals of adaptation-driven policies. Disaster risk reduction, migration and financial implications drive the formulation of adaptation policies. Adaptation measures are generally location socio-economic dependent as seen in studies in coastal cities in emergent economies [10] and urban cities in advanced economies [11].

3. **Resilience** – Climate resilience focuses on the robustness of socio-economic systems to withstand the negative impacts of climate change, its redundancy and reliability capacities, and its resourcefulness to respond quickly to a changing environment. Frameworks and measures to enhance the resilience to drought in the case of cocoa farmers in Ghana and Teff in Ethiopia are suggested in Messmer et al. [12], which included reduced tillage and planting early mature varieties.

On the whole, there is a view that the effects of climate change are inexorable and mitigating strategies must take precedence as the overarching global objective relating to climate change is to reduce the net GHG emissions while promoting an environmentally friendly and socio-economically stable society.

1.2 Climate Mitigation Strategies

The global warming potential (GWP) value of a GHG is a quantitative measure of the radiative forcing impact relative to the reference gas; CO_2. The ability to absorb and emit infrared radiation within a spectrum and the atmospheric lifetime of the gas determines its GWP. Despite being less potent than CH_4 and N_2O (GWP: 36 and 298 respectively), CO_2 is the most important GHG due to the quantity emitted.

1.2.1 Energy and Emissions Indicator

The intensive use of fossil fuels accounts for about 80% of the global CO_2 emitted, with the rest attributed to land-use changes [13]. According to the IEA 2021 Net Zero report, it is anticipated that the total global energy demand will increase by 30% between 2020 and 2050 under the current climate policies that are either actionable or announced by government bodies [14].

As a consequence, the amount of CO_2 emitted is projected to maintain the same trajectory despite an increased market share from renewable energy sources (RES), which coincides with a declining share of oil and coal in the global energy resource being deployed. The emission trend can be attributed to the increase in the prosperity of developing economies and emerging markets which outweighs the current improvements in energy efficiency and the deployment of clean energy technology.

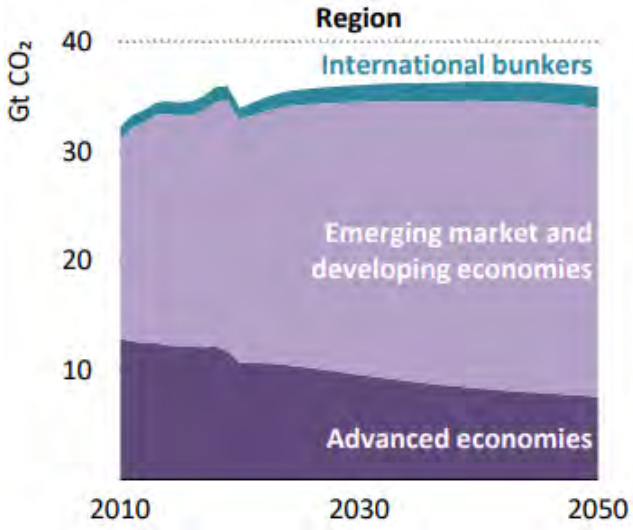

Figure 1.1: *Projected CO_2 emissions by regions under the current energy policy scenario, up to 2050. Modified from [14].*

The problem faced by the energy sector is the challenge to meet the demands of a growing global populous and commit to reducing CO_2 emissions.

1.2.2 Mitigation Measures

Generally, the strategies proposed for climate change mitigation are considered to be built upon the pillars of gains in energy efficiency and substituting fossil fuels with energy sources that emit much lower levels of GHGs. Carbon capture, storage, and utilisation are considered short-term stop-gap technologies that may be useful as long as the use of fossil energy sources is unavoidable.

Energy efficiency improvement practices, including the implementation of energy efficiency-focused building codes and standards, appliance energy efficiency standards and labelling, encouragement of energy efficient urban passenger transport, and promotion of energy service companies (ESCo), have been shown to have cut GHG emissions by 12% since 2000, as shown in Figure 1.2, and are expected to reduce them by a further 12% by 2040 [15].

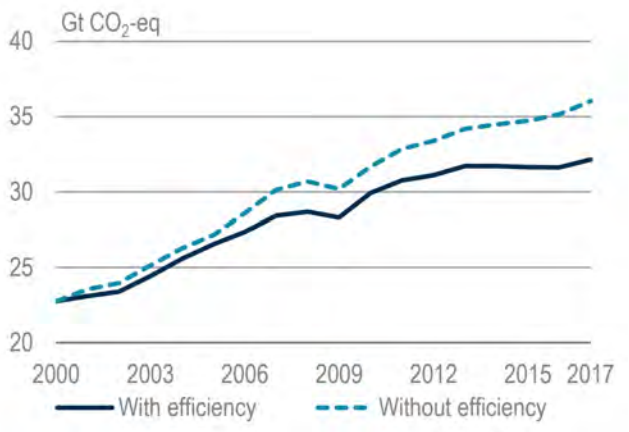

Figure 1.2: *Global energy-related GHG emissions, with and without efficiency improvements [15].*

Deploying clean energy sources such as renewable electricity and biofuels is becoming essential to transitioning to a less carbon-intensive and more sustainable energy system, with consumption from RES progressively increasing.

Carbon capture aims to separate or recover carbon dioxide from large point sources such as waste industrial streams or directly from the atmosphere. The captured carbon can be sequestered in subterranean geological formations such as depleted oil and gas fields or salt caverns; in a process known as carbon capture and storage (CCS). Despite the potential to reduce GHG emissions, CCS concurrently has some downsides associated with leakages. The effect of migration of CO_2 into neighbouring geological formations to react with minerals in long-term underground CCS remains uncertain [16].

Carbon capture and utilisation offer the prospect of re-using[3] the otherwise *waste* CO_2 as a *useful* intermediate for the synthesis of valuable chemicals or as part of a process.

However, it is clear that there is no silver bullet to mitigate climate change

[3]Captured fossil carbon that is re-used is ultimately released into the atmosphere, albeit at a reduced rate.

as there are a number of trade-offs e.g., between socio-economic barriers and stringent policies to accelerate deployment of technologies and changes in behaviour compatible with a lower-emissions world. A solution lies within a 'sweet spot' of the three mitigation options and is shown in Figure 1.3.

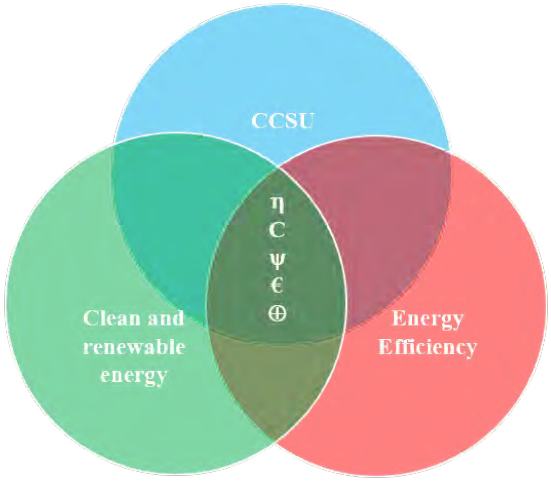

Figure 1.3: *Pillars of climate mitigation strategies; where η is energy efficiency, C is carbon flux, ψ is environmental impact, € is cost, and $\oplus$ is societal acceptance.*

1.3 The Case for Power-to-X as a Technology Serving Decarbonisation

For this research, 'Power-to-X' (PtX) will be defined as the generic conversion technology that converts electrical energy ('power') to another form of energy or chemical feedstock, X including other forms of gaseous and liquid energy vectors; with the application of an electrochemical process central to the whole operation. X can be defined as the desired energy vector and P for electrical energy. P stands for renewable electricity unless stated otherwise. Supplementary processes are employed depending on the feedstock/energy vector desired, as shown in Figure 1.4.

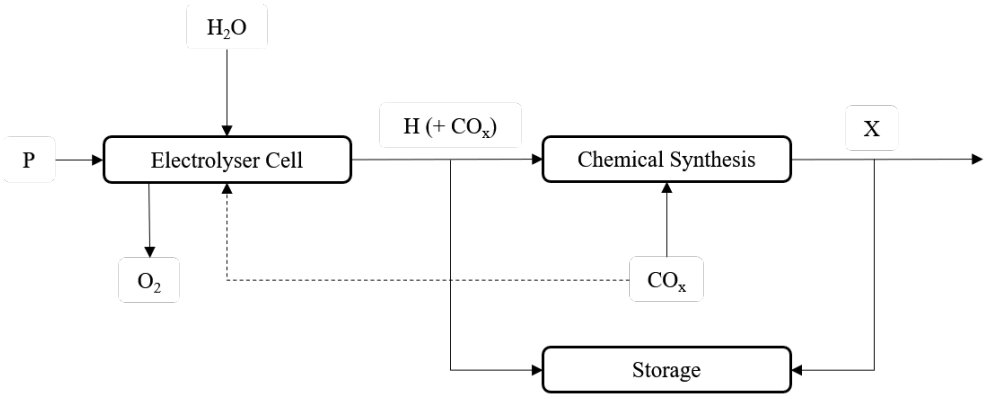

Figure 1.4: *A simplified schematic diagram of a generic PtX.*

The PtX concept is not new. In 1923, John B.S. Haldane pre-empted the need for a clean and renewable hydrogen economy and proposed using surplus power from wind turbines for the electrolytic decomposition of water to produce hydrogen [17]. A characteristic feature of PtX is that it combines mature or nearing commercialisation processes to synthesise diverse products from various feedstock. It is important that a transition technology effectively links the present with the future without creating an expensive technology lock-in.

One of the key strengths of PtX in decarbonisation is its ability to produce a large spectrum of end-products with high compatibility with the current infrastructures, including storage facilities, energy carrier networks, industrial processes

and combustion designs (Figure 1.5). The latter is of particular advantage in hard-to-decarbonise sectors like heavy transport (like road freight and aviation) where the electrification and the extent of the application of fuel cells and batteries are still uncertain [18].

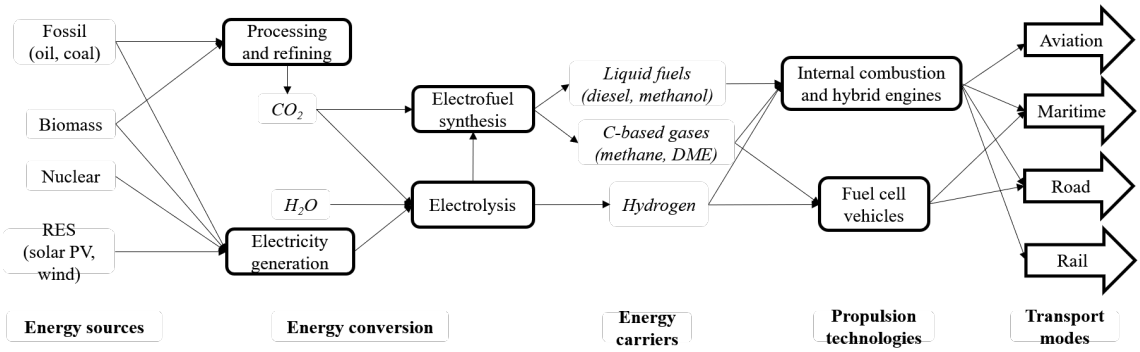

Figure 1.5: *A simple schematic of PtX routes to produce transport fuels.*

Integrating large-scale renewable energy technologies towards the deep decarbonisation of an existing energy system is not without its challenges. Nevertheless, the cost of the installation of RES (for example, solar PV and wind) is falling, and the operational cost is relatively low [19], and as a result, the share of renewable energy will increase as it falls below grid parity [4].

However, integrating RES is expected to increase the volatility of the existing grid's supply and load balance with variable time distribution of their outputs. The variability of and the non-dispatchable nature of RES unveils the electrical grid issues associated with stability. This leads to an increasing requirement for balancing services that are to be delivered through reserve markets [5] [20].

Power quality issues associated with renewable energy integration have been highlighted in studies by Liang [21] and Sinsel et al. [22]. These issues include fluctuations in frequency and voltage and harmonic distortion —due to the modularity of variable renewable energy generators and their non-synchronicity.

[4]The point at which the cost of energy from alternative sources equals that from conventional fossil sources

[5]A means to ensure the extra capacity on demand; to alleviate the volatility of electricity prices

Energy storage can provide grid stability and flexibility opportunities. Short-term options like batteries are predominantly implemented due to their ability to provide quick response and frequency services [23]. Ethical, system and environmental issues related to large-scale battery deployment are studied in the work of Dehghani-Sanij et al. [24]. Compared with batteries, PtX provides the opportunity to effectively absorb the growing capacity of renewable generation to minimise curtailment via long-term storage, owing to its inherent low self-discharge and the potential to design charge/discharge rates and storage capacities independently [25]. This makes cost scaling with a storage capacity more feasible with a strong market growth forecast post-2030 [26].

PtX processes in themselves offer a plethora of flexibility and adaptive options as expressed in Figure 1.6, especially in the context of energy security via its storage capabilities to manage the mismatch between supply and demand. Owing to their average high energy densities, rapid reaction times and capacity, PtX fuels can aid in power grid services, offering frequency and voltage regulation [27].

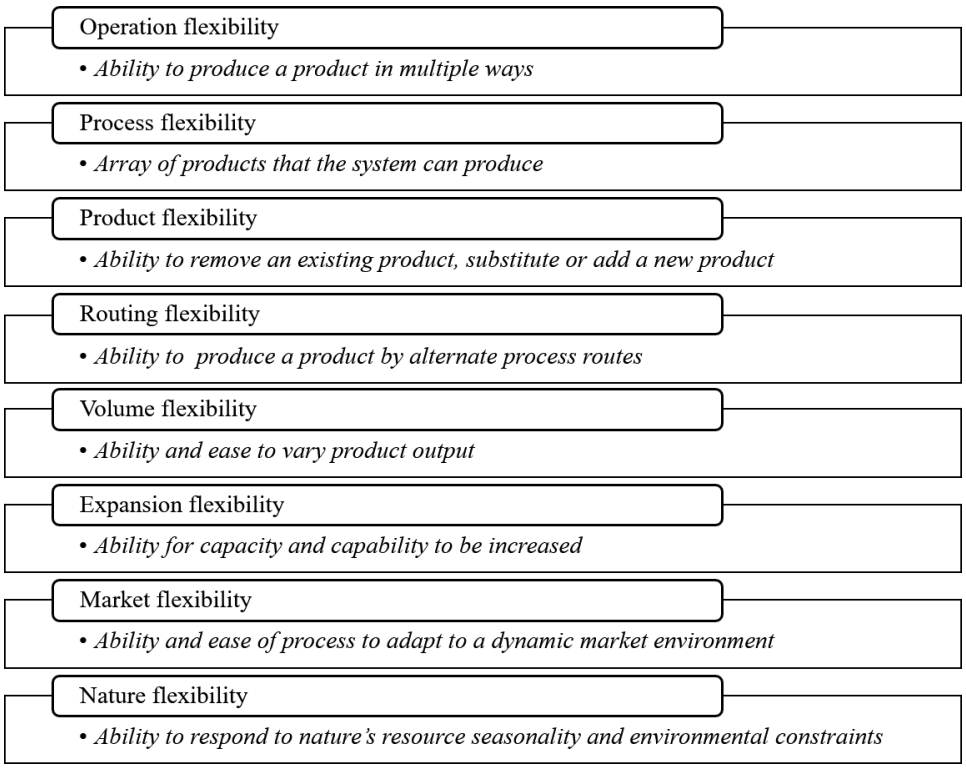

Figure 1.6: *Scope of flexibilities achievable by PtX [28, 29].*

Sectoral coupling is a multi-dimensional concept involving the energy-economic integration of different energy markets (electricity, mobility and heat) to improve grid flexibility issues in the wake of RES penetration. In addition to flexibility, sectoral coupling aims to enable the supply and consumption of different energy vectors and the application of storage technologies across different energy supply infrastructures. Sectoral coupling of the gas and electricity supply systems will require including thermal energy systems to utilise the heat generated and increase overall system efficiencies.

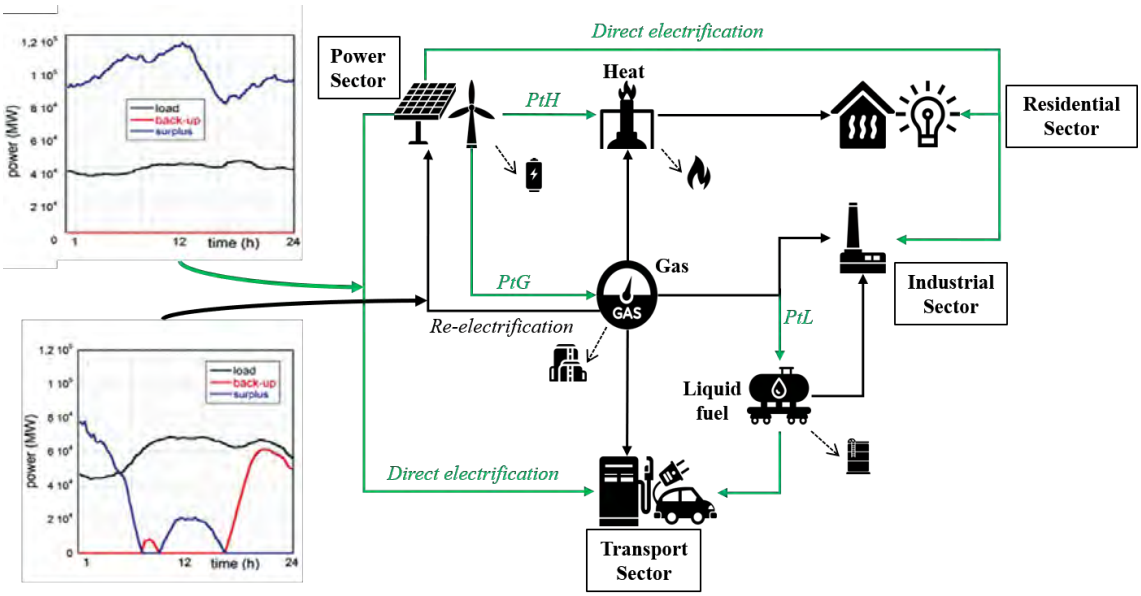

Figure 1.7: *Implementation of PtX technologies in sectoral coupling and storage facilities in RES-based systems. Dashed lines represent storage lines. Adapted from [30, 31].*

Significant developments in solid oxide electrolysis cells (power to gas conversion), which can operate as reversible fuel cells (gas to power conversion), have made sector coupling via PtX technologies more promising, and their implications are studied in [32, 33]. An illustration of an example of sector coupling in a RES system is shown in Figure 1.7. In the work of Connolly and Mathiesen [34], the socio-economic feasibility of transforming the existing energy system to a 100% RES in Ireland while implementing PtX for storage was assessed. The results suggest that the transition is economically viable, with the added benefit of providing around 100,000 direct jobs.

The conventional energy grid system configuration is based on a centralised system. The remoteness between the producer and consumer in an energy supply chain is often a cause of increased susceptibility to reliability issues, transmission losses, and incurred related costs; consequently diminishing the quality of life of the end-users socio-economically, and the liveability of the environment [35]. These systems are managed by a uni-directional demand side management, which increases the system's complexity. The spatial distribution of high-capacity variable renewable generation further compounds this problem.

It is widely accepted that, to move forward, the energy system should develop towards a nexus configuration composed of a connected, integrated and decentralised network of energy hubs to ease the transition towards a more decarbonised system [36]. A constraint of RES is that the resources are merely energy vectors and are inflexible. Figure 1.8 depicts the features of a flexible energy vector.

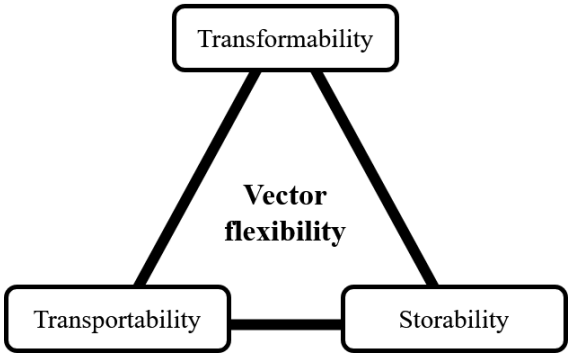

Figure 1.8: *Features of flexible energy vectors.*

While electron vectors are the primary focus of many energy systems, their storage is still economically infeasible on a large scale. The vast spectrum and storage capabilities of the PtX vectors allow the technology to encourage the transition to distributed and decentralised energy networks [37]. Analysis by Zeng et al. [38] on the role of PtX in integrating natural gas and electric power systems with bi-directional energy conversion in a distributed network shows that transmission losses in power and total energy can be reduced with increased penetration of RES.

The development of an energy nexus via or including PtX can maximise

the utilisation of the potential capacities and capabilities of RES, which are often stranded due to its diversity, distribution and fluctuations. Figure 1.9 shows a representation of centralised and decentralised systems.

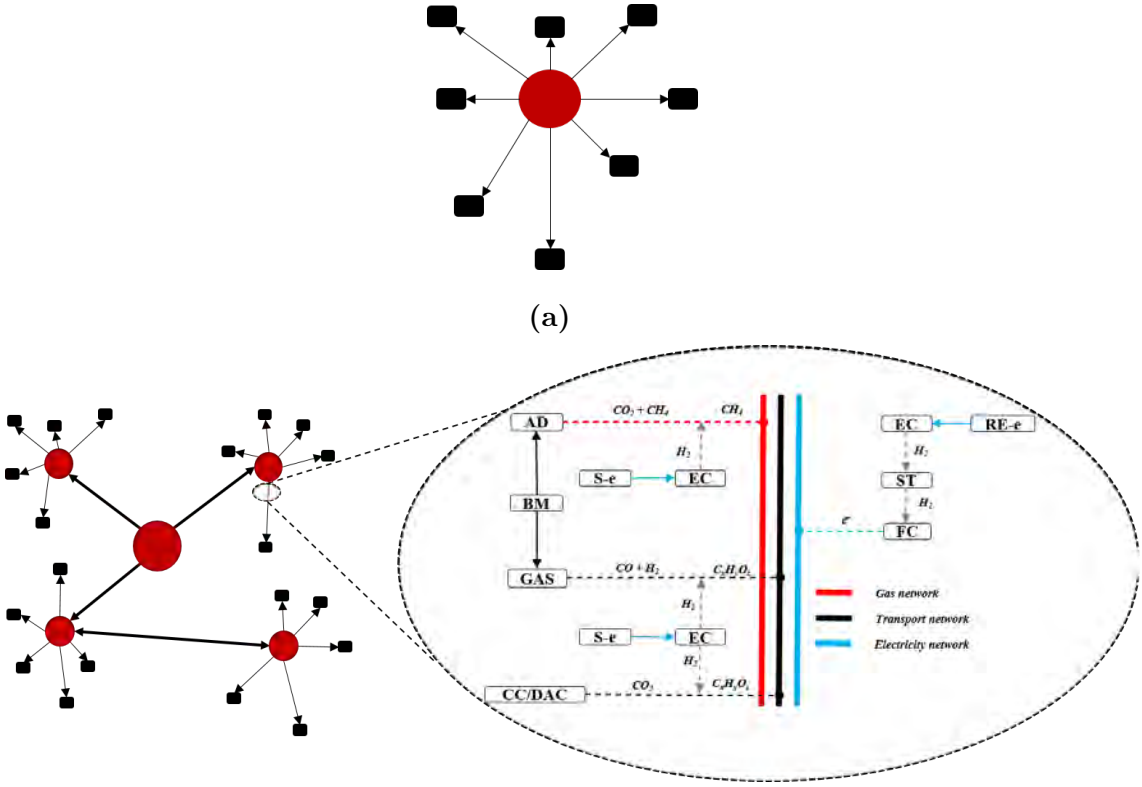

Figure 1.9: *Simplified illustration of (a) a centralised network and (b) a decentralised and connected network with PtX. AD is anaerobic digestion; BM is biomass; GAS is gasification; CC is captured carbon; DAC is direct air capture; s-e is surplus electricity; EC is electrolyser cell; RE-e is dedicated renewable electricity; ST is storage; FC is a fuel cell.*

1.4 Decarbonisation or Defossilisation?

In light of the presented points, the question of whether the immediate need for emission reduction is the absolute eradication of carbonaceous fuels or the substitution of their primary sources in the quest for an energy transition strategy. Carbon and its compounds have been woven into the very fibre of human civilisation of all technological advancement. Bypassing a conscientious transition route based on a molecular and compound bias rather than dealing with the issue on a source-by-source basis may lead to unravelling a somewhat stable albeit environmentally unfriendly energy system.

1.5 Research Questions and Contributions

The high-level research questions that are the focus of the work are:

1. How much carbon is available for CCUS?

2. What is the state of the possible synfuel routes?

3. What are the limitations to its deployment?

4. What scenarios are reasonable to achieve its deployment?

The primary aim of this study is to address specific knowledge gaps via the qualitative assessment of carbon dioxide currently available in the United Kingdom for the production of synthetic fuels via PTX, a transitionary technology. This includes the potential to reduce the rate of GHG emissions, store renewable energy in light of financial, political, and legislative restrictions, and address a "real-life" problem in the transport underclass.

Chapter Structure

The chapters in the following section are:

1. **Chapter 1** introduces the study motivation and research questions.
2. **Chapter 2** reviews the technological process of interest to this study.
3. **Chapter 3** reviews the academic literature on the associated study.
4. **Chapter 4** assesses the technological process via model simulations.
5. **Chapter 5** assesses the potential, capture cost and distribution of carbon in the United Kingdom.
6. **Chapter 6** assesses the techno-economic impact of the studied processes.
7. **Chapter 7** assesses scenarios in which the assessment may be applied.
8. **Chapter 8** assesses the performance of the electrofuels.
9. **Chapter 9** discusses the prospects and barriers to deploying electrofuels.
10. **Chapter 10** presents the final discussion points, concluding remarks and recommendations.

Chapter 2

REVIEW OF FUEL SYNTHESIS PROCESSES AND LITERATURE

This chapter reviews the current technological processes (emerging or established) that are particularly interesting to this research study. The production of hydrogen via electrolysis and recovery of carbon dioxide via carbon capture processes are considered in this chapter. This chapter concludes with the commercialised and state-of-the-art processes for synthesising the products of interest.

As previously mentioned in the Chapter 1, cost-effectiveness, energy efficiency, and environmental impacts are some of the key performance indicators for any climate change mitigation measure. Therefore, this chapter also contains a qualitative review of selected published work that focuses on the feasibility of PtX industrialisation within the scope of the aforementioned criterion. This review aims to position this study in context, validate its novelty, and present key results from previous studies as a basis for comparison with the present work. This chapter will also identify knowledge gaps and posit proposals to narrow them.

2.1 Hydrogen Production by Water Splitting

Water splitting by electricity or heat is the primary process of producing hydrogen based on renewable energy input.

2.1.1 Thermolysis

Thermolysis is the thermal decomposition of water to oxygen and hydrogen when it is subjected to very high temperature, around 2500 °C, required to minimise the Gibbs free energy to zero. Because of the high temperature required in thermolysis, thermochemical water-splitting cycles have been proposed to lower the temperature requirements and improve the overall efficiency. Such cycles include the single-stage water decomposition reaction operating at 1000 °C; and the novel two-step SnO_2/SnO cycle reactions, operating at 1600 °C and 550 °C, respectively [39].

2.1.2 Electrolysis

Electrolysis is a basic technology that uses electrical energy (partly supported by thermal energy) to split water. Water electrolysis technologies can be classified according to the applied electrolyte, which separates the two half-reactions at the anode (oxygen evolution reaction) and the cathode (hydrogen evolution reaction) of the electrolyser. The leading water electrolysis technologies are alkaline electrolysis (AEL), polymer electrolyte membrane electrolysis (PEM) and solid oxide electrolysis (SOEL), which are further discussed in the following.

Alkaline Electrolysis

Alkaline electrolysis is a mature technology that uses an aqueous alkaline solution (KOH or NaOH) as the electrolyte to transfer electrons via hydroxide anions (OH^-) to dissociate water into hydrogen and oxygen. AELs can operate atmospherically or under elevated pressure to produce a hydrogen quality of 99.5%

and up to 99.99% after additional purification (deoxidiser). Depending on the size of the electrolyser, which can range from tens of kWs to a few MWs, and the operating conditions, the efficiencies vary between 66 and 78% [40].

The partial reaction at the AEL cathode is:

$$2\,H_2O + 2\,e^- \longrightarrow H_2 + 2\,OH^- \qquad \text{(R 1)}$$

while the reaction at the AEL anode is:

$$2\,OH^- \longrightarrow \frac{1}{2}\,O_2 + H_2O + 2\,e^- \qquad \text{(R 2)}$$

AELs can operate between 20% and 100% of their design capacity and overload operation of up to 150% [41]. Fluctuating power sources mean that AEL systems have a major drawback in the long start-up times of up to 60 min due to purging operations with nitrogen [42]. Another disadvantage is that the utilised electrolytes are highly corrosive and require a system overhaul every 7 to 12 years [41].

Polymer Electrolyte Membrane Electrolysis

PEMEs, often known as proton exchange membrane electrolysis, use a polymer membrane (e.g. Nafion®) as an electrolyte. A corrosive acidic regime provided by the membrane requires using noble materials like platinum for the cathode and iridium for the anode catalysts. PEMEs generally operate from 293 K to 373 K with quoted efficiencies varying between 67 and 82% [41].

The partial reaction at the PEM cathode is:

$$2\,H^+ + 2\,e^- \longrightarrow H_2 \qquad \text{(R 3)}$$

while the reaction at the PEM anode is:

$$H_2O \longrightarrow \frac{1}{2}\,O_2 + 2\,H^+ + 2\,e^- \qquad \text{(R 4)}$$

PEMEs have a very short start-up time from both transient (in seconds) and cold operation mode (a few minutes) and operate between a load capacity of 0% to 100% to produce high-purity hydrogen (>99.99%) without the need for additional purification equipment. However, PEMEs have a shorter lifetime than AEL systems, and their lower technology readiness levels mean that it currently has a higher CAPEX than AELs [43].

Solid Oxide Electrolysis

Solid Oxide Electrolysis is also known as high-temperature electrolysis due to its high operating temperature range between 973 K to 1273 K. With high operating temperatures, SOELs could theoretically achieve high electrical efficiencies up to 100% [1] due to improved kinetics and thermodynamics favouring internal heat utilisation and steam conversion. Coupling SOELs with exothermal fuel syntheses processes like methanation and Fischer-Tropsch presents an interesting option in PtX systems. SOEL use ceramic electrolytes (e.g., ZrO_2 ceramic doped with Y_2O_3), which at high temperatures are highly conductive for oxygen ions, and have a high thermal and chemical stability [41].

The partial reaction at the SOEL cathode is:

$$H_2O^+ + 2\,e^- \longrightarrow H_2 + O^{2-} \qquad \text{(R 5)}$$

while the reaction at the SOEL anode is:

$$O^{2-} \longrightarrow \frac{1}{2}\,O_2 + 2\,e^- \qquad \text{(R 6)}$$

The biggest challenges SOEL systems faces are fast material degradation and limited long-term stability resulting from the high-temperature operation. SOELs have an interesting feature of being able to co-electrolyse H_2O and CO_2 to produce syngas ($CO_x + H_2$), a primary feed for synthetic fuels.

[1] This is theoretically achievable through the utilisation of external heat source for steam production, e.g. excess heat from industrial processes

2.2 Biogas Conversion

Biogas is the product of organic material's biological decomposition via anaerobic digestion (AD). AD is a complex anaerobic process facilitated by a distinct consortium of bacteria that drives individual phases of hydrolysis, acidogenesis, acetogenesis, and methanogenesis of organic substrates to produce a mixture of gaseous compounds (see Figure 2.1).

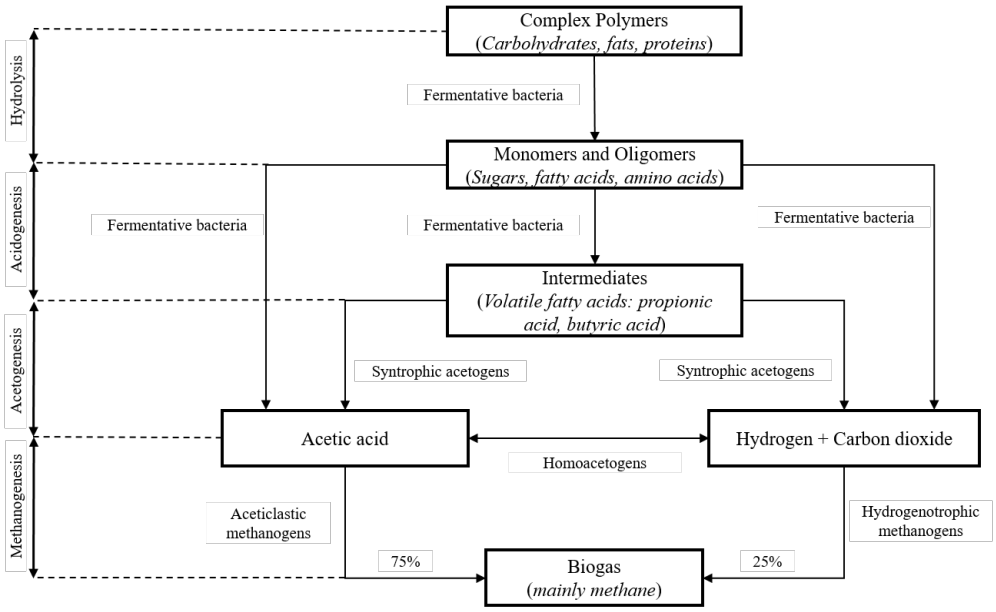

Figure 2.1: *Schematic diagram of the anaerobic digestion process of substrates in biogas production (modified from [44]).*

Biogas primarily consists of CH_4 (50 to 70%(v/v)) and CO_2 (30 to 50%(v/v)). Other components include N_2 from the air saturated in the influent of up to 3%(v/v), water vapour from medium evaporation at concentrations of (5 to 10%(v/v)), O_2 entering the process from the influent substrate at concentrations of, up to 1%(v/v).

Minor quantities of hydrogen sulphide (H_2S) from the reduction of sulphate contained in some waste streams up to 1 cL/L, ammonia (NH_3) from the hydrolysis of proteinaceous materials at up to 200 mg/m^3 and, siloxanes in concentration at 41 mg/m^3 may be present [45]. Removing harmful contaminants such as H_2S and

siloxanes and upgrading biogas is necessary to meet gas grid requirements and can increase the calorific value by 80%. Biogas is commonly upgraded by one of the following processes: (a) CO_2 stripping, (b) biological process, and (c) chemical process of which a selected few are discussed in the following.

Physical absorption is the most common technique of biogas upgrading by CO_2 removal [46]. The process uses water as a scrubbing medium and relies on the relatively high solubility of CO_2 in water compared to methane, according to Henry's law. The process can remove trace amounts of H_2S to achieve high methane concentrations of up to 99% upon dehydration [47]. Organic solvents like Selexol® can absorb three times more CO_2 than water, allowing for a more compact design without the need for dehydration. However, this process incurs a higher methane loss than the former [45].

Membrane separation provides a more economically competitive alternative to absorption techniques. The process is governed by the porosity of the membrane material and the gas diffusion along the dense area, based on Fick's law, to separate the gas components. Materials like polyimide and carbon molecular sieves are commonly used to achieve relatively low investment and operational costs for biogas upgrades. Membrane separation is, however, characterised by yielding lower methane concentrations (95% [2]) compared to physical absorption techniques [45]. Pressure swing adsorption (PSA) is based on the adhesive quality of gas components based on their respective molecular sizes onto adsorbents like zeolites. PSA is energy-intensive, incurring a high capital investment and operational costs, as it requires high-pressure systems and dedicated vessels for operation.

While it is the least employed CO_2 removal technique, the liquefaction of biogas via cryogenic separation can provide the opportunity to increase the volumetric density of biogas by a factor of 600 while storing pure CO_2 in a compact solid phase [48]. The cryogenic method takes advantage of the different condensation

[2]The rest can either be recycled or emitted within the prescribed limits

temperatures of biogas composites in a step-wise manner. Water and dissolved organic compounds are condensed and removed at 6 °C. After compression, the temperature further reduces to −25 °C, where other impurities like H_2S and siloxanes are removed. CO_2 is frozen at −78.50 °C and removed with high purity in the penultimate step before the remaining gas stream is liquefied at −190 °C as CH_4 with a purity of 99%, and the rest as N_2. However, cryogenic separation is very energy intensive (operating conditions up to 200 bar) and incurs high investment costs. Liquified methane can be directly used as a drop-in replacement for liquified natural gas, even pricing better quality —, in which case the energy expenditure for liquefaction would be justified.

The high CO_2 content in biogas provides another pathway to increase its calorific value via biological methanation. Unlike catalytic methanation, the biological process alleviates the associated economic burden of the catalyst and energy requirements by facilitating chemoautotrophic hydrogenotrophic methanogens, active within a temperature range of 0 °C to 122 °C [49]. In addition, catalytic methanation requires that the CO_2 is free from impurities (such as siloxanes and H_2S) for further processing. In contrast, biological methanation has a higher tolerance for impurities and can remove them, acting as a cleaning process [50].

Two technical configurations of upgrading biogas via biological methanation are: *in situ* and *ex-situ*. In the *in situ* concept, H_2 is directly injected into the anaerobic digester to react with the internally produced CO_2 in the off-gas. A methane recovery of 99% can be achieved in optimal conditions [45]. One technical challenge to be overcome is the regulation of the pH to levels below 8.5, above which inhibit methanogenesis is inhibited. The removal of the bicarbonate buffer, produced by the utilisation of CO_2 (see Reaction (7)), is the primary reason for the pH elevation.

$$H_2O + CO_2 \rightleftharpoons H^+ + HCO_3^- \qquad \text{(R 7)}$$

The main difference with the *ex-situ* concept is the requirement of a separate reactor. Some advantages include; (a) control of the conventional biogas process, (b) independence of biomass source, (c) flexibility for external sources of CO_2. However, the process incurs additional investment costs for the extra process step. Biological methanation is suited as a PtG concept, provided the electrical power is from renewable sources.

Syngas is an attractive intermediate in the production of synthetic fuels. Dry methane reforming (DMR) of biogas (see Reaction (8)) provides an opportunity to convert its primary components (CO_2 and CH_4, gases with high global-warming potential in their own rights) to syngas and, in a H_2/CO ratio that favours the carbonylation and hydroformylation process in the synthesis of liquid fuels.

$$CH_4 + CO_2 \rightleftharpoons 2\,CO + 2\,H_2 \quad \Delta H^{\ominus} = 247.0\ kJ/mol \qquad \text{(R 8)}$$

One major drawback is the highly endothermic nature of the process, requiring high temperatures to reach acceptable conversion rates. In addition, accompanying reactions like the Boudouard process[3] and methane cracking increases the likelihood of carbon formation and deposition, which leads to catalyst deactivation.

Steam reforming (SMR; see Reaction (9)) is the conventional method for hydrogen production from methane and can thus be applied in the production of syngas from biogas. The reaction is also endothermic and, like dry reforming, suffers from the high energy demand. In the case of biogas reforming, H_2S needs to be removed to avoid catalyst deactivation due to sulphur poisoning.

$$CH_4 + H_2O \rightleftharpoons CO + 3\,H_2 \quad \Delta H^{\ominus} = 206.0\ kJ/mol \qquad \text{(R 9)}$$

[3] $C + CO_2 \rightleftharpoons 2\,CO$

Partial oxidative reforming (POR; see Reaction (10)) uses oxygen to partially oxidise CH_4 to yield syngas.

$$CH_4 + \frac{1}{2}O_2 \longrightarrow CO + 2\,H_2 \quad \Delta H^{\ominus} = -25.2\ kJ/mol \qquad (R\ \mathbf{10})$$

POR is exothermic in nature and can be combined with DMR and SMR, providing thermal energy for the endothermic processes. Chen and Lin [51] used a spiral Swiss-roll reactor to investigate biogas conversion to syngas via catalytic partial oxidation. The results yielded a 31.12% conversion of CO_2 and a syngas yield of $2.80\,\mathrm{mol/mol_{CH_4}}$.

2.3 Direct Hydrogenation of Carbon

The comparison of the energy density of Li-ion batteries with potential PtX products in Figure 2.2, shows that the latter vectors (RHS of the figure) provide the opportunity to alleviate the problems relating to energy storage density for transport applications, also introducing an element of ease of handling. The figure also reflects the poor capacity for batteries (LI-ion in the figure) to handle large-scale energy storage, in comparison to other fuels.

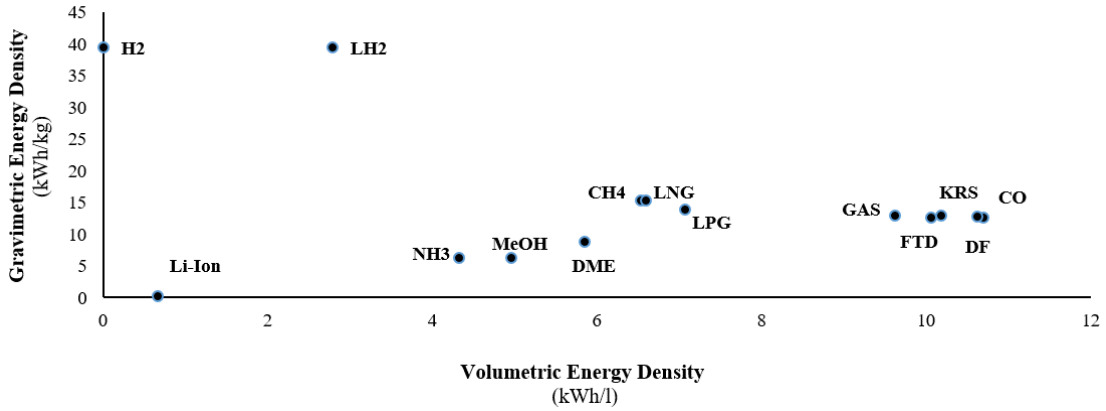

Figure 2.2: *The energy densities of various H-containing fuels in comparison, where GAS is petrol, KRS is kerosene, DF is diesel fuel, and CO is crude oil.*

This section addresses the processes that involve the direct catalytic reactions between H_2 and CO_x (CO_2 and/or CO) to produce fuels. The primary synthetic fuels considered in this section are methane, methanol, DME, and synthetic diesel.

2.3.1 Fuel Properties

The quality of transport fuels in combustion engines is described by fuel properties that include the kinematic viscosity, density, heating value, flash point, and ignition quality.

The kinematic viscosity of a fuel governs the fluid's internal resistance to gravitational forces, fuel atomisation and its spray quality. The fuel kinematic

viscosity is proportional to the fuel pump consumption and the required pump power. A low viscosity may result in potential leakages. In contrast, a high viscosity may inhibit the fuel flow rate intake, delaying the mixing of the fuel and air in the combustion chamber [52]. The former attribute is often preferred in combustion engines. Fuel density is directly proportional to its viscosity.

The heating value of a fuel defines the amount of energy generated upon complete oxidation of the fuel. A high energy content is desired regarding engine performance and thermal efficiency. The flash point is important for safely handling the fuel as it indicates the lowest temperature at which the fuel's vapour will spontaneously ignite.

The two types of internal combustion engines —compression ignition (CI) and spark ignition (SI); generally run on diesel fuel and gasoline fuel, respectively. A fuel's abnormal or uneven combustion is commonly called combustion or engine knock. Anti-knock properties of fuels are described by standardised fuel ratings —octane number (ON) and cetane number (CN). ON is the percentage of *iso*-octane in the blend of *iso*-octane and *n*-heptane, and it describes the pre-ignition resistant of gasoline fuel in an SI engine. The CN of diesel fuel is determined by a ratio of cetane and *iso*-cetane. It describes the delay time in the ignition and the reliability of the fuel ignition upon compression in a CI engine.

Table 2.1: *Selected fuel properties.*

Property	**Methane**	**Methanol**	**DME**	**FT-D**
Kinematic viscosity, $10^{-6}mm^2/s$	16.67	73.7	0.185	2.4
Lower heating value, MJ/kg	45.0	19.9	28.7	42.5
Flash point, ℃	-188	11	-41.1	52-82
Fuel rating,	130^{*O}	114^{*O}	$55\text{-}60^{*C}$	$40\text{-}55^{*C}$

* O is the octane number, and C is the cetane number.

2.3.2 Methane

The methanation reaction, also known as the Sabatier reaction, was first developed by Sabatier and Senderens [53], and developed to remove carbon oxides from feed gases in ammonia plants in the 1900s. Thermodynamically, the Sabatier reaction (see Reaction (11)) is generally treated to be a linear combination of an endothermic reverse water gas shift (rWGS) reaction (see Reaction (12)) and an exothermic CO methanation reaction (see Reaction (13)).

$$CO_{2(g)} + 4\,H_{2(g)} \rightleftharpoons CH_{4(g)} + 2\,H_2O_{(g)}, \qquad \Delta H^{\ominus} = -164.7\ kJ/mol \qquad \text{(R 11)}$$

$$CO_{2(g)} + H_{2(g)} \rightleftharpoons CO_{(g)} + H_2O_{(g)}, \qquad \Delta H^{\ominus} = 41.1\ kJ/mol \qquad \text{(R 12)}$$

$$CO_{(g)} + 3\,H_{2(g)} \rightleftharpoons CH_{4(g)} + H_2O_{(g)}, \qquad \Delta H^{\ominus} = -206.0\ kJ/mol \qquad \text{(R 13)}$$

The Sabatier reaction is a thermodynamically favourable process ($\Delta G^{\ominus} = 130\,\mathrm{kJ\,mol^{-1}}$, at low temperatures). However, reducing the carbon oxide in the aforementioned reaction (see Reaction (11)) is an eight-electron process with significant kinetic limitations, hence requiring a catalyst to realise acceptable selectivity and conversion rates [54]. Metals in groups VII to X have been the most suitable for hydrogenating CO_x to CH_4. In a study by Vannice [55], these metals were ordered according to their respective activity and selectivity:

$$\textit{Activity} : \mathrm{Ru} > \mathrm{Fe} > \mathrm{Ni} > \mathrm{Co} > \mathrm{Rh} > \mathrm{Pd} > \mathrm{Pt} > \mathrm{Ir}$$

$$\textit{Selectivity} : \mathrm{Pd} > \mathrm{Pt} > \mathrm{Ir} > \mathrm{Ni} > \mathrm{Rh} > \mathrm{Co} > \mathrm{Fe} > \mathrm{Ru}$$

Ruthenium (Ru) has the highest activity, a high CH_4 selectivity at low temperatures and a high resistance to oxidising atmospheres [56]. However, Ru, as with the other noble metals like platinum (Pt), palladium (Pd) and rhodium (Rh), is not cost-effective for industrial-scale methanation processes (rising from 7.66 €/g

in 2014, to 243.87 €/g, as at July 2020) when compared to nickel (Ni) and iron (Fe) (with the former at 0.01 €/g, as at July 2020) [57].

Fe-based catalysts gain from being the least costly of the aforementioned metals for the hydrogenation of CO_2. In a study by Kirchner et al. [58], a CH_4 yield of 54% was achieved when using nano-sized γ-Fe_2O_3 catalyst at 400 °C and ambient pressure conditions; at a molar H_2/CO_2 ratio of 200. A CO_2 conversion of 17% and CH_4 selectivity of 6% were increased to 20% and 8% respectively when the gas hourly space velocity (GHSV) was reduced from $12 \times 10^4\,h^{-1}$ to $3 \times 10^4\,h^{-1}$.

A higher selectivity for CH_4 of 65% was achieved when a pure α-Fe_2O_3 catalyst was promoted with 2 wt% of Mg, under higher pressure conditions (8 bar) and a lower GHSV of $1 \times 10^4\,h^{-1}$ [59]. An investigation by Franken and Heel [60], for a set of catalysts with 1 to 10 wt% Fe-supported on zeolite 13X at elevated pressures, showed a higher selectivity for CH_4 of 76%. However, Fe-based catalysts tend to form undesired higher hydrocarbons due to their high activity towards the rWGS reaction at elevated pressures.

Ni-based catalysts evidence high activity and selectivity towards the formation of CH_4. The catalytic performance of Ni/Hβ40 revealed a yield and selectivity of 80% and almost 100% in an experimental study in [61]. Comparable results of a CO_2 conversion of 87% and selectivity to CH_4 of $\geq$99% for Ni/MgO catalysts were achieved by [62], at operating temperatures up to 375 °C.

To achieve high CO_2 conversions, the high activation energy barrier must be overcome, which is otherwise difficult at low temperatures. However, Ni-based catalysts are often subject to deactivation due to carbon deposition and sintering of active Ni particles because of the exothermic nature of the Sabatier reaction [63]. On the other hand, the formation of nickel carbonyls in CO rich conditions at low temperatures also promotes the deactivation of Ni-based catalysts [64]. Nickel carbonyls pose health and environmental issues due to their toxic characteristics. Neverthe-

less, Ni-based catalysts remain the most common metals used in the methanation processes.

In addition to the performance of the catalysts, insight into the mechanistic steps involved in the hydrogenation of the carbon oxides is integral in identifying and understanding the kinetic limitations that should be overcome in the process operation [65]. For the hydrogenation of CO_2, there are two widely accepted mechanism schemes: (a) the dissociative scheme and, (b) the associative scheme.

The dissociative scheme postulates that gaseous carbon dioxide molecules are initially adsorbed on the surface of the catalyst and dissociate into carbonyl (CO_{ad}) and oxygen (O_{ad}) atoms. The adsorbed CO_{ad} species is subsequently hydrogenated to CH_4. In the associative scheme, the CO_2 is adsorbed as CO_{3ad}. This results in a possibility oxygenates such as bicarbonate (HCO_{3ad}), formyl (CHO_{ad}) and formate ($HCOO_{ad}$), particularly the latter is formed as an intermediate [56].

The proposed elementary steps in the CO_2 dissociative scheme is as follows (where ψ refers to a surface site on the catalyst). Each following line refers to the succeeding steps:

$$\begin{aligned}
CO_{2(g)} + 2\,\psi &\rightleftharpoons CO{\cdot}\psi + O{\cdot}\psi \\
H_{2(g)} + 2\,\psi &\rightleftharpoons 2\,H{\cdot}\psi \\
CO{\cdot}\psi &\rightleftharpoons CO_{(g)} + \psi \\
CO{\cdot}\psi + \psi &\rightleftharpoons C{\cdot}\psi + O{\cdot}\psi \\
C{\cdot}\psi + 4\,H{\cdot}\psi &\rightleftharpoons CH_4{\cdot}\psi + 4\,\psi \\
CH_4{\cdot}\psi &\rightleftharpoons CH_{4(g)} + 4\,\psi \\
O{\cdot}\psi + 2\,H{\cdot}\psi &\rightleftharpoons H_2O{\cdot}\psi + 2\,\psi \\
H_2O{\cdot}\psi &\rightleftharpoons H_2O_{(g)} + \psi
\end{aligned}$$

And the associative scheme is as thus:

$$\mathrm{CO_{2(g)}} + \psi \rightleftharpoons \mathrm{CO_{2(g)}{\cdot}\psi}$$

$$\mathrm{H_{2(g)}} + 2\,\psi \rightleftharpoons 2\,\mathrm{H{\cdot}\psi}$$

$$\mathrm{CO_2{\cdot}\psi} + \mathrm{H{\cdot}\psi} \rightleftharpoons \mathrm{HCOO{\cdot}\psi} + \psi$$

$$\mathrm{HCOO{\cdot}\psi} + \mathrm{H{\cdot}\psi} \rightleftharpoons \mathrm{HCO{\cdot}\psi} + \mathrm{OH{\cdot}\psi}$$

$$\mathrm{HCO{\cdot}\psi} + \mathrm{H{\cdot}\psi} \rightleftharpoons \mathrm{CH{\cdot}\psi} + \mathrm{OH{\cdot}\psi}$$

$$\mathrm{CH{\cdot}\psi} + 3\,\mathrm{H{\cdot}\psi} \rightleftharpoons \mathrm{CH_{4(g)}} + 4\,\psi$$

$$\mathrm{OH{\cdot}\psi} + \mathrm{H{\cdot}\psi} \rightleftharpoons \mathrm{H_2O{\cdot}\psi} + 2\,\psi$$

A study of the reaction mechanisms pertaining to the methanation of CO_2 on Ni-based catalysts was undertaken by Aldana et al. [66], revealing that the operating conditions (temperature and pressure) and the H_2:CO_2 ratio heavily influenced the pathway. As with CO_2, the hydrogenation of CO follows a dissociative route where the C-O bond is severed at the active site or by the disproportionation of CO in a Boudouard reaction; to form C_{ad} for subsequent hydrogenation [67]. In the associative mechanism of CO, carbon-hydroxyl (COH_{ad}) and formyl (CHO_{ad}) intermediates are formed by the combination of H_{ad} and CO_{ad} to encourage the breaking of the C-O bond; a kinetically difficult process in the absence of a H_2 rich environment [67].

The operating conditions and feed stream compositions influence not only the rates and mechanisms but also the effluent composition. In addition to Reactions (11) to (13), other possible side reactions can occur during the hydrogenation of carbon oxides. Such reactions include;

$$CO_{2(g)} + CH_{4(g)} \rightleftharpoons 2\,CO_{(g)} + 2\,H_{2(g)}, \qquad \Delta H^{\ominus} = 247.0\ kJ/mol \quad \text{(R 14)}$$

$$2\,CO_{(g)} \rightleftharpoons C_{(s)} + CO_{2(g)}, \qquad \Delta H^{\ominus} = -172.4\ kJ/mol \quad \text{(R 15)}$$

$$CH_{4(g)} \rightleftharpoons C_{(s)} + 2\,H_{2(g)}, \qquad \Delta H^{\ominus} = 74.6\ kJ/mol \quad \text{(R 16)}$$

$$CO_{(g)} + H_{2(g)} \rightleftharpoons C_{(s)} + H_2O_{(g)}, \qquad \Delta H^{\ominus} = -131.3\ kJ/mol \quad \text{(R 17)}$$

$$CO_{2(g)} + H_{2(g)} \rightleftharpoons C_{(s)} + 2\,H_2O_{(g)}, \qquad \Delta H^{\ominus} = -90.1\ kJ/mol \quad \text{(R 18)}$$

$$nCO_{(g)} + (2\,n + 1\,)H_{2(g)} \rightleftharpoons CnH_{2n+2(g)} + nH_2O_{(g)} \quad \text{(R 19)}$$

$$nCO_{(g)} + (2\,n)H_{2(g)} \rightleftharpoons CnH_{2n(g)} + nH_2O_{(g)} \quad \text{(R 20)}$$

It is important that the operating conditions are controlled to suppress the formation of undesired by-products, such as solid carbon produced from the reduction of carbon oxides (see Reactions (17) and (18)). The deactivation of the catalyst due to carbon deposition is one of the technical challenges faced [68].

The catalytic methanation reaction is a highly exothermic process, so good heat management and reactor design are crucial to mitigating thermodynamic limitations, preventing hot spots that might damage catalysts, and allowing for more reliable and efficient performance. Methanation reactors are generally classified according to the temperature profile within the reactor; adiabatic, isothermal and polytropic. A study by Kiewidt and Thöming [69] demonstrated that the Semenov number (Se) is appropriate to describe the kinetic and thermodynamic limitations of methanation reactors as pertaining to temperature profiles.

$$Se = \frac{Da_I \cdot B}{St} = \frac{\text{Heat production rate}}{\text{Cooling rate}} \tag{2.1}$$

Da_I, B and St, are the 1st Damköhler number and the Stanton number, respectively, further described in [69].

A low Semenov number ($Se \rightarrow 0$) describes isothermal reactors, which

fluidized-bed reactors (FBR) and three-phase reactors (TPR) fall under. They operate at moderate temperatures, promoting a high carbon oxide conversion but otherwise inhibiting reaction rates. The heat removal from both reactors is considerably effective. Common drawbacks with fluidized-bed reactors include attrition of catalysts and thermodynamic limitations due to incompatibility with high-temperature conditions [65]. Three-phase reactors are less susceptible to rapid temperature changes due to the additional heat capacity of the liquid phase [70]. However, the liquid phase also increases the limitations due to the mass transfer resistance.

Adiabatic fixed-bed reactors (AFBR) ($Se \rightarrow \infty$) have a simple design and are characterised by having high reaction rates and a wide range of operations. However, due to a high-temperature gradient, a product re-circulation system or steam addition might be required, adding a complex process step.

Polytropic reactors ($0 < Se < \infty$) like micro-reactors (MR) and cooled fixed-bed reactors (CFBR) offer the opportunity to alleviate the drawbacks of high-pressure drops and hots spots synonymous with Adiabatic fixed-bed reactors, coupled with the low outlet temperature feature of isothermal reactors. Notwithstanding, the reactor costs are considerably high.

Table 2.2 shows the characteristic features of different methanation reactors.

Table 2.2: *Comparison between methanation reactors (modified from [71]).*

Concept	FBR	TPR	AFBR	MR	CFBR
Mode	Isothermal	Isothermal	Adiabatic	Polytropic	Polytropic
Reactor Stages	1–2	1–2	2–7	1–2	1–2
Gas recycling	Occasionally	No	Frequently	No	Occasionally
Temperature (°C)	300–400	300–350	250–700	250–500	250–500
Thermal stress[1]	Low	Low	High	Moderate	Moderate
Mechanical stress[1]	Low	Low	Low	Low	Low
Process Complexity	Low	Low	High	Low	Low
Cost	Low	Low	Medium	Very high	High
TRL[2]	7	4	9	4	7

[1] On the catalyst.

[2] TRL: Technology readiness level

2.3.3 Methanol

The earliest industrial production of methanol (methyl alcohol or MeOH for the purpose of this study) was realised in 1923 by Badische Anilin und Soda Fabrik (BASF), who had developed a metal-based catalytic hydrogenation process, known as the BASF process. The primary reactions involved in MeOH synthesis are shown below in Reactions (21) and (22):

$$CO_2 + 3\,H_2 \rightleftharpoons CH_3OH + H_2O \qquad (R\ \mathbf{21})$$

$$CO + 2\,H_2 \rightleftharpoons CH_3OH \qquad (R\ \mathbf{22})$$

Reaction (22) is a combination of the following steps:

$$CO + H_2 \rightleftharpoons CH_2O \qquad (R\ \mathbf{23})$$

$$CH_2O + H_2 \rightleftharpoons CH_3OH \qquad (R\ \mathbf{24})$$

Reactions (21) and (22) are exothermic ($-61.59\,\mathrm{kJ\,mol^{-1}}$ and $-100.46\,\mathrm{kJ\,mol^{-1}}$, respectively), thus favouring lower reacting temperatures and elevated pressures. The BASF process employed ZnO/Cr_2O_3 catalyst, and operating temperatures up to 400 °C due to the low catalytic activity. In addition, pressure up to 350 bar is required to compensate for a low syngas conversion arising from less favourable thermodynamic equilibrium conditions at high temperatures [72].

Imperial Chemical Industries (ICI now Johnson Matthey) introduced a more active Cu-based catalyst suitable for lower operating conditions of 100 bar and 100 °C. An investigation by Fujitani and Nakamura [73], to ascertain the effects of ZnO in Cu/ZnO showed that the resulting Cu−Zn alloy site increases in specific activity for MeOH synthesis. Further work by the authors indicated that the synergistic effect of ZnO increases CO_2 adsorption and Cu dispersion, in addition to metallic Cu atoms that catalyse a plethora of hydrogenation steps [74].

An understanding of the reaction mechanisms on Cu-based catalysts is

essential for the enhancement of the production efficiency for the hydrogenation of COx to MeOH. The formation of formate as an intermediate specie ($HCOO_{ad}$) is a proposed pathway for Reaction (21). $HCOO_{ad}$ is formed from the reaction of the dissociated H_2 adsorbed with CO_2. The formation of a formyl intermediate (HCO_{ad}) was proposed by Grabow and Mavrikakis [75] as a H-carrier in a CO-assisted hydrogenation reaction. In addition to the formate route, the hydrocarboxyl route has been identified as a key intermediate in the water gas shift reaction involving CO_2 and CO on Cu-based catalysts [76]. Figure 2.3 depicts a summary of the proposed mechanisms in the catalytic synthesis of CH_3OH.

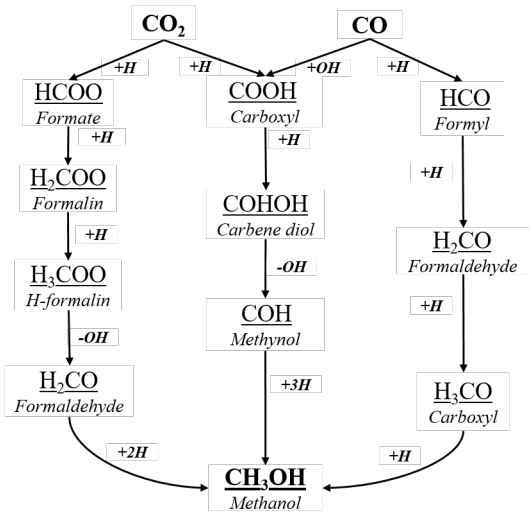

Figure 2.3: *Simplified mechanistic pathway for the hydrogenation of COx to MeOH over Cu-based catalysts. The WGS pathway is represented in the middle column (carboxyl route). Modified from [77].*

Much research has gone into improving the performance of Cu/ZnO systems in terms of selectivity, resistance to poisoning and thermal stability with dopants such as MnO/MgO [78] and Pd [79], and supports like Ga_2CO_3 [80] and Cr_2O_3 [81]. A comparative study by Angelo et al. [82] on the effects of supports of different compositions (Al_2O_3, ZrO_2, CeO_2, CeO_2-ZrO_2) showed that the metal oxides present favourable results, whilst operating at low pressures (circa. 50 bar.)

Recent developments in Cu/ZnO catalysts have achieved MeOH synthesis at atmospheric pressure conditions [83, 84]. Wang et al. [85] employed a plasma-

catalytic hydrogenation of COx with Cu/γ-Al_2O_3 in a dielectric barrier discharge to achieve MeOH yield and selectivity of 11.30 % and 53.70 %, respectively, at ambient conditions.

An appropriate reactor is necessary to preserve the longevity of the catalyst life while maintaining an acceptable product and rate of production. Methanol reactor technologies generally fall into two main categories; gas phase and liquid technologies.

Gas phase reactors are classed as either isothermal or adiabatic. Isothermal methanol reactors are characterised by high conversion rates and increased catalyst life due to an efficient heat recovery system [86]. Lurgi (acquired by Air Liquide in 2007) developed a quasi-isothermal two-stage converter system that couples a steam-raising reactor (for partial conversion) with an internally cooled tubular reactor for high methanol capacities. The Linde isothermal reactor is uniquely designed, with tubes installed in a helical configuration and positioned in the catalyst bed. This design allows for a higher heat transfer on the catalyst side than configurations with the catalyst in the tubes.

Unlike isothermal systems, adiabatic systems generally operate as a series of reactors, like the Kellogg, Brown and Root (KBR, now Halliburton) design [87]. KBR employ spherical reactors with inter-stage coolers, saving material and structural costs due to a decreased wall thickness. This results in and an increased reaction rate and decreased catalyst volume requirement.

The issue of coking in systems operating with low H/C ratio syngas (for example, coal-derived syngas) can be alleviated by employing liquid phase reactors. Liquid phase reactors allow for a more controlled removal of the reaction heat and temperature control [88]. The liquid phase methanol (LPMEOH) process developed by Air Products is based on a slurry bubble column reactor, employing fine catalysts suspended in an inert mineral oil that acts as a heat transfer medium. Syngas

compositions in excess of up to 50% of CO have been tested without adverse effects on catalysts, due to its ability to perform a pseudo-isothermal operation; avoiding excessive thermal peaks. Brookhaven National Laboratory (BNL) employed a low-pressure and temperature liquid methanol process, achieving high reactant conversions (>90%), negating the need for recycle systems.

Dimethyl Ether

Dimethyl ether (C_2H_6O or DME), by extension of the synthesis of MeOH, is a synthetic fuel of interest. DME can be synthesised via two primary reaction routes; (a) indirect route - methanol to DME (MTD), (b) direct route - syngas to DME (STD).

The MTD route involves the dehydration of MeOH to DME (reaction (25)), mostly performed over solid-acid catalysts such as γ-Al_2O_3, composite oxides ($SiO_2-Al_2O_3$, TiO_2-ZrO_2) and acidic zeolites (H-ZSM-5, HY, H-SAPO) [89].

$$2\,CH_3OH \longrightarrow CH_3OCH_3 + H_2O \qquad (R\ \mathbf{25})$$

The catalytic dehydration of MeOH to DME undergoes two competitive reaction pathways (Figure 2.4): associative and dissociative [90]. The associative pathway involves the adsorption of MeOH onto Brønsted sites of the catalyst to form DME and water. In the dissociative pathway, MeOH and water are adsorbed to form an alkyl group to an H-eliminated zeolite, while another MeOH reacts with the alkyl group to form DME, all happening sequentially.

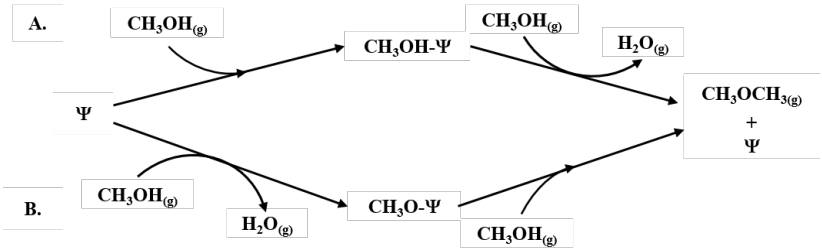

Figure 2.4: *Simple schematic of the (A) associative and the (B) dissociative pathway for the MTD reaction. ψ is the catalyst's active site.*

The main reactions in the direct route for DME synthesis are shown in Reactions (26) and (27), including the WGS and MeOH synthesis as side reactions.

$$2\,CO + 4\,H_2 \rightleftharpoons CH_3OCH_3 + H_2O \qquad \text{(R 26)}$$

$$3\,CO + 3\,H_2 \rightleftharpoons CH_3OCH_3 + CO_2 \qquad \text{(R 27)}$$

The WGS reaction is crucial in the synthesis of DME, as the generation of CO_2 can be used to facilitate the production of syngas in a methane reformer unit, as shown in Reaction (28).

$$2\,CH_4 + O_2 + CO_2 \longrightarrow 3\,CO + 3\,H_2 + H_2O \qquad \text{(R 28)}$$

Catalysts employed for STD processes are bi-functional; composed of a metallic active site such as CuO, ZnO and Cr_2O_3, for methanol synthesis; and a solid-acid component for the formation of DME from the MeOH intermediate [91].

A higher CO conversion can be achieved in the STD process over the MTD process, leading to a simpler reactor design and lower production costs [92]. However, in the former, the separation process of DME from unreacted syngas and produced CO_2 is a highly complex process. The production of additional CO_2 from the WGS reaction in the STD increases the separation complexity. Despite the thermodynamic advantage of STD, the MTD process is preferred at an industrial scale, owing to the energy-intensive and high GHG emitting nature of the syngas-generating process in STD. The MTD process has the flexibility to retrofit conventional methanol plants allowing for the possibility to change product ratios according to the demands of the market.

2.3.4 Synthetic Diesels

The Fischer-Tropsch (FT) process is a thermochemical process, developed by Franz Fischer and Hans Tropsch in the 1920s to catalytically convert synthesis gas (CO_x and H_2) to hydrocarbon products. The hydrocarbon products of FT are mostly in a liquid phase at ambient conditions, but can also be gaseous and solid. The FT process is an integral process in producing synthetic crude, or syncrude, which can be further refined to energy fuels or base chemicals. The general FT reaction stoichiometry of syncrude products is expressed in Reactions (29) to (31).

$$\mathrm{nCO} + 2\,(\mathrm{n} + \xi)\mathrm{H_2} \longrightarrow \mathrm{CnH_{2(n+\xi)}} + \mathrm{nH_2O} \qquad (\mathrm{R}\ \mathbf{29})$$

$$\mathrm{nCO} + 2\,(\mathrm{n} - \xi)\mathrm{H_2} \longrightarrow \mathrm{CnH_{(2n+1-\xi)}O} + (\mathrm{n}-1)\,\mathrm{H_2O} \qquad (\mathrm{R}\ \mathbf{30})$$

Where $\xi = 0$ or 1

$$\mathrm{nCO} + 2\,(\mathrm{n}-1)\,\mathrm{H_2} \longrightarrow \mathrm{CnH_{2n}O_2} + (\mathrm{n}-1)\,\mathrm{H_2O} \qquad (\mathrm{R}\ \mathbf{31})$$

The industrial application of the FT process involves a complex integration but consists of three fundamental operations (Figure 2.5):

1. Synthesis gas generation and preparation,
2. Fischer-Tropsch technology and,
3. Product refining and upgrading.

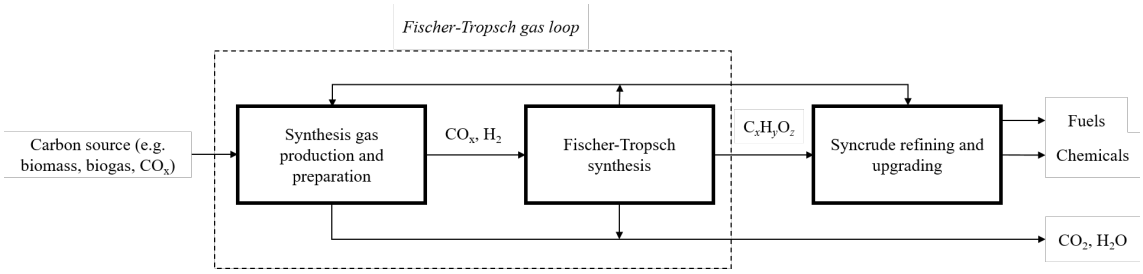

Figure 2.5: *Main design features of a typical integrated Fischer-Tropsch system.*

Synthesis gas generation and preparation

The XtL (X converted to liquid fuel) classification of an FT system refers to the feed used to produce the syngas prerequisite, where 'X' is a carbonaceous feed such as biomass, biogas, gas or power via co-electrolysis. The rWGS reaction often precedes the FT synthesis process in the event that CO_2 is used instead of CO. The conversion of biomass to syngas has been discussed in an earlier section of this chapter.

Design complexity in an FT system is that the FT reactor cannot be designed in isolation and often requires coupling with the choice of technology used to provide the synthesis gas fed to the FT reactor. While the feed for syngas production does not dictate the FT synthesis pathway, a recycle and gas loop system can be designed to favour a specific type of FT synthesis, on the account of the H_2/CO ratio of the cleaned syngas feed, typically between 1.8 and 2.1.

Fischer-Tropsch Technology

The desired syncrude composition will depend on the variation from the different FT technologies – influenced mainly by the catalyst type, reactor type, syngas composition and the operating regime. The FT operating temperature is the most determinant factor in primary syncrude composition. Therefore FT processes are conveniently classified as either high-temperature Fischer-Tropsch (HTFT) operating at 300 °C to 360 °C or low-temperature Fischer-Tropsch (LTFT) operating at 200 °C to 240 °C, commonly employed in the production of liquid fuels [93]. Table 2.3 shows the typical syncrude composition of both processes.

Table 2.3: *Syncrude properties from HTFT and LTFT based on a typical industrial operation (modified from [94]).*

FT Syncrude Property	HTFT	LTFT
Carbon number range	C_1 – C_{30}	C_1 – C_{130}
Primary product	Olefins	Waxes
Normal product phases[1] (%)		
gases (C_1–C_4)	20 – 25	5 – 10
oil	20 – 25	15 – 20
wax	0	20 – 25
aqueous organics	5	1 – 2
water	45 – 50	50 – 55[2]
Organic compound classes[1] (%)		
paraffins	20 – 30	>70
naphthenes	<1	<1
olefins	>50	15 – 20
aromatics	1 – 5	<1
oxygenates	10 – 15	5

[1] All percentages are on a mass basis.

[2] Closed gas loop, i.e., no net water gas shift conversion.

The influence of the operating conditions of a FT process extends to the conversion into different secondary products (Figure 2.6). At lower operating temperatures, the syncrude composition mainly comprises primary FT products — paraffins, olefins, alcohols, aldehydes and carboxylic acids. Hydrocarbons account for about 85% of all products of FT synthesis and are rich in linear paraffins and linear α-olefins. Secondary products like branched aliphatics and aromatics are formed at higher process temperatures. The formation of oxygenates, in smaller percentages, is found with increasing temperature.

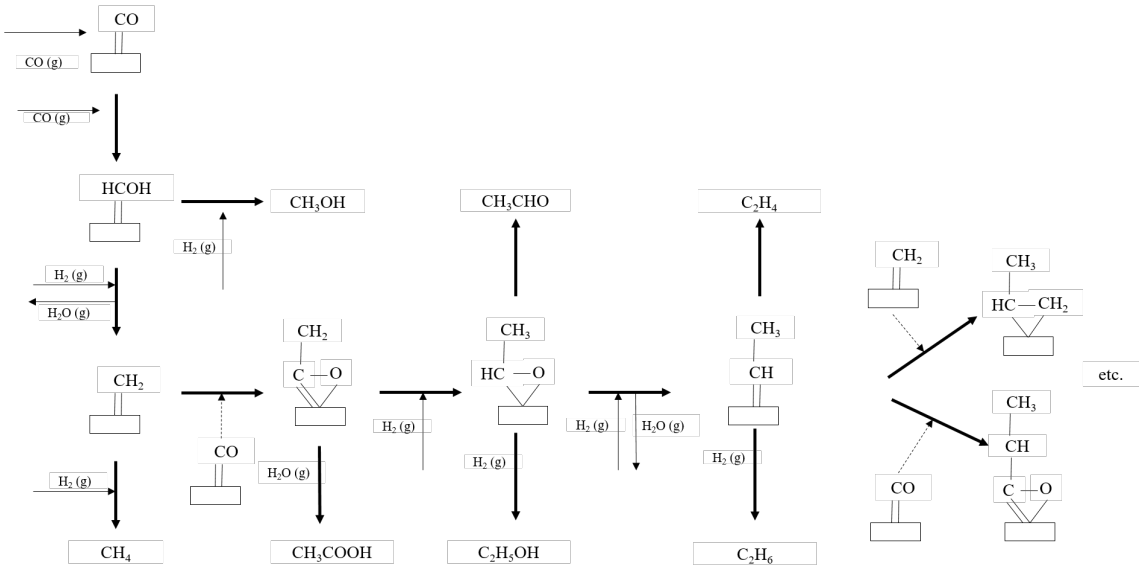

Figure 2.6: *Simplified mechanism for possible products formed during Fischer-Tropsch synthesis (modified from [95]).*

Fischer-Tropsch Reaction The FT pathway is a surface polymerisation reaction where H_2 and CO react on the surface of the catalyst *in situ*. Despite being an established process, great controversy still surrounds the reaction mechanisms in FT. Based on different reaction intermediates, three common reaction mechanisms have been proposed to govern the syncrude composition: the carbide mechanism, CO insertion, and the hydroxycarbene mechanism [95]. The nature of the formed units and the paths that the surface reaction dictates for the conversion to syncrude for each mechanism are different but are still subjected to the three major steps of a polymerisation reaction – initiation, chain growth and chain termination.

In the carbide mechanism, originally proposed by Fischer and Tropsch, both reactants are chemisorbed on the metal surface ($\mathfrak{M}$), followed by a subsequent molecular dissociation. The reaction of respective surface atoms forms intermediates ($\mathfrak{M}$-CHx) — monomers for syncrude chain propagation. However, the pathway fails to describe the formation of oxygenates. The CO insertion mechanism by Pichler and Schulz involves the insertion of additional CO molecules into the -CHx species formed after the initial dissociation of a previous CO molecule. Chain growth is

promoted further by inserting CO into absorbed hydrocarbon species [96]. The formation of hydroxycarbene ($\mathfrak{M}$-CHOH) intermediates, as postulated by Anderson and Emmett, is responsible for the formation of carbon-to-carbon bonds. The three different mechanisms are summarised in Figure 2.7.

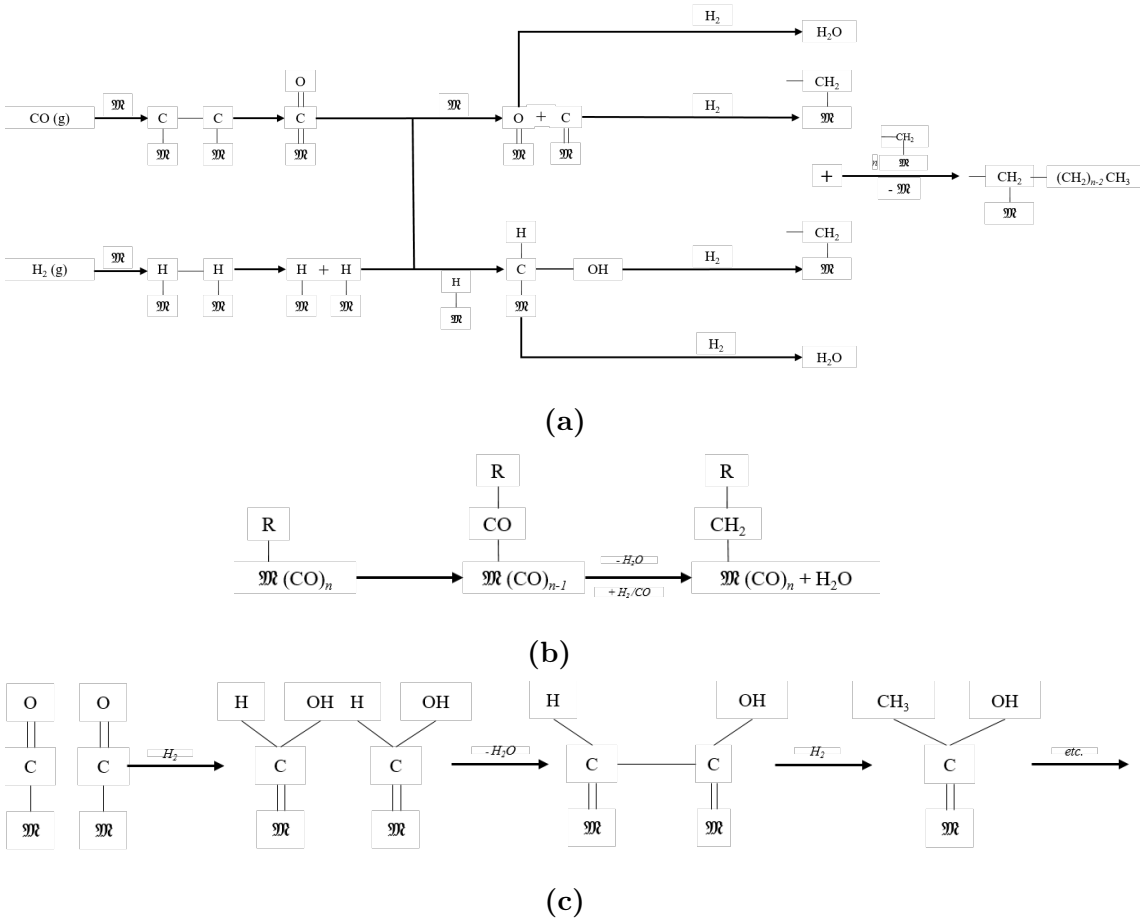

Figure 2.7: *Schematics for Fischer-Tropsch reaction pathways: (a) initiation and chain growth steps in the carbide mechanism, (b) general chain growth pattern in the CO-insertion mechanism, (c) mechanism scheme of formation of hydroxycarbene intermediates and chain growth pattern (modified from [95]).*

Fischer-Tropsch Catalysts Metals with an electronic configuration of d^7 such as Ru, Fe, Co, and Ni have been identified as the most suitable for FT catalysis. Aside from costs, challenges in choosing FT catalysts include chain growth probability and the control of CO activation in the selective formation of desired products with high selectivity and activity.

Chain Growth Probability The degree of the carbon number distribution during the FT synthesis is determined by the chain growth probability property of a catalyst (α), commonly described by the Anderson-Schulz-Flory (ASF) model, represented in Equation (2.2).

$$x_n = n(1-\alpha)^2 \cdot \alpha^{n-1} \tag{2.2}$$

x_n is the mass fraction of the carbon atoms contained within the n carbon atoms, and $(1-\alpha)$ is the probability of chain termination. The chain growth probability of a catalyst can be further expressed in terms of the propagation rate (r_p) to promote chain growth and the termination rate of monomers (r_t).

$$\alpha = \frac{r_p}{r_p + r_t} \tag{2.3}$$

The α-value has a correlation with the carbon length of syncrude; light hydrocarbons (C_1 – C_4) are predicted with a higher selectivity at smaller α-values, and heavier hydrocarbons (C_{21+}) with catalysts with higher α-values. Figure 2.8 shows the distribution of syncrude composites as a function of α-values.

The typical α-values of Fe-based catalysts and Co-based catalysts are 0.5 to 0.7 and 0.7 to 0.8, respectively [95]. Surface desorption affects the α-values of catalysts, thus influenced by the operating temperature and the choice of the FT process (i.e. HTFT and LTFT) [98].

Hydrogenation Activity In addition to being CO polymerisation catalysts, FT catalysts also partake in hydrogenation. Ni-based catalysts have a low average molecular weight, and their small particle size leads to a very high hydrogenation activity power compared to its chain growth ability, making it irrelevant as an industrial FT catalyst [99]. The degree of the hydrogenation activity of iron is

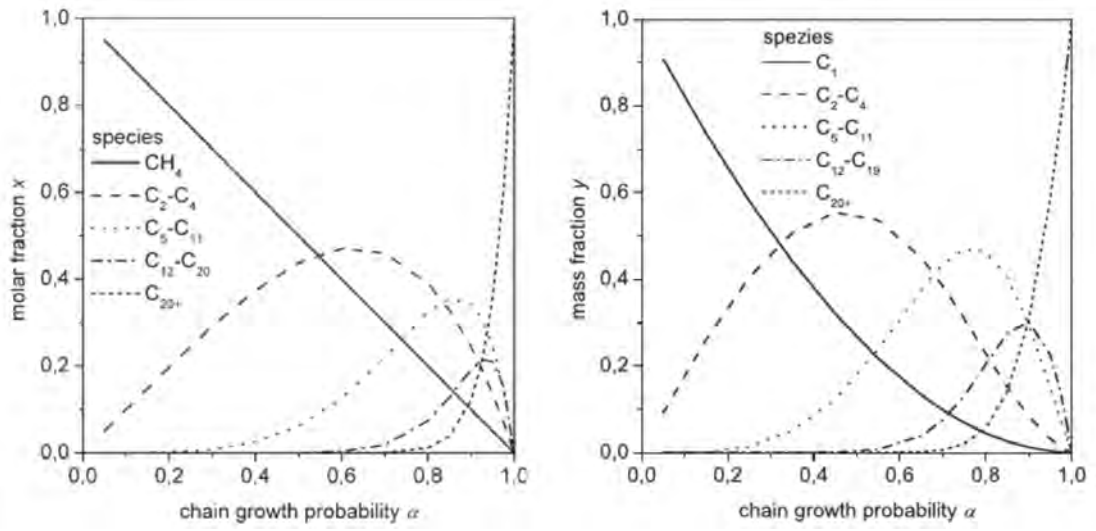

Figure 2.8: *Product distribution in Fischer-Tropsch synthesis as a function of chain growth probability [97]*

.

less than cobalt, resulting in syncrude products from Fe-based FT synthesis more olefinic and containing more oxygenates than Co-based FT synthesis [98].

Water Gas Shift Activity Fe-based catalysts have a higher WGS reaction (see Reaction (32)) activity compared to Co-based catalysts, which have very little WGS activity. The WGS activity of an Fe-based catalyst can lead to a loss of CO as an FT feedstock by forming CO_2; and in the reverse reaction, increase the production of water — a kinetic inhibitor for an Fe-based catalyst [95]. Conversely, it allows the utilisation of a syngas feedstock containing CO_2 or depleted of hydrogen [97]. The WGS activity of an Fe-based catalyst has a significant effect on the FT gas loop design due to its ability to self-condition the syngas by adjusting the H_2/CO ratio [94].

$$CO + H_2O \rightleftharpoons CO_2 + H_2 \qquad \text{(R 32)}$$

Fischer–Tropsch Reactors The highly exothermic nature of the hydrogenation and polymerisation of CO in FT processes necessitates that heat management takes

precedence in the design of reactors and subsequent development of catalysts. As a result, the choice of catalysts and reactors goes hand-in-hand with FT processing. The different reactors can be categorised, depending on the cooling concept applied: (a) internal cooling, (b) external cooling via gas or liquid recycle streams and, (c) direct cooling by the staged distribution of feed streams.

The multi-tubular fixed-bed (MTFB) configuration is a robust reactor with a design akin to a vertical shell-and-tube heat exchanger. A significant drawback in MTFB reactors arises from the need to minimise pressure drop by adjusting the size of the catalyst particles and tube diameters. Conversely, this can result in decreased volumetric catalytic productivity and the formation of hot spots in the tubes [94, 97].

Slurry bubble column reactors (SBC), mainly applied in gas-liquid-solid reactions, employ fine catalyst powders suspended in FT liquids. Whilst being less expensive than MTFB reactors and having good thermal control, the catalyst must be designed to be attrition resistant without compromising on activity and ease of suspension. Unlike SBC reactors, fluidised bed reactors are only used for HTFT processes due to its capacity for only gas-solid reactions.

Syncrude refining and upgrading

The refining of crude oil is comparable to FT syncrude. However, the latter consists of four phases: gas, organic liquid, aqueous liquid and organic solid, at ambient conditions. While it is possible to repurpose conventional crude oil refineries for FT syncrude, the high proportions of oxygenates, olefins and the aliphatic nature of the heavier fractions from LTFT processes must be considered [98].

The refining process proceeds with a syncrude recovery, separating it from unconverted syngas. The recovered syncrude undergoes a stepwise cooling and phase separation before the fractions are sent to an atmospheric distillation unit for

further fractionation before refining. Alternatively, the FT reactor product can be directly fed into an atmospheric distillation unit (ADU), in a bid to reduce the energy consumption in the aforementioned cooling steps. Rodríguez Vallejo and Klerk [100] introduced the hot products of the FT reactor into a pressurised distillation unit, and their investigation revealed an improved liquid recovery and reduced thermal duties.

The refining technology applied in the downstream processing of syncrude depends on the choice of the final products; fuels and/or chemicals.Refining technologies include [98]:

- Double bond isomerisation to improve the octane numbers of olefins,
- Dimerisation and oligomerisation of olefins, increasing their solubility, a desirable quality when blending with motor gasoline,
- Etherification to improve motor-gasoline quality,
- Aromatic alkylation for benzene reduction to meet the required regulations of petrochemicals,
- Hydrotreating and hydroisomerisation for hydrocarbon processing.

2.4 Large Scale Synthetic Fuel Production Facilities

The Lurgi and TREMP (Topsøe's Recycle Energy-efficient Methanation Process by Haldor Topsøe) concepts, based on adiabatic fixed-bed concepts, are the most commercially established catalytic methanation technologies. The largest facilities currently in operation have a daily output of 4.8 Mio. m^3 and 3.8 Mio. m^3 of SNG by the aforementioned companies, located in the USA and China respectively [101].

Methanex and Johnson Matthey are two of the largest producers of methanol. They use natural gas as the primary feedstock and convert via a series of SMR and ATR in different configurations. The Methanex plant in New Zealand has an annual operating capacity of 2.2 Mio. t. At the same time, Johnson Matthey has recently commissioned the largest coal-to-olefins facility, with an annual methanol capacity of 63 Mio. t in China [102].

Large-scale production facilities are often subsidiaries of methanol production plants. TOYO Engineering operates a total of four fuel-use DME production plants in China. DME is produced via the dehydrogenation of methanol starting from natural gas or coal as a feedstock. The four plants have a combined daily capacity 4.7 t [103]. Liquid hydrocarbon production by FT is a widely commercialised technology established in the 1940s. Sasol in South Africa is the largest FT facility with an annual operating capacity for synfuel production over 8 Mio. t [104]. Sasol combines the gasification of coal with FT to achieve their desired products.

2.5 Previous Techno-economic Analysis Studies on PtX

As of June 2020, there are 220 demonstration PtX projects in Europe (80% of global projects), of which have either been realised, completed or are in planning phases [105]. Despite the extensive ongoing research in this area, challenges remain due to the number of possible system configurations, the diverse products, the scale of deployment and the end-usages of PtX — there exists a complexity in the standardisation of the feasibility of its deployment and establishment of PtX as a climate change mitigation measure. For instance, Denmark is focused on injecting hydrogen or synthetic methane into the natural gas grid. In contrast, hydrogen as a transport fuel takes precedence in the United Kingdom. On the other hand, Spain prefers to extend PtX for re-electrification with combined heat and power technologies (CHP), while Germany promotes interest in all possible spheres.

Renewable energy-oriented technologies are subjected to stringent economic assessments due to the high capital investments incurred due to their main characteristic; replacing fuel costs with upfront investment. Despite the sizeable investments needing to be reclaimed, the energy sector is a well-developed market with established structures and pricing such that the periodic cost-effectiveness of emerging technologies can be economically appraised. Techno-economic analysis (TEA) is a conventional metric used to deduce a process's technical feasibility and economic viability, assessing the associated risks and consequently identifying the mitigation actions. The conventional methodology of a TEA follows a pattern as follows;

1. Process design or configuration, depending on the end product or service required,

2. Mass and energy balance to determine productivity and energy efficiency of the process,

3. Cost estimations to estimate capital investments and operating expenditure,
4. Profitability analysis to forecast the profit margins and,
5. Sensitivity analysis to negotiate through bottlenecks by evaluating how modifying values of independent variables influence another selected variable under defined sets of assumptions.

A key performance indicator commonly implemented in TEA is the levelised cost of a predefined component 'X' (LCOX), where 'X' is usually represented as electricity or as energy. LCOX is an economic metric used to comparatively assess the cost of production of a unit 'X' over the assumed lifetime. Unless stated, the currencies are converted to the Euro (€) by the year of publication, using the XE currency converter [106].

$$LCOX = \frac{\sum_{n=0}^{N} \cdot \frac{(I_n + OM_n + F_n)}{(1+d)^n}}{\sum_{n=1}^{N} \cdot \frac{Q_n}{(1+d)^n}} \tag{2.4}$$

N is the project operation time in years, I_n is the investment expenditure in year n, OM_n is the operation and maintenance cost, F_n is the fuel/energy input cost, d is the discount rate, and Q_n is the amount of the key material/energy (X) that is produced. A discount rate is the rate of interest that is applied to all future cash flows of an investment over its lifespan to deduce its net present value.

The technical performance will primarily be evaluated by the system efficiency within the scope of the system being assessed, i.e. the ratio between the energy vector produced and the electricity consumed by the process.

69% of Europe's PtX projects are dedicated to hydrogen production, with another 22% focused on further hydrogen processing to methane [105]. Using biogas as a feedstock, the profitability of power-to-gas (PtG - hydrogen and methane) plants with 6 different system ratings, with a central focus on the impact of the electrolyser

rating and technology (alkaline electrolyser; AEL and polymer electrolyte membrane electrolyser; PEMEL) and overall system efficiency was assessed by Parra and Patel [107]. The authors assumed that plants were connected to the Swiss wholesale market: for the purchase of electricity and selling products to the gas grid. Simulated results showed that the attainable life cycle system efficiency peaked at 65% in a 1 MW plant. Despite the effect of the economy of scales, larger electrolyser systems (up to 1000 MW) did not significantly reduce the LCOE.

Conforming to the concept of levelised costs, the authors introduced a levelised value (LVOX) metric representing the annualised total revenue accrued by a PtX system regarding vector production. Regarding the LVOE at 1000 MW, the longer durability of AEL allowed it to perform better than PEM electrolysers, despite offering higher efficiencies, albeit prevalent only at the beginning of life. The value of the plant increased when several value-adding services such as oxygen (a by-product of electrolysis), heat and frequency control were included to generate income. Optimum results yielded an $LCOE_{H_2}$ of 89.97 €/MWh_t and an $LVOE_{H_2}$ of 130.91 €/MWh_t , for a 1000 MW plant using alkaline electrolysis.

In a follow-up study in [108], a direct air capture (DAC) unit was employed as an additional source of CO_2 in a 1 MW PtG systems based on PEM electrolysers. The size of the DAC unit was designed proportionally to the available heat provided by the methanation reaction. The LCOE of hydrogen and methane was 98.24 €/MWh_t and 178.53 €/MWh_t respectively; the LVOE was 121.85 €/MWh_t and 133.19 €/MWh_t respectively. The economic performance was most sensitive to the cost of electricity, natural gas prices, and the degradation rate of the stack.

However, the authors overlooked that the cost of CO_2 (upgrading, compression and transportation) greatly contributes to the overall operating expenditure (OPEX) in their assumption that it is obtained free of charge, especially when a CO_2 levy and biogas premium has been added to the income generated. In addition, the disclosure of the economic impact of the operation at partial loads when the

wholesale electricity prices are very high would present a truer reflection of economic viability.

The energy performance analysis through the thermal management of an SOE was the foundation for a techno-economic analysis for the production of synthetic natural gas by integrating high-temperature electrolysis and methanation in [109, 110]. The authors used Aspen Plus® software to model two power-to-methane (PtM) 10 MW_e plants, based on the integration of steam electrolysis and co-electrolysis of steam and carbon dioxide with a methanation reactor. By varying the operating voltages of the SOE stack, the co-electrolysis plant achieved a higher efficiency of 81.4% against 76.0% for steam electrolysis. However, the higher efficiency rating was offset by a lower cost of production of 637.87 €/kW for steam electrolysis against 729.00 €/kW for co-electrolysis due to the lower operating costs.

The same group proceeded to compare two 10 MW_e PtG plants based on SOE to synthesise methane and methanol following steam electrolysis with the same methodology [111]. The methane plant yielded a higher efficiency at 77.1% when compared to the methanol plant at 58.8% due to the former's lower energy demand for external heating and compression. The economic performances were compared with the industrial price of natural gas at 32.84 €/MWh and a domestic price at 71.00 €/MWh . The comparative lower and upper bound prices for methanol (based on lower heating values; LHV) was set at 61.24 €/MWh and 79.88 €/MWh respectively. By varying the capital costs of an SOE based on expert valuation (2500 €/kW; current, 1050 €/kW to 450 €/kW in 2030), the production cost of the methanol plant was about 31% higher than that of the methane-producing plant.

However, the sensitivity analysis demonstrated a similar economic performance due to the larger methanol market. A near-zero electricity cost is currently required to reach a break-even point for the lower boundary price of both fuels. At lower SOE costs, the break-even point becomes more dependent on the cost of CO_2. The authors' optimistic scenario further suggested a CO_2 price of 2.66 €/t

to 3.55€/t , coupled with the electricity price and carbon tax to be set at zero. This implies that electricity will be provided from a surplus renewable source alone, signifying a lower utilisation factor.

A comparable study investigating the relationship between various parameters and the LCOE of methane via PtG with PEM routes was attempted in [112]. By modelling various cost and efficiency scenarios, the obtained base values for the LCOE were 124€/MWh in 2020, 105€/MWh in 2030 and 93€/MWh in 2040, based on a defined bid price and average electricity cost on the Irish single electricity market. The LCOE was dominated by electricity costs (56%) in all scenarios, dropping to 55€/MWh in a zero electricity cost scenario, i.e. exclusive consumption of otherwise curtailed electricity.

The work, however, does not implicitly consider associated costs like grid connection and equipment maintenance in the zero-cost electricity assumption and its implication in low utilisation factors even in high renewable energy capacity scenarios. This was followed by a subsequent study investigating the interactions between the electricity bid price and operating hours in increasing VRE shares in [113]. Nominal reductions in expenditure did not make the LCOE more competitive. However, promoting renewable incentives, valorisation of oxygen, increased revenues for gaseous fuels, and exemptions from taxes and grid access payments would make PtG financially more viable [114].

The performance of PtG plants operating entirely on the German electric residual profile of a future based only on RES was investigated in [115]. Methane is produced via a methanation unit, thermally integrated with several SOE modules. A projected installed RES capacity and demand profile were used to obtain a surplus and deficit profile. The RES capacity was dominated by photovoltaic generation and wind power, resulting in a high frequency of oscillations due to their fluctuations. The PtG plant was sized based on the energy profile and a chemical storage facility in the event of high surpluses to accommodate the continuous operation. Results

demonstrated that the overall PtG system efficiencies slightly increased up to 77% with increasing plant capacity. On the other hand, the plant utilisation factor decreases as the plant capacity expands. Using estimated specific costs in 2050, an optimal plant capacity of 7 MW was determined based on an LCOE range of 60.20 €/MWh to 224.90 €/MWh; partially comparable with industrial and domestic fossil-based natural gas prices at 56.70 €/MWh and 110.36 €/MWh respectively.

Nonetheless, uncertainties owing to the unpredictability of future costs and performance of electrolysers and electrochemical storage, as well as the forecasting of future climatic events, could further limit the validity of the results. The authors' assessment did not include the impact of oxygen valorisation and taxation.

A model of a biogas plant integrated into an SOE-based PtM system to produce methane for a cogeneration system in Germany, with a design output of 2500 kW_{th} and 1000 kW_e, was developed by [116] using the ChemCad 6.3 software. The required electrical power was assumed to be obtained from an off-shore wind park. The resulting LCOE was 260 €/MWh with a payback time of 4 years, making the plant economically feasible. The author also accounted for economic incentives according to the European Directive 2013/12/5; however, the research did not state whether the wind farm was included in the overall capital expenditure (CAPEX) and the impacts of electricity prices on the overall costs. It would be important to consider the logistics of electricity transmission from off-shore to in-land where the location of the biogas plant and the transportation costs of feedstock has to be considered.

Recent improvements in biological methanation (further description available in other sections) give rise to using organic waste as a feedstock for renewable fuels. The economic potential of an 18 MW_e microbial PtG plant in Belgium was investigated in [117]. The energy model was designed in a Microsoft Excel spreadsheet. The production cost of biomethane was estimated at 2.10 €/m^3 which is equivalent to 197.99 €/MWh and 122.56 €/MWh with grid and tax exemptions, and future costs

of electrolysers. To meet requirements for unrestricted injection of biomethane into the Swiss and German gas grid ($CH_4 \geq 96$ v/v%, $H_2 \leq 2$ v/v%), the techno-economic analyses of 6 configurations of two-step methanation and upgrading technologies; fixed bed, bubbling fluidised bed, and membrane separation, was undertaken in [118, 119]. A fixed inlet volume stream of biogas at $200\,\mathrm{N\,m^3/h}$ was used as a basis for the model designed on Athena Visual Studio and MATLAB software.

The production costs of biomethane were 102 €/MWh to 108 €/MWh were estimated with an optimum PtX efficiency of 59%. Revenues from the sale of process heat and oxygen increased the profitability by 11 €/MWh. Both studies were based on AEL, which is not extensively considered within the scope of this study. It was suggested that the business case could be improved if CO_2 valorisation for producing synthetic liquid fuels and other added-value chemicals was considered.

The German Aerospace Centre has been active in power-to-liquid (PtL) analysis, having conducted several TEA studies using Aspen Plus for process simulations. A liquid hydrocarbon plant based on a $1\,\mathrm{GW_{LHV}}$ input of hydrogen via PEM electrolysis was modelled to investigate the potential of storing dedicated fluctuating renewable energy in [120]. The PtL process incorporating reverse water gas shift (rWGS) and Fischer-Tropsch synthesis (FTS) processes achieved an efficiency of 44.6%, yielding net production costs of 11.17 € to 19.22 € per GGE (gasoline gallon equivalent) for electrolyser costs of 306.00 €/kW to 1147.52 €/kW . Costs related to the electrolyser and RES; and the load hours showed the highest impact on the production costs. The study gives no indication on the source of CO_2; thus, its related costs are not included in the analysis.

In a subsequent study by Albrecht et al. [121], the comparison of the energetic and economic performances of biomass-to-liquid (BtL), power and biomass-to-liquid (PBtL) and PtL processes was assessed with kerosene and diesel as target products. Syngas was supplied by thermochemical conversion of biomass in the BtL process, while hydrogen from water electrolysis via PEM and anthropogenic

CO_2, and including CO_2 from DAC, was required as feedstock in the PtL and PBtL processes. Based on the energy performance, an in-house economic tool was used to simulate the production costs of the FT fuels, as shown in Table 2.4.

Table 2.4: *Summary of the techno-economic study by Albrecht et al. [121].*

XtL Concept	**BtL**	**PBtL**	**PtL**
Efficiency	%	%	%
X-to-Liquid	36.3	51.4	50.6
Overall Plant	82.6	65	66.8
Carbon Conversion	24.9	97.7	98
Plant Capacity (t/h)	2.9	11	2.9 11
Net Production Cost(€/l_{GE}) [1]	2.34	2.24	2.85 2.74

[1] Based on an electricity price of 105 €/MWh

Sensitivity analyses revealed that BtL is superior at high electricity costs, while PtL and PBtL benefit from lower electricity costs. Results from a follow-up study by Dietrich et al. [122] showed that the total capital investment for PtL was 37% lower than BtL, which was estimated at 1050 m€ for a plant capacity of 11 t/h fuel production, and PBtL at 742 m€. Capital costs for the gasifiers and PEM electrolysers dominated the plant costs. The authors obtained comparable results of 2.01 €/l_{GE} based on an electricity price of 49.90 €/MWh from wind turbines in their most recent study in [123]. A more focused BtL analysis is found in the work of Peduzzi et al. [124]. The authors investigated the economic performance of the production of liquid fuels by employing H_2O and CO_2 electrolysis via SOELs. Fuel production costs between 1.71 €/l_{DE} and 1.95 €/l_{DE}, with electricity produced by an onsite gas turbine using off-gases from a steam network via a Rankine cycle.

Additionally, analysis of PtL was carried out in the work of Schemme et al. [125]. The authors investigated the economic assessment of many electrofuels,

including paraffinic fuels and DME (dimethyl ether). For their analysis, the H_2 production from PEMELs was decoupled to yield a production cost of 2.30 €/l_{DE} for synthetic diesel and 1.85 €/l_{DE} for DME, based on an electricity price of 0.10 €/kWh.

The techno-economic performance of producing aviation fuels via PtX was studied in [126], considering DAC and concentrated sources of CO_2. The production costs from the assessment was 139.68 €/MWh from DAC and 96.12 €/MWh from concentrated sources when high temperature electrolysers were employed. With low-temperature electrolysers, the production costs were higher at 148.68 €/MWh from DAC and 106.92 €/MWh from concentrated sources [127], due to lower efficiencies and fuel output. The cost of renewable electricity was assumed to be 40.00 €/MWh and a 43% load capacity. The report, however, did not include the process specifications for the technical assessment, nor did it include carbon pricing and taxes in the economic analysis.

The synthesis of methanol (CH_3OH) via PtX presents another proposition to produce speciality chemicals with CCU technologies. An investigation by Nyári et al. [128] to assess the feasibility of the utilisation of CO_2 in a 5 kt/d chemical-grade CH_3OH plant presented a levelised cost of around 109.96 €/MWh_{LHV} (700 €/t) , based on a O_2 valorisation target of 100 €/t ad an electricity price of 30.00 €/MWh. However, assumptions based on a daily reception of 7 kt/d of pure CO_2 from unspecified industrial sources for high negative prices might be considered very optimistic. A similar approach undertaken in [129], revealed CH_3OH production cost of 105.49 €/MWh_{LHV} (589 €/t), despite a CO_2 purchase at a sequester price. The lower price could be attributed to the direct coupling of the PtX plant to a coal-fired power plant, while on the other hand, it led to a severe decrease in overall plant performance in the later study.

Bos et al. [130] considered integrating a stand-alone DAC system with PtX for the production of CH_3OH. Electricity is provided by wind turbines installed on site. The cost of production of renewable CH_3OH was estimated to be 143.28 €/MWh_{LHV}

(800€/t). It should be noted that the AELs were employed in this study and that SOELs, though at higher current capital cost, could lower the production cost due to the heat integration gains of the latter. Hank et al. [131] undertook a comparative study in the production of CH_3OH via PtX using electricity from various sources and CO_2 from biogas and ammonia. A production cost of 108.90€/MWh_{LHV} (608€/t). The cost of electricity used in the analysis was 31.10€/MWh to 32.80€/MWh, which included a tax reduction in the grid connection fees.

The direct integration of PtX with point sources to offset the current high cost of carbon capture is becoming a subject of exploration as a decarbonisation measure, as seen in [132]. The authors reviewed current projects that aim to integrate PtX into the iron and steel industry (market entry from 2025) in different configurations as in Figure 2.9.

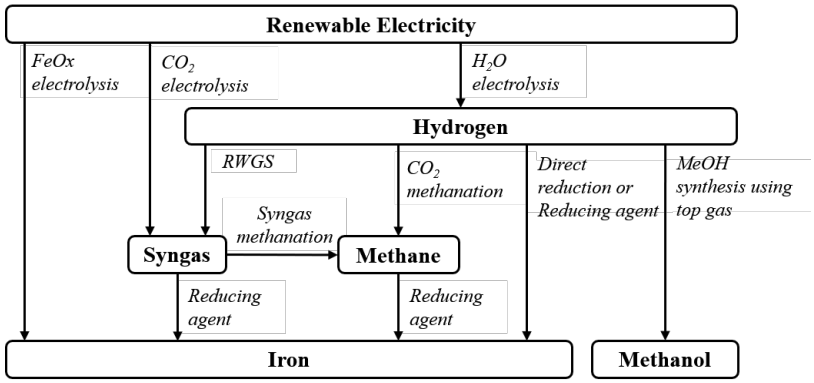

Figure 2.9: *Configurations of PtX technologies integration in Iron and Steel production plants.*

The product of the PtX processes can either be incorporated into the iron-making processes or as a final valuable chemical product. The direct integration of hydrogen can achieve a carbon reduction of up to 21.4% compared to a reference plant, while syngas and methane achieve 15.8% and 16.5% carbon reduction, respectively. Integrating PtX technology with biomass gasification processes can greatly increase carbon conversion from 35% to 100%, as shown in a study by Zhang et al. [133]. Depending on the fuel produced (CH_4, CH_3OH, DME or jet fuels), system efficiencies

were up to 68% with the application of SOE, compared to 51% with state-of-the-art biomass-to-fuel systems, based on a plant capacity of 60 MW_{th} biomass input. A range of LCOX of 78.88 €/MWh to 147.89 €/MWh was estimated from the study.

In considering reference locations other than Europe, a study by Kassem et al. [134] was carried out on integrating dairy farming with PtG to maximise waste management and grid decarbonisation in New York state of the United States of America (USA). The process components consist of dairy manure processing via anaerobic digestion and hydrothermal liquefaction to produce CO_2 for the downstream synthesis of gas grid compliant CH_4.

The study yielded an LCOX range of 76.85 €/MWh to 179.31 €/MWh . The revenues from hydrochar and biocrude oil co-products that lowered the LCOX to 32.02 €/MWh to 115.27 €/MWh . The study showed that the most critical factor for the economic viability of the system were carbon credit incentives like the renewable fuel standard (RFS) and the low carbon fuel standard (LCFS), both of which are not actionable for this study; RFS does not incentivize PtM, and LFCS is only applicable to transport fuels in the state of California.

California is the reference location for a study by Di Salvo and Wei [135] for decarbonising the industrial sector via PtG. The CO_2 feedstock is assumed to be purchased from a CCS process integrated with a cement production plant. The LCOX of CH_4 from the PtG was estimated at 376.11 €/MWh with a high opportunity for cost reduction with the price of electricity and the capital cost of the electrolysers. While there are no direct incentives for the proposed pathways, the authors estimate that the range of carbon taxes required to achieve production price parity with conventional CH_4 is 71.43 €/t_{CO_2} to 714.34 €/t_{CO_2} , dependent on the system capacity factor.

As of 2020, Japan has the highest number of operational hydrogen refuelling stations within the global context [136]. The anticipated increase suggests a growing

interest in hydrogen deployment strategies, including PtG in Japan. A case study by Li et al. [137] assessed the potential of PtG to resolve surplus RES generation and decarbonise the energy system in Japan. The applied scenario was based on an increased RES-grid connection encouraged by the feed-in-tariff mechanism and the resulting balancing complexity caused by the former. The cost of H_2 of production was estimated at 146.33 €/MWh to 292.66 €/MWh based on low heating values. The high values can be attributed to the low capacity factors, the gross share of RES, RES generation mix, and patterns of electricity generation and consumption profiles. In a follow-up study, the authors also concluded that further cost reduction relies on improvements in conversion efficiencies and the capital costs of electrolysers.

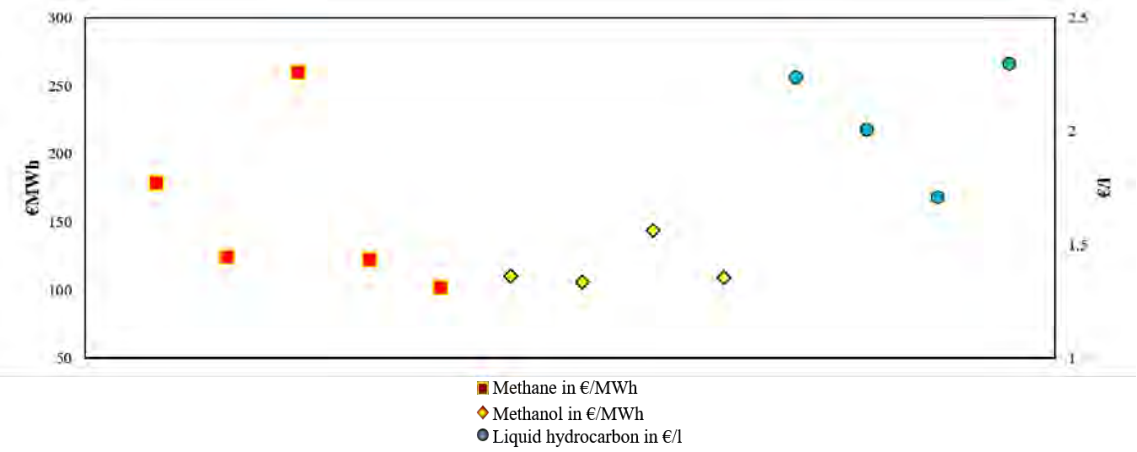

Figure 2.10: *Summary of the levelised cost of the product (best case scenarios) from selected literature [108, 112, 116–118, 121, 122, 124, 125, 128–131].*

Figure 2.10 shows a summary of the LCOE of CH_4, CH_3OH and liquid hydrocarbons from selected literature, revealing the wide range of values owing to the plethora of techno-economic parameters considered and applied in the evaluations of different authors.

Overviews of PtX demonstrations and projects have been previously covered in the work of Chehade et al. [138] and Thema et al. [139]. Since most actionable PtX tasks are situated in Europe, it will be the primary subject of study. The primary source of energy is considered critical to the deployment of PtX. Around 48% of PtX projects employ RES, although there is no evident preference [105]. Twelve of those projects rely on surplus electricity from those sources that would have been otherwise curtailed. 32% of all significant European PtX projects engage in downstream hydrogenation of CO_2, with 27 projects utilising biogenic carbon sources. Seven projects integrate Climeworks AG DAC technology, often integrated with SOEL, to produce CO_2.

The ETOGAS Audi e-gas plant, located in Werlte, Germany, is an established power-to-methane facility in operation since 2013. The system comprises of two 3 MW AELs powered by four 3.60 MW off shore wind turbines [140]. CO_2 is sourced from biogas from a biomethane plant near produce 1000 t of CH_4 per annum

via chemical methanation, with a base system efficiency of 54%, based on a load capacity of 45.7% [141]. The 12 MW Energy Valley Delfzijl PtX plant was recently launched in The Netherlands in 2020 to produce CH_4 for grid injection [139].

The George Olah Renewable Methanol plant in Svartsengi, Iceland, is the first industrial-scale production of fuel from CO_2, uses 6 MW electrolysers to produce up to 4000 t of CH_3OH per annum, has been operational since 2012. Currently, the largest power-to-methanol plant is the 20 MW EU-funded Djewels project plant in Delfzijl, The Netherlands. The demonstration project aims to produce CH_3OH from RES in a bid to scale up towards a 100 MW [142].

The reviewed literature shows a growing appreciation for PtX technologies. However, most conclusions are drawn based on the product's unit prices founded on a predetermined set of parameters. Without proper consideration, this could reduce the feasibility of the process to a false dilemma. The scope of the studies is often limited to technical performance and optimisation of the product synthesis alone.

In contrast, extraneous variables like the availability of the feedstock, its spatial distribution and the implication of the end-use of the products are not given greater eminence. The categorisation and availability of the various feedstock present the primary bottleneck in producing synthetic fuels. The spatial distribution of the feedstock informs on the density of feedstock in relation to a pre-existing energy system. An assessment dictates the prioritisation of the products and their end uses based on a case-by-case socioeconomic perspective. The product greatly impacts the economic viability and the associated supporting policies, whether as a precursor to high-value chemicals, energy vectors or fuels. This study will build upon the excellent work done in the previous assessments to address the gaps mentioned in line with the research questions stated in earlier chapters of this study.

Chapter 3

MODEL ASSESSMENT OF FUEL SYNTHESIS

This chapter follows on from the preceding section of this thesis to model and simulate the technological process of interest as discussed in Chapter 2. The modelling for all processes is developed for this study by its author, with a licenced copy of Aspen Plus® *v.*11.1 to maintain consistency of results and parameters. The models include the production of hydrogen via co-electrolysis in SOE, recovery of CO_2 from a typical point source and synthesis of the already discussed energy vectors. This chapter concludes with a technical summary of the model simulations.

3.1 Model Development of Electrolysis Process

In addition to the previously stated benefit of the thermal coupling between downstream processes and the SOEs to improve energy savings, the aspirations for a degree of carbon neutrality via the utilisation of CO_2 as a feedstock makes co-electrolysis a suitable mode of operation in this work.

$$CO_2 + 2\,e^- \longrightarrow CO + O^{2-} \quad \text{(R 33)}$$

$$CO_2 + H_2O \longrightarrow CO + H_2 + 1.5\,O_2 \quad \text{(R 34)}$$

In co-electrolysis , Reaction (33) occurs simultaneously with Reactions (5) and (6) summarised as Reaction (34). Additionally, chemical reactions such as the reverse water-gas shift (rWGS - Reaction (35)) and methanation (Reaction (36)) would occur, often in favourable conditions where composites of metallic Ni are present.

$$CO_2 + H_2 \rightleftharpoons H_2O + CO \quad \text{(R 35)}$$

$$CO + 3\,H_2 \longrightarrow CH_4 + H_2O \quad \text{(R 36)}$$

It is broadly postulated that the production of CO in the electrolysis process is dominated by the endothermic rWGS reaction rather than the electrochemical reduction of CO_2 due to the slower kinetics of the latter [143, 144]. Conversely, some of the produced syngas may internally react to form methane. Due to the exothermic nature of methane formation, operating at lower temperatures and higher pressures will contribute to higher methane and lower syngas proportions in the products. A high methane content is undesirable for downstream processes like the Fischer-Tropsch and can result in up to a 20% decrease in efficiency, compared to atmospheric pressures [145, 146].

$$CO + H_2 \rightleftharpoons C_{(s)} + H_2O \quad \text{(R 37)}$$

$$2\,CO \longrightarrow C_{(s)} + CO_2 \quad \text{(R 38)}$$

Other undesirable consequences of high-pressure operation include high coke deposition during methane formation, carbon formation and deposition at the cathode through Boudouard reactions (Reactions (37) and (38)). The effects of the pressurised operation of co-electrolysis have been extensively studied by Wang et al. [147].

The minimum energy required to sustain the co-electrolytic conversion of H_2O and CO_2 is dictated by thermodynamics as described in Equation (3.1):

$$\Delta H = \Delta G + T \cdot \Delta S \tag{3.1}$$

ΔH represents the total energy demand for the reaction as a function of temperature, ΔG is the contribution in the form of electrical energy and $T\dot{\Delta}S$ is an entropy term representing the heat energy contribution. ΔH can be further expressed in terms of the maximum cell potential, also known as the thermoneutral voltage (V_{tn}), at a given temperature as seen in Equation (3.2).

$$V_{tn} = \frac{\Delta H}{n \cdot \mathfrak{F}} \tag{3.2}$$

Figure 3.1 further describes the relationship between the thermodynamics of co-electrolysis for syngas production, operating temperature and the total electrical voltage required, where n is the number of electrons transferred and $\mathfrak{F}$ is the Faraday constant.

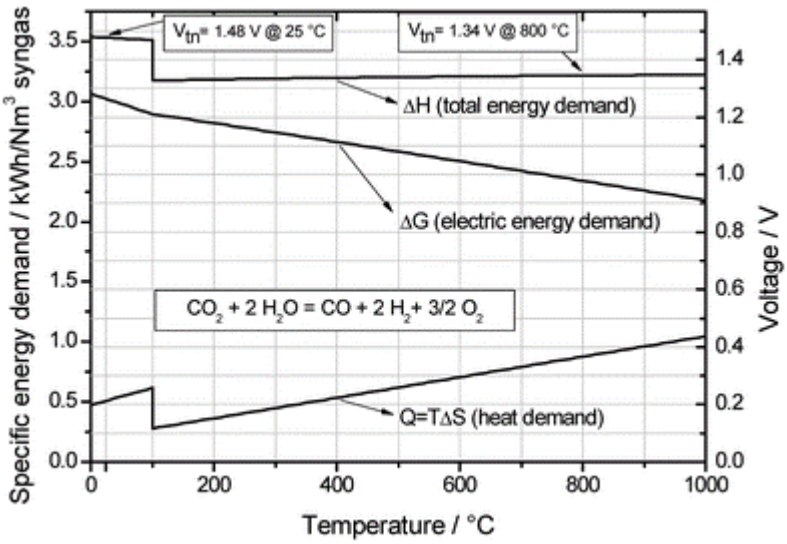

Figure 3.1: *Thermodynamics of syngas production via co-electrolysis as a function of temperature and specific energy demand [148].*

The performance of the SOE to be developed in this work is predicted by applying a one-dimensional, steady-state, macro-level model. This is achieved through an electrochemical model to describe the relationship between the operating conditions, gas specie concentrations, and current density with respect to the electrical cell potential to ascertain the energy consumption of the process.

The electrochemical model introduces the concept of irreversible energy losses in the SOE, also called overpotentials, that occur during the passage of current through the cell to cause joule heating. The resulting cell performance is expressed in a graphical representation of the relation between the voltage and current density — polarisation curve.

The operating voltage (V_{op}) is obtained from the equilibrium voltages and current-dependent overpotentials and, is different for each electrochemically active specie. As a result, the electrolysis of H_2O and CO_2 are considered as separate transfer pathways in the model. V_{op} is expressed in Equation (3.3) as:

$$V_{op} = V_{N,i} + V_{act,i}^{her} + V_{act,i}^{oer} + V_{ohm,i} + V_{int,i} \qquad i = \mathrm{H_2, CO} \tag{3.3}$$

The Nernst voltage $V_{N,i}$ is the minimum voltage required to initiate the electrochemical reaction at a given temperature. While it can be assumed that it should be the same for the individual gas specie, studies have shown that they have different values [149, 150], further expressed in Equations (3.4) and (3.5):

$$V_{N,\mathrm{H_2}} = 1.253 - 0.0002456 \cdot T + \frac{\mathfrak{R} \cdot T}{2\mathfrak{F}} \ln \left[\frac{y_{\mathrm{H_2}} \cdot \sqrt{P \cdot y_{\mathrm{O_2}}}}{y_{\mathrm{H_2O}}} \times \left(\frac{P}{P_{std}} \right)^{0.5} \right] \tag{3.4}$$

$$V_{N,\mathrm{CO}} = 1.46713 - 0.0004527 \cdot T + \frac{\mathfrak{R} \cdot T}{2\mathfrak{F}} \ln \left[\frac{y_{\mathrm{CO}} \cdot \sqrt{P \cdot y_{\mathrm{O_2}}}}{y_{\mathrm{CO_2}}} \times \left(\frac{P}{P_{std}} \right)^{0.5} \right] \tag{3.5}$$

T is the operating temperature, $\mathfrak{R}$ is the gas constant, $\mathfrak{F}$ is the Faraday constant, P is the operating pressure and y_i is the component molar fraction at the triple-phase boundary (TPB). The Nernst equations above are valid at temperatures between 600 K and 1200 K [149]. The ohmic overpotential V_{ohm}, arises from resistance to the ionic and electronic conductivity of electrolyte and electrode materials and contact resistance between cell components. The electrode and contact are negligible and are not considered in the expression below:

$$j = \frac{V_{ohm}}{\delta_e} \cdot \left(\frac{k_e}{T} \cdot e^{-\frac{E_m}{\mathfrak{R} \cdot T}} \right) \tag{3.6}$$

and in addition, the overpotential due to the interconnect, V_{int}

$$j = \frac{V_{int}}{\delta_{int}} \cdot \left(\frac{k_{int}}{T} \cdot e^{-\frac{E_{int}}{\mathfrak{R} \cdot T}} \right) \tag{3.7}$$

j is the current density, δ_i is the thickness of the material of interest, k_i is the pre-exponential factor, and E_i is the activation energy of the Arrhenius expression of the material. The activation overpotential V_{act} is associated with overcoming the reaction energy barriers at the electrode–electrolyte interface and the electric field due to the transfer of charged particles across the interface by ions. The Butler-Volmer equation is used to describe the relationship between V_{act} and j through a series of equations below (Equations (3.8) to (3.13)):

$$p_i^* = \frac{\Gamma_i}{\gamma_i} \times \sqrt{2 \cdot \pi \cdot \mathfrak{R} \cdot T \cdot M_i} \times k_{d,i} \cdot e^{-\frac{E_{d,i}}{\mathfrak{R} \cdot T}} \qquad i = \mathrm{H_2, CO, CO_2} \quad (3.8)$$

$$p_{\mathrm{O_2}}^* = k_{d,\mathrm{O_2}} \cdot e^{-\frac{E_{d,\mathrm{O2}}}{\mathfrak{R} \cdot T}} \quad (3.9)$$

p^* is the equilibrium pressure of the specie at the TPB, Γ is the surface site density, γ is the sticking coefficient, M is the molecular weight, and E_d is the desorption activation energy.

$$j_i^* = k_i \cdot e^{-\frac{E_{act,i}}{\mathfrak{R} \cdot T}} \qquad i = \mathrm{H_2, CO, O_2} \quad (3.10)$$

j^* is the saturation exchange current density. The exchange current density j_0 is the net current at the TPB and can be determined as:

$$j_{0,\mathrm{H_2}} = j^*_{0,\mathrm{H_2}} \times \frac{\left(\frac{p_{\mathrm{H_2}}}{p^*_{\mathrm{H_2}}}\right)^{0.25} \cdot (p_{\mathrm{H_2O}})^{0.75}}{1 + \left(\frac{p_{\mathrm{H_2}}}{p^*_{\mathrm{H_2}}}\right)^{0.5}} \tag{3.11}$$

$$j_{0,\mathrm{CO}} = j^*_{0,\mathrm{CO}} \times \frac{\left(\frac{p_{\mathrm{CO_2}}}{p^*_{\mathrm{CO}}}\right)^{0.25}}{1 + \frac{p_{\mathrm{CO}}}{p^*_{\mathrm{CO}}} + \frac{p_{\mathrm{CO}}}{p^*_{\mathrm{CO_2}}}} \tag{3.12}$$

$$j_{0,\mathrm{O_2}} = j^*_{0,\mathrm{O_2}} \times \frac{\left(\frac{p_{\mathrm{O_2}}}{p^*_{\mathrm{O_2}}}\right)^{0.25}}{1 + \left(\frac{p_{\mathrm{O_2}}}{p^*_{\mathrm{O_2}}}\right)^{0.5}} \tag{3.13}$$

The applied Butler-Volmer are found in Equations (3.14) to (3.17):

$$j_{\mathrm{H_2}} = j_{0,\mathrm{H_2}} \times \left(e^{\frac{\mathfrak{F}\cdot(1+\beta^{oer}_{\mathrm{H2}})\cdot V^{her}_{act,\mathrm{H2}}}{\mathfrak{R}\cdot T}} - e^{-\frac{\mathfrak{F}\cdot\beta^{her}_{\mathrm{H2}}\cdot V^{her}_{act,\mathrm{H2}}}{\mathfrak{R}\cdot T}} \right) \tag{3.14}$$

$$j_{\mathrm{H_2}} = j_{0,\mathrm{O_2}} \times \left(e^{\frac{\mathfrak{F}\cdot\beta^{oer}_{\mathrm{H2}}\cdot V^{oer}_{act,\mathrm{H2}}}{\mathfrak{R}\cdot T}} - e^{-\frac{\mathfrak{F}\cdot\beta^{her}_{\mathrm{H2}}\cdot V^{oer}_{act,\mathrm{H2}}}{\mathfrak{R}\cdot T}} \right) \tag{3.15}$$

$$j_{\mathrm{CO}} = j_{0,\mathrm{CO}} \times \left(e^{\frac{\mathfrak{F}\cdot\beta^{oer}_{\mathrm{CO}}\cdot V^{her}_{act,\mathrm{CO}}}{\mathfrak{R}\cdot T}} - e^{-\frac{\mathfrak{F}\cdot(1+\beta^{her}_{\mathrm{CO}})\cdot V^{her}_{act,\mathrm{CO}}}{\mathfrak{R}\cdot T}} \right) \tag{3.16}$$

$$j_{\mathrm{CO}} = j_{0,\mathrm{CO}} \times \left(e^{\frac{\mathfrak{F}\cdot\beta^{oer}_{\mathrm{CO}}\cdot V^{oer}_{act,\mathrm{CO}}}{\mathfrak{R}\cdot T}} - e^{-\frac{\mathfrak{F}\cdot\beta^{her}_{\mathrm{CO}}\cdot V^{oer}_{act,\mathrm{CO}}}{\mathfrak{R}\cdot T}} \right) \tag{3.17}$$

β is the asymmetry charge-transfer co-efficient of the electrodes, and the superscripts *oer* and *her* are oxygen evolution reaction and hydrogen evolution reaction, respectively.

The electrochemical model is validated with experimental data from [147, 151, 152] and is illustrated on a comparison basis in Figure 3.2.

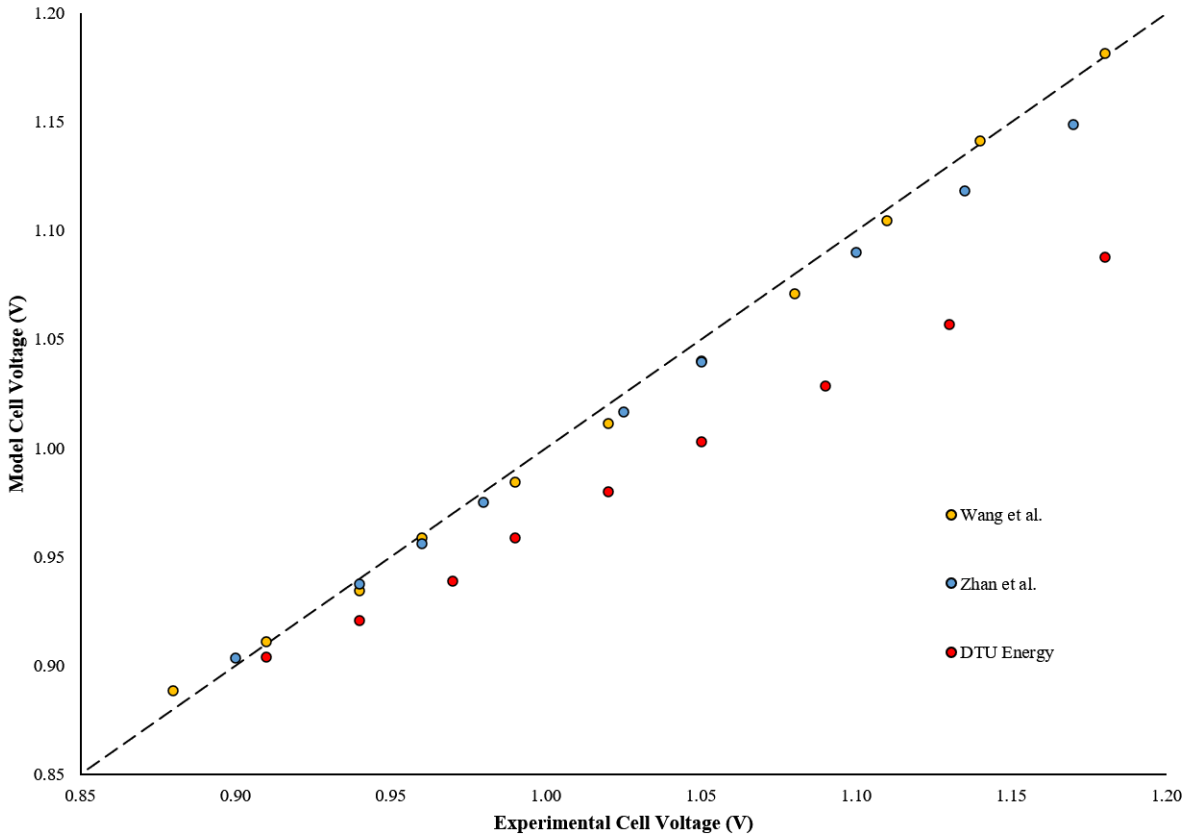

Figure 3.2: *Parity chart illustrating the comparison between model results and different experimental data from the literature. Modified from [147, 151, 152].*

As shown, the model is in agreement with experimental data from Wang et al. [147] and Zhan et al. [152], with the largest variance at 4%. However, larger differences of up to 12% were observed when compared with data from work at DTU Energy conversion [151]. The difference could be due to the difference in the distinctive cell geometry - such as the electrolyte thickness and electrode thickness, which affects the parametric values employed in the model (see Table 3.1) and, ultimately, the cell electrochemistry.

The operation of the aforementioned SOE system is further illustrated in the Aspen Plus® *v*.11.1 software. The Peng-Robinson property package is selected for its suitability for non-polar or mildly polar mixtures like hydrocarbons and light gases.

Table 3.1: *Electrochemistry parameters for the SOE model [147, 152].*

Parameter	**H_2**	**CO**	**CO_2**	**O_2**	**Unit**
k	594113.9	1.61E+07	-	41783.22	A/cm^2
E_{act}	108400	131380	-	88750	J/mol
Γ	2.60E-05	2.60E-05	2.60E-05	-	mol/m^2
γ	0.01	0.5	1.00E-05	-	-
k_d	1.453	3.56E+11	6.45E+07	4.90E+09	$1/s$
E_d	88120	111270	25980	2.0E+05	J/mol
M_i	2015.68	28009.7	44008.7	31998	$g/kmol$
β_{her}	0.7	0.5	-	-	-
β_{oer}	0.1	0.1	-	-	-
δ_e	1.20E-05				m
δ_m	1.50E-05				m
k_e	3.60E+05				$S.K/m$
k_m	5.2645				$S.K/m$
E_e	8.00E+04				J/mol
E_m	40850				J/mol

The following assumptions are considered in this model [146, 153–156]:

1. One-dimensional flows,
2. Ideal mixing,
3. Thermo-neutral conditions in the electrolyser operation,
4. Steady-state operations,
5. Negligible heat losses in the stack,
6. Negligible pressure losses in streamlines,
7. Negligible impurities in the CO_2 input stream.

Due to the rWGS reaction being the dominant producer of CO, the SOE process is modelled in three stages — equilibrium reactions on either side of the electrochemical reactions. The RGIBBS (a Gibbs minimization reactor) unit is used to model the former, and an RSTOIC (a stoichiometry-based reactor) is used to model the electrochemical reaction, with a conversion set at 70% [146, 156]. The hydrogen mole fraction in the electrolyser inlet stream was set to 10% to avoid Ni re-oxidation at the cathode [157]. Uniform temperatures and pressures across units within the SOE were achieved through calculator blocks written in FORTRAN to obtain the desired syngas composition for downstream processes.

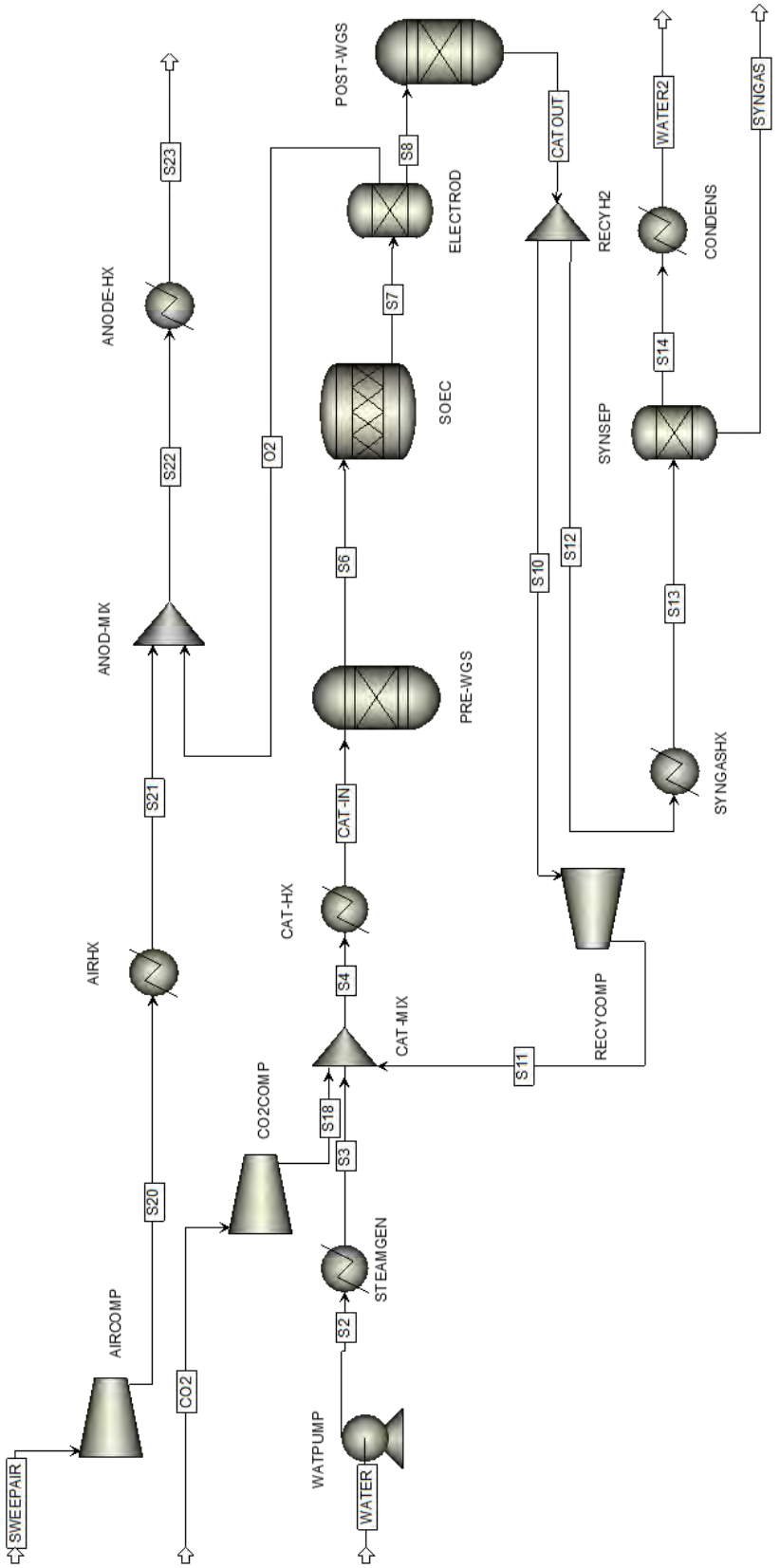

Figure 3.3: *Process flow diagram of SOE system developed on Aspen Plus® v.11.1*

3.2 Model Development of Carbon Capture Process

A model of a solvent-based carbon capture process, as described in a previous chapter, is designed by the simulation software model, Aspen Plus® *v*.11.1. The model is based on a CO_2 post-combustion capture by chemical absorption-stripping, consisting of reactive absorption by an aqueous chemical solution followed by a solvent regeneration by reactive stripping.

Monoethanolamine (MEA) is chosen as the capture solvent due to its associated widespread studies [158]. The primary reactions involved in the $CO_2-MEA-H_2O$ system are represented in Reactions (39) to (43).

$$2\,H_2O \rightleftharpoons H_3O^+ + OH^- \quad \text{(R 39)}$$

$$MEA^+ + H_2O \rightleftharpoons H_3O^+ + MEA \quad \text{(R 40)}$$

$$HCO_3^- + H_2O \rightleftharpoons H_3O^+ + CO_3^{2-} \quad \text{(R 41)}$$

$$CO_2 + MEA + H_2O \rightleftharpoons MEACOO^- + H_3O^+ \quad \text{(R 42)}$$

$$CO_2 + OH^- \rightleftharpoons HCO_3^- \quad \text{(R 43)}$$

The proposed design utilises a *RadFrac*™ model that accounts for reactive absorption-stripping phenomena, including: (a) component diffusion in multiple phases, (b) equilibrium and kinetic reactions, (c) vapour-liquid and gas-liquid equilibria, (d) non-ideal thermodynamics and, (e) simultaneous material and energy transfer.

Due to a typically low Murphree efficiency (around 0.2) for the reactive absorption of CO_2 as described in Figure 3.4 indicative of a deviation from phase equilibrium conditions [159], a rate-based approach is used to model the process.

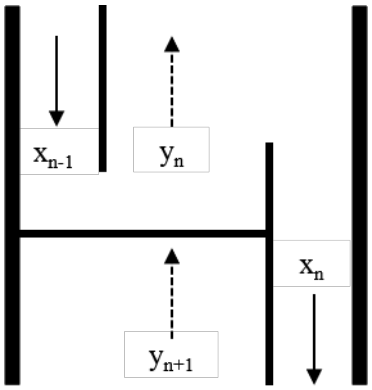

Figure 3.4: *Illustration of the Murphree efficiency E_M, expressed in terms of mole fractions. $E_M = (y_n - y_{n+1})/(y^* - y_{n+1})$, where y^* is the concentration of vapour in equilibrium with the liquid on tray n.*

The rate-based approach accounts for mass transfer limitations due to chemical kinetics by separating the liquid and gas phases with respective films in an interface, based on the two-film theory developed by Lewis and Whitman [160].

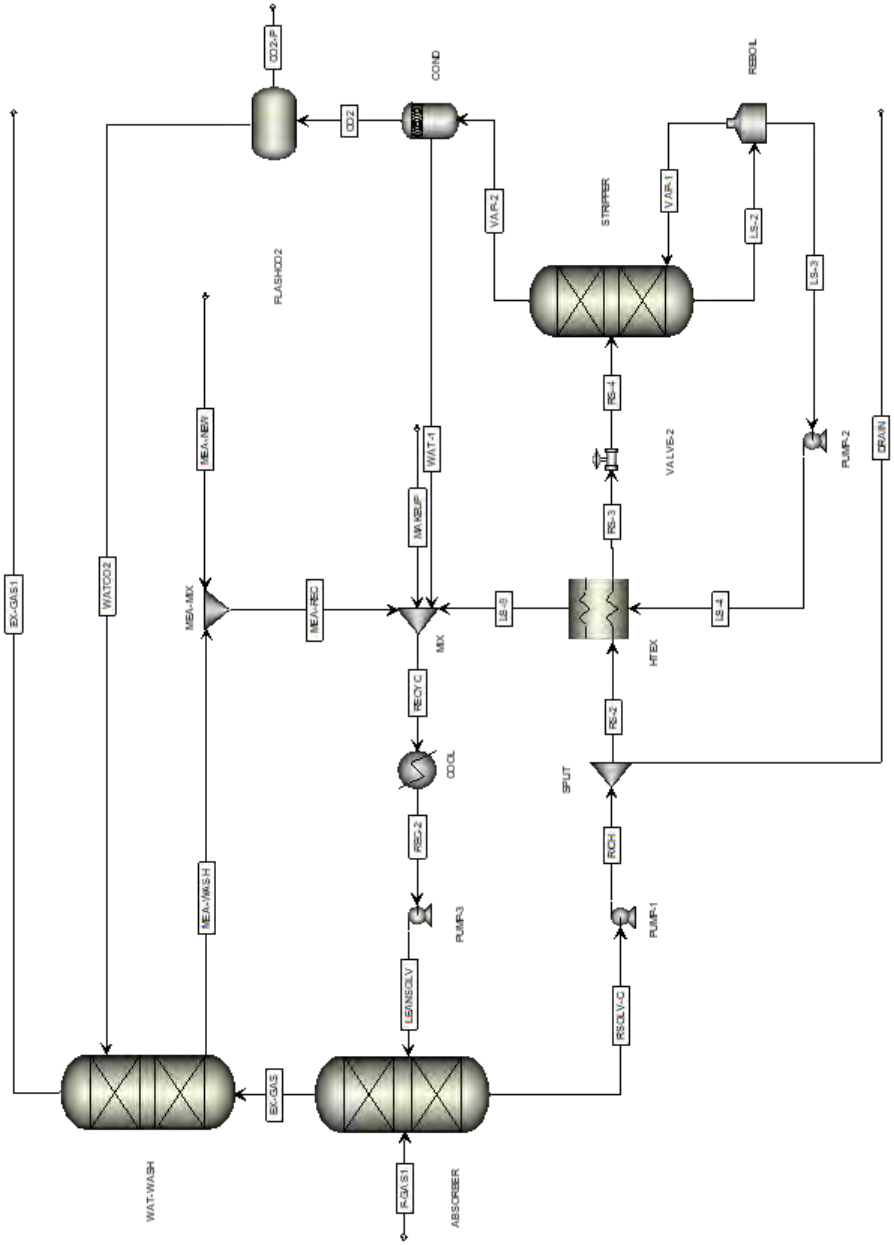

Figure 3.5: *Process flow diagram of MEA-based carbon capture system developed on Aspen Plus® v.11.1*

Figure 3.5 shows the process flow diagram of the CO_2 post-combustion capture modelled on Aspen Plus® *v*.11.1. The process is based on a typical industrial flue gas with a composition of 21% of CO_2 by mass and a 30 wt% MEA aqueous solution. It is assumed that pollutants such as SO_2 and NO_2 has been removed *a priori*.

The CO_2-rich flue gas enters the absorber in a counter-current fashion to the liquid solvent, initiating the absorption process. Rich solvent from the bottom of the absorber is heated in a cross-heat exchanger before entering the stripper column, which is also counter-current with vapour from the reboiler. The stream exiting the top of the stripper comprised mainly of CO_2 and H_2O is partially condensed, where concentrated CO_2 in the gaseous phase is sent for compression. The regenerated solvent exiting the stripper is recycled to the absorber via the aforementioned cross-heat exchanger to continue the process.

Due to the exothermic nature of the absorption process, significant amounts of solvents escape the top of the absorber along the exhaust gases due to vaporisation. To reduce the solvent's evaporative loss and minimise the economic and environmental consequences thereafter, a wash water section is added using the water from the condenser as a solvent.

The absorber and stripper models are validated using experimental data from pilot plant facilities, especially in the analyses of the typical temperature bulge in the absorber column and the evaluation of reboiler duty of the stripper column as per the methodology in [161].

The operation of the absorption process is heavily typified by a plethora of heat transfer phenomena, primarily due to the exothermicity and the counter-current flow of the solvent and feed stream. The gradient in temperatures of the rich/lean solvents results in water vaporisation/condensation at different column positions. The resulting temperature profiles along the column show a distinct temperature

bulge — indicating the column performance. The implications of temperatures in CO_2 absorption by aqueous monoethanolamine have been extensively studied by Kvamsdal and Rochelle [162].

The developed absorber was validated using experimental from two pilot plant facilities with different scales and operating conditions: (a) laboratory scale absorption plant by Tontiwachwuthikul et al. [163] and, (b) large scale absorption/desorption plant described Razi et al. [164].

To determine the minimum height of the absorber column as a cost-effective measure, a sensitivity to solvent flow was carried out without compromising the column performance. The absorber performance is optimised under high-pressure and low-temperature conditions to facilitate the interaction between the solvent and the gas. Figure 3.6a shows that a depressing of the temperature profile as the effective solvent flow rate L_0^{eff} decreases – a decrease in the liquid/vapour ratio, for better performance. The optimum effective flow achieved is $1.196 \cdot L_0^{min}$, which agrees with the value of $1.2 \cdot L_0^{min}$ obtained from the experimental data sufficient to ensure the absence of temperature bulges in the absorber. A CO_2 removal of 89.69% was achieved as shown in Figure 3.6b, in agreement with the value of 90% obtained from the experimental data in [165].

Using the same cost-cutting procedure for the stripper dimensions, a liquid temperature profile assessment was carried out while varying the column height. Operation of stripper columns are maximised under increasing temperatures to reduce the solubility of the gas. It is therefore essential to avoid isothermal zones. Analyses of Figure 3.7 shows that an MEA recovery rate greater than 99% can be achieved whilst using the same optimum effective flow of $1.196 \cdot L_0^{min}$ and a temperature gradient that is higher than $1K/m$. This is in close agreement with a 100% MEA recovery achieved in experimental data in the work of Dugas [166] from a pilot plant.

The developed model achieved an 87% CO_2 removal rate at a purity greater

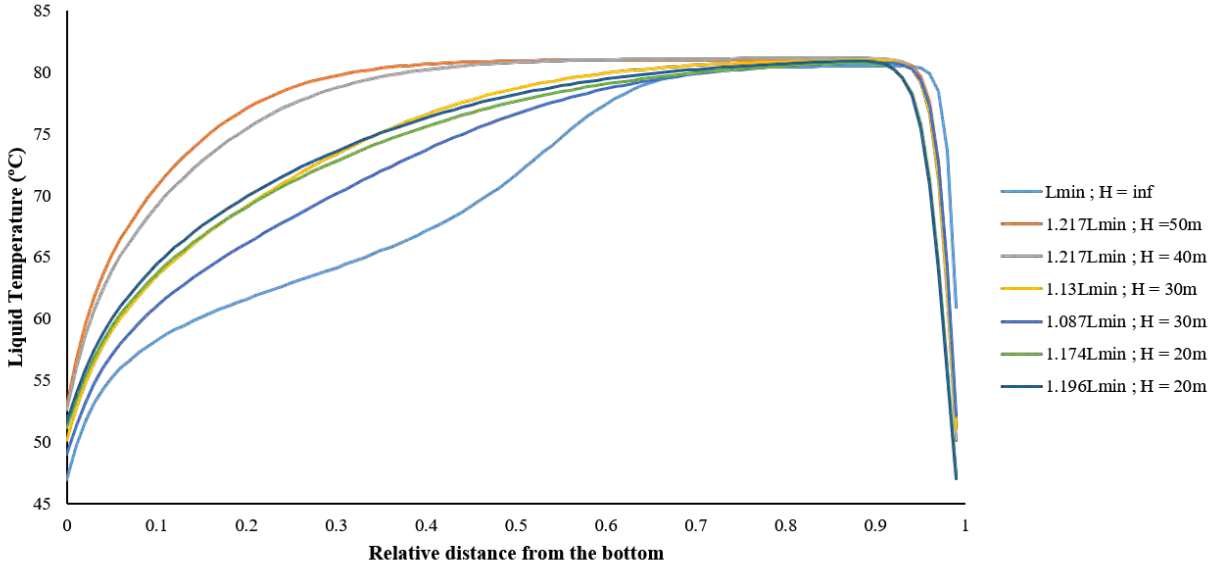

(a) *Variation of liquid temperature for different multiples of the minimum solvent flow rate L_{min} and column height, H.*

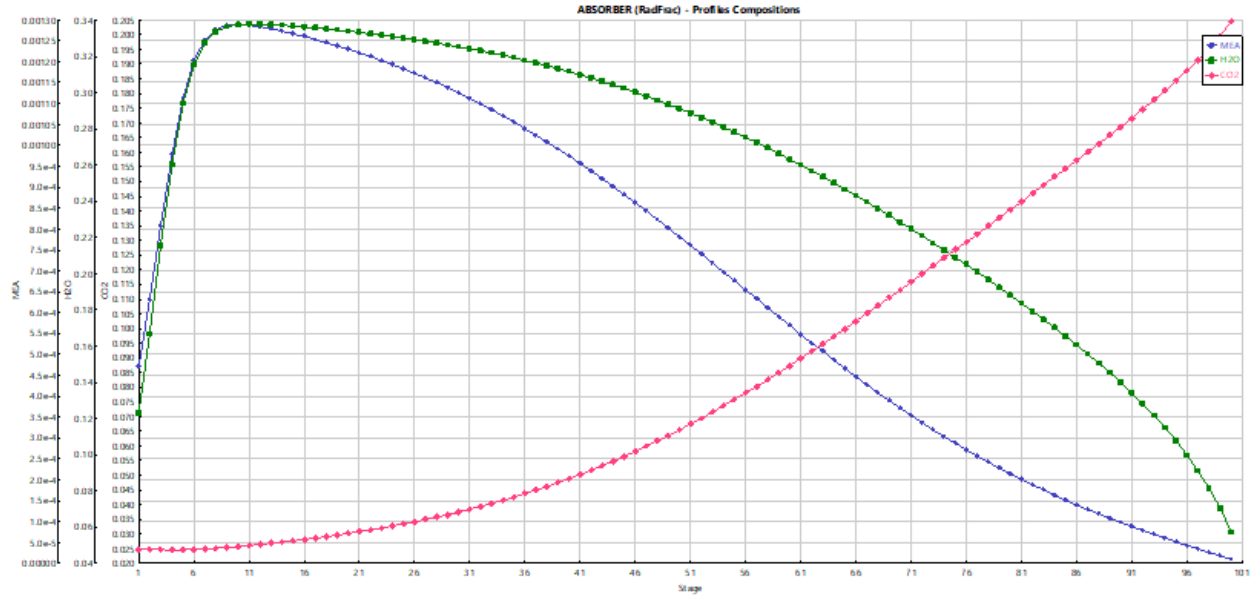

(b) *Absorber column composition.*

Figure 3.6: *Absorber column performance.*

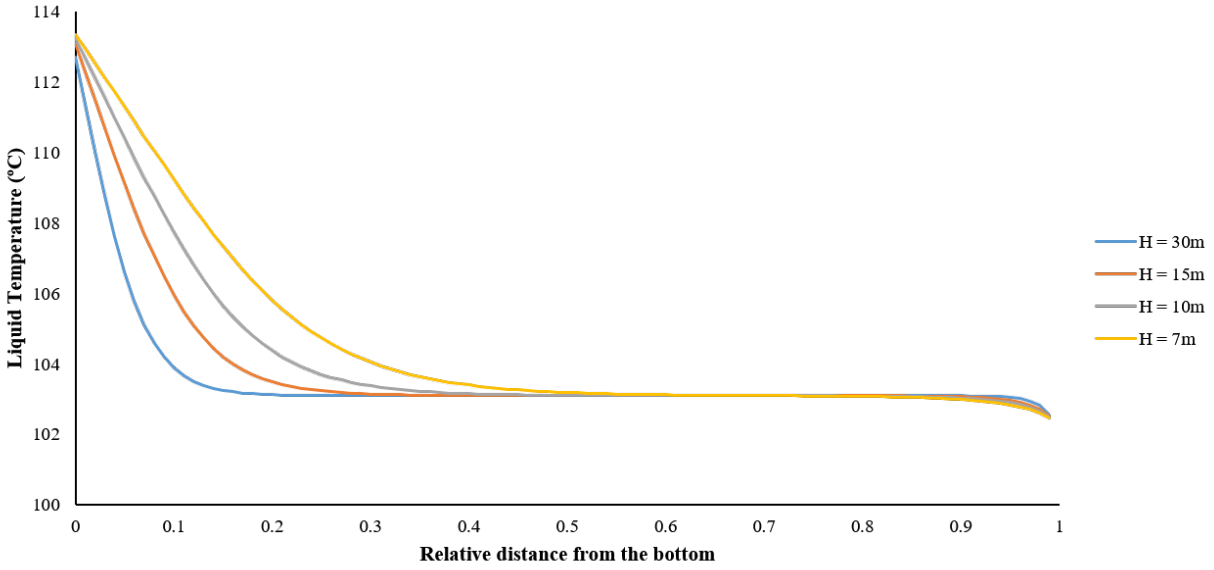

(a) *Variation of liquid temperature for different column heights, H.*

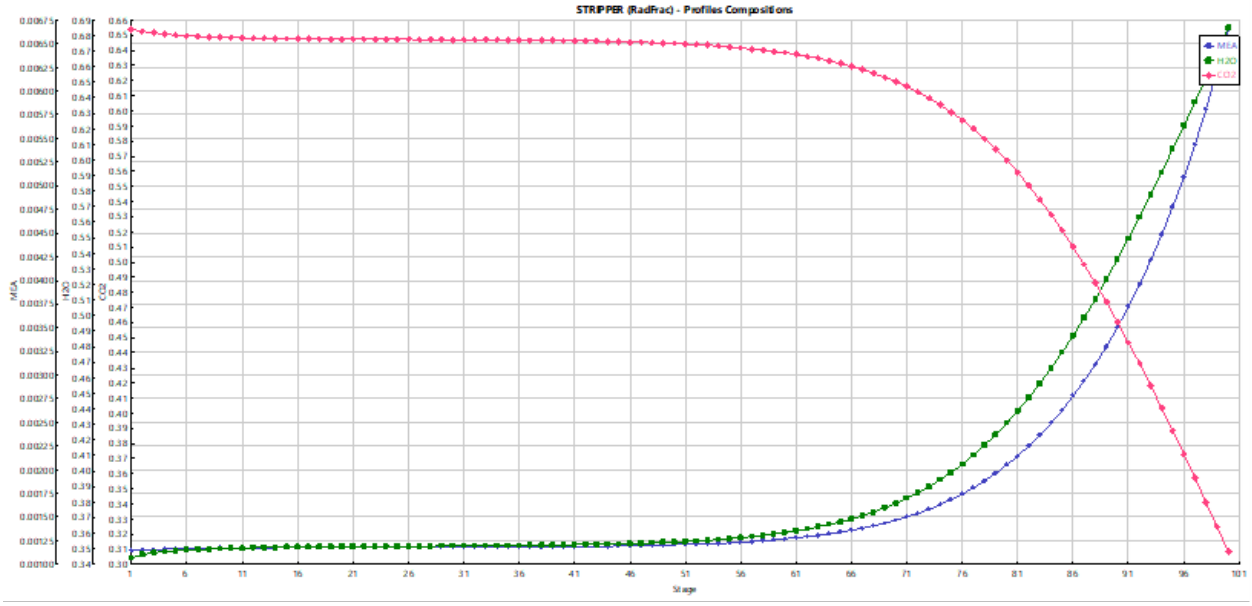

(b) *Stripper column composition.*

Figure 3.7: *Stripper column performance.*

than 99%. Additionally, in accordance with the threshold limit value – time-weighted average of MEA in the exhaust gas is several magnitudes below the prescribed 3ppm limit. It is noted that whilst not within the scope of this work, an extra CO_2 purification process could be retrofitted to capture CO_2 from the exhaust gas if required.

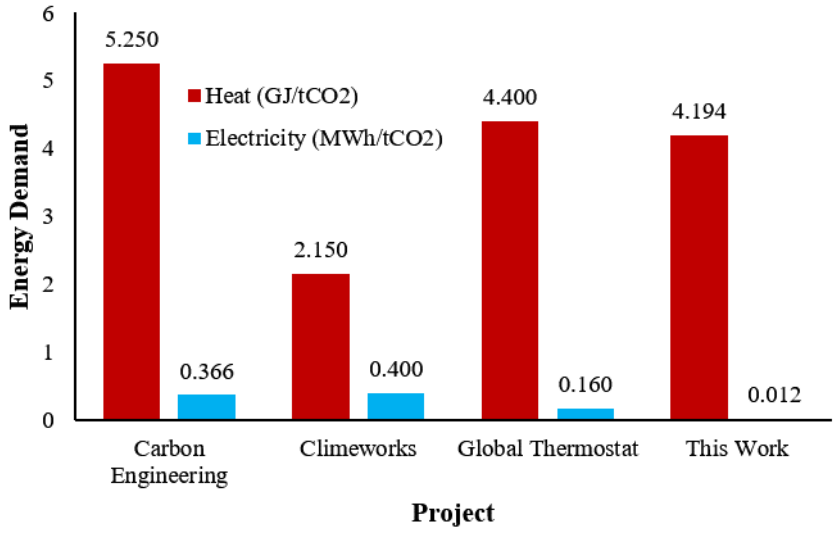

Figure 3.8: *Primary energy consumption for the carbon capture system modelled in this work, in comparison to other projects [167].*

The energy requirement is largely dominated by the heat of regeneration for the solvent and is expressed by the stripper reboiler duty (Q_{reb}) as shown in Equation (3.18).

$$Q_{reb} = \underbrace{(n_{\mathrm{CO_2}} \Delta H_{\mathrm{CO_2}})}_{\text{Heat of desorption}} + \underbrace{(\bar{m}_{solv} \bar{C}_p (T_{in} - T_{out}))}_{\text{Sensible heat}} + \underbrace{(n_{vap,\mathrm{H_2O}} \Delta H_{vap,\mathrm{H_2O}})}_{\text{Heat of vaporisation}} \tag{3.18}$$

Figure 3.8 shows the energy consumption based on the MEA-based post-combustion carbon capture process in comparison to other current projects. The variations are mainly due to to the different technologies applied for each project. Global Thermostat and Climeworks utilised amine-based solid sorbents. A KOH-based absorption process was utilised, which incurs a high amount of energy for the

calcination process required for the solvent recovery. The resulting heat demand of 4.19 GJ/t_{CO_2} from the model is in agreement with value of 4.20 GJ/t_{CO_2} achieved in a separate work undertaken by Kothandaraman et al. [168]. The relatively low electricity demand could be attributed to the absence of compression of CO_2 for transportation and storage purposes in this work.

3.3 Model Development of the Hydrogenation of COx to synthetic fuels

In this section, the synthesis of the fuels of choice is modelled and simulated in this work for further assessment. The simulation for the design of a process is necessary for the technical assessment, in optimising an established or recently developed system and in the eventual scale-up of the process, as required. The software Aspen Plus® *v*.11.1 will be used to simulate the processes onward to allow for detailed designs and comparisons.

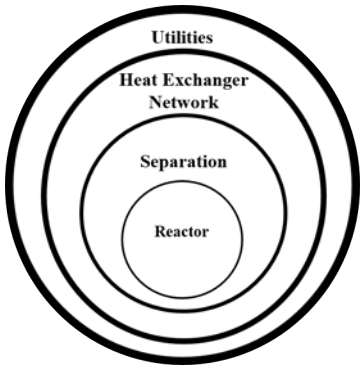

Figure 3.9: *The onion model for a process design.*

Based on the Douglas 'onion' model hierarchical structure of a process design (See Figure 3.9), the reactor takes precedent [169]. This work simultaneously employs two approaches for the reactor design —kinetic and thermodynamic modelling.

Kinetic modelling is essential to studies in identifying the interactions between the formulation of catalysts and their behaviour within a reaction environment. The implementation of a catalyst's kinetic parameters can be used to establish the mode of operation of a reactor, to predict the size of the reactor, and to compute the pressure drop along the dimension of the reactor, typically by the Ergun momentum balance equation (See Equation (3.19)).

$$\frac{dP}{dZ} = 150 \cdot \frac{(1-\varepsilon)^2 \mu u_g}{\varepsilon^3 d_p^2} + 1.75 \cdot \frac{(1-\varepsilon)\rho u_g}{\varepsilon^3 d_p} \tag{3.19}$$

P is pressure, Z is reactor length, μ is the effectiveness factor used for the intra-particle transport limitation, u_g is the linear velocity of the fluid phase, d_p is the particle diameter, ρ is the density of catalytic bed, and ε is the void fraction of the catalytic bed.

Kinetic models and data from selected published literature are employed in Aspen Plus® using the Langmuir–Hinshelwood–Hougen–Watson (LHHW) rate model in the following form:

$$r = \frac{(\text{kinetic term})(\text{driving force})}{\text{adsorption term}} \tag{3.20}$$

Kinetic parameters such as the pre-exponential factors of the rate and adsorption coefficients are derived from the Arrhenius and Van't Hoff equations (Equations (3.21) and (3.22)).

$$k_i = \exp\{\theta_{k,i}\} \cdot \exp\left\{\theta_{E,i}\left(1 - \frac{T_{ref}}{T}\right)\right\} \tag{3.21}$$

$$K_j = \exp\{\theta_{k,j}\} \cdot \exp\left\{\theta_{H,j}\left(1 - \frac{T_{ref}}{T}\right)\right\} \tag{3.22}$$

$$\theta_{k,i} = \ln\left(k_{i,T_{ref}}\right) \tag{3.23}$$

$$\theta_{K,j} = \ln\left(K_{j,T_{ref}}\right) \tag{3.24}$$

$$\theta_{E,i} = \frac{E_{A,i}}{\Re\, T_{ref}} \tag{3.25}$$

$$\theta_{H,j} = \frac{\Delta H_j}{\Re\, T_{ref}} \tag{3.26}$$

k is the rate constant, K is the thermodynamic equilibrium constant, θ is the pre-exponential factor, i and j are the reactions and species, respectively.

The Gibbs free energy minimisation method is implemented via Aspen Plus® for the thermodynamic characterisation, which is based on the principle that

the total Gibbs energy of a system (G^t) is at its minimum at chemical equilibrium. G^t is defined as:

$$G^t = \sum_{i=1}^{N} n_i \mu i \tag{3.27}$$

n_i and μ_i is the number of moles and chemical potential of species i, with the latter defined as:

$$\mu_i = G_i^\circ + \Re T \ln\left(\frac{f_i}{f_i^\circ}\right) \tag{3.28}$$

G^t is further expressed in Equation (3.29) as:

$$G^t = \sum_{i=1}^{N} n_i G_{f,i}^\circ + \sum_{i=1}^{N} n_i \Re T \ln\left(\frac{n_i}{n_{tot}}\right) \tag{3.29}$$

The Lagrange multiplier method is the most appropriate method to perform the minimisation of the Gibbs free energy, and it is defined in Equation (3.30) as:

$$L = G^t - \sum_{j=1}^{k} \lambda_j \left(\sum_{i=1}^{N} a_{ij} n_i - A_j\right) \tag{3.30}$$

$$\sum_{i=1}^{N} a_{ij} n_i = A_j, \qquad j = 1, 2, 3, \ldots, k \tag{3.31}$$

a_{ij} is the number of atoms of the jth element in each mole of species i, A_j is the total number of atoms of the jth element in the reaction mixture, L is the Lagrangian function, and $\lambda_j = \lambda_1, \ldots, \lambda_k$ are Lagrange multipliers.

A study by Gao et al. [170] demonstrated that the Gibbs free energy minimisation method in the thermodynamic analysis of the hydrogenation of COx is

comparable with results from experimental data and is thus effective for understanding the reaction environments.

The application of co-electrolysis of CO_2 and H_2O necessitates that the syngas composition has to be monitored. A syngas modular (Z) is used to qualify the feed composition for each fuel synthesised. Z is defined in Equation (3.32):

$$Z = \frac{x_{H_2} - x_{CO_2}}{x_{CO} + x_{CO_2}} \tag{3.32}$$

x_i is the molar fraction of the species in the feed gas.

Where possible, the mode of reactor operation will be adiabatic due to its lower costs and simpler design over isothermal reactors, thus having a higher potential for feasible scalability and energy integration, especially with the coupling with a high temperature electrolyser system.

In a bid to recover useful heat energies and reduce the burden of the utilities on operating costs, process heat exchangers are used to recover (a) the latent heat of condensation of steam from inter-stage cooling trains and, (b) steam from the combustion of unreacted gases via heat recovery steam generators.. Electrical work is extracted from the high pressure steam as it expands through a steam turbine.

Further heat is recovered from the effluent stream by employing a Classius-Rankine cycle, producing more electrical energy. Figure 3.10 shows the schematic of a conventional Rankine cycle and is described as follows:

- 1-2: Working liquid undergoes isentropic compression via a system pump,
- 2-3: Heat is transferred from an external source to the pressurised liquid isobarically until it reaches the saturation temperature,
- 3-4: The saturated vapour stream undergoes isentropic expansion through a

gas turbine, where heat is converted to mechanical energy and subsequently electricity via an electrical generator,

- 4-1: The working fluid is liquefied upon condensation facilitated by an external cooling source before recycling to the pump again.

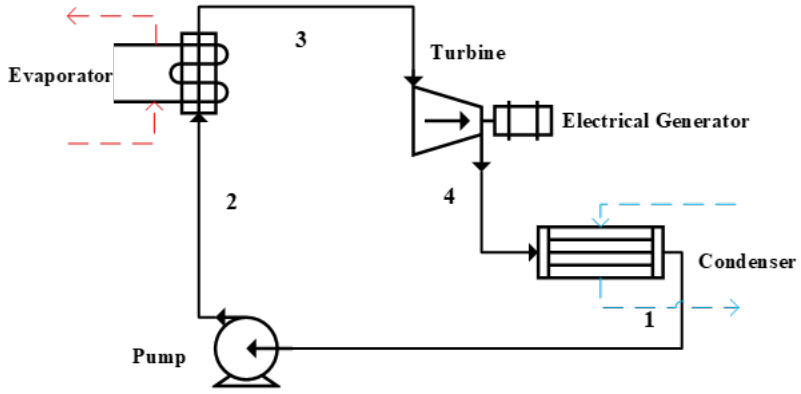

Figure 3.10: *A simple schematic of a Rankine cycle*

Methane Synthesis

The physical property method employed to model thermodynamic and transport properties is the Peng-Robinson property package method for non-polar or mildly polar mixtures like hydrocarbons and light gases such as H_2 and CO_2. It is based on a cubic equation of state model developed by Peng and Robinson [171].

The kinetic models (Equations (3.33) and (3.34)) employed were developed by Kopyscinski et al. [172] over a commercial Ni–alumina catalyst (50% Ni/Al_2O_3) in a fixed bed reactor. The reactor is modelled using an RPLUG kinetic reactor within the simulator.

$$r_1 = \frac{k_1 \, K_C \, p_{CO}^{0.5} \, p_{H_2}^{0.5}}{\left(1 + K_C \, p_{CO} + K_{OH} \, p_{H_2O} \, p_{H_2}^{-0.5}\right)^2} \tag{3.33}$$

$$r_2 = \frac{k_2 \left(K_\alpha \, p_{CO} \, p_{H_2O} - \frac{p_{H_2} \, p_{CO_2}}{K_{eq}}\right)}{\left(1 + K_{CO} \, p_{CO} + K_{OH} \, p_{H_2O} \, p_{H_2}^{-0.5}\right)^2} \tag{3.34}$$

The rate equation is based on the assumption that the rate-determining step for the proposed reaction mechanism is:

$$C{\cdot}\psi + H{\cdot}\psi \rightleftharpoons CH{\cdot}\psi + \psi \tag{R 44}$$

The conversion of the carbon oxides is considered the limiting step; thus, the flow fraction of the H_2 in the feed gas is varied to ascertain the optimum value of the syngas modulus, Z.

By varying the syngas modulus of the feed flow rate on ASPEN, it can be established that the optimum range for CH_4 output is when $Z = 3 \pm 0.5$ as described in Figure 3.11 above. This value is kept constant throughout the course of this assessment.

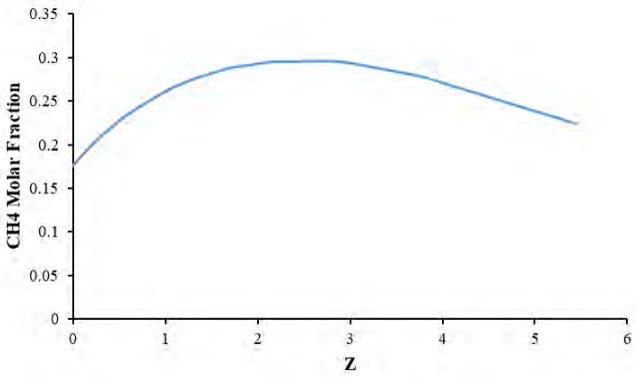

Figure 3.11: *Effect of syngas modulus on CH_4 production.*

A series of sensitivity analyses were carried out to determine the effect of the operating conditions on the catalytic performance within a single reactor. From the analyses in Figure 3.12, the temperature range of interest is from 280 °C to 320 °C. At this temperature range, the rate of CH_4 production increases with the activity of the reactants. Based on previous results, varying the pressure as shown in Figure 3.13 reveals that an increase in pressure has a minimal impact, especially at higher temperatures due to the exothermal nature of the methanation reaction.

In addition, it is noted that CO is completely converted under the condition of 15 bar and 280 °C.

However, the kinetic model is only valid for a temperature range 200 °C to 400 °C for isothermal reactors alone. Carbon deposition and pressure loss are also assumed to be negligible.

The Aspen RGIBBS unit is used to design the reactor to simulate a thermodynamic model. The operating feed gas composition and operating conditions from the previous section are carried over into this design, especially a pressure upper limit of 15 bar. The reactor's operation mode follows the conventional adiabatic fixed-bed reactor model.

Due to the exothermic nature of methanation, a temperature increase within

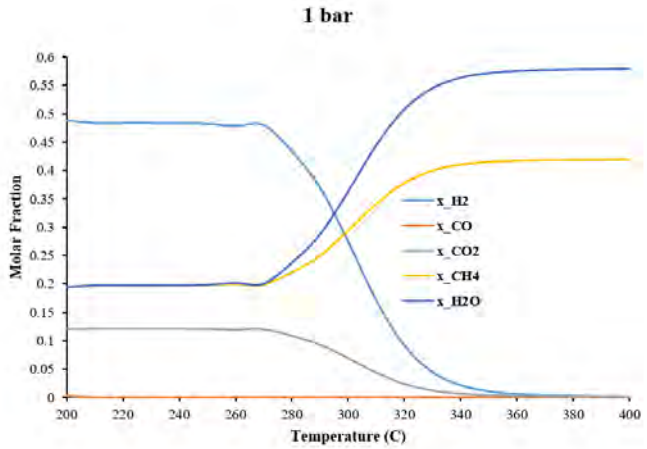

(a) *1 bar*

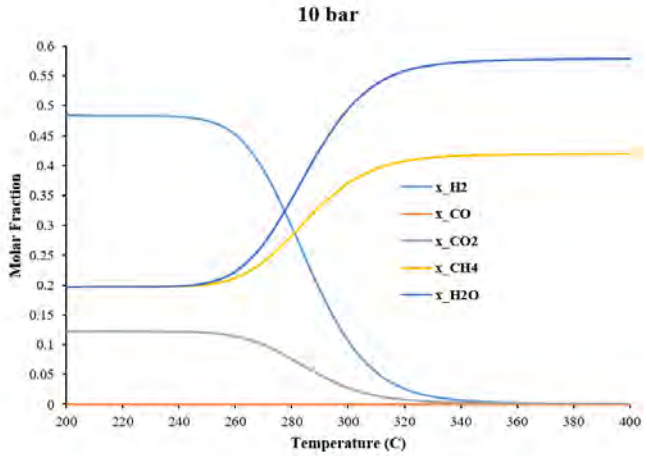

(b) *10 bar*

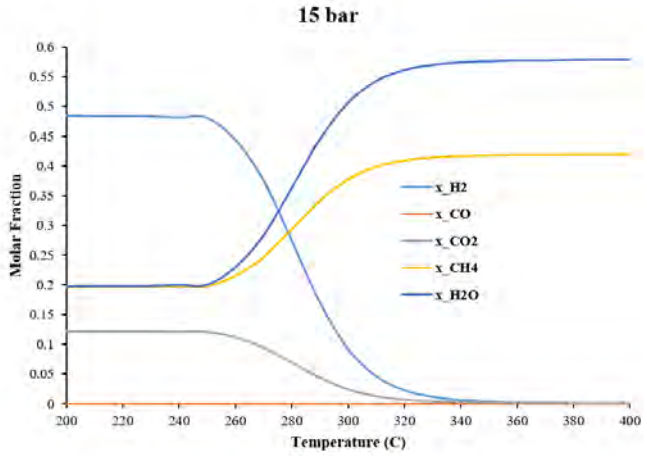

(c) *15 bar*

Figure 3.12: *Effect of pressure*

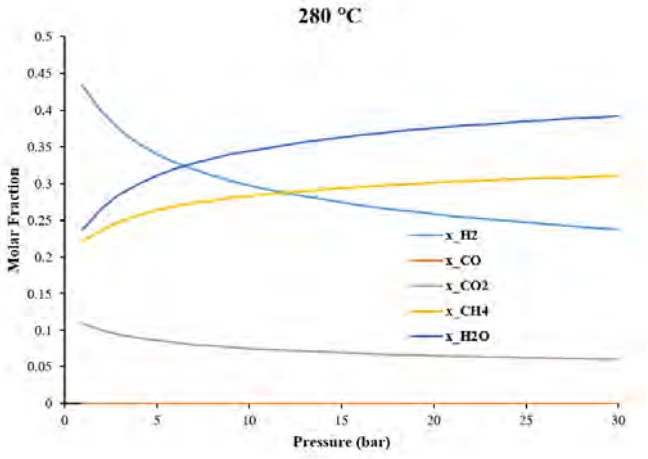

(a) *280 ℃*

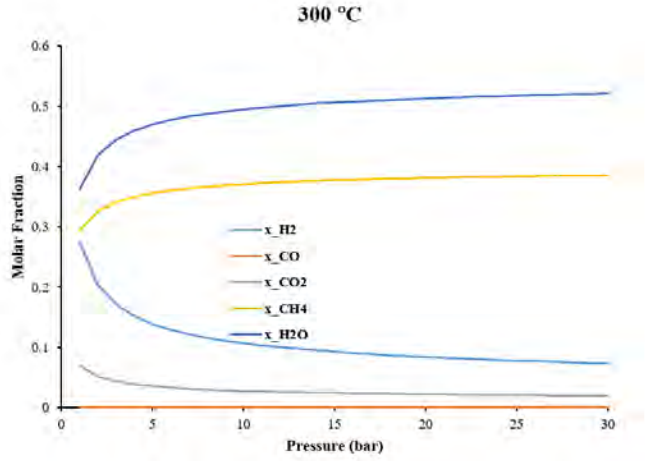

(b) *300 ℃*

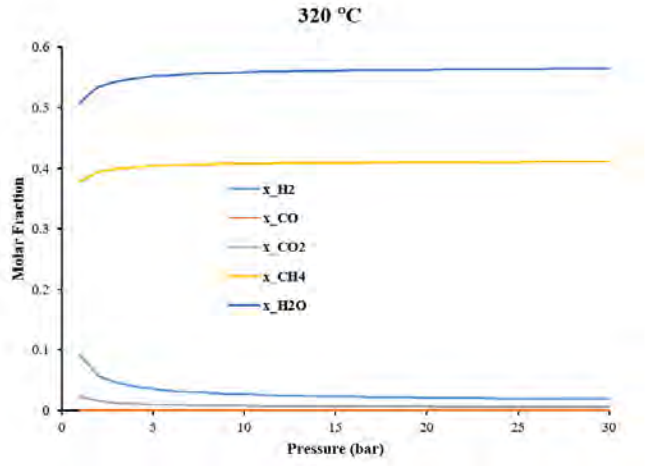

(c) *320 ℃*

Figure 3.13: *Effect of temperature*

the system can create a thermal runaway and the deactivation of the catalyst. A multistage intermediate cooling can be implemented to reduce the temperature of the feed stream and encourage an equilibrium conversion. CO methanation is more exothermic than CO_2, and thus the formers' conversion serves as the basis for the reactor design with Equation (3.35).

$$\dot{Q} - \dot{W} + \sum_{i=1}^{n} F_i H_i \Big|_{in} - \sum_{i=1}^{n} F_i H_i \Big|_{out} = 0 \tag{3.35}$$

F_i is the molar flow and H_i is the enthalpy of the species i in the reactor and are further defined below in Equations (3.36) and (3.37) as:

$$F_i = F_{\mathrm{CO},0}(\theta_i + v_i X_{\mathrm{CO}}) \tag{3.36}$$

$$H_i = \int_{T_{Ref}}^{T} C_{pi}\,\mathrm{d}T \tag{3.37}$$

The correlation between the conversion of CO and temperature can be expressed in Equation (3.38) as:

$$X_{\mathrm{CO}} = \frac{\int_{T_{Ref}}^{T} \cdot \sum_{i=1}^{n} \theta_i \cdot C_{pi}\,\mathrm{d}T}{-\left(\Delta H_R^{\circ}(T_{Ref}) + \int_{T_{Ref}}^{T} C_p\,\mathrm{d}T\right)} \tag{3.38}$$

Analysis from Figure 3.14 (base design), based on a feed inlet temperature at 280 °C, show that a minimum of 4 adiabatic reactors would be required to achieve a high CO conversion in a feed stream with a value of $Z = 3$. It also shows that the exit temperatures are very high, especially after the first reactor, which may lead to degradation and thermal instability due to the sintering of typical commercial catalysts, such as Ni/Al_2O_3 [173].

A recycle gas loop can be employed to decrease the reaction temperature

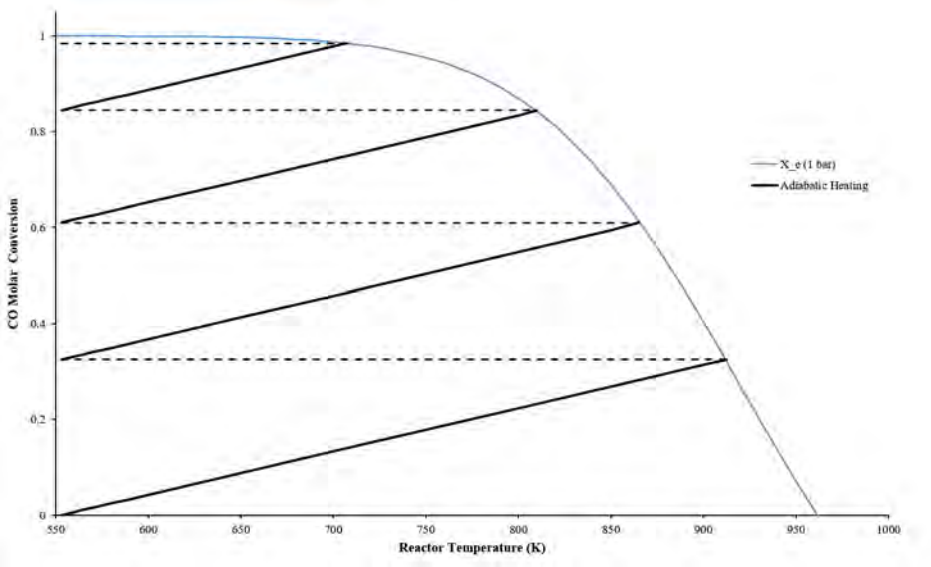

Figure 3.14: *Relation between CO conversion and reactor temperature, with inter-stage cooling, at 1 bar. Horizontal lines represent inter-stage cooling.*

and consequently achieve higher conversion. The effect of varying the recycle ratio with the conversion and CO and H_2 is shown in Figure 3.15.

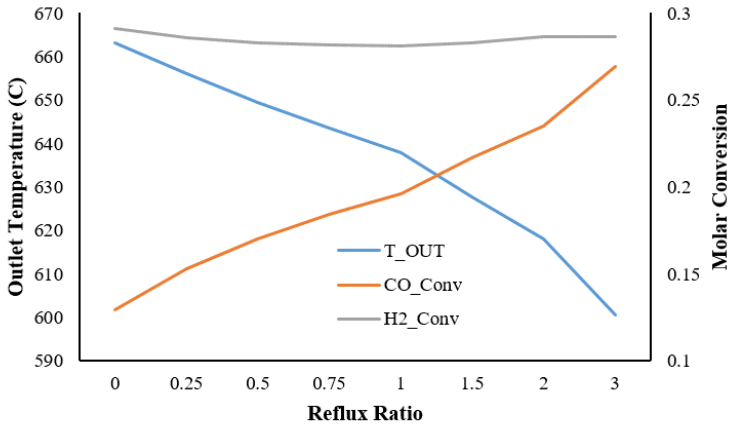

Figure 3.15: *The effect of recycle ratio on the conversion of methanation reactants at 1 bar.*

With an increasing recycle ratio, a decrease in the reactor outlet temperature is seen and an increase in the conversion of CO, but this has minimal effect on H_2 concentration. However, a higher concentration of CH_4 in the recycle gas can lead to coke deposition due to thermal cracking. A minimum operating pressure of

15 bar is therefore recommended to minimise the catalyst deactivation due to carbon deposition [170].

Figure 3.16 shows the flowsheet of the modelled methanation process consisting of four adiabatic reactors with inter-stage cooling and water condensation between reactors.

The operating conditions for the reactors is 280 °C and 15 bar with unit pressure drops for the reactors and condensers, assumed to be 0.30 bar and 0.60 bar respectively. All reactors operate at the same pressure.

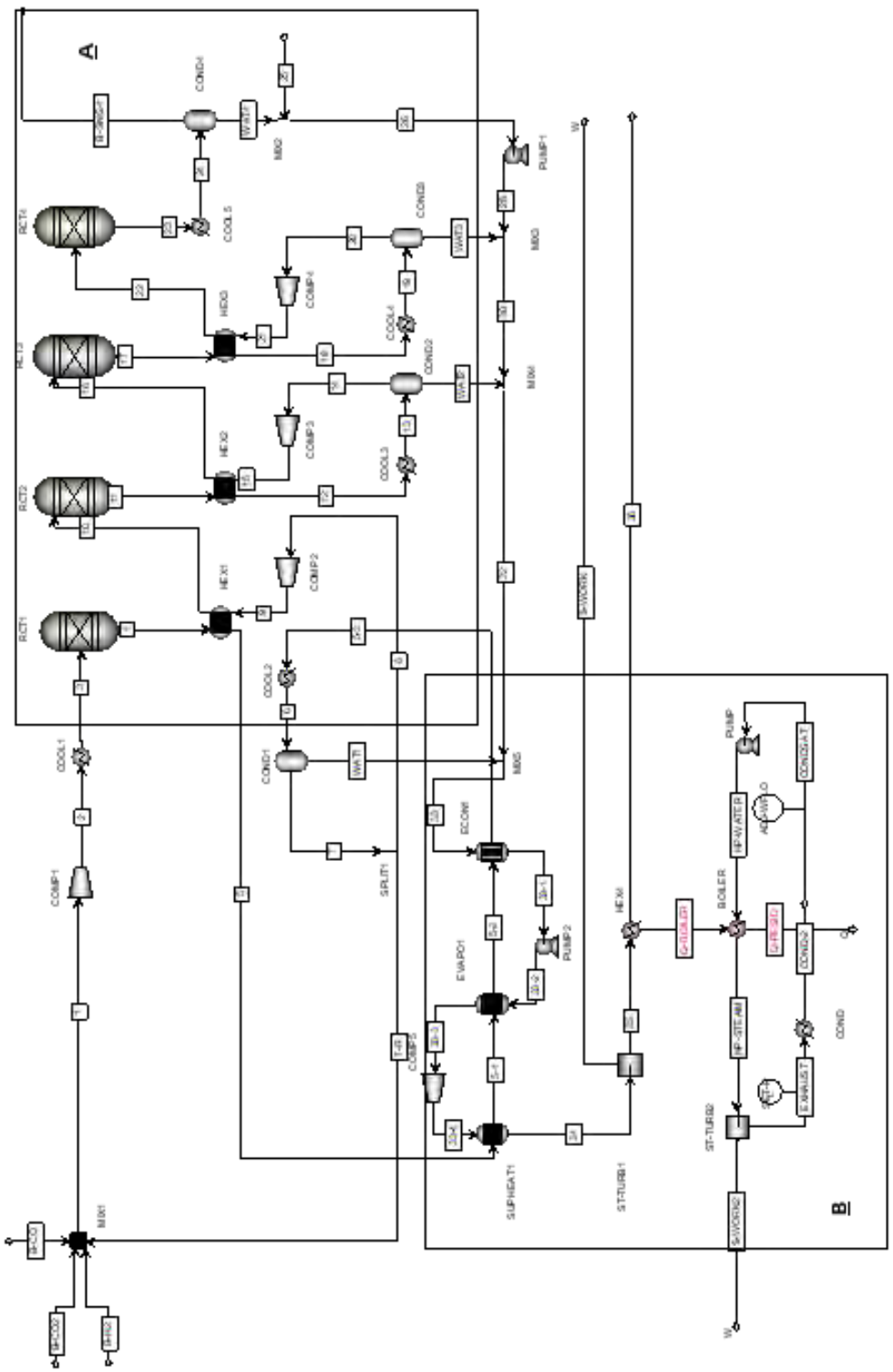

Figure 3.16: *Process flow diagram for the methanation plant showing A) synthesis section and, B) heat recovery section.*

Methanol Synthesis

The *modus operandi* for assessing methanol synthesis follows the same pattern as methane synthesis in the previous sections.

The Aspen RGIBBS unit is used to model a reactor to ascertain the optimal feed composition and operating parameters. The influence of the syngas modulus Z is shown in Figure 3.17:

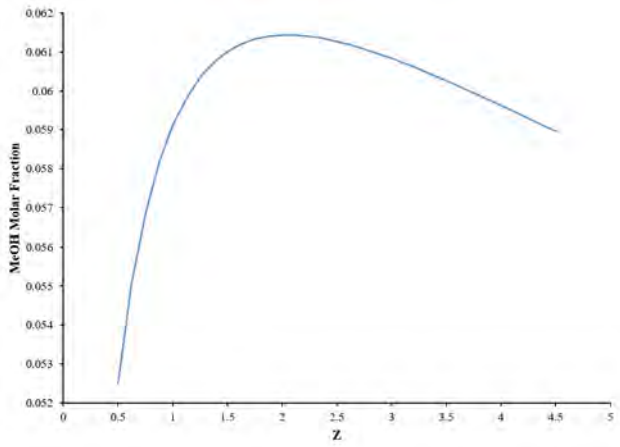

Figure 3.17: *Effect of syngas modulus on CH_3OH production.*

Analysis shows that the optimum flow of H_2 is at $Z = 2 \pm 0.25$.

The employed kinetic model Equations (3.39) to (3.41) were developed by Graaf et al. [174] over a Cu/Zn/Al/Zr catalyst, which is suitable for reactants containing CO and CO_2, and capable of taking the WGS reaction into account. The reactor is modelled using an Aspen RPLUG model block. The RPLUG model block is a rigorous model for plug flow reactors, which assumes that perfect mixing occurs in the radial direction and that no mixing occurs in the axial direction.

$$r_{\mathrm{CO}} = \frac{k_A K_{\mathrm{CO}} \left[f_{\mathrm{CO}} f_{\mathrm{H_2}}^{1.5} - f_{\mathrm{CH_3OH}} / \left(f_{\mathrm{H_2}}^{0.5} K_{P,A} \right) \right]}{\left(1 + K_{\mathrm{CO}} f_{\mathrm{CO}} + K_{\mathrm{CO_2}} f_{\mathrm{CO_2}} \right) \left[f_{\mathrm{H_2}}^{0.5} + \left(K_{\mathrm{H_2O}} / K_{\mathrm{H_2}}^{0.5} \right) f_{\mathrm{H_2O}} \right]} \tag{3.39}$$

$$r_{H_2O} = \frac{k_B K_{CO_2} \left[f_{CO_2} f_{H_2} - f_{H_2O} f_{CO} / K_{P,B} \right]}{\left(1 + K_{CO} f_{CO} + K_{CO_2} f_{CO_2}\right) \left[f_{H_2}^{0.5} + \left(K_{H_2O} / K_{H_2}^{0.5} \right) f_{H_2O} \right]} \tag{3.40}$$

$$r_{CO_2} = \frac{k_C K_{CO} \left[f_{CO_2} f_{H_2}^{1.5} - f_{CH_3OH} f_{H_2O} / \left(f_{H_2}^{1.5} K_{P,C} \right) \right]}{\left(1 + K_{CO} f_{CO} + K_{CO_2} f_{CO_2}\right) \left[f_{H_2}^{0.5} + \left(K_{H_2O} / K_{H_2}^{0.5} \right) f_{H_2O} \right]} \tag{3.41}$$

The rate equation is based on the assumption that the rate-determining step for the proposed reaction mechanism is:

$$H_2CO{\cdot}\psi_1 + H{\cdot}\psi_2 \rightleftharpoons H_3CO{\cdot}\psi_1 + \psi_2$$

Figure 3.18 show that CH_3OH is favoured under conditions of low temperature and very high pressures under adiabatic conditions. Results from the thermodynamic and kinetic models also show a good correlation.

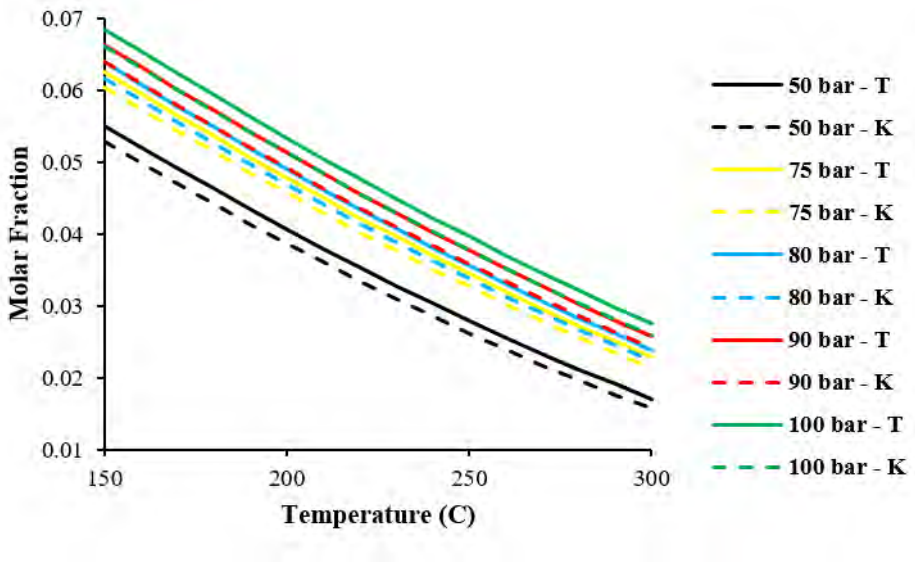

Figure 3.18: *Effect of operating parameters on CH_3OH production using thermodynamic (T) and kinetic (K) models from author's own analysis.*

The kinetic model developed by Graaf et al. [174] was accounted to be valid for an operating temperature range of 470 K to 550 K, and pressures up to 85 bar

[175]. These operating conditions served as the model limits in this work. Two-phase quenched reactor systems are favourably suited for CO-rich feed gas, for example, from co-electrolysis, which is thus employed in this study [174]. The gases exiting the reactors are cooled and separated. Some of the unreacted gases are recycled back to the reactor while the rest are combusted in a heat recovery system described earlier. The methanol stream is purified in a distillation column to obtain a high-purity product.

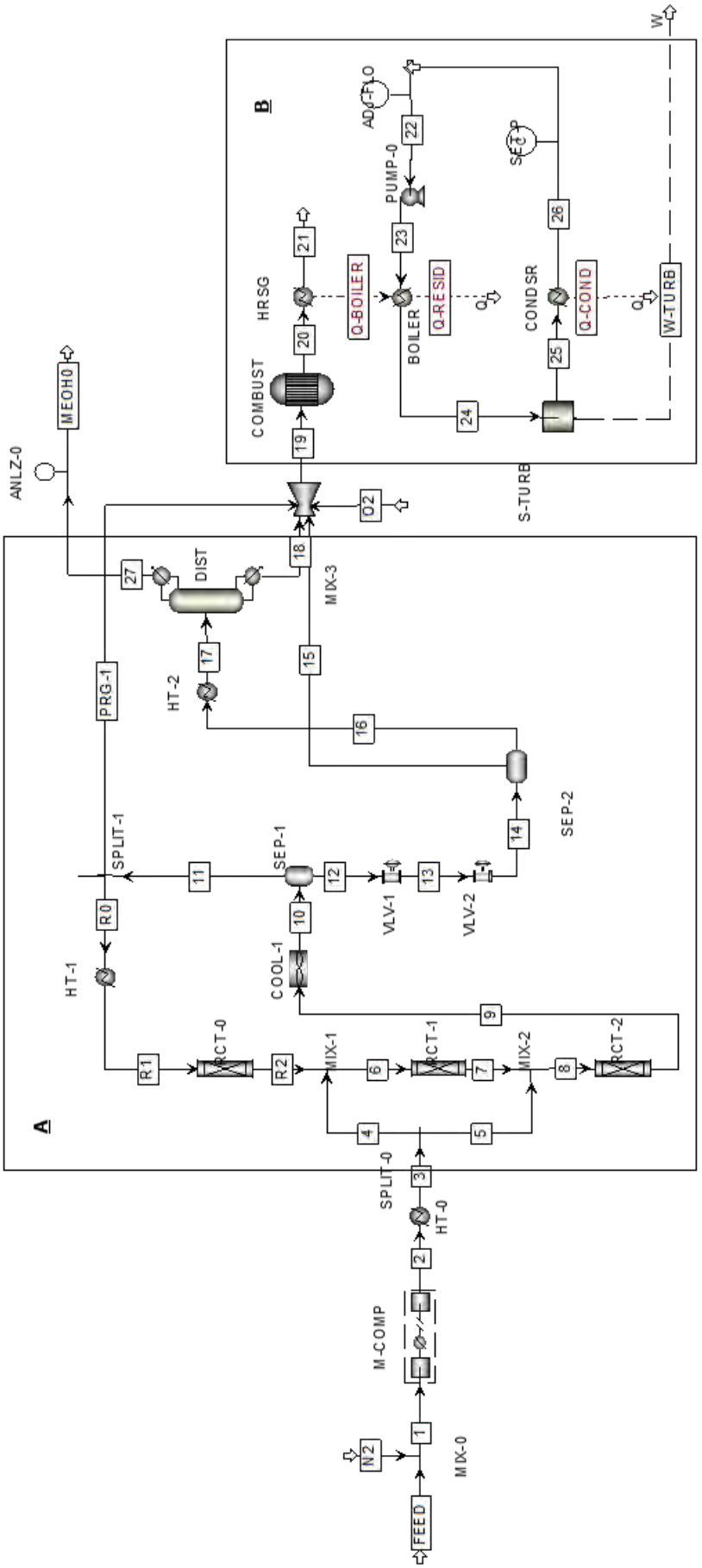

Figure 3.19: *Process flow diagram for the methanol plant showing A) synthesis section and, B) heat recovery section.*

Dimethyl Ether Synthesis

The *modus operandi* for assessing DME synthesis follows the same pattern as methane synthesis in the previous sections. The indirect MTD process is chosen due to its maturity and simplicity.

The kinetic model employed in Equation (3.42) was developed by Bercic and Levec [176] over a γ-Al_2O_3 catalyst in a gas-phase reaction. The rate-determining step was determined to be the intraparticle heat and mass transport limitations. The reactor is modelled using an RPLUG model block.

$$r_{\mathrm{DME}} = \frac{k_{DME} K^2_{\mathrm{CH_3OH}} \left[C^2_{\mathrm{CH_3OH}} - \left(C_{\mathrm{H_2O}} C_{\mathrm{DME}}\right) / K_{P,DME}\right]}{\left[1 + 2 \cdot \left(K_{\mathrm{CH_3OH}} C_{\mathrm{CH_3OH}}\right)^{0.5} + K_{\mathrm{H_2O}} C_{\mathrm{H_2O}}\right]^4} \tag{3.42}$$

Figure 3.20 shows the process flow diagram of the DME model as an extension from the methanol synthesis section described in an earlier section. The methanol output is converted to DME in an MTD reactor. The DME output is cooled and purified in a distillation column. The set purity for the DME product is set to 99.99%.

The concentration of methanol on the effluent wastewater was designed to be below 10,000ppm, in accordance with the limits stated in [177]. Due to the complexity and energy-intensive nature of the separation of methanol and water, especially at lower concentrations of the former, a simple membrane block is employed, as it is beyond the scope of this work [178].

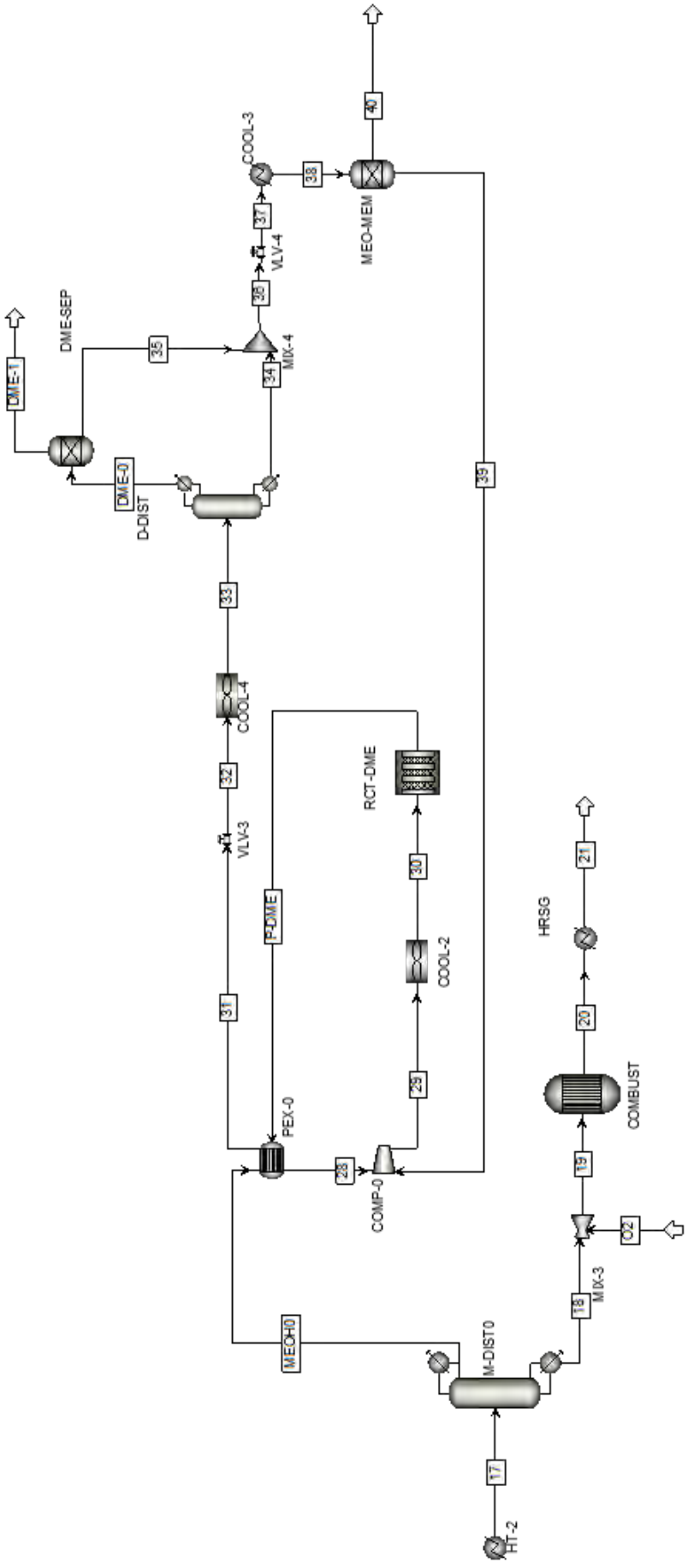

Figure 3.20: *Process flow diagram of DME synthesis.*

Fischer-Tropsch Liquid Synthesis

The loss of tractability and heavy computational loads are constraints associated with modelling systems with many molecular components like FT, especially when employing rigorous and complex kinetic models. The ASF distribution method is implemented to replicate realistic component distributions consistent with existing kinetic models.

Following discussions in earlier sections, a low-temperature Fischer-Tropsch (LTFT) process which utilises high α-catalysts like cobalt predominantly produce a syncrude with a higher paraffin wax content is chosen in this study. Diesel is the main target product of this study and is represented by n-alkanes. To further simplify the model, only n-parrafins, 1-olefins and oxygenates are considered as the main FT products in this study (See Table 2.3).

However, despite the elegance of the ASF distribution method, there are observable disparities in comparison with FT product distribution from experimental data as shown in Figure 3.21.

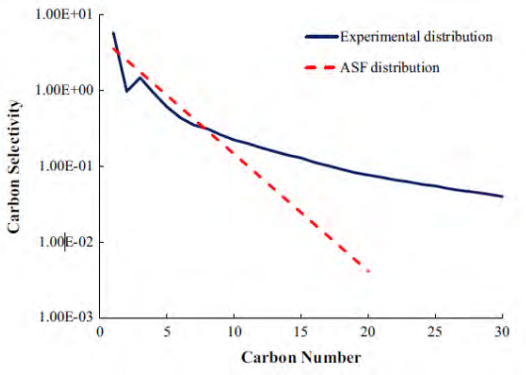

Figure 3.21: *ASF product distribution in comparison to experimental FT. Modified from [179].*

The main deviations include (a) lower selectivity to methane, (b) higher selectivity to ethylene and (c) divergence at long-chain hydrocarbons. The variances have been further discussed in [180]. To better describe the deviation of the product distribution at higher carbon numbers, a double-alpha concept is applied, as seen in

Figure 3.22.

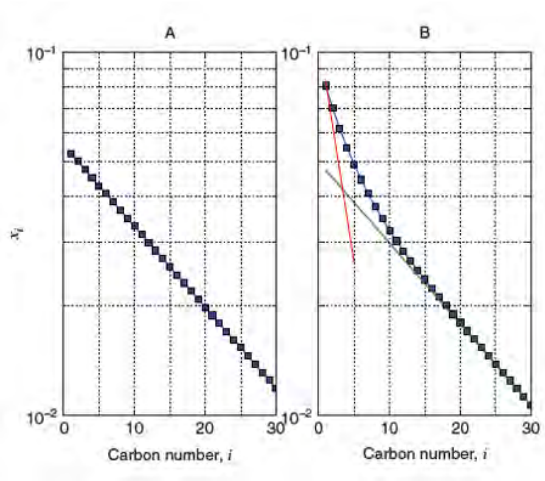

Figure 3.22: *The ASF-plots of (A) molar distribution with one propagation probability α = 0.95, and (B) where 90% of the distribution is produced with α = 0:95 and 10 is produced with α = 0.75 [181].*

Kinetic models developed by Todic et al. [182] on the hydrocarbon product distribution based on the CO-insertion mechanism earlier explained are used to describe the polymerisation growth factors for paraffins (α_1) and olefins (α_2) respectively in Equations (3.43) and (3.44).

$$\alpha_1 = \frac{k_3 \cdot K_1 \cdot P_{CO}}{k_3 \cdot K_1 \cdot P_{CO} + k_{7M} \cdot \sqrt{K_2 \cdot P_{\mathrm{H_2}}}} \tag{3.43}$$

$$\alpha_2 = \alpha_1 \cdot e^{0.27} \tag{3.44}$$

The reactions for the hydrogenation of CO for the FT production of paraffins and olefins are described in Reactions (45) and (46).

$$\mathrm{CO} + \mathrm{U_1H_2} \longrightarrow \sum_{i=1}^{\infty} \mathrm{v_{i,1}C_iH_{2i+2}} + \mathrm{H_2O} \tag{R 45}$$

$$\mathrm{CO} + \mathrm{U_2H_2} \longrightarrow \mathrm{v_{1,2}CH_4} + \sum_{i=2}^{\infty} \mathrm{v_{i,2}C_iH_{2i}} + \mathrm{H_2O} \tag{R 46}$$

$v_{i,x}$ and U_i are the stoichiometric coefficients and the stoichiometric usage of hydrogen is further described in Equations (3.45) to (3.48).

$$v_{i,1} = (1-\alpha_1)^2 \cdot \alpha_1^{i-1} \tag{3.45}$$

$$v_{i,2} = (1-\alpha_2)^2 \cdot \alpha_2^{i-1} \tag{3.46}$$

$$U_1 = \sum_{i=1}^{\infty} (i+1) \cdot v_{i,1} + 1 \tag{3.47}$$

$$U_2 = 2v_{1,2} + \sum_{i=2}^{\infty} i \cdot v_{i,2} + 1 \tag{3.48}$$

To manage the possibly infinite number of molecular products, lumping of components as described in [181] is introduced and described below in Equations (3.49) to (3.55).

$$S_{[1,N]} = \sum_{i=1}^{N} x_i \tag{3.49}$$

$$S_{[N,M]} = (1-\alpha) \sum_{i=N}^{M} \alpha^{i-1} \tag{3.50}$$

$$v_{[N,M]} = \sum_{i=N}^{M} v_i \tag{3.51}$$

$$\bar{n}_{n,[N,M]} = \frac{\sum_{i=N}^{M} i \cdot \alpha^{i-1}}{\sum_{i=N}^{M} \alpha^{i-1}} \tag{3.52}$$

$$\bar{n}_{n,[N,\infty]} = N + \frac{\alpha}{1-\alpha} \tag{3.53}$$

$$\bar{n}_{W,[N,M]} = \frac{\sum_{i=N}^{M} i^2 \cdot \alpha^{i-1}}{\sum_{i=N}^{M} i \cdot \alpha^{i-1}} \tag{3.54}$$

$$\bar{n}_{W,[N,\infty]} = \frac{\left(N - 1 + \frac{1+\alpha}{1-\alpha}\right) \cdot \left(N + \frac{(1+\alpha)\cdot\alpha}{(1-\alpha)^2}\right)}{N + \frac{\alpha}{1-\alpha}} \tag{3.55}$$

The FT product distribution is modelled on Aspen Plus® *v*.11.1 and applies

the Peng-Robinson property package method. The reactor is modelled using an Aspen RSTOIC model block. The carbon selectivities towards methane, paraffins, olefins and oxygenates is based on the work of Shafer et al. [183] over a Co/γ-Al_2O_3 catalyst and a H_2/CO of 2. In light of recent developments, a slurry bubble column reactor is chosen as it enables a high CO conversion per pass (between 80% and up to 90%), compared to conventional fluidized and fixed-bed reactors (40% to 50%) [93, 184, 185].

The correction of the ethylene deviation is based on the work of Pandey et al. [186] over a 20% Co/ 0.5 Reγ-Al_2O_3 catalyst. The experimental data show that deviation is corrected by a factor of 94%, predominantly via the following reactions:

$$C_2H_4 + H_2 \longrightarrow C_2H_6 \qquad \text{(R 47)}$$

$$C_2H_4 + CO + H_2 \longrightarrow \sum_{i=3}^{\infty} C_iH_{2i+2} + H_2O \qquad \text{(R 48)}$$

A high content of heavier paraffins is a direct result of cobalt-based LTFT, and thus further process steps are required to improve the yield and quality of the target middle distillate cuts. While LTFT products exhibit an advantageous characteristic of high cetane numbers (>75) for transport fuels, *n*-paraffins display undesirable cold flow properties – increasing the likelihood of inject nozzle blockages as a result of the crystallization of high molecular *n*-paraffins.

Hydro-processing combines hydroisomerisation to improve the flow property and hydrocracking to increase the yield of the middle distillate cuts. In accordance with the work of Baltanas et al. [187], only the direct cracking of *iso*-paraffins is considered, following the hydroisomerisation of *n*-paraffins.

The hydroisomerisation and hydrocracking reactions are modelled with Aspen's RPLUG model units with rate equations developed by Pellegrini et al. [188].

$$r_{iso}(i) = \frac{k^0_{iso}(i) \cdot e^{-E_{iso}/\Re T}}{ADS} \cdot (f_{n-C}(i) - f_{iso-C}(i)/K_{eq}(i)) \tag{3.56}$$

$$r_{crk}(i) = \frac{k^0_{crk}(i) \cdot e^{-E_{crk}/\Re T} \cdot f_{iso-C}(i)}{ADS} \tag{3.57}$$

$$ADS = f_{\mathrm{H_2}} \left[1 + \sum_{i=1}^{70} K_{L_{n-C}}(i) \cdot f_{n-C}(i) + \sum_{i=4}^{70} K_{L_{iso-C}}(i) \cdot f_{iso-C}(i) \right] \tag{3.58}$$

Paraffin and olefins products up to C_{20}, *n*-eicosane and 1-eicosane, respectively, were added from the Aspen Plus® *v*.11.1 component bank was added in the model. Higher carbon number products were lumped into a pseudocomponent (C_{20+}). Oxygenates up C_5 (1-pentanol) and the pseudocomponent (C_{6+}) were also added. Figure 3.23 illustrates the process flow diagram of the FT synthesis process.

The modelled process consists of a syngas conditioning section to set the H_2/CO ratio to the desired specification of 2. A series of conversion reactors is used to model the FT synthesis to account for the ethylene deviation. The FT products are further processed in an atmospheric distillation unit. The primary target fuel synthesised in this model is diesel fuel and, naphtha as a co-product. Light gases are processed downstream to recover the otherwise expensive H_2 for the hydro-processing section via a series of autothermal and water gas shift reactors, making the system more self-sufficient. A power generation section is also added to recover useful energy from the heat of combustion of waste effluents.

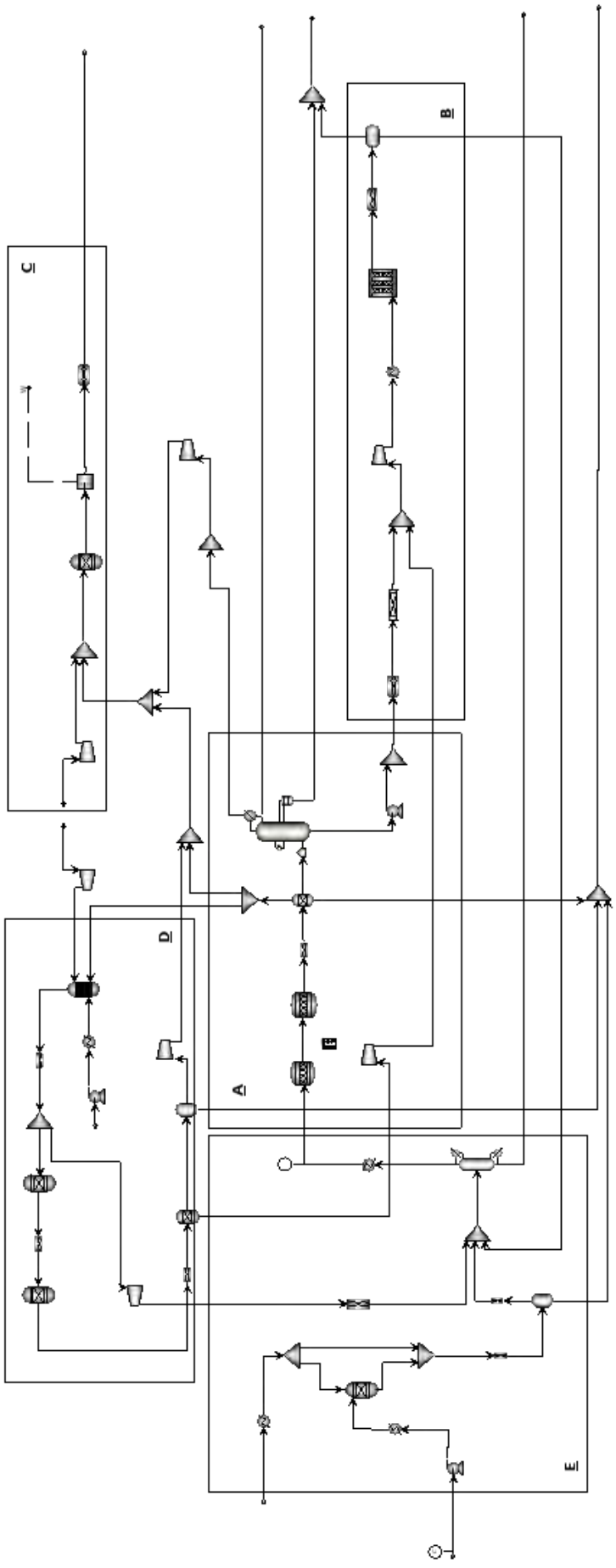

Figure 3.23: *Process flow diagram of FT liquid synthesis showing A) FT product synthesis section, B) hydro-processing section, C) power generation section, D) H_2 recovery section and E) syngas conditioning section.*

3.3.1 Results from synthetic fuel simulation

The basis for the model simulation is a flow rate of 100 kg/h of pure CO_2 fed into a co-electrolysis SOEL process. The electrolyser unit is coupled with the modelled fuel synthesis unit to minimise storage and transportation-associated costs. Where feasible, the exchange of materials between process units is employed to realise a closed process cycle; for example, enriched sweep air from the SOEL unit can be utilised as an oxidiser in downstream combustion processes.

Subsequently, heat integration is optimised following a heat exchange network (HEN) design for each process to minimise utilities and save on related operational costs. The heat integration procedure is carried out on the Aspen Energy Analyzer software, which applies principles from Pinch Analysis (10 °C in this work), the Grand Composite Curve for utility load allocation and the heat exchanger area target based on the Bath formula shown below Equation (3.59).

$$A = \sum_{k=1} \cdot \frac{1}{\Delta T_{LM,k}} \cdot \left(\sum_{i}^{\text{hot streams}} \cdot \frac{q_i}{h_i} + \sum_{i}^{\text{cold streams}} \cdot \frac{q_i}{h_i} \right) \tag{3.59}$$

A is the target area, k is the thermal conductivity, i is the i-th enthalpy interval, ΔT_{LM} is the logarithmic mean interval temperature difference at each interval, q is the amount of energy transferred at each interval and, h is the heat transfer of the stream.

The choice of utility streams is dictated by the minimal energy costs and related CO_{2e} emissions. For example, steam generation takes precedence over cooling water where possible as a cooling utility. The generated steam can be further utilised as a secondary utility on-site or as an off-site revenue stream.

Thermodynamic efficiencies are described for comparison of the processes and their respective configurations in Equations (3.60) to (3.62).

$$\eta_{SOE} = \frac{\Sigma_{syngas} \cdot \dot{m}_j \cdot LHV_j}{IV_{SOE} + Q_{net,SOE} + \Sigma_{SOE} \cdot \dot{m}_i \cdot LHV_i} \tag{3.60}$$

$$\eta_X = \frac{\Sigma_X \cdot \dot{m}_j \cdot LHV_j \left(+W_j\right)}{\Sigma_{syngas} \cdot \dot{m}_i \cdot LHV_i} \tag{3.61}$$

$$\eta_{Total} = \frac{\Sigma_X \cdot \dot{m}_j \cdot LHV_j}{IV_{SOE} + Q_{net,system} + W_{aux} + \Sigma_{SOE} \cdot \dot{m}_i \cdot LHV_i} \tag{3.62}$$

$\dot{m}$ is the flow rate, IV is the power requirement for the SOEL at the chosen operational point, Q is the heat requirement and W is the electrical requirement for the auxiliary components. The operational voltage of the SOEL unit is the obtained thermoneutral voltage (V_{tn}) between 1.55 V and 1.61 V which is in agreement with values found in [189].

Table 3.2: *Results based on a flow rate of* 100 kg/h *of pure CO_2, at NTP.*

Metric	Unit	Methane	Methanol	DME	Diesel	Naphtha
X output	kg/h	36.898	30.803	36.595	13.203	1.611
Energy Content	MJ/h	1870.77	599.40	1055.21	104.44	70.24
SOEL H_2O feed	kg/h	185.998	129.301	129.301	55.411	55.411
SOEL air feed	kg/h	436.613	332.839	332.839	205.242	205.242
Flue gas by-product	kg/h	0	945.468	614.803	286.389	286.389
Flue gas CO_2 molar content	%	0	3.90	3.13	4.30	4.30
Net electrical (AUX)	kW_e	60.035	70.487	52.181	14.065	14.065
Heating requirement	kJ/hr	2.68E+05	1.881E+06	1.008E+06	2.449E+05	2.449E+05
Cooling requirement	kJ/hr	1.099E+06	2.598E+06	1.553E+06	7.652E+05	7.652E+05
Steam generation	kJ/hr	2.41E+05	0	4.12E+03	3.00E+05	3.00E+05
Total cost index	$Cost/hr$	9.88	33.20	18.19	4.19	4.19
η_{SOE}	%	80.1	81.98	81.98	86.51	86.51
$\eta_{X(+W_j)}$	%	80.85 (90.26)	35.55 (59.46)	61.40 (74.24)	16.37 (28.9)	16.37 (28.9)

Table 3.2 shows the results of the model simulations for the synthesis of fuels via the hydrogenation of CO_2 in conjunction with a SOEL unit, modelled on Aspen plus. The primary specification for the methane product for its suitability in transport and application is described by the Wobbe Index (WI). The WI is a measure of the interchangeability of a gas when it is to be used as fuel and is derived from the expression in Equation (3.63).

$$WI = \frac{HHV_{SNG}}{\rho_{SNG}/\rho_{air}} \tag{3.63}$$

The WI of the methane modelled in this work (49.74 MJ/m^3) meets the United Kingdom's National Grid specification set out by in the Gas Safety (Management) Regulations 1996 (GS(M)R) (47.20 MJ/m^3 to 51.41 MJ/m^3).

The key performance indicator of diesel fuel is the cetane number (CN) —, the measure of the thermal stability and the ease at which a fuel can be thermally decomposed in the presence of an oxidant in a pressurised environment. In addition to engine combustion and the cold startability of diesel fuel, studies have shown that the CN inversely influences the particulate matter (PM) exhaust emissions from combustion [190, 191]. While it was not possible to ascertain the CN of the modelled diesel fuel without experimental procedures, the work of Jenčík et al. [192] reports that FT-diesels have higher CNs than the value of 51 set by the EN 590 standard for conventional fossil fuel-derived diesel in the United Kingdom.

The engine performance and emissions are also influenced by the fuel density. The density of the modelled fuel is 777.19 kg/m^3 which is in agreement with the range of 770 kg/m^3 to 785 kg/m^3 found in [193, 194] for XtL diesel fuels. While studies from emissions testing by European Programme on Emissions, Fuels and Engine Technology (EPEFE) have demonstrated that a lower diesel fuel density reduces PM and NOx emissions, the overall fuel economy depreciates as the fuel consumption increases and power output reduces [195]. Downstream densification is required to

meet the EN 590 Euro 6/VI specification of 815 kg/m^3 to 840 kg/m^3. Alternatively, the synthesised fuel can be blended with fuels derived from other sources or further refined for other niche applications.

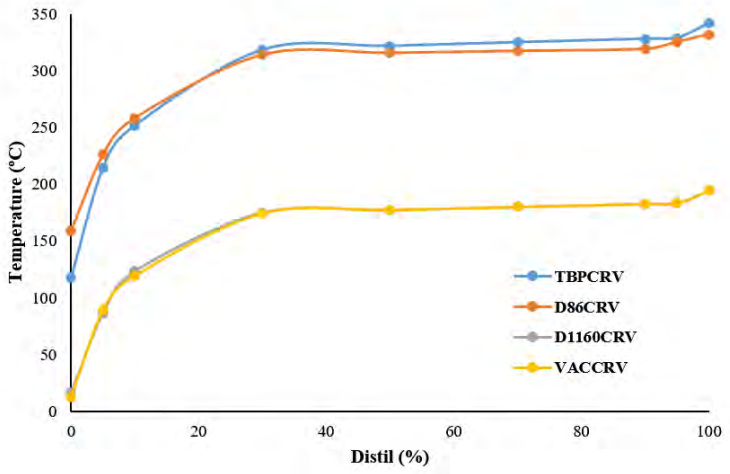

Figure 3.24: *Distillation curve for FT diesel fuel modelled on Aspen Plus.*

Figure 3.24 shows the distillation curve for the FT-diesel fuel. The distillation curves indicate the fuel's quality in its ability to evaporate and mix with an oxidant upon injection. The distillation curve's result in Figure 3.24 agrees with results found in the experimental procedures undertaken in [192].

Table 3.2 also shows the energy requirement for each process. The methane synthesis process showed the least heating utility requirement, following the optimisation of the HEN. Conversely, the FT process has the highest utility requirement, primarily due to the process's overall complexity and HEN optimisation. However, the FT process has the least electrical balance of plant (BOP) requirement, owing to the power generation island included in the design. There is also an opportunity in the FT process to recover useful heat in the form of steam generation that can be utilised in the SOEL unit or the CC unit, depending on its proximity.

The final unit configurations and approaches applied in these simulations are constrained by time, the scope of detail and reproducibility. The simulation results provide the foundation for the analyses carried out in the following chapters.

Chapter 4

ASSESSMENT OF A CIRCULAR CARBON ECONOMY

This section of this thesis seeks to address the question of "How much CO_2 is readily available for downstream valorisation as e-fuels?". The chapter begins with the assessment of the global CO_2 potential, based on open-source data, followed by the associated carbon capture costs and environmental impacts. The scope of the study is then narrowed to the United Kingdom, including the spatial distribution of potential carbon sources.

4.1 Supply Side Evaluation

The concept of a circular economy seeks to exploit the recycling of material flows in order to balance economic growth and societal development with environmental and resource use to achieve sustainability [196]. A circular carbon economy represents the circular movement of carbon atoms through a series of energy-related processes, from an initial stage as components in an energy vector in the form of a carbon-based fuel, through its emission stage as an effluent, to a final stage where it is either sequestered away or reintroduced into the cycle as shown in Figure 4.1. The CCE aims to incorporate 'clean' technologies to transform 'waste' carbon into a valuable 'asset' in a bid to reduce the impact of the initially released carbon unit.

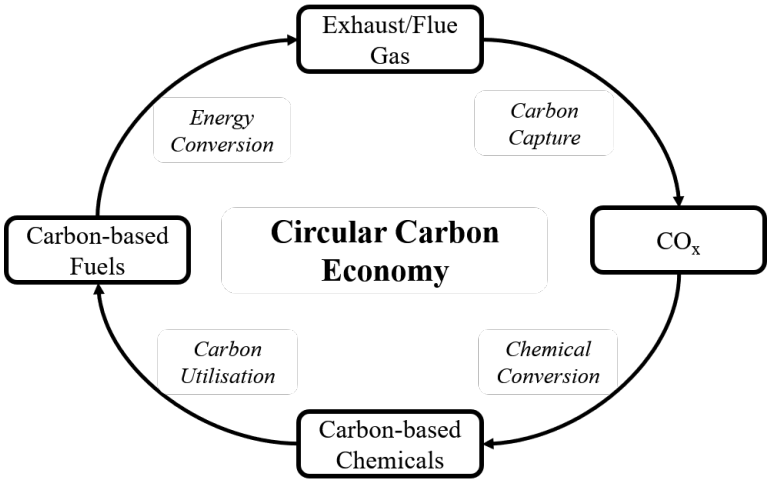

Figure 4.1: *Schematic representation of a circular carbon economy.*

A broader scope of the CCE described in Figure 4.1 will include fuel and CO_2 inputs to compensate for other utilisation and chemical products, accounting unavoidable emissions and sequestered carbon, resulting in a closed carbon cycle.

It is imperative that each section of the carbon cycle is properly assessed to ascertain its viability as a key component in the deployment of the PtX process. The cycle is categorised into (a) the supply side — carbon emissions and carbon capture, and, (b) demand side — carbon utilisation.

The Current Global Scale of Carbon Emissions

Within the context of this chapter, 'carbon emissions' — by the combustion of fossil fuels or biogenic resources, including biological processing, would be used interchangeably with 'carbon sources', describing the point of supply of carbon for the initiation of the proposed carbon economy cycle. The assessment of carbon sources would be limited to centralised anthropogenic point sources that can be coupled with current and proposed carbon capture technologies, which will be further defined in this chapter.

The scope of this assessment solely focuses on exhausts from large stationary stacks (>0.10 $GtCO_{2e}$ per year) whilst excluding carbon emissions from non-industrial and mobile sources such as those in the transport sector and small stationary processes like heating boilers in domestic and service sectors.

Anthropogenic emissions account for 32.80 $GtCO_{2e}$ per year of the total global emissions [197]. Despite the considerable volume available, the diverse quality of in the exhaust flue gases poses a technological and economic constraint that must be surmounted in order to realise a carbon economy. The point sources discussed here are categorised into four groups of emitters:

Fossil-Based Energy Generation

The combustion of natural gas and coal for energy generation is the largest point source of emissions, responsible for 63%(v/v) of all the emissions that can be captured as conferred in this report. They account for the lower range of CO_2 concentrations at 3%(v/v) to 15%(v/v), depending on the fuel type [198]. Despite calls to phase out coal power stations, the global capacity has increased to 2024.10 GW by the end of 2018 due to China's rapid deployment [199].

Large Industrial Processes

Large-scale production and processing of metals such as iron and steel are major emitters of CO_2, primarily due to the carbon-intensive smelting reduction process of iron oxide in blast furnaces as summarised in Reactions (49) and (50) below.

$$Fe_2O_{3(s)} + 3\,C_{(s)} \longrightarrow 2\,Fe_{(l)} + 3\,CO_{(g)} \quad \text{(R 49)}$$

$$Fe_2O_{3(s)} + 3\,CO_{(g)} \longrightarrow 2\,Fe_{(l)} + 3\,CO_{2(g)} \quad \text{(R 50)}$$

The clinkering step in the production of cement is responsible for up to 60% of the CO_2 emissions of the production process due to the chemical calcination of limestone, as in the Reaction (51) below.

$$CaCO_{3(s)} \longrightarrow CaO_{(s)} + CO_{2(g)} \quad \text{(R 51)}$$

Both industries make up the majority of the large industrial point sources, accounting for 12 % of the total direct global CO_2 emissions at 4.30 $GtCO_{2e}$ per year, with a CO_2 content of 14%(v/v) to 35%(v/v) in their effluent gases [200, 201].

Biotechnological Processes

The high concentration of CO_2 in biogas (30%(v/v) to 50%(v/v)) from the anaerobic digestion of biogenic material provides viable options to capture carbon for implementing a circular carbon economy. Furthermore, emissions from fermentation and bioethanol production contain a very high concentration of CO_2 of about 99%(v/v) as in Reaction (52), also containing small amounts of sulphur and organics, [202].

$$H(C_6H_{10}O_5)_nOH \longrightarrow 2\,nC_2H_5OH + 2\,nCO_2 \qquad (R\ \mathbf{52})$$

From a molar balance in Reaction (52), 0.95 kg of CO_2 is produced for every 1 kg of bioethanol produced.

High Purity Point Sources

This category focuses on processes that produce a stream of CO_2 with a purity in excess of 99%. Natural gas processing, production of industrial hydrogen, synthetic fuels and ethylene oxide all contribute to the chemical subsector being the third largest emitter of CO_2 at 1.10 $GtCO_{2e}$ per year [201]. Industrial hydrogen is produced at large scale via thermo-chemical processing of fossil fuels as an intermediary, primarily for the synthesis of ammonia in the Haber-Bosch process and metal processing as seen in Figure 4.2.

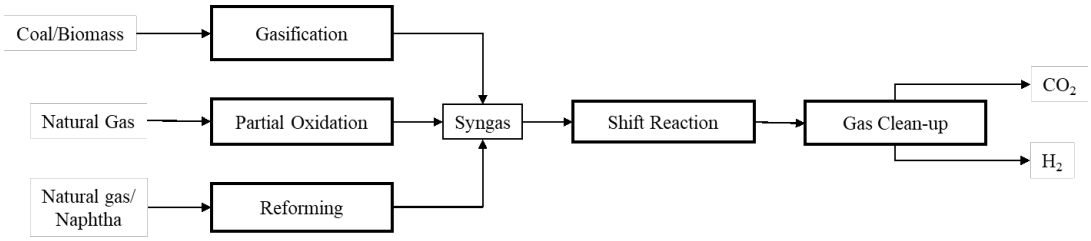

Figure 4.2: *Simplified process of industrial hydrogen production from fossil feedstock.*

Ethylene oxide can be produced from ethylene via direct oxidation; however, the parallel oxidation of ethylene oxide produces CO_2 [203], as shown in Figure 4.3.

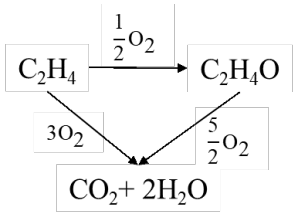

Figure 4.3: *Oxidation pathways of ethylene to yield ethylene oxide or carbon dioxide.*

Overview of Carbon Capture Processes

The initialisation of carbon capture begins with separating CO_2 from a bulk stream of gases. Three separation techniques for achieving a CO_2-rich stream, including but not limited to the ones in this study, are hereby briefly described.

Solvent-based Systems

Solvent systems are based on the selective absorption of CO_2 from a flue gas stream and regeneration of the solvent by reversible desorption reactions. The classification of solvents depends on their reactivity in the primary solution [204].

Physical solvents such as methanol and dimethyl ether of polyethylene glycols (DMEPEG); are employed in commercial processes, Rectisol® and Selexol® respectively, apply Henry's law by which the selected gas species are absorbed in high pressures and desorped in subsequently reduced pressure conditions [205].

The general reaction between chemical solvents and CO_2 in a liquid phase results in a reduction in the equilibrium partial pressure and an increase in the mass driving force [206]. CO_2 is consumed at the interface, consequently increasing the CO_2 concentration gradient at the interface.

The increased CO_2 absorption rate of chemical solvents like amines, ammonia and salt solutions leads to higher absorption and desorption mass transfer coefficients when compared to physical solvents. However, the employment of chemical solvent systems incurs a higher cost for materials due to corrosion, the presence of side reactions, and predominantly, a higher energy requirement for solvent regeneration [205, 207, 208].

Solvent regeneration can contribute up to 80% of the total energy requirement for a carbon capture process [209]. An experimental study by Bhatti et al. [210], showed that the addition of solid acid catalysts like MoO_3 and V_2O_5 to a

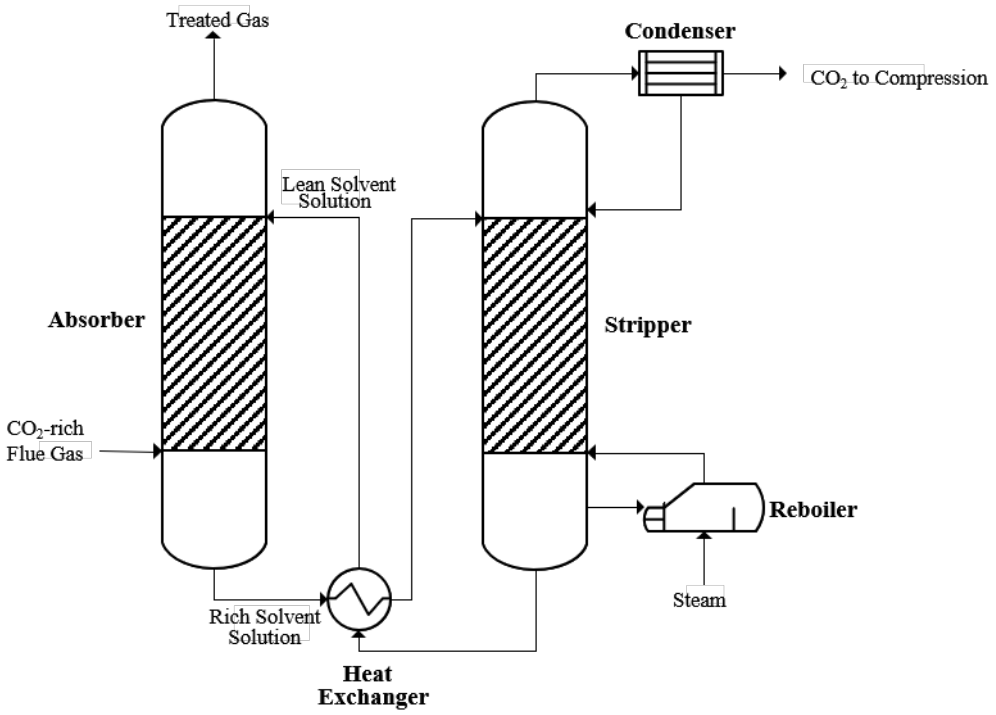

Figure 4.4: *A simplified schematic of a chemical solvent-based carbon capture process.*

monoethanolamine (MEA) solvent-based process reduced the heat duty required for solvent regeneration with a 94% upon the base case and CO_2 desorption rate of up to 105%. Figure 4.4 illustrates a simple schematic of a chemical solvent process for a carbon capture process.

Sorbents and Looping Systems

Adsorption processes for the capture of CO_2 have an added advantage over conventional absorption processes as they bring a reduction in environmental impact and energy penalties. CO_2 removal by adsorption is generally categorised based on three different mechanisms and the materials employed therein.

Solid sorbents like metallic organic frameworks (MOF), zeolites, silica, and polymeric materials, are resilient materials that can withstand high operational temperatures. However, there is a need for further development of new adsorbents that offer better tolerance to impurities, better chemical stability in wet conditions, higher CO_2 capture capacities and selectivity, and operate at lower temperatures

[211, 212].

The reversible desorption process is energy intensive and a challenge remains to match the most ideal process to determine the driving process in terms of pressure, temperature, concentration, etc., for the overall capture process. Several regenerative processes such as vacuum swing adsorption (VSA), temperature swing adsorption (TSA), temperature/vacuum swing adsorption (TVSA), and electrical swing adsorption (ESA) technologies have been extensively studied to meet required CO_2 specifications and feed conditions [213–216].

Carbonate looping is the second mechanism based on the absorption of CO_2 by a metal oxide (Me_xO) to form a solid carbonate. Silicates, zirconates, hydrotalcites, and oxides of potassium, magnesium and calcium are promising materials. CO_2 is removed from the flue gas upon contact with the Me_xO, in a carbonator, operating at elevated temperatures between 450 °C and 900 °C (depending on the sorbent) [217]. A high purity CO_2 stream is subsequently recovered from the metal carbonate (Me_xCO_3) in a calciner as depicted in Figure 4.5.

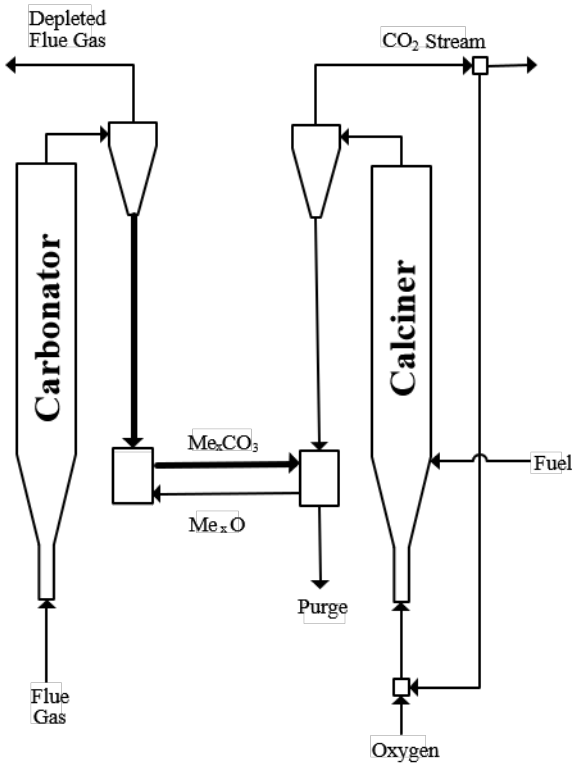

Figure 4.5: *Simplified process diagram of carbonate looping process for carbon dioxide capture.*

Results from a simulation study by Rolfe et al. [218], evaluating the technical performance of a 600 MW pulverised power plant retrofitted with a calcium-based carbonate looping system, resulting in an efficiency penalty as low as 7.4% compared to a solvent-based system. The energy requirement for the air separation unit (ASU) used to supply oxygen is a major contributor to the energy penalty in this system. Furcas et al. [219] achieved a further reduction in the energy penalty of 4% compared to the reference case when utilising trona ($Na_2CO_3 \cdot NaHCO_3 \cdot 2H_2O$) — a sodium-based sorbent in a carbonate looping system; without the requirement of an ASU.

Chemical looping combustion (CLC) is the third adsorption mechanism that utilises a metal oxide as an oxygen carrier in an alternating redox reaction for the purpose of capturing CO_2 as shown in Reactions (53) to (55) below.

$$(2\,n + m)Me_xO_y + C_nH_{2m} \longrightarrow (2\,n + m)Me_xO_{y-1} + mH_2O + nCO_2 \qquad (R\ \mathbf{53})$$

$$(2\,n + m)Me_xO_{y-1} + (n + 0.5\,m)O_2 \longrightarrow (2\,n + m)Me_xO_y \qquad (R\ \mathbf{54})$$

$$C_nH_{2m} + (n + 0.5\,m)O_2 \longrightarrow mH_2O + nCO_2 \qquad (R\ \mathbf{55})$$

The net enthalpy of the CLC redox cycle is equal to that of a conventional combustion process. It thus does not incur any extra energy penalty or direct cost for the capture of CO_2.

CLC relies heavily on oxygen carriers that must have high reactivity with fuels and high oxygen transport capacities while being resistant to attrition resulting from multiple redox cycles [220, 221]. Oxygen carriers like Fe_2O_3, NiO and Mn_3O_4 are typically supported by ZrO_2, SiO_2 and Al_2O_3. However, these carriers have a very high manufacturing cost, and are, thus, the subject of much ongoing research.

Recent developments in oxygen carriers have produced metal oxides that have the capacity to spontaneously release oxygen under inert conditions, referred to as chemical looping with oxygen uncoupling (CLOU). They vastly improve the combustion kinetics of solid fuels as demonstrated in studies by Adánez-Rubio et al. [222] where high CO_2 capture and 100% combustion efficiency were achieved in a biomass combustion plant.

Membrane Systems

Membrane separation technologies operate on the principles of permeability and selectivity of a species across a material. The permeability of a membrane is a function of the *solubility* of the species — a thermodynamic factor, describing the interaction between the two interfaces; and *diffusivity* — the kinetic factor, determined by the rate at which the penetrating species passes through the material by a driving force [223].

The availability of high-performance materials in terms of permeability makes membrane separation flexible and economical, provided that a high concentration of a CO_2 stream is not desired [224]. The current challenge for membrane separation technology is the development of high selectivity materials that are economically competitive with absorption systems; for processes with emissions that have low CO_2 concentrations [225].

Mixed matrix membranes produced by integrating inorganic materials in the polymeric structure of the membrane have all shown promising results in terms of selectivity of CO_2 [211]. Li et al. [226] showed that Matrimid®/CNTs/GO — a composite of carbon nanotubes and graphene oxide in a Matrimid® matrix showed superior performance in terms of CO_2 selectivity for biogas (CO_2/CH_4) and flue gases (CO_2/N_2) of 85 and 81, respectively, compared to 34 and 33 for pure Matrimid® membranes.

Overview of Carbon Capture Configurations

The criteria for selecting the appropriate separation technique for CO_2 capture is non-exhaustive but is often narrowed down to financial implications, especially in the event of a retrofit to an existing point source. The cost metrics for CO_2 capture are generally expressed as a function of the incurred efficiency/energy penalty by the added process step and the overall performance of the retrofitted plant. Discussed herein are the three configurations for the aforementioned separation techniques with a point source.

Pre-combustion Configuration

The separation of CO_2 occurs during the preprocessing of the combustion fuel. The process begins by the gasification of the carbonaceous fuel to produce a fuel gas primarily consisting of hydrogen and carbon monoxide — syngas. Depending on the industrial process, the syngas is converted to hydrogen and carbon dioxide in a shift reactor; the former is used as a low-carbon fuel upstream, and the latter is separated out.

The described process is prevalent in integrated gasification combined cycle (IGCC) and natural gas combined cycle (NGCC) power plants, and the high operating pressure and CO_2 concentrations make them a feasible candidate for this configuration. Roussanaly et al. [227] employed three different separation techniques for a pre-combustion carbon capture assessment of a lignite-fired IGCC power plant. The evaluations showed a levelised cost of electricity (LCOE) between 91 €/MWh and 120 €/MWh, compared to 65 €/MWh and a CO_2 capture ratio (CCR) between 81.8% and 89.0%. Similar results for a CCR of 90% and an LCOE of 75.33 €/MWh to 81.65 €/MWh were obtained by Cormos and Cormos [228].

The limitations to the retrofit of pre-combustion capture to combined cycle power plants are related to gas turbine design. The operational windows of conventional gas turbines are very limited, and variations in fuel properties can lead

to issues, such as the mismatch of compressor turbine fluid dynamics and reduced mechanical resistance of components [229].

Post-combustion Configuration

The application of post-combustion capture is independent of the fuel type and its processing, making it an attractive choice of a separation technique for retrofitting. However, a prohibition of its deployment is due to the high energy intensiveness associated with the regeneration and recovery of separation materials as described in previous sections.

Quotes from various studies for reboiler duties based on standard absorber/stripper processes for various CO_2 capture absorbents are between $2\,GJ/t_{CO_2}$ and $4\,GJ/t_{CO_2}$ [230, 231]. Post-combustion capture via adsorption has significantly higher energy requirements, between $4.50\,GJ/t_{CO_2}$ and $9\,GJ/t_{CO_2}$ [232]. An assessment by Osagie et al. [233] revealed an increase in the LCOE by 75.2% from 42.70 \$/t, for a post-combustion capture plant retrofit.

Oxy-fuel Combustion Configuration

The principle of oxy-fuel combustion is analogous to that of pre-combustion capture, but the carbon-based fuel is combusted in a nitrogen-lean environment. Pure oxygen (>95%(v/v)), usually produced by a cryogenic ASU, is used to replace air as an oxidant. This preference offers an opportunity to employ compact boiler designs and reduce boiler heat losses, incurring lower capital costs [234]. In addition, the high oxygen concentration leads to lower carbon monoxide emissions, enhanced desulphurisation efficiencies, a reduction in energy required to recycle the flue gas, and an increased CO_2 concentration to be separated [235].

However, there are still many technical challenges prohibiting the large-scale deployment of oxy-fuel combustion, including heat transfer and fluid dynamics issues, boiler designs are further discussed in [235, 236]. In a comparative study

for the deployment of a calcium looping process or chemical looping air separation technique, with oxy-fuel combustion in pulverised coal power plants, results showed an LCOE between 62.35 $/MWh and 80.74 $/MWh compared to 52.65 $/MWh, a 53.4% increase, for a reference plant [237].

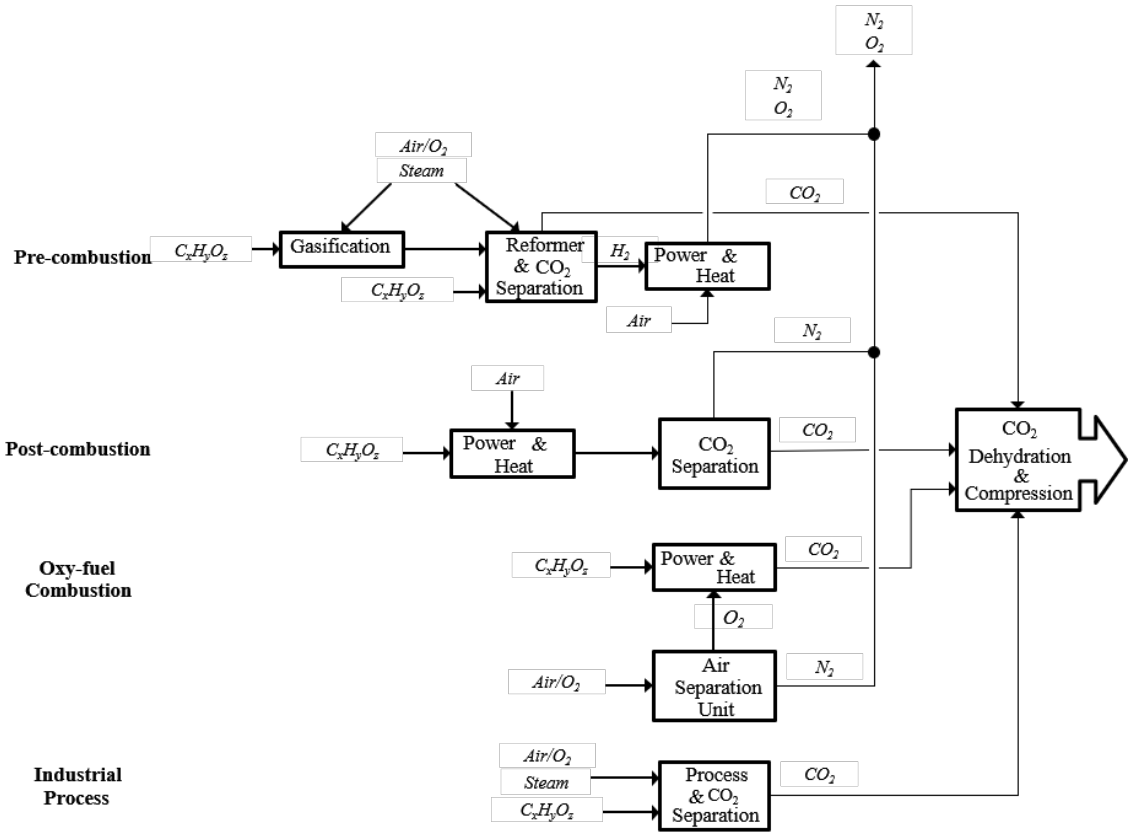

Figure 4.6: *Simplified carbon capture configurations.*

Figure 4.6 is a schematic diagram of the various carbon capture configurations, as described above.

As of June 2021, there are 27 operational commercial CCS facilities globally, with a further 102 under development and another four under construction [238]. The Drax Power Station in North Yorkshire, United Kingdom (UK), is retrofitted with two pilot bioenergy with carbon capture and storage (BECCS) facilities in a bid to initially capture 17 $MtCO_2$ per year as part of the "Zero Carbon Humber CCUS" hub in the UK [239]. The operation employs Mitsubishi Heavy Industries (MHI) post-combustion capture technology with the KS-21^{TM} solvent.

Upon approval of California's Low Carbon Fuel Standard and the United States' 45Q tax credit in 2024, 1PointFive's DAC1 is set to become the largest DAC facility in the world [239]. The facility will employ Carbon Engineering's KOH/calcination technology (see Figure 4.7)to capture up to 1 $GtCO_2$ per year.

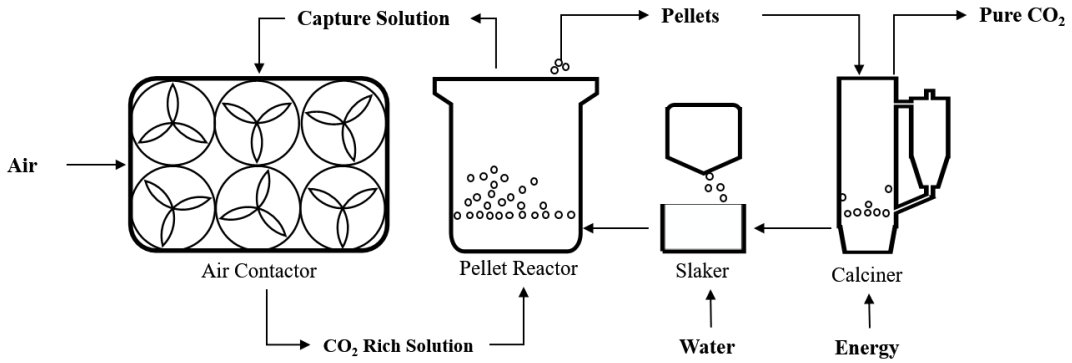

Figure 4.7: *A simple schematic of Carbon Engineering's DAC technology. Modified from [240].*

The Northern Lights will launch as the first cross-border open source, CO_2 transport and storage infrastructure network, in partnership with Equinor, Shell and Total [239]. The project will aim to transport and store up to 5 $GtCO_2$ per year from various industrial sites, including a cement factory in Brevik and Fortum Oslo Varme, a waste-to-energy facility located in Oslo, to offshore storage underground.

4.2 Assessment of CO2 Sources for Carbon Capture

This section considers an assessment of CO_2 for the large-scale implementation of carbon capture technologies in an attempt to develop a circular carbon economy in the context of climate change mitigation.

Particularly in the case of CCU, where the unit of carbon is re-emitted at a later point in its life cycle, it is imperative that there is a marginal environmental benefit when compared to conventional processes. Likewise, in a business case where the benchmark cost of a unit of captured carbon is closely related to the buying price of the same unit of carbon as a feedstock in CCU, cost competitiveness is necessary to facilitate large-scale deployment.

Carbon Capture Costs

A prevailing challenge to the widespread adoption of carbon capture lies in the difficulty in estimating the actual costs associated with its deployment. This is due to the scarcity of data from operational projects, coupled with the disparity in methodology, varying point sources, capture configurations and financial variables (including storage and transport infrastructures).

Carbon capture costs ($€/t_{CO_2}$) can be generally expressed by two different measures to define the efficiency or energy penalty incurred compared to the same point source without carbon capture — captured and avoided.

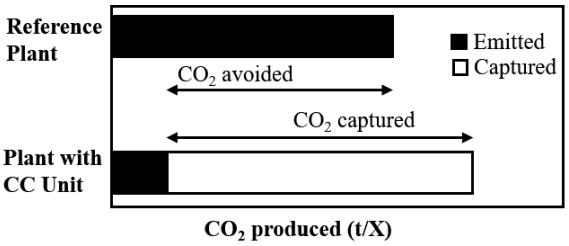

Figure 4.8: *Comparison between CO_2 captured and CO_2 avoided. The increased CO_2 from the CCS plant results from loss in overall efficiency due to the additional energy required for capture, transport and storage, and any possible leakage.*

The cost of captured CO_2 demonstrates the feasibility of the application of a carbon capture process alone, at a specified market value of a unit of CO_2, as an industrial asset. Financial viability is achievable if these costs are remunerated by revenue from environmental incentives, such as carbon taxes, and by CCU income from the products. Storage and transport process steps are included in the cost of avoided CO_2 thus representing a full CCS chain. It considers the actual CO_2 abatement along the chain, making it more relevant to environmental analyses. The avoided and captured costs are described by Equations (4.1) and (4.2).

$$\text{Cost of } CO_2 \text{ avoided} = \frac{\text{LCOX}_{CCS} - \text{LCOX}_{Ref}}{(t_{CO_2}/X)_{Ref} - (t_{CO_2}/X)_{CCS}} \tag{4.1}$$

$$\text{Cost of } CO_2 \text{ captured} = \frac{\text{LCOX}_{CC} - \text{LCOX}_{Ref}}{(t_{CO_2}/X)_{Cap}} \tag{4.2}$$

Where, $LCOX$ is the levelised production cost of a unit product, X, and t_{CO_2}/X is the CO_2 emission intensity of the point source per unit of X produced. To estimate the potential of CO_2 supply, a supply cost function in employed as described in Equation (4.3).

$$p(q) = p_i \; \forall \; q \; \in \; \left] \; q_{i-1};\; q_i \; \right] \tag{4.3}$$

for the space $\cup$ as the union of all intervals

$$\cup_{i=1}^{n} \left(q_{i-1};\ q_i\right]$$

$$p_1 \leq\ p_2\ \leq\ \ldots\ \leq\ p_n$$

Where, i is the rank of the CO_2 emitting source, n is the number of ranked sources, p_i is the average carbon capture cost of source ranked in *ith* position in $€_{2018}$ / t_{CO_2}, q_i is the aggregated capturable emissions of sources ranked $\leq -i$ in Gt_{CO_2} per year.

The cost of captured CO_2 is the financial metric of choice and is shown in Table 4.1, for respective point sources. The capture costs have been converted to € based on the 2020 Oanda exchange rates, and any data older than 2018 have been adjusted with the annual Chemical Engineering Plant Cost Index (CEPCI). Table 4.1 shows the global potential CO_2 supply from recent estimates. Average values are taken from the selected literature listed. Capture rates are based on the best available technology.

Table 4.1: *The potential of capturable CO_2 from point sources and associated capture costs, from a global context.*

Source	**CO_2 Content**	**Capture Rate**	**Capturable Emissions**	**Capture Costs** (i)[1]	**Ref.**
	$\%(v/v)$	$\%$	$Mt\mathrm{CO_2}/yr$	$€_{2018}/t_{\mathrm{CO_2}}$	
DAC	400 *ppm*	50	>10000	145.87 (15)	[241]
Coal Power Plant	12–15	90	8785.26	45.4 (5)	[242, 243]
NG Power Plant	3–10	90	2677.59	77.45 (10)	[242, 243]
Iron and Steel	15	90	1980	59.1 (7)	[244, 245]
Cement	14–33	75	1687.5	93.37 (12)	[244, 246]
Refinery	3–13	75	637.5	108.4 (13)	[242, 245]
Petroleum Power Plant	3–8	85	697.67	72.25 (9)	[242]
Ethylene	95	90	234	34.29 (4)	[242]
Pulp and Paper		90	226.8	140.84 (14)	[245, 247]
Aluminium	<1	85	216.75	78.5 (11)	[248, 249]
Bio-energy	3–8	80	58.4	67.65 (8)	[243]
Hydrogen	70–90	95	51.3	19.21 (2)	[242]
Fermentation[2]	100	100	40.1	16.29 (1)	[242, 250]
NG Processing	5–70	65	32.5	48.59 (6)	[242, 251]
Ammonia	100	80	21.54	28.10 (3)	[242, 245]

[1] i is capture cost rank.

[2] includes bioethanol production.

Environmental Merit Order

An environmental merit order curve is used to rank potential sources of CO_2 according to their marginal environmental impacts at the point of capture, against their supply volume. This assessment method is not a rigorous life cycle analysis and thus, does not consider the downstream allocation of a unit of carbon but assesses the *production* of a unit of usable carbon for comparative analysis. A unit product of carbon is 1 t of compressed CO_2.

Marginal Environmental Impacts

Marginal CO_2 emissions ($M_{CO_2-eqv,min}$) of a point source describes the ratio of the additional CO_2 emitted after the capture process to the CO_2 produced by the capture process M_{CO_2-p} is described by Equation (4.4), and is measured in $t_{CO_2eq}/t_{CO_2product}$.

$$M_{CO_2-eqv,min} = (M_{CO_2-e} + M_{CO_2-th} + M_{CO_2-fs} + M_{CO_2-og} + M_{CO_2-tr} - M_{CO_2-fg}) \ / \ M_{CO_2-p} \tag{4.4}$$

The other variables are described in the following equations:

$$M_{CO_2-e} = M_{CO_2-p} \cdot W_e \cdot GW_e \tag{4.5}$$

$$M_{CO_2-th} = M_{CO_2-p} \cdot Q_{th} \cdot GW_{th} \tag{4.6}$$

$$M_{CO_2-fs} = M_{CO_2-p} \cdot E_f \cdot GW_{fs} \tag{4.7}$$

$$M_{CO_2-f} = M_{CO_2-p} \cdot E_f \cdot e_{CO_2,f} \tag{4.8}$$

$$M_{CO_2-fg} = M_{CO_2-mp} \cdot GW_{mp} \tag{4.9}$$

$$CCR = \frac{M_{CO_2-p}}{M_{CO_2-fg} + M_{CO_2-f}} \tag{4.10}$$

$$M_{CO_2-og} = (1 - CCR) \cdot (M_{CO_2-fg} + M_{CO_2-f}) \tag{4.11}$$

$$M_{CO_2-tr} = M_{CO_2-p} \cdot GW_{tr} \tag{4.12}$$

Where M_{CO_2-i} are the CO_2 fluxes. W_i, Q_i and E_i are the specific energy demands of electricity, heat and fuel respectively required per unit of CO_2 produced. GW_i is the GHG factor for the generation of energy required, $e_{CO_2,i}$ is the specific CO_2 emissions factor for fuel combustion, and CCR is the carbon capture ratio. The subscripts, $e, th, fs, og, tr, fg, p, f, mp$ represent electricity, thermal, fuel supplied, off gas, transport, flue gas, product, fuel and main product respectively.

Compiling and rewriting the previous equations yields the following simplified equation:

$$M_{CO_2-eqv,min} = -1 + W_e \cdot GW_e + Q_{th} \cdot GW_{th} + E_f \cdot GW_f + GW_{tr} \tag{4.13}$$

'-1' represents the baseline for marginal CO_2 emissions when compared with the reference capture scenario.

The environmental impact of CO_2 transport is based on the approach of European *CO_2 deserts* maps developed by Middleton et al. [252]. For a CO_2 demand of 5 Mt per year for CCU, it is estimated that the transport distance within the EU is below 200 km. Inland transport by pipeline with a GHG emission factor between 0.01 and 0.02 kg_{CO_2eq}/tkm is assumed, thus yielding an associated transport emission factor of 0.02 $t_{CO_2eq}/t_{CO_2product}$.

The marginal emissions for DAC is assessed here with the *proviso* that the carbon capture process is situated in close proximity to the point of utilisation – making transportation impacts negligible, therefore $GW_{tr} = 0$.

Table 4.2 shows the average specific energy demand required to capture one unit of CO_2 from different point sources.

Table 4.2: *Specific Energy Demands for CO_2 Capture from Point Sources (Including CO_2 Compression up to 10 bar*

	Average Energy Demand $(GJ/t_{CO_2,product})$				
Source	**Electricity**	**Heat** [1]	**Natural Gas**	**Coal**	**Ref.**
Air via DAC	1.62		6.17		[241, 253]
Coal Power Plant	0.49	1.75			[228, 242]
NG Power Plant		2.55			[242, 254]
Iron and Steel	0.87	4.27 (2.69)	0.16		[242, 255]
Cement	0.34	4.22 (3.2)	0.16	0.84	[242, 256]
Refinery		2.07 (0.65)	6.38		[242, 257]
Petroleum Power Plant		0.22			[242]
Ethylene	0.29	0.17			[242, 257]
Pulp and Paper		5.3 (4.28)			[247, 258]
Aluminium		3.7			[248, 249]
Bio-energy		3.4			[254]
Hydrogen	0.44	0.09	0.15		[242, 257]
Fermentation[2]	0.36				[242, 257]
NG Processing	0.3				[242, 257]
Ammonia	0.33				[242, 257]

[1] includes steam

[2] includes Bioethanol production

Figure 4.9 shows the relationship between the cost of carbon capture from each point source and their respective marginal environmental impact in terms of the average specific energy demand for the capture.

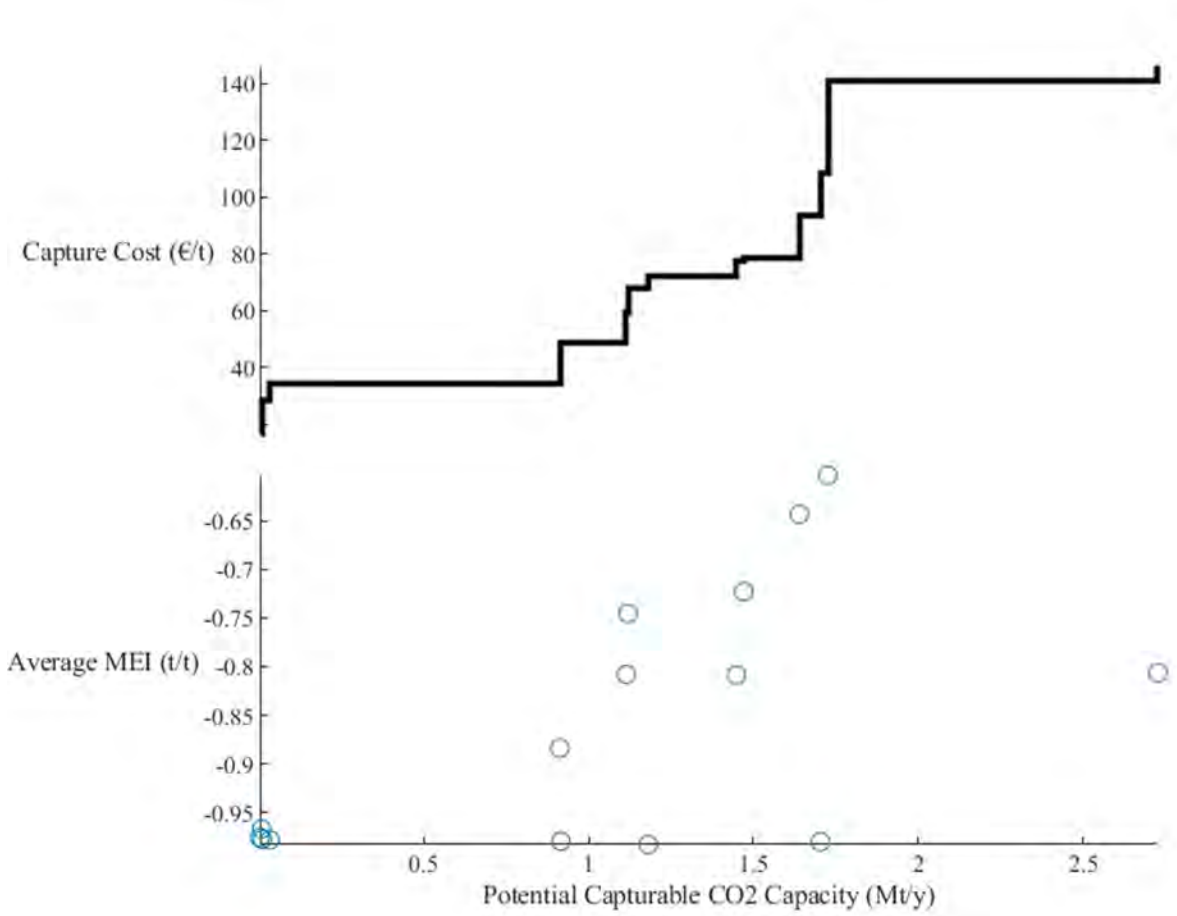

Figure 4.9: *Carbon capture cost and marginal environmental impacts from point sources, in a global context.*

High purity sources like ammonia, bioethanol and ethylene production incur the lowest capture cost $<35\,€/t_{CO_2}$, and a cumulative capacity up to 350 Mt per year. This trend is similar to the results from the marginal environmental impact assessment. The negative value indicates the potential of CO_2 emissions, with high purity sources mitigating up to 0.98 $t_{CO_2eq}/t_{CO_2product}$. Mitigation from high-capacity sources like coal and natural gas power plants are lower at 0.84 $t_{CO_2eq}/t_{CO_2product}$. The impact values from petroleum power plants, refineries and natural gas processing plants do not correlate with the costs, due to the diversity in data from the literature, and owing to the plethora of processes and diversities in petrochemical and hydrocarbons

involved.

Based on average environmental impacts, preference should be given to CO_2 point sources from the left side of the graph toward the right, as the demand increases.

4.3 The Potential and Spatial Distribution of Recyclable Carbon in the United Kingdom

The advent of the COVID-19 pandemic in 2020 led to the largest proportional reduction of CO_2 emissions in a single year in the United Kingdom by 10.7% [259]. The reductions in emissions were driven by the impact of the global pandemic and a series of national lockdowns resulting in reduced transport and business activity. In addition, the reduction is further strengthened by a record increase in the generation of electricity from renewable sources to 47% in the first quarter of 2020, compared to 35.9% in the previous quarter, resulting in a record high of low carbon generation of 62.1% and a record low for fossil fuel generation of 35.4% [260].

However, the ease of lockdown and restrictions will be expected to cause a surge in energy consumption and, subsequently, a rebound by 'retaliatory emissions', as socio-economic activity resumes to a semblance of 'normalisation' [261]. Historically, territorial emissions have been intrinsically linked with societal affluence.

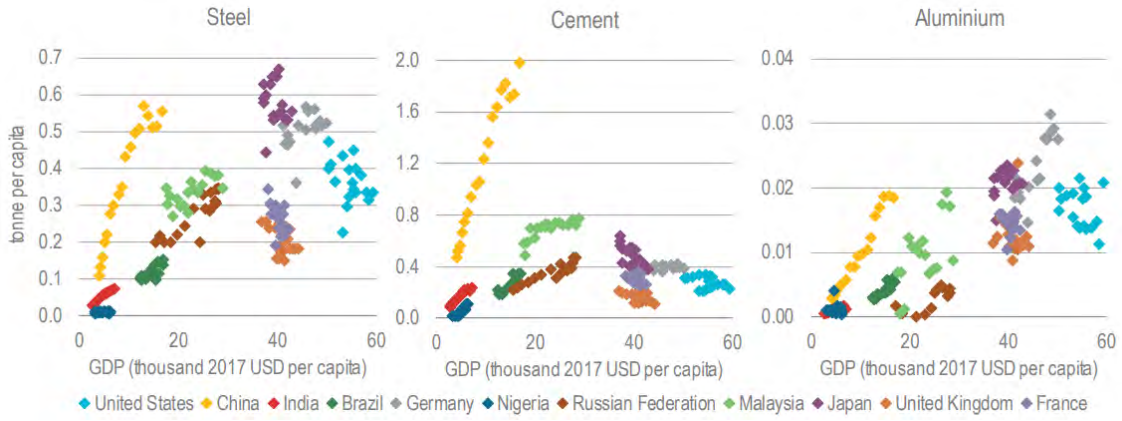

Figure 4.10: *Per capita material apparent consumption and per capita GDP for selected countries from 2000 to 2017 [262].*

Figure 4.10 reflects the correlation between the GDP of a country and its demand for materials (steel, cement and aluminium) manufactured in industries that are central to the development and economic growth of countries. It reflects how the demand for the aforementioned material is set to increase with societal affluence,

consequently increasing industry-related emissions.

In April 2021, the government of the United Kingdom, set forth the world's most ambitious climate target to reduce emissions by 78% by 2035 compared to 1990 [263]. The sixth Carbon Budget as part of the new targets includes pathways to mitigate emissions in traditionally 'difficult to decarbonise sectors' in aviation and maritime services, for the first time. This makes the United Kingdom an interesting case study in the context of this work, as it concerns the utilisation of carbon dioxide via PtX. It is therefore expedient to assess the distribution of potential carbon dioxide sources in the United Kingdom.

The term 'recyclable carbon' used in this work refers to carbon dioxide that is readily available and can be captured economically within the constraints of the current carbon technologies and at a purity that meets the specified transport and storage requirements. The onshore transportation of carbon dioxide can be classed as either modular transport or pipeline transport.

Modular transport uses vessels conveyed by railway or road media, to supply refrigerated carbon dioxide for specialist end-use such as medical, food and supercritical fluid services. The criteria stated by BS-4105 (type 2) and EIGA Doc 70/17 declare that the specified requirements for carbon dioxide are in excess of 99.5% purity by volume [264, 265]. Transportation by pipeline is often dictated by the concerns and requirements for safe and efficient transport of carbon dioxide. While there is no generally specified composition for pipeline transport, regulations require operators to carry out appropriate safety assessments and set entry requirements. Analyses by Wetenhall et al. [266] on the effect of carbon dioxide composition from various carbon capture technologies on pipeline network design, showed that up to 4% of impurities is acceptable from a safety standpoint. This is in accordance with the 95% grade specified in the Net Zero Teesside Project in the United Kingdom for pipeline distribution [267].

To this end, carbon from coal-fired power plants (and including other fossil fuel-based power generation plants) will not be considered, as its phase-out has been brought forward from 2025 to 2024 to expedite the goal of the United Kingdom to achieve net zero emissions by 2050 [268]. Atmospheric carbon dioxide will also not be considered in this section due to its pervasiveness, and relatively high energy and economic penalties the process of DAC currently incurs.

The principle of carbon utilisation can be succinctly described as the net flux of a carbon unit to, from, and within the lithosphere and the atmosphere. The quality of a carbon unit is therefore linked to its source, validating the following phrase:

"All carbon emissions are not created equally!"

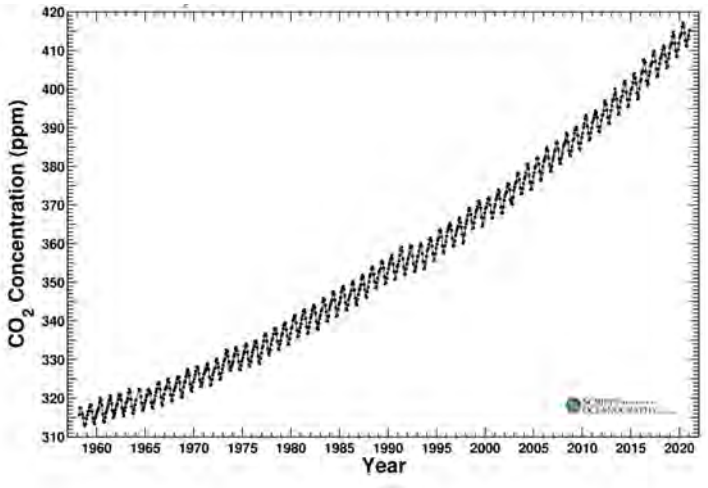

Figure 4.11: *Monthly Average Carbon Dioxide Concentration: Last updated February 2021[269].*

However, the scope and timescale for the age of the carbon unit from the time of 'agitation' must be specified. While Figure 4.11 shows the progressive increase in the concentration of carbon dioxide in the atmosphere, it estimated that between 15% and 20% of all anthropogenic emissions have been absorbed by terrestrial ecosystems since the tail end of the industrial revolution, and up to 40% by the hydrosphere, as corroborated in Figure 4.12 [270, 271].

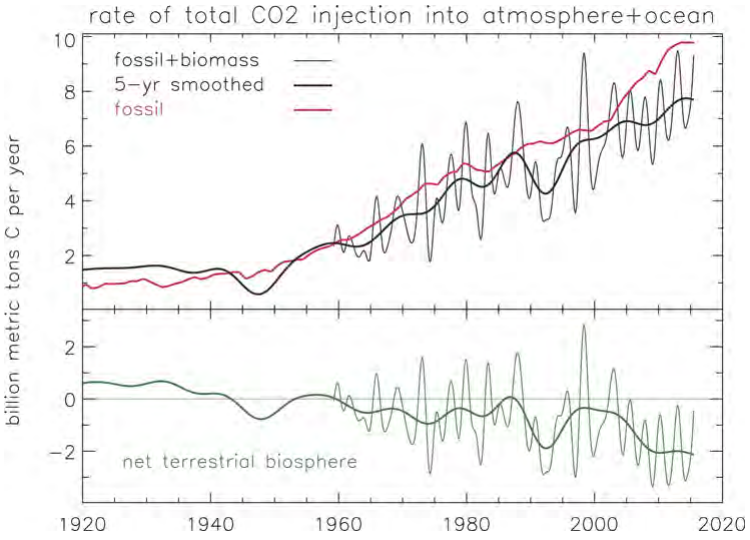

Figure 4.12: *Upper panel: Total CO_2 injection is the sum of the observed rate of atmospheric increase plus the amount that is calculated to enter the oceans. It is the sum of fossil-fuel emissions and net emissions from the terrestrial biosphere (there is no other substantial source). Lower panel: When the fossil-fuel contribution is subtracted from the total CO_2 injection, the net terrestrial emissions turn out to be mostly negative (meaning net uptake by terrestrial ecosystems) since the middle of the 20th century. [272]*

In this work, the boundary origin of the carbon unit is from the point of material transformation of the carbon-based feedstock i.e., the conversion of C to CO and CO_2. The carbon dioxide sources considered are categorised based on the following quality (a) green carbon, (b) brown carbon and, (c) black carbon.

Green Carbon Sources

These sources primarily refer to carbon-based biogenic materials indigenously sourced from the photosynthesis of atmospheric carbon dioxide in plants, including wood products, animal slurry and food waste. Carbon dioxide is captured as these materials undergo conversions such as anaerobic digestion and gasification.

Anaerobic digestion can contribute to CO_2 potential as a by-product in the production and processing of biogas. Biogas predominantly consists of methane (50% to 75% - depending on the feedstock), which includes crop residues, animal manure and slurry and food waste [273]. There are 579 plants (as of April 2021) in operation that produce biogas via anaerobic digestion in the United Kingdom, primarily for the downstream use in combined heat and power (CHP) processes and bio-methane injection into the grid [274].

Upon purification (mainly the removal of siloxane and desulphurisation), the utilisation of biogas in CHP can achieve high overall efficiencies up to 90%, compared to fossil-based power stations at 35% to 40% [275]. A study by Pröll and Zerobin [276] on a biogenic-based CHP process, showed a CO_2 emission intensity of $0.33\,kg_{CO_2}/kW\,h$ to $0.37\,kg_{CO_2}/kW\,h$. These values are in agreement with emission intensity of $0.33\,kg_{CO_2}/kW\,h$ to $0.35\,kg_{CO_2}/kW\,h$ found in [277]. The upper limit of $0.37\,kg_{CO_2}/kW\,h$ is considered in this work to account for a progressive and higher carbon capture rate to calculate the amount of carbon dioxide output from these processes dedicated to CHP services.

While there is no specific information for the load factor for biogas CHP plants, the DUKES 2020 publication shows different values for bioenergy (62.8%), anaerobic digestion (63.4%) and, CHP (59.1%) [278]. An upside value of 80% is chosen as the load factor for the CHP plants, to reflect the proposed influx of bioenergy in the United Kingdom.

The production of bio-methane requires CO_2 to be stripped from the biogas

product, to achieve a methane purity in excess of 95% (comparable to natural gas) via the upgrading processes described in a separate section of this work. Currently, 90 plants in the United Kingdom partake in the production of biomethane via anaerobic digestion [274]. Presently, there exists no legislative prohibition on the grade of biomethane that can be injected into the gas network; sources from two biomethane operators in the United Kingdom indicate that a minimum methane content in bio-methane is about 98%, with another including a 1.5% nitrogen content [279–281]. It can be therefore assumed that the potential of carbon dioxide available from biogas upgrading plants is nearly identical to the fraction of the carbon dioxide content of the biogas feedstock, assuming a high capture rate of 99%.

The potential of carbon dioxide is also dependent on the primary feedstock used to produce biogas. Due to the variability in the characteristics of the feedstock – digestibility of the total solid component and the destruction of the volatile solid component, and the operating conditions – hydraulic residence times, temperature, and, loading times, typical values for the composition of biogas for various feedstocks were obtained from the literature.

Table 4.3: *Characterisation of typical feedstock used for biogas production in the United Kingdom.*

Category	Feedstock	CH_4 (%)[1]	CO_2 (%)[1]	Units[2]	Refs.
1	Animal Slurry	60.9	29.7	34	[282]
2	Energy Crops	51.5	48.5	64	[283]
3	Food Waste	55	35	25	[284]
4	Agricultural Residues	58	27.91	15	[285]
5	Brewery Waste	65.9	30.7	8	[286]
6	Landfill/MSW[3]	53.3	37.1	4	[287]
7	Edible Oil	62.5	37.5	1	[288]

[1] Volumetric component fraction in biogas.

[2] Number of plants that use the specified feedstock according to [274].

[3] MSW: Municipal solid waste.

To determine the carbon potential, the carbon dioxide fraction less the other impurities are used with the predominant feedstock (in terms of raw mass fractions).

Pyrolysis involves the thermal degradation of organic materials in the absence or with a limited supply of oxidants in an inert environment, producing solid char, bio-oil, and non-condensable vapours. The complexities associated with the preparation of the feedstock, cleaning and upgrading of the pyrolysis oil are some the main challenges with the commercial deployment of pyrolysis [289].

Gasification is a self-sufficient process that permits recovery of the energy content of carbon than pyrolysis (see Reactions (56) to (58); 72% recovery.), is used to convert biomass to primarily produce valuable syngas – requiring less post-recovery work.

The full combustion of C yields:

$$C_{(g)} + O_{2(g)} \longrightarrow CO_{2(g)}, \qquad \Delta H^{\ominus} = -393.5\ kJ/mol \qquad \text{(R } \mathbf{56}\text{)}$$

In the partial oxidation (gasification) of C produces CO

$$C_{(g)} + \frac{1}{2} O_{2(g)} \longrightarrow CO_{(g)}, \qquad \Delta H^{\ominus} = -110.5\ kJ/mol \qquad \text{(R } \mathbf{57}\text{)}$$

Further partial oxidation of the producer gas (CO) produces CO_2 - 72% of $-393.5\ kJ/mol$

$$CO_{(g)} + \frac{1}{2} O_{2(g)} \longrightarrow CO_{2(g)}, \qquad \Delta H^{\ominus} = -283.0\ kJ/mol \qquad \text{(R } \mathbf{58}\text{)}$$

Gasification is most suited to and developed for lignocellulosic-based wastes such as wood materials and waste, meaning that biomass feedstock with higher ash content ($>$ 9 w/w%) like straw, energy crops, oil seed crops, and grasses are not recommended for gasification, due to their tendency to clog reactors [290]. Currently, it is estimated that around 4.5 Mtpa of waste wood are generated every year in the United Kingdom [291]. However, the availability of wood waste for biomass processing is subject to a waste hierarchy according to the Waste Incineration Directive and Industrial Emission Directive - set to minimise the disposal of waste and prioritise prevention and reuse. This implies that around 55.3% of the total wood waste is dedicated to biomass processes.

Principally, the potential of carbon dioxide via wood waste is contingent upon the guaranteed capacity to process the feedstock. Despite being a mature concept, gasification is yet to attain full commercialisation in the United Kingdom. Of the advanced thermal conversion plants that have been proposed in the United Kingdom (circa 130), only eight are in operation.

Figure 4.13: *Current wood waste gasification projects in the United Kingdom [292].*

Figure 4.13 shows the locations of the current wood waste gasification plants in operation in the United Kingdom, with an installed capacity of around 333 kt per year. A study by Dinca et al. [293] showed that 0.53 kg_{CO_2}/kW h to 0.68 kg_{CO_2}/kW h was achievable in a sawdust IGCC plant with carbon capture. According to the DUKES 2020 document, the load factor of all bioenergy technologies was 62.8%. However, to account for the closing down of coal facilities, a higher load factor of 72.8% is considered (similar to plant biomass stations like Drax).

High-purity carbon dioxide is a by-product of bioethanol production via fermentation, a mature process used to manufacture alcoholic beverages in the United Kingdom. It is estimated that there are 361 distilleries in operation in the United Kingdom. Owing to its rich whisky heritage, Scotland accounts for up to 80% of the United Kingdom's distillery capacity and, 20% of the United Kingdom's food and drinks exports [294]. According to the 2015 report by Roland Arnison [295],

243.5 ML of beer was produced in Scotland. The data for whisky production from grain and malt is provided by [296] and [297]. This is with regard to a pure alcohol capacity of 800.26 ML per annum.

Table 4.4: *Summary of potential green CO_2 in the United Kingdom.*

	Biogas CHP	**Upgrading Biomethane**	**Wood Waste Gasification**	**Fermentation**[1]
Units	570	90	4	>211
Installed Capacity	466.09[2]	50831.82[3]	46.3[2]	617.87[4]
Load Factor, (%)	80	47.7	72.8	90[5] & 75[6]
Mass of CO_2, (Mt/yr)	2.82	0.32	0.33	0.51
Total, (Mt/yr)			3.98	

[1] Scotland alone.

[2] MW_e.

[3] Nm^3/h.

[4] ML/yr.

[5] Grain whisky.

[6] Malt whisky.

Brown Carbon Sources

In this work, brown carbon refers to feedstock with a heterogeneous mix of organic and inorganic carbon-based materials such as municipal solid waste (MSW). The physical classification of household MSW in various income group economies is described in Table 4.5.

Table 4.5: *General classification of MSW and by different income economies. Modified from [298].*

Class	Examples	High (%)	Middle (%)	Low (%)
Organic	Food and garden wastes	64	56	28
Paper	Cardboard, tissue	6	12	30
Plastic	Polythene, LDPE	9	13	11
Metal & glass	Non-/ferrous, ceramics	6	7	13
Others	Stones, clothes, batteries	15	12	18

In 2018, the United Kingdom generated 26.40 Mt of household waste, with England accounting for 83.4% of the total waste, and is thus the subject of this study. As with wood waste, the processing of MSW is subject to a hierarchy by the Waste Framework Directive (2008/98/EC) that aims to promote waste prevention whilst restricting waste to landfill (see Figure 4.14). The WFD stipulates that the amount of recycled household MSW progressively increases to 65% of the total weight by 2035.

Figure 4.14: *Waste hierarchy from the Waste Framework Directive 2008/98/EC [299].*

Additional restrictions imposed by the Landfill Directive (1999/31/EC) to prevent and reduce the adverse environmental impacts as a result of landfilling waste has led to an increase in landfill taxes to ensure that the disposal of wastes incurs a heavy economic burden. As a consequence, the diversion of waste from landfill sites and increasing recycling rates has resulted in the rapid adoption of incineration facilities and energy recovery through direct combustion of MSW as shown in Table 4.6.

Table 4.6: *Management of all Local Authority collected waste financial year figures, England, 2015/16 to 2019/20 (in kt) [300].*

Waste disposal method	**15/16**	**16/17**	**17/18**	**18/19**	**19/20**
Landfill	5,133	4,136	3,213	2,756	2,169
Recycled/composted	11,065	11,252	10,860	10,926	10,949
Incineration	9,259	10,182	10,846	11,205	11,633
Other	668	748	706	699	816
Total	26,124	26,319	25,626	25,586	25,568

The waste incineration process was originally implemented as a waste volume reduction strategy (up to 90%) but is now predominantly coupled with energy recovery systems. Unlike the previous thermal conversion technologies discussed (pyrolysis and gasification), incineration is a full oxidative combustion process without requiring intensive feedstock pre-treatment. Incineration is a mature and fully commercialised technology with 115 facilities in deployment in the United Kingdom as of 2016 [301].

However, incineration has less desirable environmental impacts than gasification, as revealed in a study by Tang et al. [302]. Health concerns due to the formation of toxic waste ash, dioxins, and furans, especially from PVC-containing plastics from incineration processes, are subject to scrutiny and opposition from community groups in the United Kingdom. Despite recent failures, the anticipated success of the deployment of the first MSW gasification plant by Kew Technology and

the Energy Technologies Institute in Aldridge could pave the way to more financial incentives to improve the TRL of gasification technologies in the United Kingdom.

Studies on the gas composition of thermal processing of MSW by gasification show a carbon dioxide intensity of $0.54\,\mathrm{kg_{CO_2}/t_{MSW}}$ to $0.79\,\mathrm{kg_{CO_2}/t_{MSW}}$ [303–305]. To account for the current rate of MSW gasification in the United Kingdom, a conservative value of $0.20\,\mathrm{kg_{CO_2}/t_{MSW}}$ is chosen to assess the potential of brown carbon from MSW in the United Kingdom. Based on the data from Table 4.6, there is a minimum brown carbon potential of 2.33 Mt per year.

Black Carbon Sources

Black carbon refers to carbon dioxide sourced from established industrial sources that are primarily fossil fuel-fired, and because of their societal relevance (see Figure 4.10) are considered inexorable. High volumes of flue gases also characterise them.

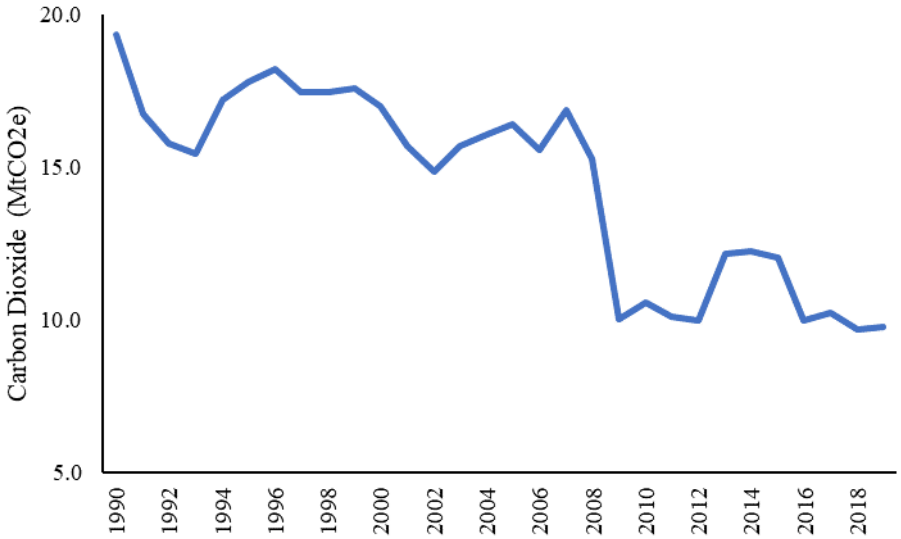

Figure 4.15: *CO_2 emissions from industrial processes, United Kingdom 1990-2019 [306].*

In 2019, around 10 Mt of carbon dioxide was estimated to have been emitted by industrial processes in the United Kingdom. From Figure 4.15, it is evident that there is a degree of regularity in the emissions from 2010 onward, providing an opportunity for consistently available CCU feedstock. The emissions could be from established and considered hard-to-decarbonise plants. In the United Kingdom, cement, iron and steel production account for a high proportion of territorial emissions (about 28%) [307, 308]. In addition, Figure 4.16 corroborates that the cement and iron and steel industries (behind ammonia and hydrogen) are most readily approachable for coupling with carbon technologies. The width of the peaks indicates the variation in the levelised costs across various scenarios.

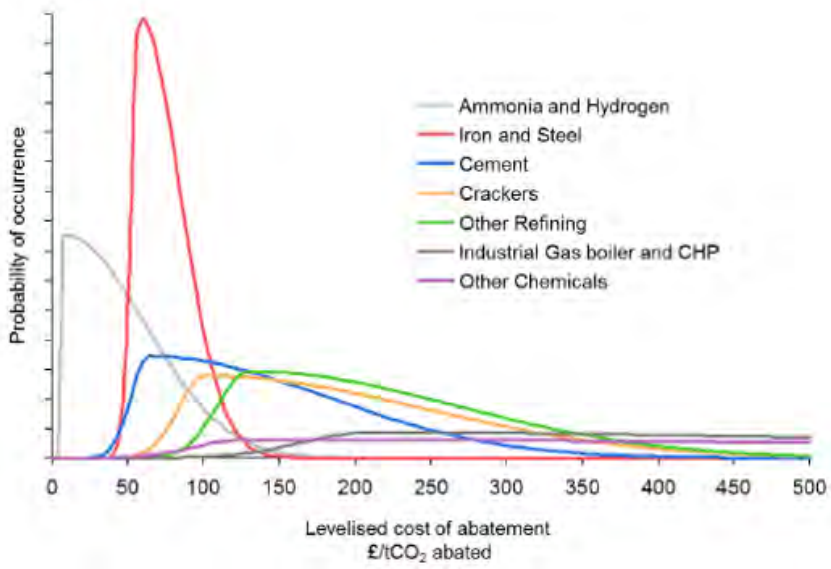

Figure 4.16: *Typical distribution of levelised cost of abatement for each sub-sector by 2025 [309].*

Around 70% of carbon dioxide emitted from cement production, emanates from process emissions in clinker production (as previously stated in Reaction (51)). According to the annual report by the Mineral Product Association (MPA), 9.08 Mt of cement was produced from 23 sites in the United Kingdom. The potential of carbon dioxide from clinker production is estimated from Equation (4.14).

$$\mathrm{CO}_{2cement} = \left[\sum_{i} (M_{c,i} \times C_{cl,i}) - Imp + Exp\right] \times EF_{cl} \times CF_{CKD} \tag{4.14}$$

Where $M_{c,i}$ is the mass of cement produced of type i, $C_{cl,i}$ is clinker fraction of cement of type i, Imp is the imports for consumption of clinker, Exp is the exports of clinker, $EFcl$ is the emission factor for clinker and, CF_{CKD} is the corrections factor for cement kiln dust. $EFcl$ is derived from the following Equation (4.15):

$$EF_{cl} = f_{cl}^{\mathrm{CaO}} \cdot \frac{M_r^{\mathrm{CO_2}}}{M_r^{\mathrm{CaO}}} \tag{4.15}$$

Where f_{cl}^{CaO} is the ratio of CaO in clinker. Based on the production of 90% Portland cement, the emissions of black carbon from cement production in the United Kingdom is 4.73 Mt per year (excluding direct emissions from fossil fuel combustion and indirect emissions from electricity use – around 30% of the total emissions). This equates to a carbon dioxide to cement ratio of $0.52\,\mathrm{t_{CO_2}/t_{cement}}$ which is in agreement with the value of $0.54\,\mathrm{t_{CO_2}/t_{cement}}$ in [310].

As briefly described in an earlier section (see Reactions (49) and (50)), 70% of the emissions in the iron and steel-making emanate from heating processes, primarily fired by coal, and the subsequent flue gases from iron ore reduction in the blast furnace (BF). Steel is produced downstream of the iron-making processes in the basic oxygen (BOF) or electric arc furnaces (EAF), and sulphur and carbon are further removed from molten iron in the form of carbon oxides. Activity data from the Iron and Steel Statistics Bureau (ISSB) is used to estimate the potential of black carbon from the iron and steel industry in the United Kingdom as given by Equation (4.16).

$$\mathrm{CO}_{2iron/steel} = \sum_{i} (M_i \times EF_x) \tag{4.16}$$

Where M_i is the mass of pig iron or semi-finished steel ingots and EF_x is the emission factor for the production method of type x – BF alone, BOF or EAF. It is estimated that 25.27 Mt of carbon dioxide is generated per year from the production of 12.33 Mt iron and steel materials.

Summary of Estimated Carbon Sources

Table 4.7 shows an estimation of the CO_2 potential viable for CCUS in in the United Kingdom. As stated earlier, CO_2 from fossil fuel-based power generation plants are not included partly to the uncertainty surrounding their prospective decommissioning in the near term.

Table 4.7: *Summary of potential of CO_2 in the United Kingdom per annum.*

Type	Potential (Mt)	Notes
Green		
Biogas in CHP	2.82	
Biomethane upgrade	0.32	
Wood waste gasification	0.33	
Alcohol fermentation	0.51	Scotland alone
Brown		
MSW gasification	2.33	England alone
Black		
Cement	4.73	
Iron	7.49	
Steel	17.77	
Total	36.31	

Aside from the ability to continuously resolve technical challenges, insufficient policy instruments and financial incentives have been noted as the biggest challenges to the rapid deployment of conversion technologies, especially in the downstream capture of green and brown carbon. The deployment rate of AD plants in the UK is intrinsically linked with the availability of government funding and financial incentives, despite the potential of 90 million tonnes of manure and slurry that remain untapped in the UK [273]. The number of new AD plants commissioned in the UK declined from a peak of 79 in 2014 to 6 in 2017 as a result of the aforementioned lack of financial incentive (see Figure 4.17).

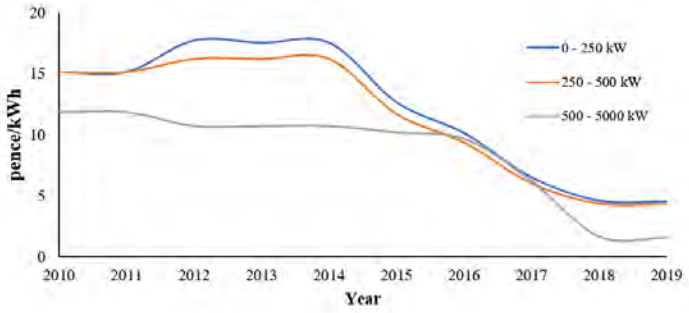

Figure 4.17: *Change in generation tariff rate for anaerobic digestion [311]*

The drive to increase the gasification of waste would benefit from financial mechanisms like the Renewable Heat Incentive (RHI) and the Renewable Transport Fuels Obligation (RTFO) that support heat or gas-to-grid applications and proposals towards liquid fuels in the UK.

The future prospect with regard to the availability of CO_2 from green and brown carbon sources is very dependent on supporting policies and mechanisms for the preceding conversion technologies as part of the overarching climate change mitigation measures in the UK.

Distribution of Carbon Dioxide from Sources in the United Kingdom

In addition to the availability of carbon dioxide feedstock, feasible opportunities of CCU technology and the potential market of CO_2-derived products depend on the overall product-market proximity from a point source to the end-use customer. The availability of infrastructure for transporting carbon dioxide (and other feedstock, including hydrogen) to designated processing facilities should be considered in the overall feasibility. The costs of carbon dioxide transportation are heavily contingent on the mode of transport and the distance between relevant locations.

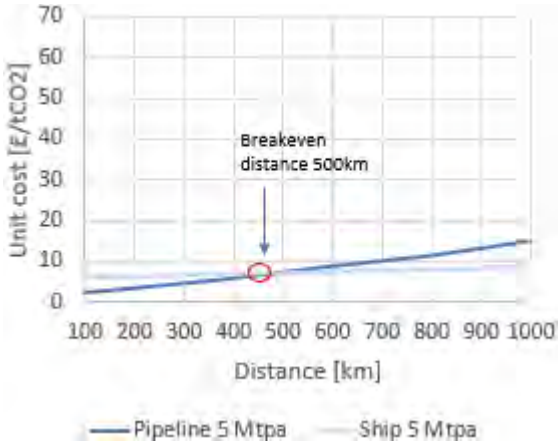

Figure 4.18: *Unit cost of transporting 5MtCO_2 via pipeline and shipping [312].*

A study based on the United Kingdom (as shown in Figure 4.18) revealed that onshore and territorial transportation of carbon dioxide via pipelines is cheaper than an offshore port to storage transfer via shipping at moderate distances (up to 500 km). Also in agreement is a report by Brownsort et al. [313]; and considering that the United Kingdom extends about 965 km longitudinally and a latitudinal distance of 485 km, onshore pipeline deployment is a feasible option.

Regarding the costs of dedicated carbon dioxide pipelines, it is assumed that the existing and matured gas pipeline can be utilised/re-purposed for carbon dioxide transportation. In addition to the considerable disparity in the process experience and operating history, a major limitation in the repurpose of conventional natural pipelines for carbon dioxide transfer arises from the difference in the thermophysical

properties of carbon dioxide and natural gas.

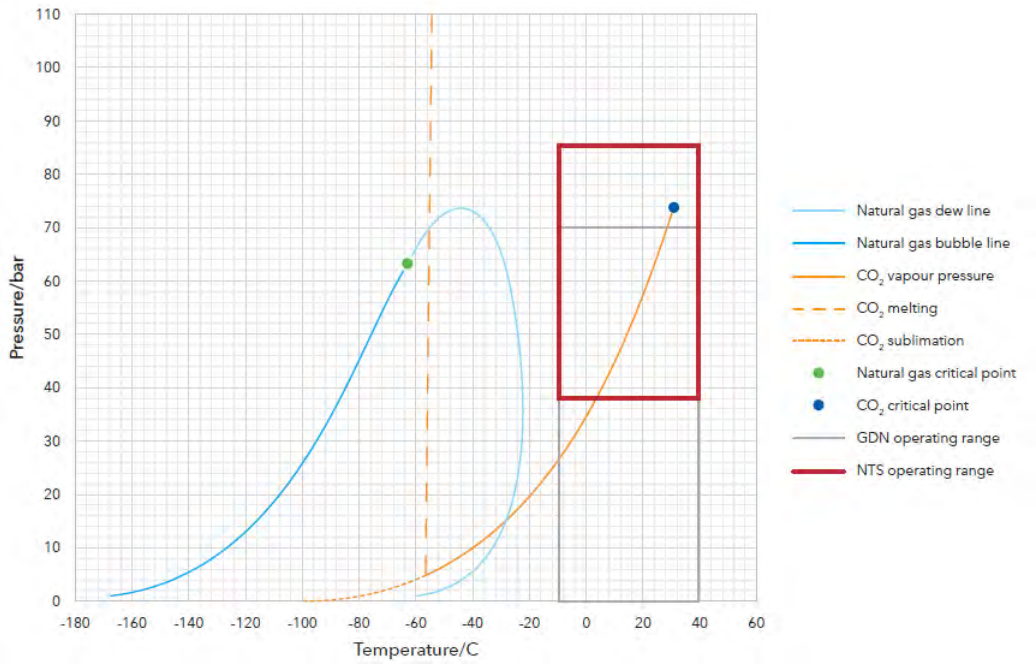

Figure 4.19: *Phase envelopes of natural gas and pure carbon dioxide.*

As shown in Figure 4.19, the onshore national transmission system (NTS) and the gas distribution network (GDN) are designed to operate around 85 bar and 75 bar respectively, at the local ground and ambient temperatures. Above the critical point (73.80 bar and 31.10 °C), carbon dioxide exists as a dense phase liquid — an efficient state of transportation, preventing sudden pressure drops as a result of phase changes. A slight deviation from the critical point can have a butterfly effect on the density of carbon dioxide, subsequently increasing the risk of complications for compressor units and pipeline failure in a two-phase system. Typically, carbon dioxide is transported between 85 bar and 150 bar due to minimum supercritical phase conditions and economic concerns, respectively [314].

However, due to the lack of carbon dioxide pipeline infrastructure in the United Kingdom, the existing gas pipeline corridors can be used to determine possible routes for deploying carbon dioxide-dedicated pipelines. The spatial distribution of potential carbon sources is overlaid on the gas transmission network of the National

Grid in Figures 4.20 to 4.23 using QGIS v.3.18.

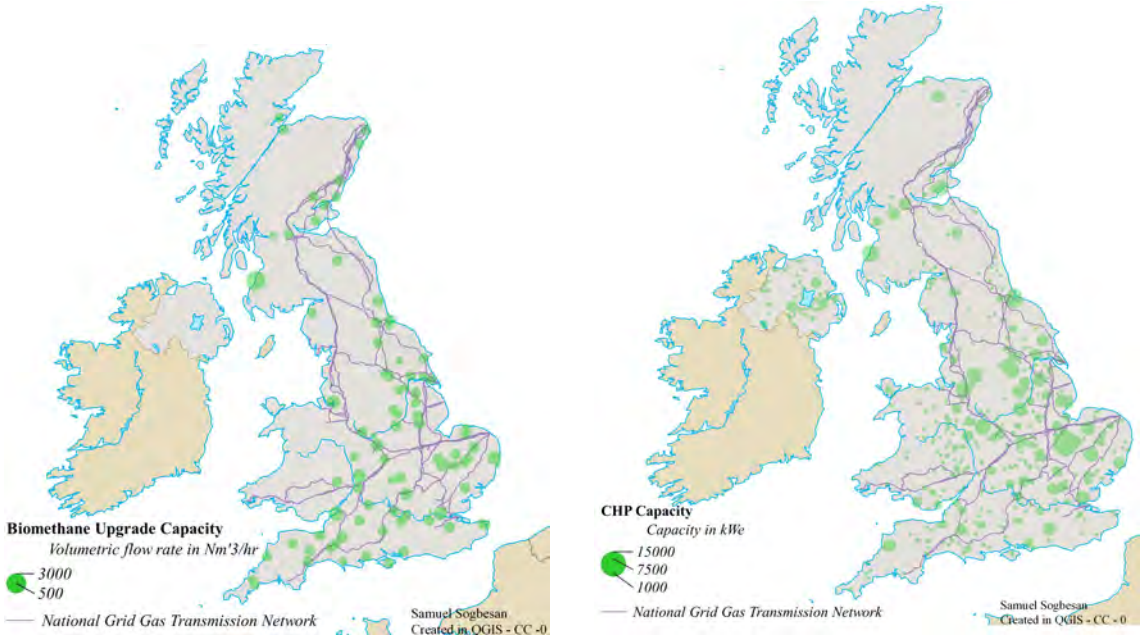

(a) *Biomethane Upgrade* **(b)** *Biogas-fired CHP*

Figure 4.20: *Spatial distribution of potential sources of green carbon from biogas utilisation in the United Kingdom in relation to the gas transmission network of the National Grid. Author's own work.*

Figures 4.20, 4.21 and 4.23 portray the location of carbon sources, as described in previous sections of this chapter, in the United Kingdom. The bubbles on the individual maps represent the amount of assessed recyclable carbon according to their size. Figure 4.22 represents the amount of municipal waste collected by the local authority, for the major regions of England.

Spatial analysis shows that there are feasible opportunities to deploy hubs as part of a decentralised CCU network. The ACT Acorn project established by the European Commission under the Horizon 2020 Programme for Research and Innovation aims to deliver a low-cost CCS system by 2023 in the UK [315]. Initial financial estimations of the project suggest that the costs to repurpose a hydrocarbon pipeline for CO_2 transportation may cost 1 to 10% of the cost of building and installing a new pipeline.

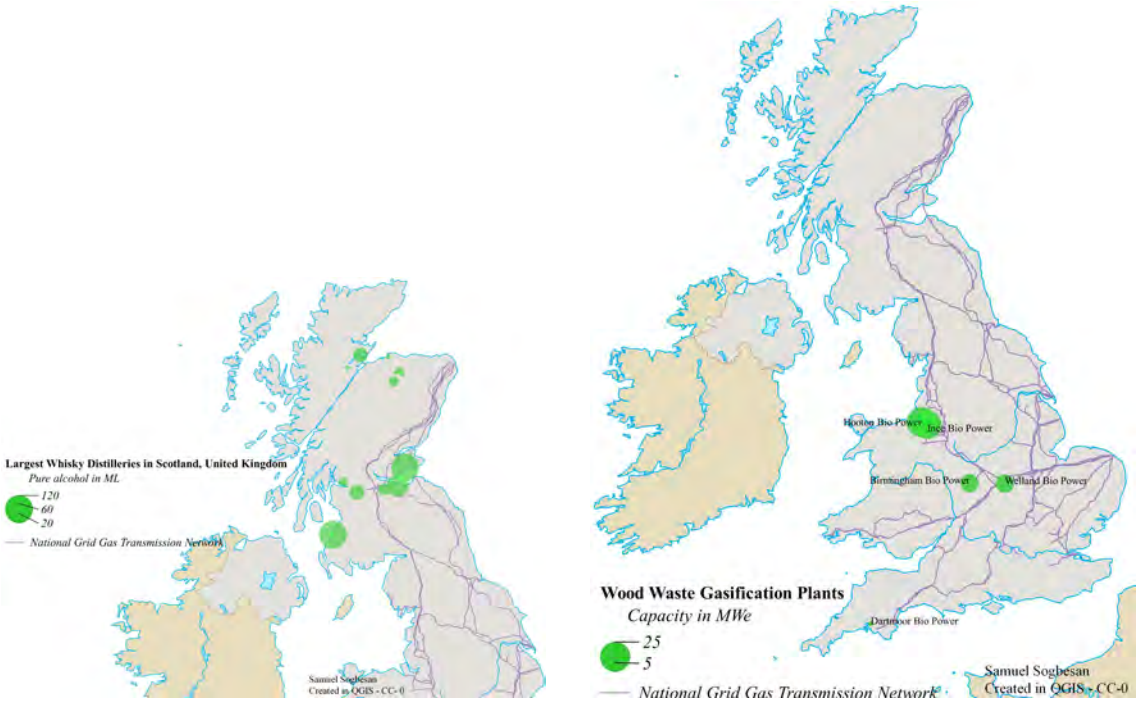

(a) *Whisky distillery in Scotland* **(b)** *Wood waste gasification*

Figure 4.21: *Spatial distribution of potential sources of green carbon from whisky distillery in Scotland and potential wood waste gasification in the United Kingdom in relation to the gas transmission network of the National Grid. Author's own work.*

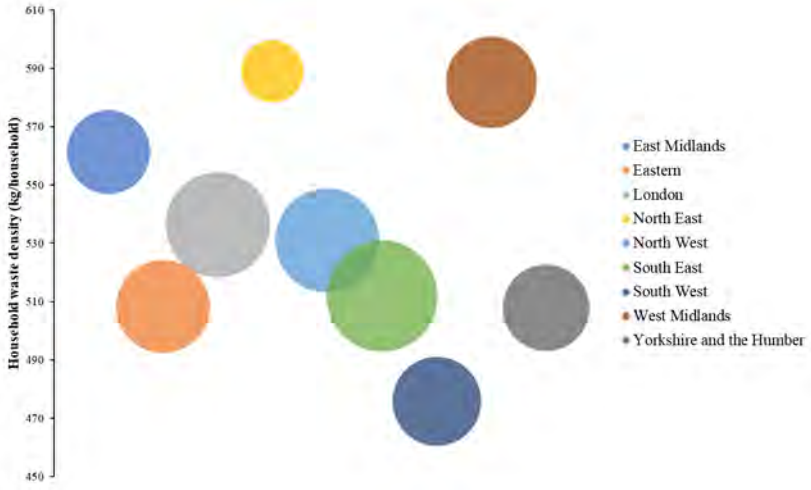

Figure 4.22: *Graphical representation of local authority collected waste, England by region, as a function household density.*

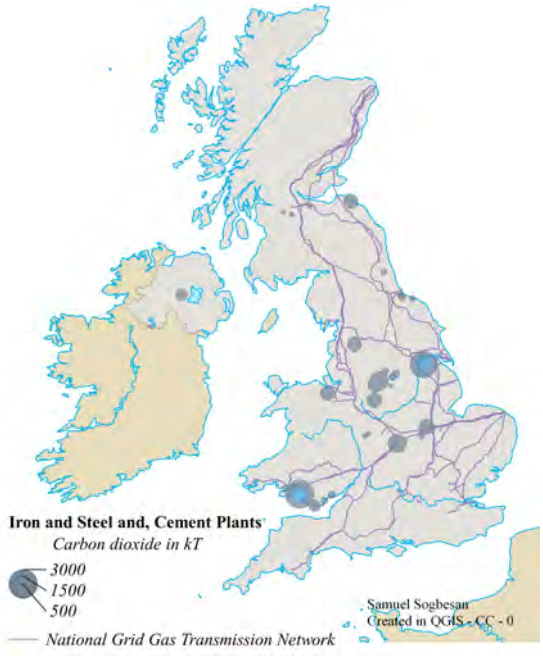

Figure 4.23: *Spatial distribution of potential sources of black carbon from iron, steel and cement plants in the United Kingdom in relation to the gas transmission network of the National Grid. Author's own work.*

It can be observed that the Yorkshire, Humber and East Midlands regions are interesting clusters for carbon sources. This is corroborated by the data analysis in Figure 4.24, based on the aggregate point sources of carbon dioxide emissions in the United Kingdom.

Furthermore, this region is proximal to all the potential CO_2 storage formations for the United Kingdom continental shelf (see Figure 4.25), useful in the encouraging attempt to synergise CCS and CCU as feasible decarbonisation measures.

However, as the deployment of CCU is also business case dependent, the Scottish and North English belt offers an opportunity to utilise higher purity carbon dioxide and presumably available curtailed electricity, to further the deployment of PtX technologies.

In recent years, excessive amounts of constraint payments (see Figure 4.26) have been made to wind farm operators to curtail wind electricity, to compensate

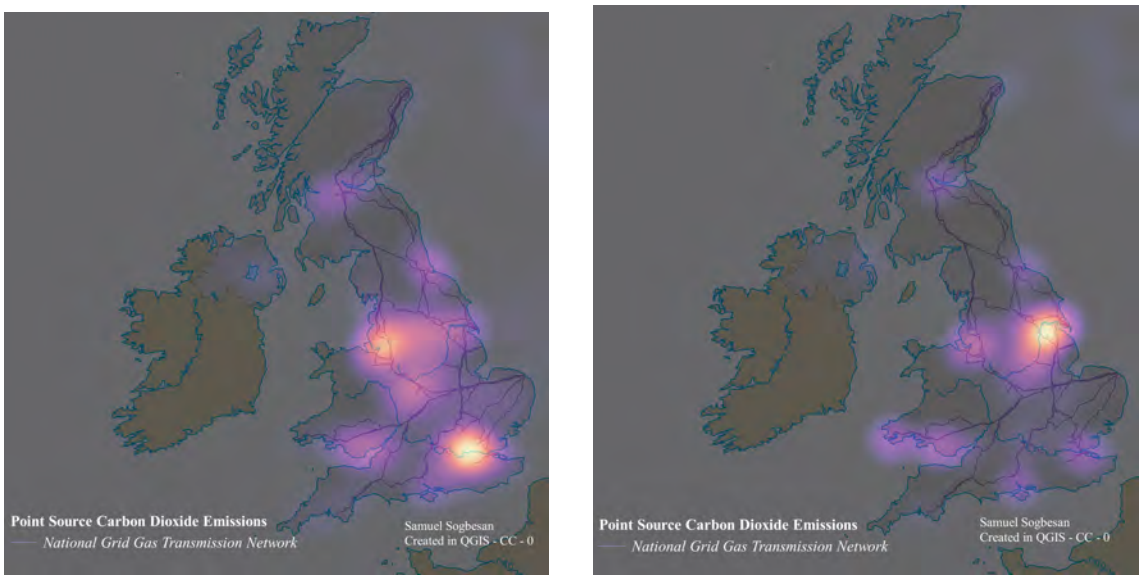

(a) *Point source density* **(b)** *Point source intensity*

Figure 4.24: *Spatial distribution of potential sources of carbon from all point emissions in the United Kingdom in relation to the gas transmission network of the National Grid. Author's own work.*

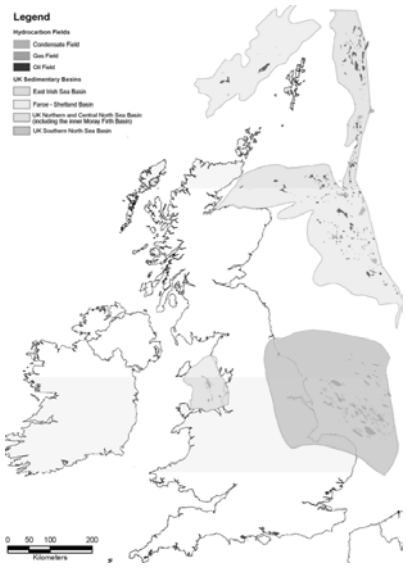

Figure 4.25: *Map showing the location of offshore hydrocarbon fields and the major oil and gas-bearing sedimentary basins in the United Kingdom continental shelf [316].*

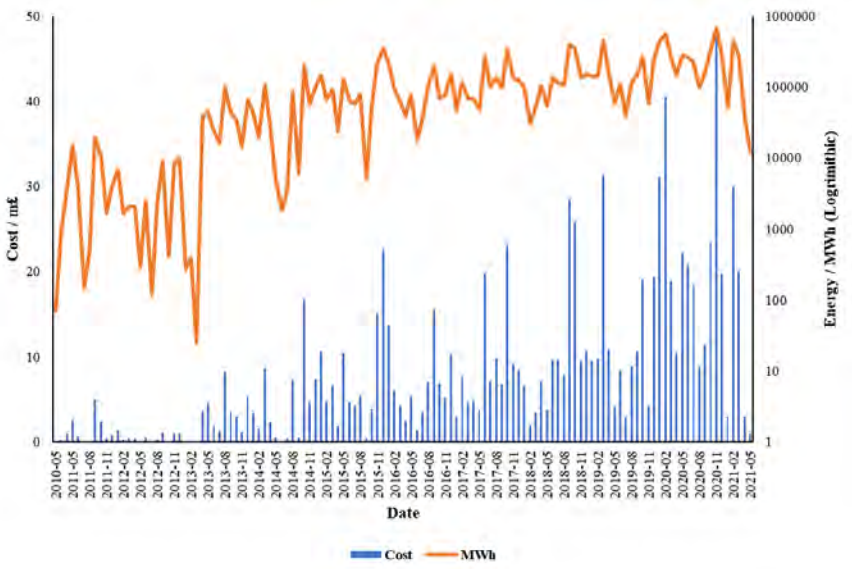

Figure 4.26: *Constraint payments for wind farms under the balancing mechanism for curtailed generation (modified from [317]).*

for the loss of revenues and subsidies such as the Renewable Obligation Certificates (ROC). This has come under scrutiny, especially as the cost is ultimately burdened by bill charges to electricity consumers through the Balancing Services Use of Systems (BSUoS).

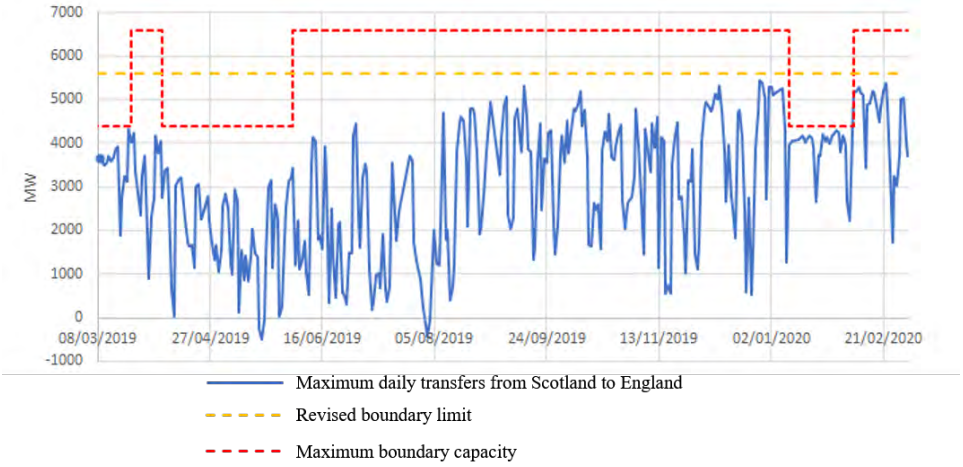

Figure 4.27: *Aggregate maximum daily transfer from Scotland to England (2019 – 2020), showing three deviations from the proposed 6.6 GW to 4.4 GW, reflecting the offline operation of the Western Link HVDC interconnector. [317].*

A key factor in this issue surrounds pressing questions on the reliability of the Western Link high-voltage, direct current (HVDC) interconnector designed

to alleviate the grid constraint issues and increase cross-country transfer of wind-generated electricity across the aforementioned border. The highest peak in the constraints payments was directly related to faulty operations of the Western Link HVDC interconnector, incurring payments of over £1 million per day. The impact of the Western Link HVDC interconnector operation is summarised in Figure 4.27. The yellow dashed line represents the boundary capacity of 5.70 GW prescribed in [318]. The red dashed line represents the maximum boundary capacity set to 6.60 GW, following the Western Link HVDC interconnector deployment. The dips in the boundary represent periods of offline activity of the interconnector resulting in constraint payments to Scottish wind farms.

4.4 Chapter Discussion

This section presented the potential of the primary feedstock required for developing electrofuels in the United Kingdom. The analysis assessed inexorable carbon dioxide sources, including renewable and non-renewable sources in the United Kingdom. The analysis also assessed the amount of renewable electricity that could be otherwise curtailed for the electrolysis process.

The analysis showed that a considerable amount of CO_2 (36 Mt) can be recovered from large industrial sources annually. The amount is about 11% of the total amount of GHG emitted in the United Kingdom (331 Mt in 2022) [319]. This amount represents a significant reduction potential in the overall GHG emissions in the United Kingdom, compared to the 2.4% reduction achieved in the previous year.

Chapter 5

TECHNO-ECONOMIC ANALYSIS

This section follows the previous chapters to conduct economic analyses of the developed model systems. This section will seek to evaluate the financial viability of the discussed projects and address economic-related questions like "How much?" and "Is it worth it?". The analyses will employ field-tested and industry-standardised modelling techniques in their investigation.

5.1 Goal of Techno-economic Assessment

This chapter aims to assess the techno-economic viability of synthetic fuel production through the valorisation of captured CO_2 in the United Kingdom in 2030[1]. The study is conducted from a research and development perspective to ascertain the major cost drivers to support investment decisions, given the different types of fuels that are considered the subject of this study. The results of this chapter do not indicate the pathways' technical performance but depict the most probable economic performance given the stated assumptions and the current public knowledge. The analysis is based on a chemical plant size that valorises 100 t/h of CO_2. The results obtained from the previous analysis are shown in Table 5.1.

Table 5.1: *Annual energy output of fuels produced from 100t/hof CO_2 and 8,000 capacity hours.*

Metric	Methane	Methanol	DME	FTL [1]
Fuel energy content (PJ/yr)	14.97	5.64	8.44	1.28(0.88)
SOE Capacity (MW)	802.6	582.3	582.3	342.5

[1] Bracketed values represent the Naphtha by-product

5.2 Economic Analysis Methodology

The economic models for the modelled CCU plants take the capital, operational and maintenance expenditures into account via a bottom-up approach based on detailed steady-state process models, equipment sizing, utility and energy balances. The economic analyses employed the Aspen Process Economic Analyzer ® (APEA) *v.11.1*, based on USD ($) for the first quarter of 2018. The currency is then updated to GBP (£) for the year 2022 to reflect the region of analysis.

APEA uses the Icarus Evaluation Engine —, a knowledge-based evaluation

[1] In reference to the proposed ban on the sale of new iCE vehicles in the UK

technology based on a core design, estimating, and scheduling to produce preliminary unit component design and generate vendor cost procedures to develop comprehensive economic estimates. APEA is described as an industry-standard tool, and a high degree of accuracy has been validated in a study by Li et al. [320]. APEA is also employed due to the ease of integration with the modelling software used in previous analyses.

5.2.1 Techno-economic Inventory

Feedstock Input

Identifying the relevant system parameters and the quality of detail is critical to a proper techno-economic analysis. Economic data in the following analysis was obtained from academic literature, historical data and databases. However, it must be stated that the validity of the data was location and scenario dependent. To this end, where the available data was not satisfactory (especially in components at relatively early technology maturity), average data from literature sources was used as an input estimate for the assessment. A degree of variability was applied to the analysis to accommodate the ambiguity in certain data.

The CO_2 input price is dependent on the system boundaries and the technical specifications of the fuel synthesis processes described in Chapter 3 and Chapter 4. At the time of this study, there were no open access data to the availability and pricing of CO_2 in the United Kingdom. Due to the lack of such data, the location cost was extended to Europe and obtained from the average cost of traded CO_2 (0.08 £/kg) across Europe [321]. The operation was assumed to be continuous and close to the CO_2 point source; therefore, the costs associated with transport and storage were neglected in the reference assessment. The process design was based on the high purity CO_2 estimated in Chapter 4, approximated to 100 t/h , assuming 8000 annual operating hours.

The production of electricity is outside the boundaries of this analysis and

is regarded as a purchased commodity. Like CO_2, transport and storage costs for electricity are neglected in the base case assessment. The base electricity input price (58.10 £/MWh) is based on the average wholesale industrial prices for small to medium plants[2], excluding the Climate Change Levy in the United Kingdom [322]. The price is from Q3 2022 (100% increase from the same period in the previous year) and is thus not reflective of the prices before the Russia-Ukraine war.

Capital and Operating Costs

The investment costs are based on the ASPEN process model simulations described in Chapter 3. Process equipment and components are loaded, mapped and individually sized according to material and energy flows in the aforementioned APEA programme, where procurement, design and labour costs are estimated. All process equipment is made from stainless steel (BS SS 304/18Cr-8Ni) (highly resistive to corrosion with strong mechanical properties) with the exception of high-pressure process equipment (>20 bar), which is made from carbon steel (A-285C) with a monolithic lining of 50% alumina refractory gunning mix (GUN50) for high-temperature process equipment. An initial base cost for the installed solid-oxide electrolyser was assumed to be 800 £/kW_e [323]. Due to the varying syngas modulus for each process, the electrolyser capacity varied from 517 MW_e to 802 MW_e. The utility usage following a heat exchange network analysis was also included in the economic assessment of this work. Location factors and cost escalation were taken into account in the economic analysis as shown in Table 5.2.

[2]Annual electricity consumption between 500 to 1,999 MWh

Table 5.2: *Investment parameters (base case).*

Parameter	Value	Unit
Project location	Europe/UK	
Length of start-up period	20	weeks
Annual operating hours	8000	hours
Analysis period	20	years
Desired internal rate of return	10	% p.a.
Contingency rate	18	% p.a.
Tax rate	40	% p.a.
Working capital	5	% p.a.
General & administrative expenses	8	% p.a.
Project capital escalation	5	% p.a.
Operating & maintenance escalation	3	% p.a.
Products escalation	5	% p.a.
Raw material escalation	3.5	% p.a.
Utility escalation	3	% p.a.
Depreciation method	Straight-line	
Salvage value	5	% p.a.
Methane selling price	0.90[324]	£/kg
Methanol Selling Price	0.45[325]	£/kg[a]
DME selling price	0.71	£/kg[a]
M-Dist selling price	1.76[326]	£/L
Naphtha selling price	0.73[327]	£/kg[a]

[a] kg to MJ conversion. CH_4 - 50.7; CH_3OH - 19.8; DME - 28.8; Naphtha - 43.61

Fuel selling prices based on vending to end consumers

Investment Parameters

The contingency rate is prescribed for budget allowances due to cost uncertainties in the project phase. The applied rate is based on user-defined parameters, including the process description, complexity and project type. The escalation parameters indicate the rates at which goods and services may increase over a project period. The salvage rate approximates the worth of the capital costs at the end of the economic life of the project. The depreciation rate describes how the value of an asset decreases with time. The straight-line method was chosen as it is the most commonly used method. It is estimated by dividing the difference between the total project cost and the salvage value by the economic length of the project. The values applied in the base case scenario are default values prescribed by APEA based on the location, contingency parameters, tax rates and process types.

Due to the scarcity of information, the fuel prices cited in this work were obtained from various sources based on the global market in 2022.

5.2.2 Economic Profitability Indicators

This study considers the Net Present Value (NPV) as the dynamic profitability indicator of choice as it considers multiple time periods, cash flows and the risk inherent in making investment projections about the future. The NPV is calculated using the following equation in

$$NPV = -TCI + \sum_{t=1}^{n} \frac{CF}{(1+r)^t} \tag{5.1}$$

Where TCI is the total capital investment, CF is the cash flow after tax, r is the discount rate, and t is the number of time periods. The engineering, procurement and construction periods are considered in the analysis to give a more realistic reflection of the cash flows. The discount rate r is used to discount the future cash flows of the investment to account for the value of money at the time of analysis. The base case results are shown in Table 5.3.

Table 5.3: *NPV and payback period results from the base case scenario.*

Metric	Methane	Methanol	DME	FTL
CAPEX, (£bn)	1.38	0.72	0.74	1.39
NPV, (£bn)	-2.56	-2.45	-1.84	0.55
Payback period, (yr)	20.24	20.67	20.21	4.38

The initial assessment showed that only producing synthetic diesel is profitable within the limits of the prescribed assumptions. The reproduction of other fuels shows that the process only becomes profitable beyond the 20-year analysis period. A further analysis was carried out in the following sections.

5.3 Interpretation of Results

5.3.1 Sensitivity Analysis

Local sensitivity analyses were carried out for all fuel synthesis processes under the base case scenario to identify and rank the key cost variables that have the most influence on the NPV. The capital cost of the electrolyser unit, the unit price of electricity, the unit price of CO_2 feedstock, the fuel selling price and the interest rate were the selected variables to carry out a parametric analysis with a range of ±50% of the base case values. The results show that the electricity unit price and the fuel selling cost show the most significant variance of calculations within the prescribed bounds of analysis as shown in Figure 5.1 and Figure 5.2.

For methane production, the NPV shows the most significant sensitivity towards the price of electricity, primarily for the electrolysis section. The selling price of a unit of methane closely follows this. Therefore, the process benefits from allocating incentives and policies to promote producing renewable 'green' methane from curtailed electricity[3]. Likewise, the profitability of methanol production is heavily influenced by electricity prices. The production of methanol shows significant sensitivity towards the employed interest rate. The interest rate deduces the cost of borrowing money for a task. Interest rates are extraneous and mainly subject to stock market conditions, inflation of the economy and governmental monetary policies. The interest rates provide compensation for bearing risk. Therefore the more significant the implied risk from the lender, the larger the interest rate and the lower the NPV. Methanol production shows more susceptibility than methane to interest rates due to the poorer financial performance of the analysed revenue received. This is further reflected in the more extended payback period.

The sensitivity analysis of DME follows the same trend as methane and is thus subject to the same explanation. The selling price of synthetic diesel has the

[3]Note: It is not to be implied that curtailed electricity does not incur a purchase cost.

(a) *Methane*

(b) *Methanol*

Figure 5.1: *Sensitivity analysis assessment of the synthesis of methane and methanol in the base case assessment (Based on the conversion of* 100 t/h *of* CO_2*) and the assumptions listed in Table 5.2..*

(a) *Dimethyl Ether*

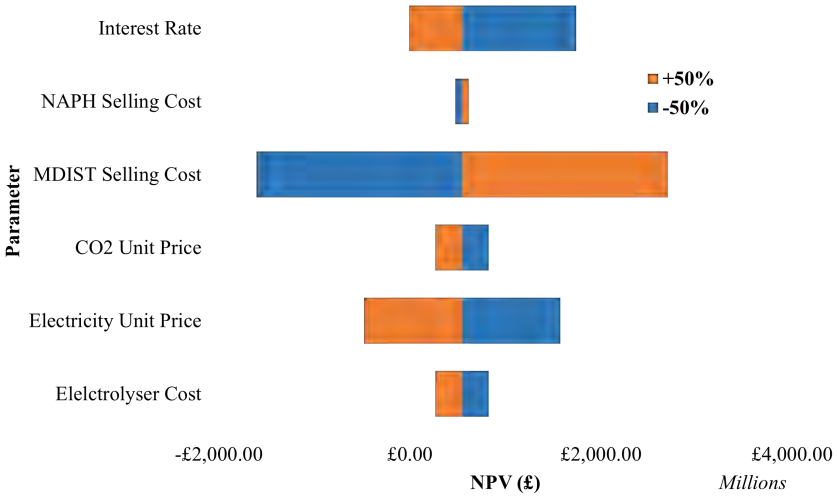

(b) *Fischer-Tropsch*

Figure 5.2: *Sensitivity analysis assessment of the synthesis of dimethyl ether and Fischer-Tropsch liquids in the base case assessment (Based on the conversion of* 100 t/h *of* CO_2*) and the assumptions listed in Table 5.2.*

most influential impact on the NPV. However, it should be noted that the significant variance is primarily due to the current price of road transport diesel at the time of writing (£1.76 per litre, owing to the geo-political situation between Russia and Ukraine).

A multivariate analysis was carried out with the two most influential variables for each fuel synthesis to investigate the impact of their combined influences on the NPV, based on the assumptions listed in Table 5.2. The fuel selling price and the electricity purchase price were considered highly influential in all cases as they significantly impact the operating costs and the revenue generated. Their combined impact on the NPV is analysed and expressed in Figure 5.3 and Figure 5.4.

Under the prescribed parameters, producing methane and DME shows a greater sensitivity to profitability with a variance in the fuel selling price, than with the electricity purchase price. There is, therefore, more margin to operate at lower fuel prices. However, the profitability of producing methanol is more constrained by the variability in the price of electricity. The production of FT liquids shows profitability for all variations in electricity prices up to a fuelling price reduction of up to £0.7 per litre. Finally, the analysis shows that profitability is achieved when the electricity purchase price is reduced by 70%-90% (i.e, £6.8 to £17.4 per MWh), in all cases. It should be noted that fuel surcharges are included in the fuel selling prices, and their isolated variability is not considered in this analysis.

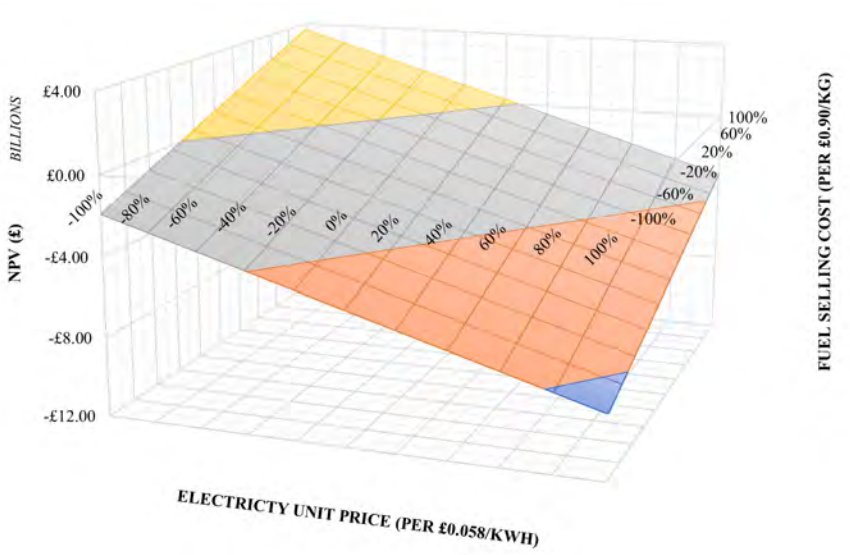

(a) *Methane Production Analysis*

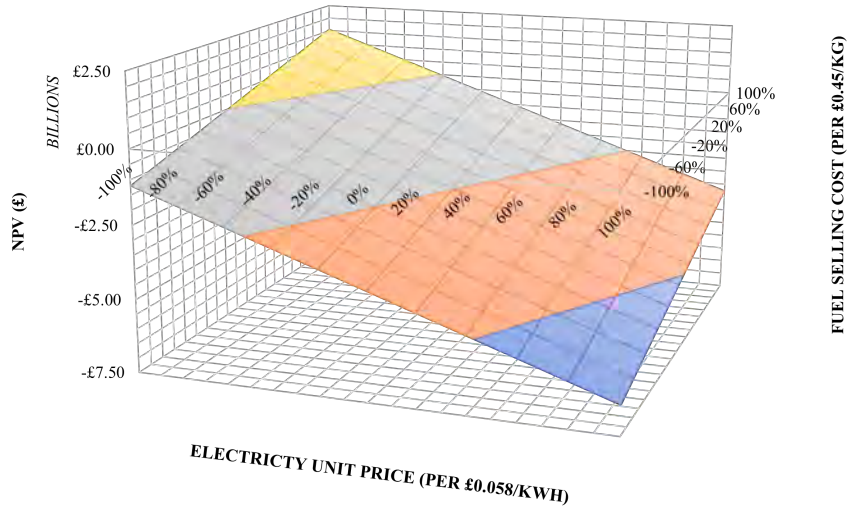

(b) *Methanol Production Analysis*

Figure 5.3: *Multivariate analysis assessment of the synthesis of methane and methanol in the base case assessment - relative to axis values (Based on the conversion of* 100 t/h *of* CO_2*) and the assumptions listed in Table 5.2.*

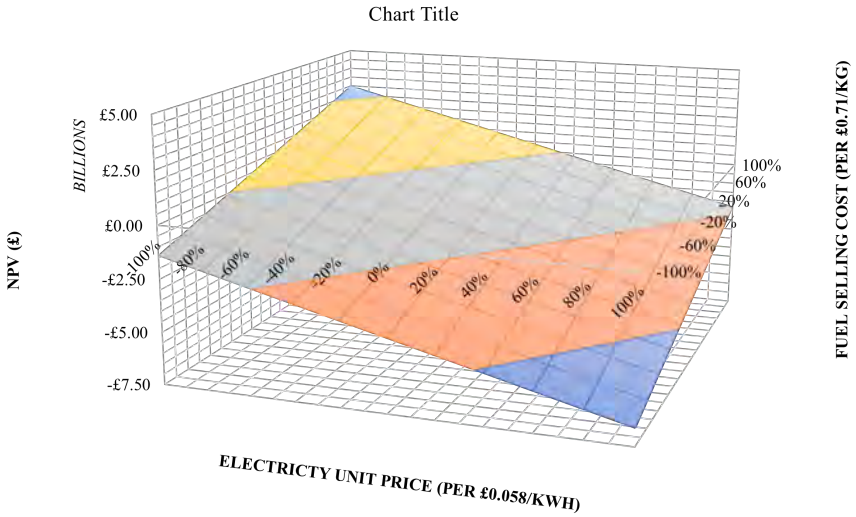

(a) *Dimethyl Ether Production Analysis*

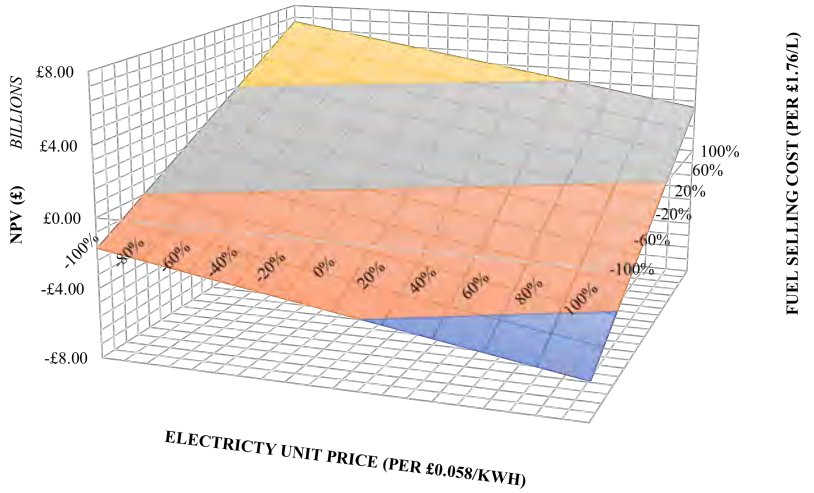

(b) *FT Liquids Production Analysis*

Figure 5.4: *Multivariate analysis assessment of the synthesis of methane and methanol in the base case assessment - relative to axis values (Based on the conversion of* 100 t/h *of* CO_2*) and the assumptions listed in Table 5.2.*

5.3.2 Uncertainty Analysis

While the output of the sensitivity analyses is important to improve the inventory data for assessing the impact of change to input parameters, the results are merely indicative and still depend on the set of baseline assumptions. A degree of uncertainty resulting from a lack of confidence in knowledge about the future specific values of the influential parameters in the assessment context still exists. Uncertainty analysis can address more prognostic questions of future developments. A probabilistic uncertainty analysis was conducted in this study by Monte Carlo simulations using the NPV on Microsoft Excel. Probability distribution functions (PDF), $\mathbb{P}_X$ were assigned to input parameters $\mathbf{X} = (X_1, \ldots, X_n)$, to generate an estimated probability distribution of output variables $\mathbf{Y} = (Y_1, \ldots, Y_n) = g(\mathbf{X})$. A cumulative distribution function, $F_Y(y) = \int f_Y(y)$ could be realised as a further output.

A key challenge in this methodology was characterising the selected input parameters and their respective PDFs. The guideline devised by Hawer et al. [328] was used to quantify the PDFs uncertainty input variables as shown in Figure 5.5.

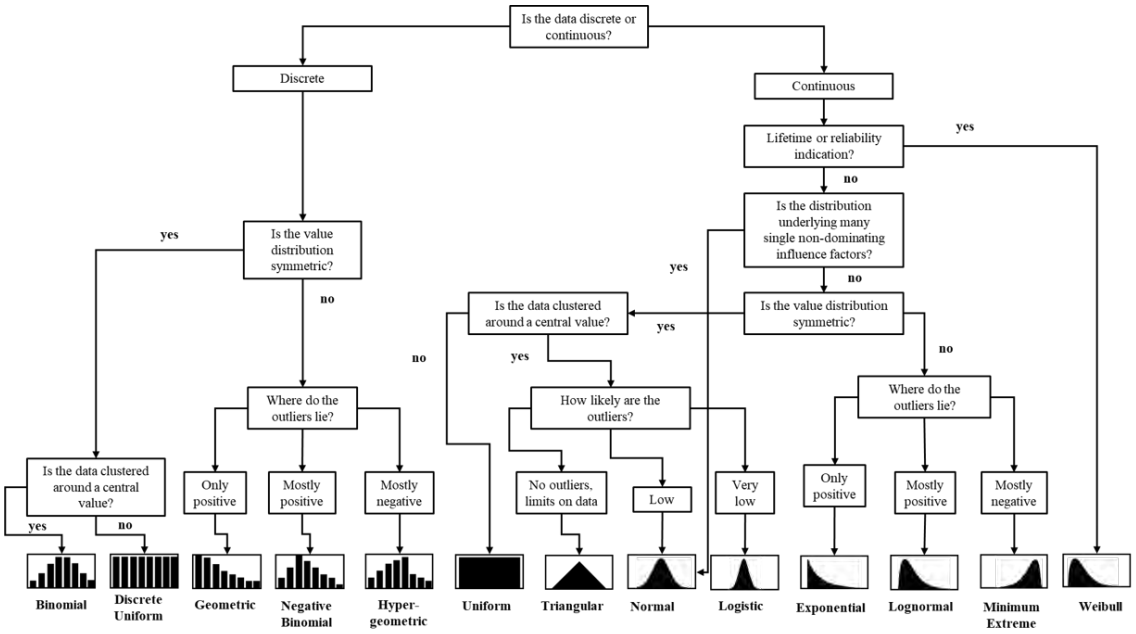

Figure 5.5: *Guideline for the classification and quantification of uncertainty (modified), based on Hawer et al. [328].*

The key parameters evaluated in the uncertainty analysis assessment, their associated PDFs and characteristics are summarised in Table 5.4. A normal distribution was considered for the variation of interest rates. Normal distributions are useful for very characterised systems due to the central limit theorem [4]. CAPEX costs were analysed using a Beta distribution based to model a set of bounded random variables using previous experiences. The normalisation constants applied in this assessment were obtained from [329]. A triangular distribution was used to describe the limits of operational hours. A discrete distribution was used to model perceived or possible pricing options as related to the implementation of carbon taxes/credits. Bernoulli distribution is a discrete distribution where random variables are limited to two outcomes. For sources of high purity CO_2, a Bernoulli distribution was applied to depict the possibility of obtaining the carbon dioxide for free or for a feedstock price. This was further coupled with a normal distribution to obtain the final purchase price. A lognormal distribution is used instead of a normal distribution to eliminate the propensities to extremely low or negative electricity prices as they are deemed unrealistic for this assessment.

[4]The central limit theorem dictates that a sample becomes normally distributed as the data size gets larger

Table 5.4: *Description of statistical distributions used in the present study.*

Parameter	Distribution	μ [a]	σ [b]	Comments
Interest rate	Normal	100%	10%	
Operational hours	Triangular	-	-	Min = 50%, Max = 110%
SOEC Unit CAPEX	Beta	100%	-	Min = 70%, Max = 150%
				α^{c}= 2, β^{c}= 3
CO_2 purchase price	Discrete	-	-	No carbon tax = 50%
				Carbon tax = 20%
Electricity purchase price	Lognormal	100%	10%	
Fuel selling price	Uniform	-	-	Min = 100%, Max = 200%

[a] Mean

[b] Standard deviation

[c] Beta distribution constants

Due to the impacts of the ongoing geopolitical dispute between Russia and Ukraine and the current fuel duty[5] imposed in the UK, coinciding with the COVID-19 pandemic, a maximum fuel selling price of 200% is assumed for this analysis in a uniform distribution.

A Monte Carlo simulation model is set up via a macro on Microsoft Excel to run at least 10,000 simulations. A confidence interval (CI) (Equation (5.2)) of 95% is used to measure the degree of uncertainty within the provided sample.

$$CI = \bar{x} \pm z \times \frac{s}{\sqrt{n}} \tag{5.2}$$

Where $\bar{X}$ is the sample mean, Z is the confidence level value, s is the sample standard deviation and n is the sample size.

[5] £0.579 per litre at the time of writing

The impact of uncertainties on the NPV after a 20-year period was assessed from results following the global sensitivity analysis as illustrated in Figures 5.6 to 5.9.

Table 5.5: *NPV results of the Monte Carlo Simulations (10,000 runs per fuel).*

Parameter	Methane	Methanol	DME	FT-L
Mean (m£)	31.1	-1364.2	-459.9	2496.4
Minimum (m£)	-144.1	-5.619.6	-4502.1	-464.8
Maximum (m£)	173.9	716.9	2581.9	8257.6
Low CI (m£)	30.4	-1378.9	-476.6	2470.5
High CI (m£)	31.9	-1349.5	-443.4	2522.4
Probability of loss (%)	20.7	98.0	70.8	0.5

Table 5.5 expresses the results obtained from the Monte Carlo simulation analysis, based on the assumptions made in Table 5.4. The range of values between the low and high confidence intervals indicates the likelihood (at least 95%) of where the calculated values and the true mean of the data will lie within the confines of the prescribed parameter. The probability of loss was calculated to assess the likelihood of a profitable investment.

The Monte Carlo analysis seeks to indicate the degree of profitability as a key economic indicator in the economic analysis as prescribed in this chapter while taking uncertainty and variabilities into account. The result, therefore, provides the likelihood of investment risk within the confines of the allocated parameters.

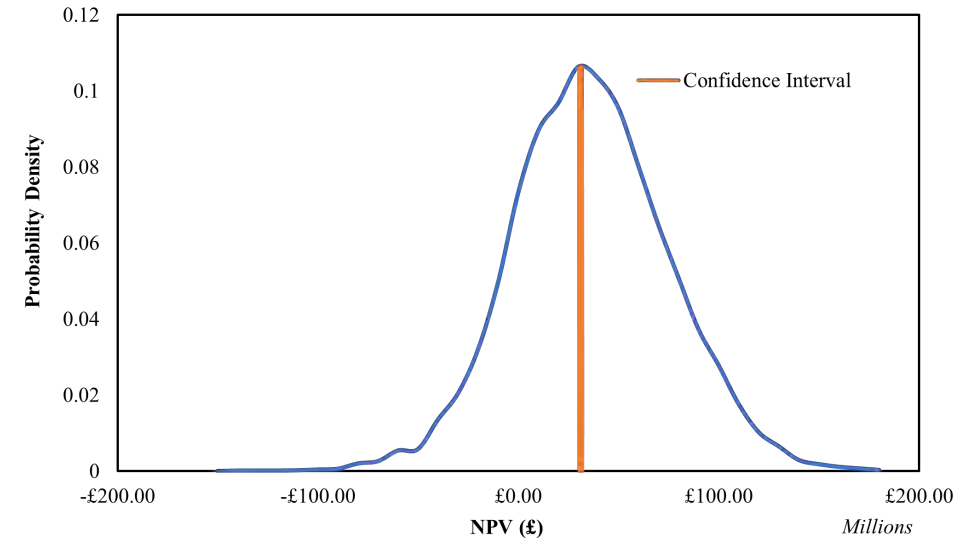

(a) *Probability Density*

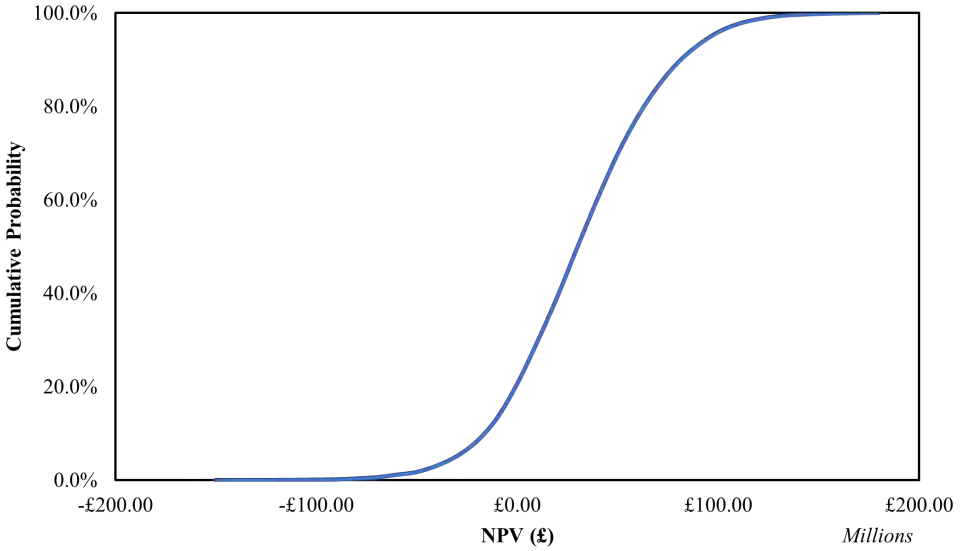

(b) *Cumulative Probability*

Figure 5.6: *Probability Distribution from global sensitivity analysis for the methane synthesis plant. NPV based on a 20-year period*

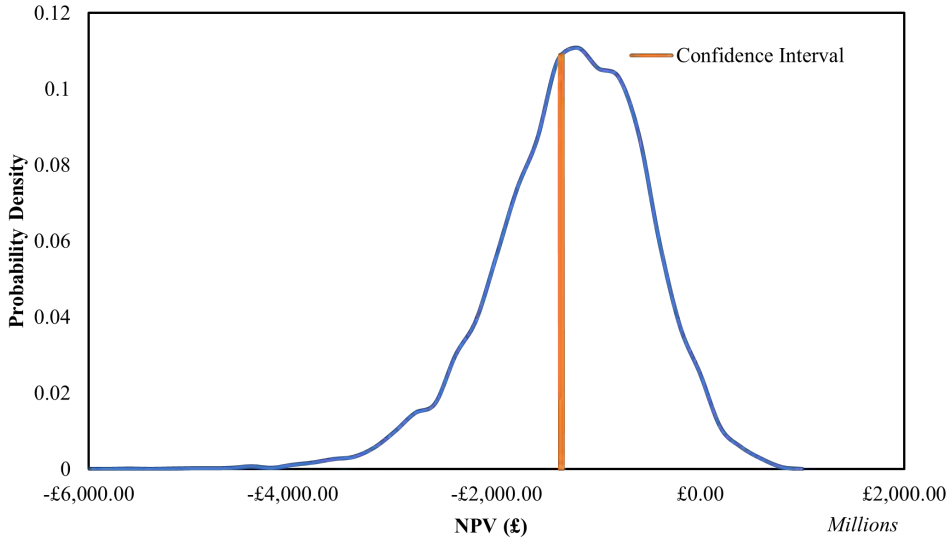

(a) *Probability Density*

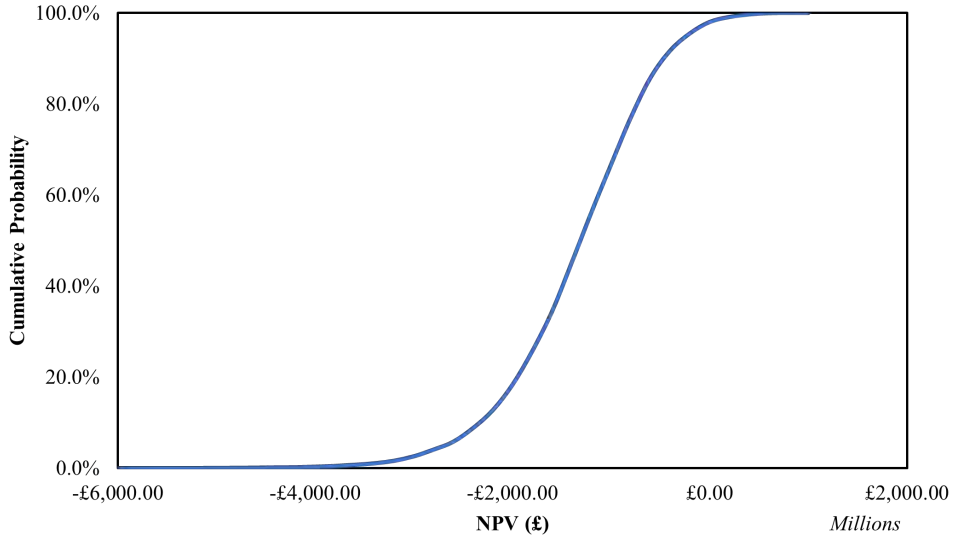

(b) *Cumulative Probability*

Figure 5.7: *Probability Distribution from global sensitivity analysis for the methanol synthesis plant. NPV based on a 20-year period*

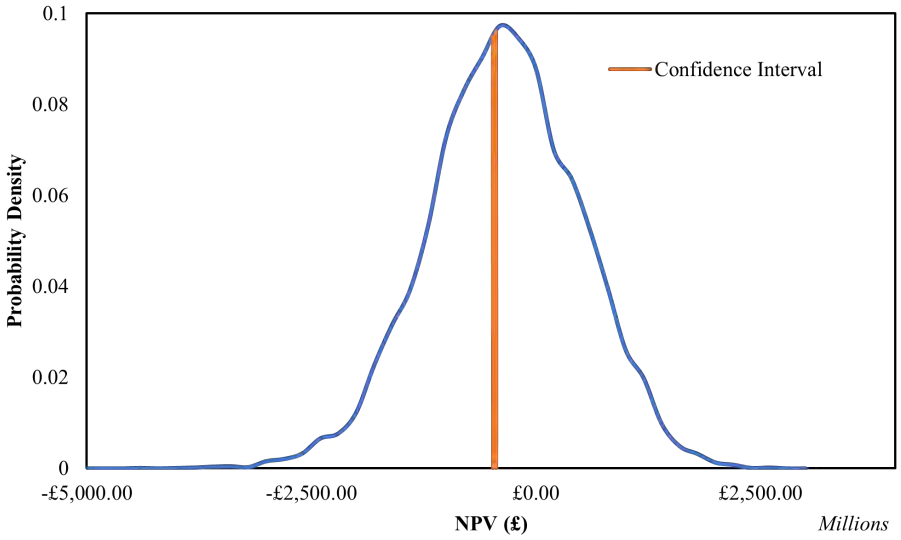

(a) *Probability Density*

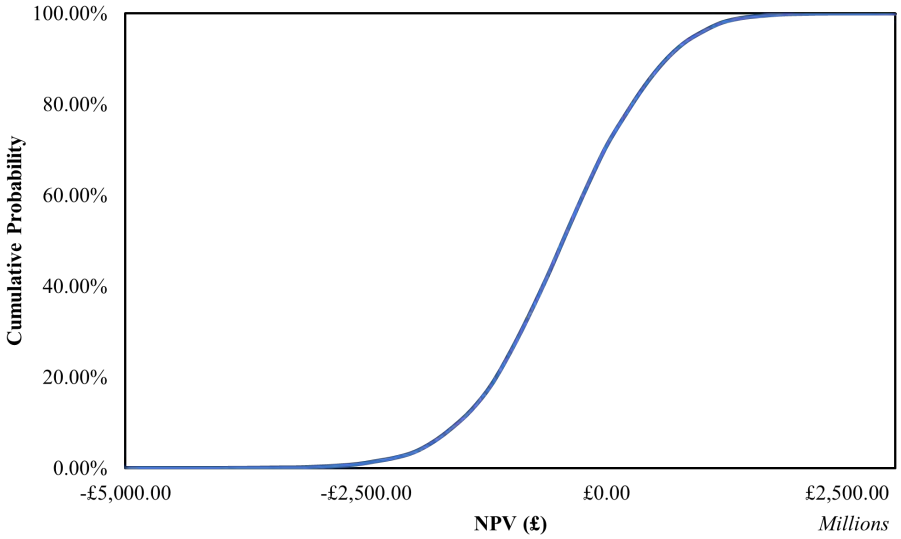

(b) *Cumulative Probability*

Figure 5.8: *Probability Distribution from global sensitivity analysis for the dimethyl ether synthesis plant. The NPV is based on a 20-year operating period.*

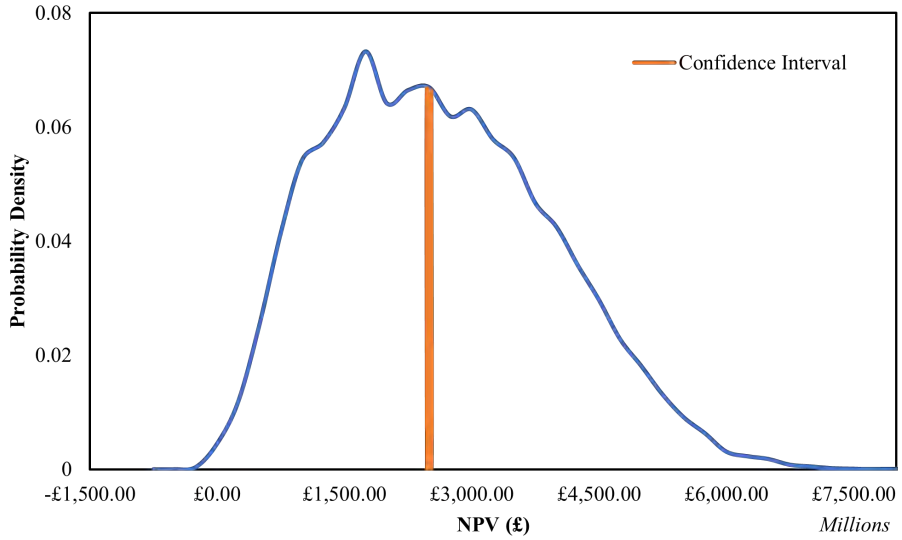

(a) *Probability Density*

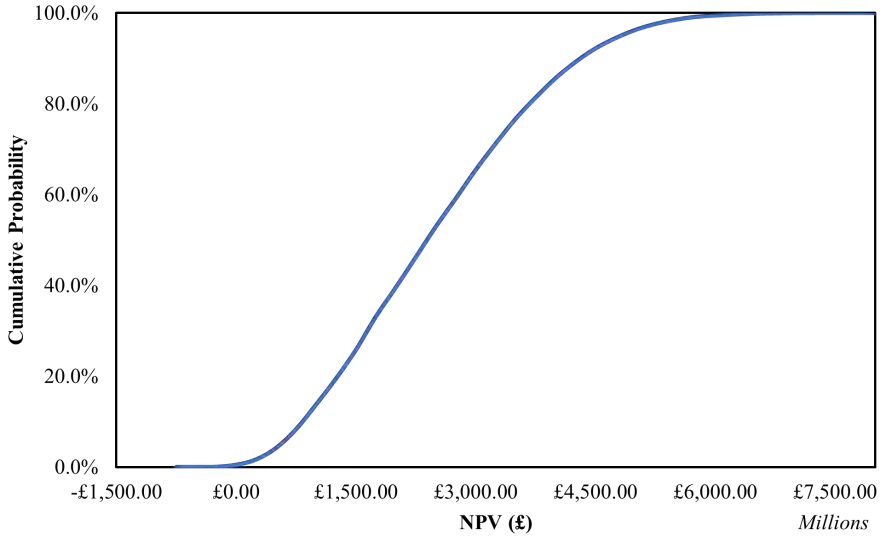

(b) *Cumulative Probability*

Figure 5.9: *Probability Distribution from global sensitivity analysis for the Fischer-Tropsch fuels synthesis plant. The NPV is based on a 20-year operating period.*

Under the assumptions stated in Table 5.4, the probability density results are expressed as a bell-shaped curve, similar to a normal distribution. The cumulative probability curves are reflective results of the former, providing probabilities for an observation that will be less than or equal to the value specified.

The results show that producing synthetic diesel and methane has the lowest investment risks, with confidence intervals in positive NPV values. Methanol presents the highest investment risks and should thus be considered unprofitable under the presented assumptions. The irregularity in the uncertainty analysis curve of synthetic diesel can be attributed to the additional and combined effects of the naphtha by-product and the diesel fraction, as considered in the analysis.

5.4 Chapter Discussion

The overarching goal of this techno-economic study was to assess the economic performance of synthetic fuel production by hydrogenating carbon dioxide. The scope of the economic study spanned from the receipt of renewably-sourced electricity (from Scotland, as stated in Chapter 4) and carbon dioxide from various sources across the United Kingdom, up to the production of the fuels. The analysis was based on a chemical plant size that valorises 100 t/h of CO_2.

The performance indicators from the techno-economic analysis based on the modelled plant configurations and economic assumptions indicate that synthetic diesel and methane production are the most profitable. The performance of the former can be attributed to the global economic and geopolitical situation at the time of the study by way of the relatively higher fuel selling price. And in cases where the selling price of diesel is reduced by 50%, it still fares better than the rest (referring to the base case.).

The results presented in this analysis are expressed as a range of values rather than unique values in time. This is done to account for fluctuation in variables such as fuel and commodity prices, market trends and uncertainties that are not easily predicted.

Chapter 6

SCENARIO AND PERFORMANCE ANALYSIS

Following the previous chapter, the use and application of the analysed data are put into the context as described in the introductory chapters. The questions of "What are the prospects of these technologies?" and "What can we achieve in the prescribed time frame" are considered in this section of the study.

This section presents an opportunity also to consider analysis from an energetic perspective. The results of this chapter will seek to address efficiency-related questions and emission intensity at the vehicle tailpipe. Furthermore, this section will highlight areas where more research can be done to understand the opportunities for energy reduction along the production chain.

6.1 Goal of the Scenario and Performance Analysis

The goal of this part of the thesis is to give an indication of how well synthetic fuels will support the transition to Net Zero in the transport system. The scenario assessed is that of a slow progression of CCS technologies towards being part of a Net Zero energy system. In this scenario, the ban on the sale of petrol and diesel vehicles by 2030 and all non-zero emission vehicles by 2035 in the United Kingdom is expected to be enforced[1]. Nevertheless, it is assumed that the deployment of CCS technologies will not be available at scale towards and by 2050. It is assumed that not even carbon sequestration by afforestation will be sufficient and feasible on a large enough scale to support the net-zero targets

[1]Fuel cell and battery vehicles are not considered in this analysis due to their small share in the number of operable vehicles in the United Kingdom. However, their impacts are briefly discussed in further chapters in this work.

6.2 Scenario Analysis Methodology

To determine the demand for fuel for road transportation in 2030, the historical data on the registration of newly purchased vehicles and licensed vehicles in the United Kingdom were analysed. The historical data was collated from BEIS to maintain consistency with the various sections of this study. The data series were analysed to forecast the number of fossil fuel propulsion-engine vehicles that will be manufactured, on sale in the United Kingdom and legally licensed for road usage. Due to the inconsistency in the trend resulting from limitations caused by the COVID-19 pandemic, the historical data was considered up to 2019 not to thwart the analysis of the COVID-19 year peculiarities.

The Holt method was used to generate a forecast on the production and the probable number of road vehicles considering historical data from 2000 to 2019. The Holt method uses a double exponential smoothing factor to account for changes in levels and trends in the absence of seasonality. The predicted data, $\hat{y}$ (Equation (6.3)) is obtained from the level (l_x); of the series (y_x) in time, (Equation (6.1)) and the smoothed data trend. b_x (Equation (6.2)).

$$l_x = \alpha \cdot y_x + (1 - \alpha) \cdot (l_{x-1} + b_{x-1}) \tag{6.1}$$

$$b_n = \beta \cdot (l_x - l_{x-1}) + (1 - \beta) \cdot b_x \tag{6.2}$$

$$\hat{y}_{x+k} = l_x + b_x \cdot k \tag{6.3}$$

Where α and β are the smoothing factors, the two smoothing factors are optimised using two forecasting error measures: the root mean squared error

(Equation (6.4)) and the mean absolute percentage error (Equation (6.5)), from n data samples.

$$RSME = \sqrt{\sum_{x=1}^{n} \cdot \frac{(\hat{y}_x - y_x)^2}{n}} \tag{6.4}$$

$$MAPE = \frac{1}{n} \cdot \sum_{x=1}^{n} \cdot \frac{|(y_x - \hat{y}_x)|}{y_x} \cdot 100 \tag{6.5}$$

Following the initial analysis, the data showed that up to 93% of the newly registered road vehicles were driven by internal combustion engines (ICE) powered by diesel or gasoline, of which 79% were registered as cars. Based on average fuel consumption of 5.40 l/100km [330] for all road vehicles, a heating value of 45 MJ for petrol and diesel fuels and, annual mileage of 10000 miles per year, the fuel demand forecast is illustrated in Figure 6.1.

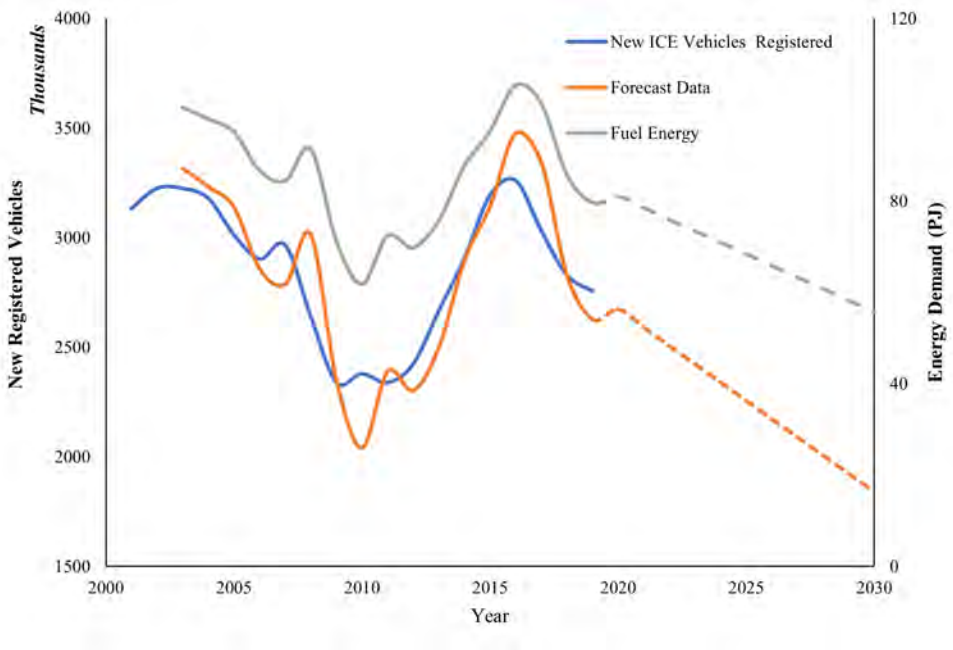

Figure 6.1: *Historical data and forecast data of newly registered road vehicles in the United Kingdom up to 2030, including fuel demand.*

The dip in the registrations of new vehicles in Figure 6.1 is attributed to the 2008-2010 automotive industry crisis, caused by the 2007-2008 financial crisis and, subsequently, the Great Recession in the United Kingdom.

Data for the newly registered vehicles and fuel consumption [330] over the last 20 years is used in conjunction with Equation (6.1) to Equation (6.5) to forecast the number of newly registered ICE vehicles cars until 2030. Figure 6.1 shows that the forecast fuel demand (55.75 PJ per year) for the newly registered vehicles is significantly higher than the amount available from the annual conversion of 100 t h^{-1} of CO_2 by a single plant (equivalent to the total amount of 'green, carbon assessed in Chapter 4), as shown in Table 6.1. As the heat of evaporation of water cannot be recovered in the fuel consumption of the engines, the energy is given in terms of its lower heating value. Therefore, it is proposed to consider the regional demand of Scotland due to its proximity to point sources of high purity CO_2 described in Chapter 4 and renewable electricity.

Table 6.1: *Annual energy content of synthetic fuels based on a plant valorisation of 100 tonnes of CO_2 per hour in PJ.*

Methane	Methanol	DME	FT-L
14.97	5.64	8.44	1.28 (0.88)

Figure 6.2 shows that the fuel demand forecast for newly registered vehicles up to 2030 in Scotland is around 3.90 PJ per year. The reason for the peculiar shape of the graph is the same for the previous vehicle registration data. A subsequent analysis for the total amount of road vehicles in operation in Scotland, taking into account the de-registered vehicles taken off the road and the 'legacy'[2] vehicles, showed that a fuel demand of 82.59 PJ will be required per year from 2030.

The results show that the fuels synthesised (excluding Fischer-Tropsch

[2]Legacy vehicles refer to legally licenced road vehicles that are currently in operation (at the time of writing)

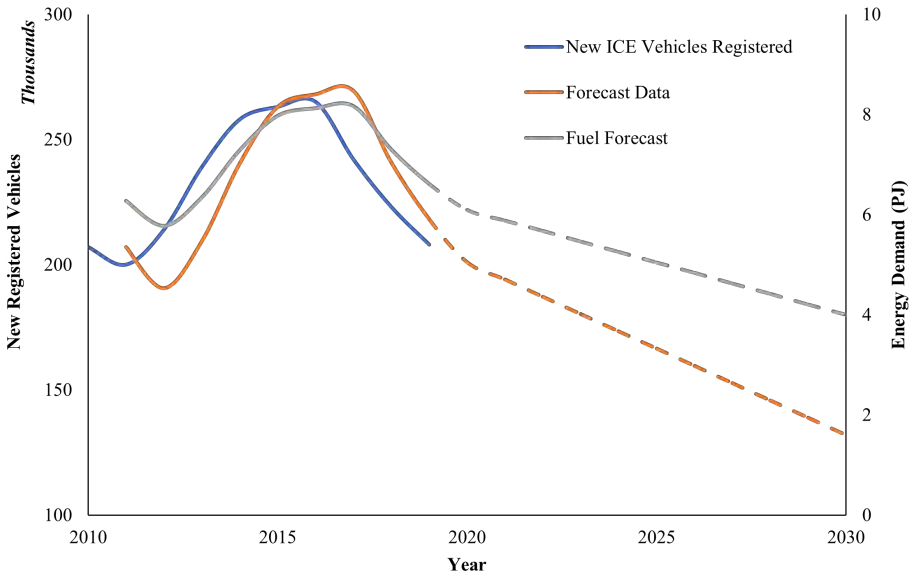

Figure 6.2: *Historical data and forecast data of newly registered road vehicles in Scotland up to 2030, including fuel demand [317].*

diesel) from CO_2 derived from whiskey distilleries in Scotland and the upgrade of biomethane are sufficient to cover the fuel demand for newly registered vehicles in the Scottish region, from 54% (for synthetic diesel) to 375% (from methane). The analysis also shows that multiple or higher capacity plants may be required to cover the total fuel demand in Scotland. It should be noted that efficiency losses during fuel conversion in the absence of engine modifications are not taken into account.

6.3 Multi-plant Analysis

Analysis from Chapter 5 showed the influential impact of the unit price of electricity on the economic performance of the synthetic fuel systems. Given the potential of CO_2 assessed in Chapter 4, it is important to consider the potential of renewable electricity available for the process as a potential bottleneck.

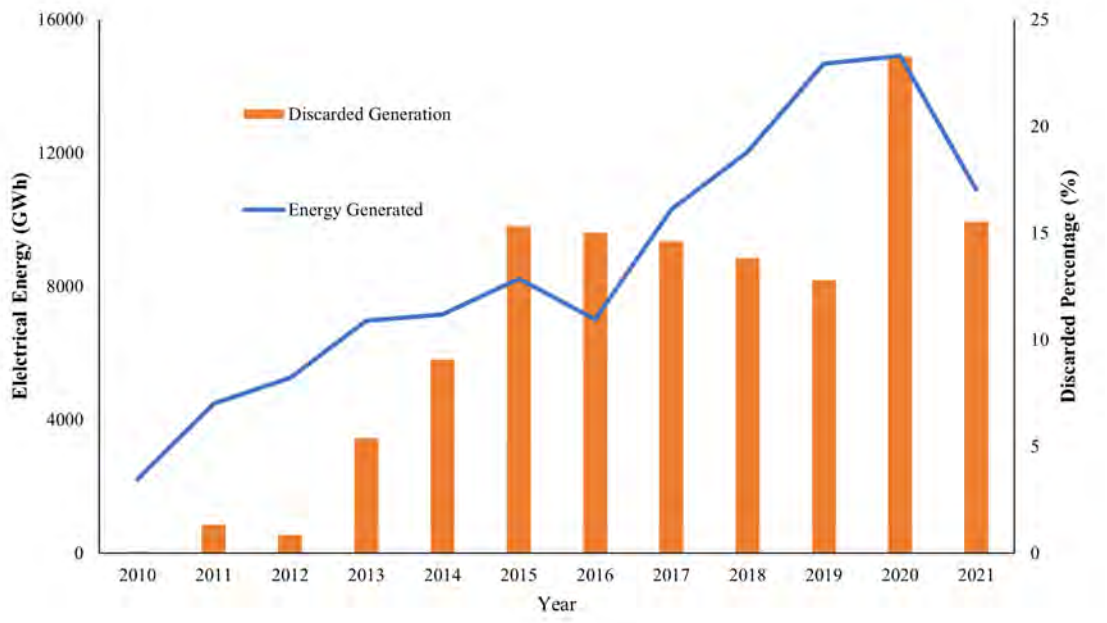

Figure 6.3: *Historical data of curtailed generation and constraint payments in the United Kingdom. Data collected from [317].*

When a situation arises such that a transmission network is unable to transfer power between the points of generation and demand due to physical limitations, the power generation node is advised to cease production by the system operators. This is referred to as electricity curtailment, a control mechanism to manage power flows and system stability of the power network. Power generators are remunerated with constraint payments for their temporary exclusion from the power market.

Figure 6.3 illustrates the amount of wind energy discarded due to the

failure of the Western Link[3] and output curtailment due to the inadequacy of the grid to accommodate the energy produced. Currently, the curtailed generation is proportional to the amount generated, which is expected to increase with the proposed wind capacity in Scotland.

Table 6.2: *The proposed and total Scottish onshore and offshore wind energy programmes.*

Capacity	**Onshore** (MW)	**Offshore** (MW)	**Combined** (MW)
Operational	8,440	1,892	10,332
Under construction	430	1,948	2,378
Consented	4,640	2,362	7,002
Leased awaiting consent	-	4,250	4,250
ScotWind auction 2022	-	24,826	24,826
Repowering and Extensions	11,320[a]	-	11,320
Imminent auctions	-	6,000[b]	6,000
Total	24,830	41,278	66,108

[a] includes 10,000 MW repowering old wind farms and 1,320 MW extensions to wind farms.

[b] includes 1,500 MW ScotWind re-auction and 4,500 MW INTOG auction.

Table 6.2 shows that the proposed wind energy capacity in Scotland could reach up to 66 000 MW by 2030, which is a magnitude greater than the peak demand of 5500 MW [331]. Therefore, a significant proportion of wind energy will be discarded in the absence of electrical grid reinforcement. Additionally, the average constraint payments to wind farms are significantly higher at 70 £/MWh than the average price of electricity at a rate of 58 £/MWh. The storage and utilisation of excess renewable electricity provide an opportunity to reduce the annual constraint payments.

In order to estimate the cost and capacity of subsequent plants, N-th plant economics will be applied in the following section. The viability and future cost

[3]The Western Link is high voltage direct current cable that runs from the west coast of Scotland to Wales

competitiveness is assessed by using a hybridised costing method: a bottom-up approach to estimate the first-of-its-kind (FOAK) system and an experience learning curve to estimate the future costs of subsequent Nth-of-its-kind (NOAK) systems, at commercial scales. It should be noted henceforth that NOAK values are qualified as projected capital cost values rather than absolute capital cost values.

FOAK systems represent plants that are yet to be widely commercialised; therefore, careful consideration must be taken in their description as they tend to be oversized and with redundant equipment in initial design phases. The systems are divided into major technology systems: CO_2 capture and compression, electrolysis section, and fuel synthesis. See Equation (6.6).

$$R_{\text{composite}} = \sum_{i} \left[R_{\text{system element},i} \cdot \frac{TPC_{\text{system element}}}{TPC_{\text{overall system}}} \right] \tag{6.6}$$

where TPC (total project cost) is described as:

$$TPC_i = TDC \cdot (1 + f_{indirect}) \cdot (1 + f_{process} + f_{project}) \tag{6.7}$$

TDC is the total direct costs. $f_{indirect}$ relates to the expenditures such as service facilities, engineering and consultancy costs. $f_{process}$ describes the additional costs incurred to offset the uncertainties from the development status of the technology as it relates to the maturity level, while $f_{project}$ describes additional site-specific costs.

Technology-specific learning rates (R_x), are applied to individual plant sections to obtain prospective plant costs expressed by Equation (6.8).

$$TPC_{\text{NOAK}} = TPC_{\text{FOAK}} \cdot N^{-b} \tag{6.8}$$

where b is described as:

$$b = \frac{log(1 - R)}{log(2)} \tag{6.9}$$

Where TPC_i is the total plant cost, N is the number of plants to be constructed and, b is the learning rate exponent. The values for the input variables are shown in Table 6.3.

Table 6.3: *Assumed indirect costs, contingencies, and learning rates for system elements*

	CO_2 C & C.[a]	**SOE**	**Fuel Synthesis**	**Ref.**
R_{sys}, %	10	20	3 - 5	[332]
$f_{indirect}$	14	17	-	$(a.o.e)$
$f_{process}$	28	35	-	$(a.o.e)$
$f_{project}$	35	30	-	$(a.o.e)$

[a] carbon capture and compression

a.o.e - Author's own estimations and judgements based on various literature research.

Where uncertain, the values are assumed based on the author's own research and opinion of the TRL of the system elements.

A TDC of £145 per tonne of CO_2 was prescribed for the carbon capture and compression system and an electrolyser system cost of £800 per kilowatt for the following evaluation. A sensitivity range of ±10% was used to assess the impacts of varying TDCs. The results of the analysis (N_{max} = 43 100 t/h plants)[4] are shown in Figure 6.4 and Figure 6.5.

[4]This is based on the total available CO_2 stock estimated in Chapter 4.

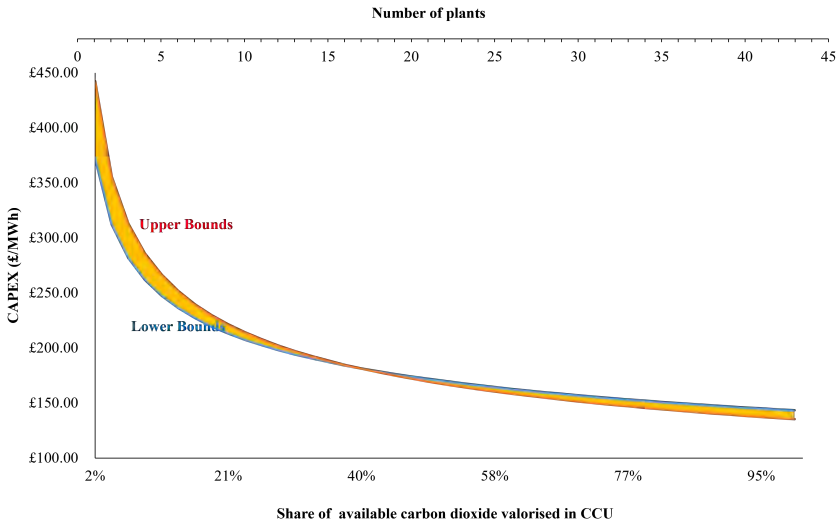

(a) *Methane with R-bounds (16.13% to 19.62%). Electrolyser share bound limits (72% to 88%).*

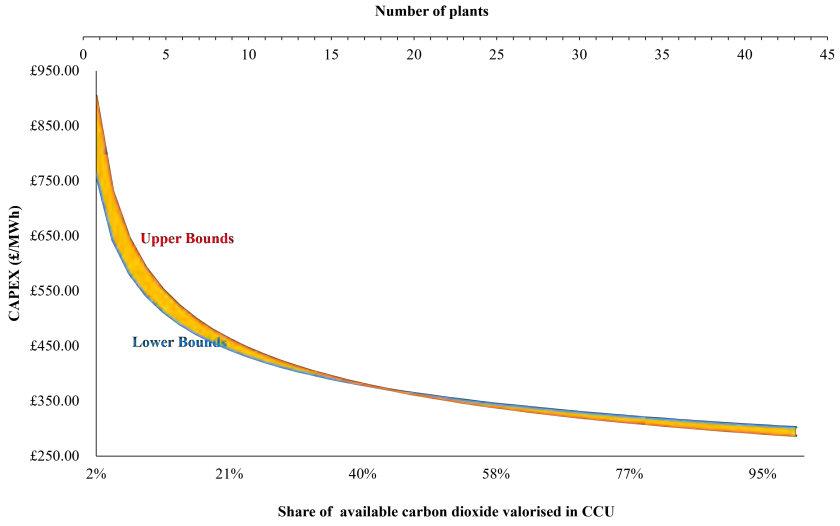

(b) *Methanol with R-bounds (15.68% to 19.06%). Electrolyser share bound limits (68% to 83%).*

Figure 6.4: *Technology learning curves for synthetic fuel capital costs and a TDC sensitivity range of* $\pm 10\%$.

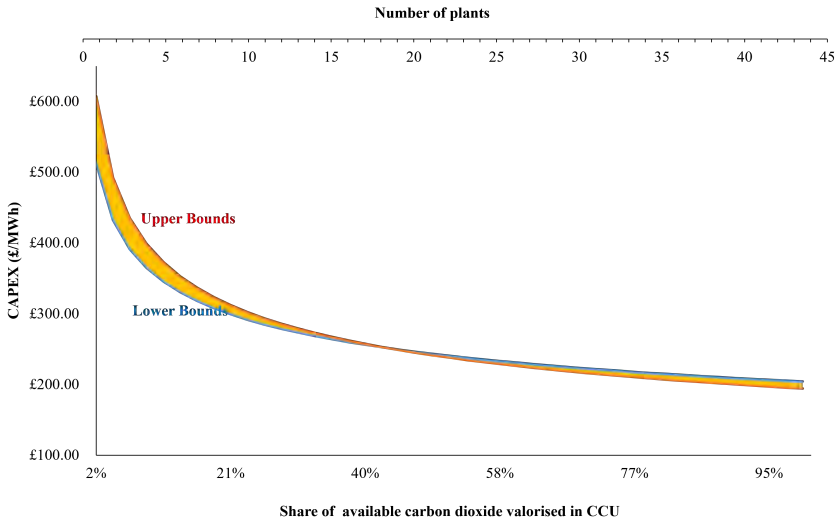

(a) *DME with R-bounds (15.6% to 18.95%). Electrolyser share bound limits (67% to 82%).*

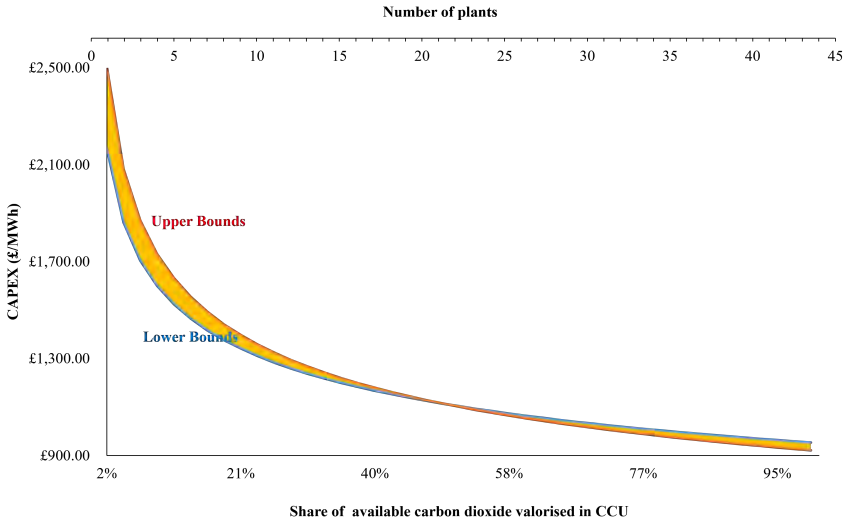

(b) *FT-synfuels with R-bounds14.03% to 16.82%). Electrolyser share bound limits (55% to 67%).*

Figure 6.5: *Technology learning curves for synthetic fuel capital costs and a TDC sensitivity range of* $\pm 10\,\%$.

The results of the the multi-plant analysis are expressed in Figure 6.4 and Figure 6.5. The analysis shows that the CAPEX (upper and lower bounds) of constructing similar plants with the capacity of valorising 100 t/h of CO_2 can achieve reduction potentials by 56.2% for methane, 62.5% for methanol, 50% for DME and 56.3% for synthetic diesel production.

Following an economic assessment, this section presents an opportunity also to consider analysis from an energetic perspective. The results of this chapter will seek to address efficiency-related questions and emission intensity at the vehicle tailpipe. Furthermore, this section will highlight areas where more research can be done to understand the opportunities for energy reduction along the production chain.

6.4 Well-to-Tank analysis

This section describes the impacts from the point of production of the synthetic fuels to the distribution and storage of the fuels at the point of market delivery, i.e., refuel stations.

6.4.1 Distribution to Market

The availability and distribution of electricity as the primary energy carrier in PtX pathways is the first step in describing the overall chain efficiency of the production of synthetic fuels. The electricity considered in this study is derived from sustainable undepletable renewable energy sources (particularly wind energy), so energy efficiency is considered from the initial point of the output of the generator (primary electricity) and therefore set at 100%. The fossil-derived energy used in the manufacture, operation and maintenance of these conversion installations is not considered within the scope of this analysis.

However, transmission and distribution losses are taken into account. Analysis of recent BEIS data suggests that approximately 9% of the electricity produced is lost on the electrical transmission pathway to the customer [259].

6.4.2 Transformation near Market

This section refers to all the conversion processes involved in the production of fuels according to the desired specifications. These processes include the capture of CO_2, the production of syngas via co-electrolysis and the synthesis of fuels.

Carbon Dioxide Capture and Conditioning

The CO_2 required for the processes are recovered from the point sources assessed in Chapter 4. The capture process and purity are further described in Chapter 3. The energy expended in the carbon capture process is $4.19\,\mathrm{MJ/kg_{CO_2}}$ (using MEA absorption processes as described in earlier chapters), with the exception of pure-CO_2 effluent streams which incur not energy expenditure to purify.

The Linde-Hampson process[5] was used to assess the energy expended for the liquefaction of CO_2 for purification and storage. An energy demand of $0.77\,\mathrm{MJ/kg_{CO_2}}$ was determined based on a liquefied condition of 15 bar, for inland road transport.

Syngas Production via Co-electrolysis

The SOE unit was modelled to operate under different feed conditions to account for the varying syngas modulus required downstream of the operation as described in Chapter 3. The energy expended for the syngas production processes was between $1.16\,\mathrm{MJ/MJ_{H_2-CO_x}}$ and $1.25\,\mathrm{MJ/MJ_{H_2-CO_x}}$, depending on the syngas modulus.

Production of Synthetic Fuels

Evaluation of the energy expended in the production of the fuel is directly related to the net inflows of the process required to produce the fuels according to the prescribed specifications, with the model configurations described in Chapter 3.

[5]The Linde-Hampson process is liquefaction process based on the regenerative cooling and compression of gases

As a result of the exothermic nature of the process and the limitation in reactant conversions, electrical power is produced and accounted for here. Extra steam generation is not considered in this analysis due to the complexities associated with heat integration modelling. Any extra steam that could be generated would only be considered by its economic impact as it is not included during the operation of the process. Hence its energetic value is considered inconsequential for this analysis.

The production of 1 MJ (LHV) of methane and DME incurs a total energy expenditure of 0.53 MJ and 0.50 MJ respectively. The energy expenditure for the production of 1MJ of methanol and syn-diesel (including naphtha), is 1.44 MJ and 1.14 MJ respectively. The lower values for methane and DME are due to the higher ratio of generated electricity[6] to the product.

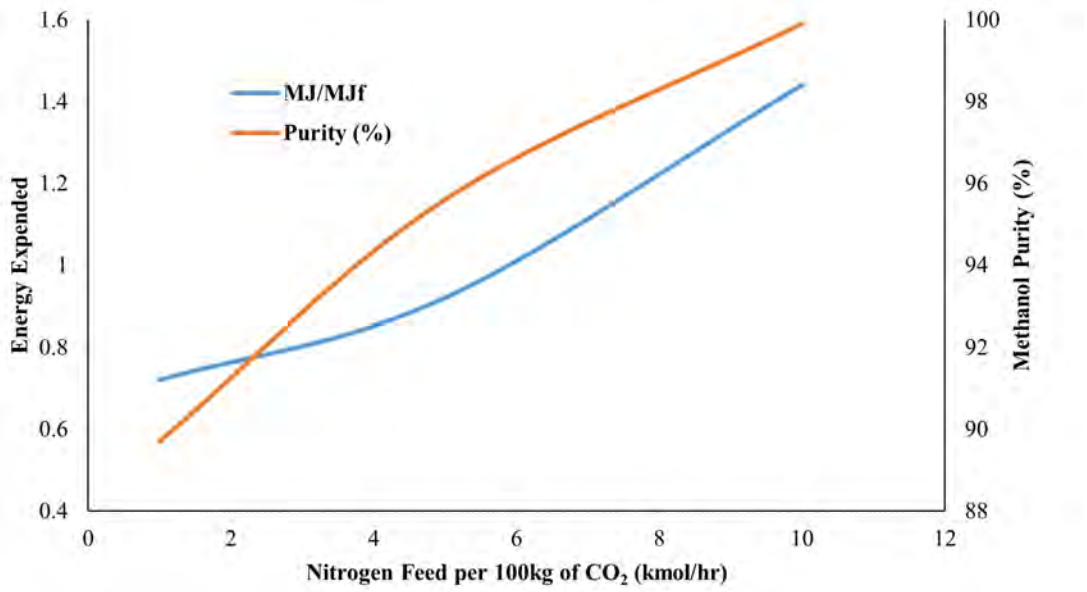

Figure 6.6: *Methanol purity as a function of nitrogen feed and energy expended.*

Figure 6.6 shows the trade-off between the specified purity of methanol and the energy expenditure over varying nitrogen feed flows (to shift the chemical

[6]From the excess heat recovery in process models

equilibrium) in the modelled configuration. This assessment was carried out by varying the flow rate of nitrogen feed flow (used to drive the forward reaction) as a function of the output methanol purity and additional energy requirements on the ASPEN simulation described in an earlier chapter. More primary energy is expended across the process units with an increase in the molar fraction of nitrogen in the system in a bid to increase the product purity. To maintain methodological consistency, the specified purity of over 99% is maintained.

6.4.3 Conditioning and Distribution to Use

This section considers the later stages of deploying synthetic fuels from the point of production to the point of refuelling for end-use in vehicles. The analysis considers short (<150 km) and long-distance (>150 km) distribution within the United Kingdom.

The current pressure standard for compressed natural gas (CNG) vehicle tanks is 200 bar, while the fuel station compressor is set to 250 bar for quick delivery. DME-fuelled vehicles require the fuel to be injected in a liquid phase into the combustion chamber at pressures up to 30 bar to avoid premature vaporisation in the pipe works. The energy required for compression and distribution is obtained from the average of isothermal (Equation (6.10)) and adiabatic (Equation (6.11)) compression duties.

$$E_{iso} = p_0 \cdot V_0 \cdot \log\left(\frac{p_1}{p_0}\right) \tag{6.10}$$

$$E_{adi} = p_0 \cdot V_0 \cdot \frac{\gamma}{\gamma - 1}\left(\left(\frac{p_1}{p_0}\right)^{\frac{\gamma-1}{\gamma}} - 1\right) \tag{6.11}$$

Where p_0, p_1, V_0, γ represent the initial fuel pressure, vehicle tank pressure, fuel volume and the heat capacity ratio of the gases. Figure 6.7 describes the relationship between the compression ratio of the gases and the required energy.

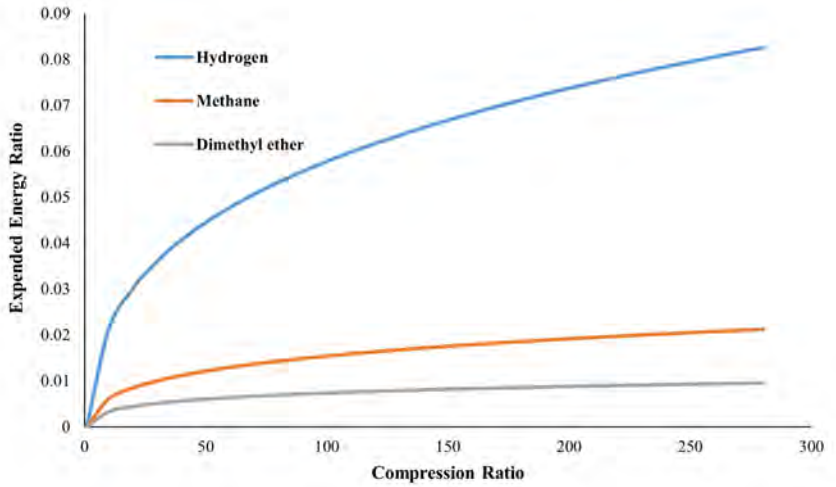

Figure 6.7: *The expended fuel energy in gas as a function of compression ratios. Hydrogen gas is included for reference.*

The analysis of Figure 6.7 shows that the compression process consumes 2.05% and 0.51% of the energy stored in methane and DME, respectively. Methanol and syn-diesel are liquid under standard conditions and thus suitable for storage and distribution without the need for further pressure conditioning.

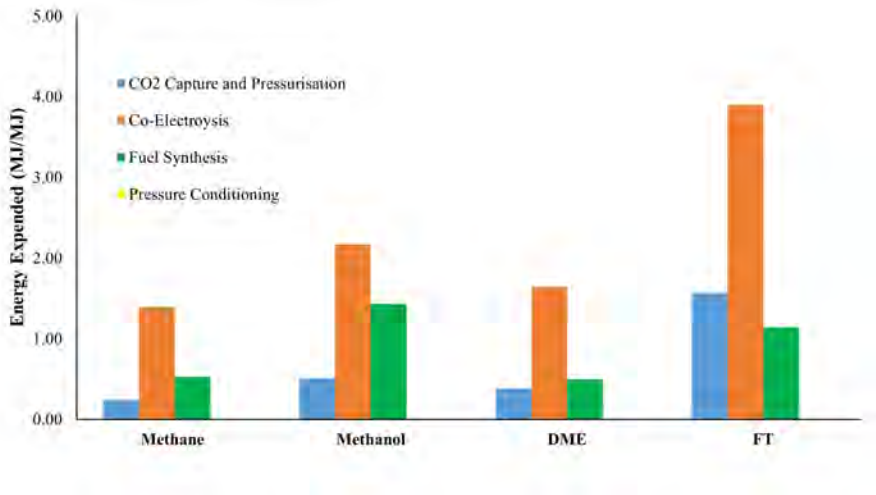

Figure 6.8: *Energy expended to the production of 1 MJ of synthetic fuel.*

The amount of energy required for the production of 1 MJ of synthetic fuels as described is shown in (Figure 6.8). In all cases, the production of syngas via co-electrolysis greatly dominates the production process. The production of synthetic diesels (FT) incurs the largest energy expenditure and this could be attributed to the complexity and selectivity of the desired primary fuel fraction (and resulting by-product) during the production process. The production of methane and DME require the lowest amount of energy as they do not require conditioning during the production process. Despite the further requirement for compression, the overall energy expenditure is less for liquid fuels.

6.5 Tank-to-Metres analysis

The tank-to-metres (TtM) assessment is based on the analysis of data from simulation results with a chassis dynamometer from Hänggi et al. [333] and a chosen drive cycle. The TtM analysis is divided into a wheel-to-metres (WtM) and tank-to-wheels (TtW) approach. The methodology for the WtM analysis is based on the model stated in Guzzella, Sciarretta, et al. [334], which uses a power balance (Equations (6.12) to (6.15)) to estimate the mechanical energy demand for propulsion systems in engines.

$$\bar{F}_a(t) = \frac{1}{x_{tot}} \cdot \frac{1}{2} \cdot \rho_{air} \cdot A_f \cdot c_d \cdot \sum_{i \in trac} \bar{v}_i^3(t) \cdot h \tag{6.12}$$

$$\bar{F}_r(t) = \frac{1}{x_{tot}} \cdot m_v \cdot g \cdot c_r \cdot \sum_{i \in trac} \bar{v}_i \cdot h \tag{6.13}$$

$$\bar{F}_{acc}(t) = \frac{1}{x_{tot}} \cdot m_v \cdot \sum_{i \in trac} \bar{a}_i(t) \cdot \bar{v}_i(t) \cdot h \tag{6.14}$$

$$\bar{F}_w(t) = \bar{F}_a(t) + \bar{F}_r(t) + \bar{F}_{acc}(t) \tag{6.15}$$

Where $\bar{F}_i$ is the tractive force with respect to power loss due to aerodynamic drag (a), rolling friction (r) and acceleration (acc). A_f is the vehicle frontal area, c_d is the aerodynamic drag coefficient, c_r is the rolling friction coefficient, and m_v is the mass of the vehicle. The worldwide harmonized light vehicles class 3 test cycle (WLTC class 3) Figure 6.9 is used to obtain the average energy consumed per distance travelled, using speed profiles x_i, $\bar{v}$ and $\bar{a}$. Based on a vehicle mass of 1450 kg ([330], the average energy demand is 0.42 MJ/km.

The data from the WtM analysis are used to obtain the TtW values is

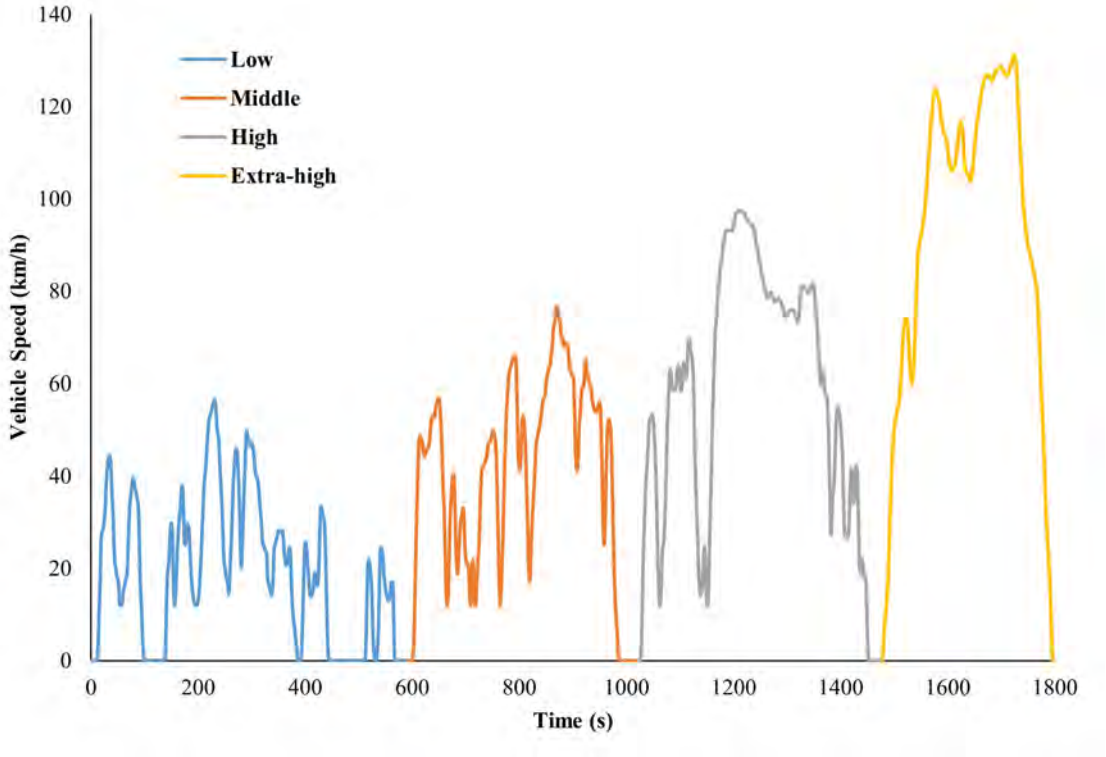

Figure 6.9: *WLTP test cycle profile [335]*

obtained from the work of Hänggi et al. [333], which used the chassis dynamometer measurements of 14 EURO-6b passenger car types to evaluate the propulsion system model parameters ($c_{1,pos}$, $c_{0,pos}$, $c_{1,neg}$, $c_{0,neg}$) used in Equation (6.17) and Equation (6.18).

$$P_w(t) = \bar{F}_w \cdot \bar{v}_i(t) \tag{6.16}$$

$$P_c(t) = \begin{cases} c_{1,pos} \cdot P_w(t) + c_{1,pos}, & P_w(t) \geq 0 \\ c_{1,neg} \cdot P_w(t) + c_{1,neg}, & P_w(t) < 0 \end{cases} \tag{6.17}$$

$$\eta_{TtW}(t) = \begin{cases} \frac{P_{w(t)}}{P_c(t)}, & P_w(t) \geq 0 \\ max\left(0, \frac{P_{w(t)}}{P_c(t)}\right), & P_w(t) < 0 \end{cases} \tag{6.18}$$

Where P_c is the chemical power of the fuel stored in the vehicle tank and η_{TtW} is the ratio of the former with the wheel power P_w. It should be stated that the authors assumed that methanol and methane vehicles perform equally, while Fischer-Tropsch (FT) diesel and DME powertrains perform equally. The TtW values are 1.94 MJ/km for methanol and methane, and 1.91 MJ/km for FT diesel and DME respectively.

Recent work by A. Huss [336] based on the future technical development of passenger cars in Europe (from 2025 onwards) showed an energy consumption of 1.37 MJ/km to 1.42 MJ/km for spark ignition engines and 1.29 MJ/km to 1.31 MJ/km for compression ignition engines with the WLTC class 3 procedure. These values will be used in this study onward. A value of 0.70 MJ/km is used as a reference for hydrogen fuel cell-driven vehicles [337]. Figure 6.10 shows the WTW efficiencies of the analysed processed chain.

The analysis shows that the pathway for producing methane and DME for ICE vehicles is more efficient than methanol and synthetic diesel, despite their extra requirement for compression at the point of use. Due to the variability of the model configurations, the analysis indicates an opportunity to improve the overall system opportunities during the phase of fuel synthesis. The production of syngas via solid-oxide co-electrolysis, presents another opportunity, given its current TRL.

Figure 6.10: *Calculated WTW efficiencies of the whole process chain. A hydrogen FC vehicle is used for a comparative reference. Efficiency losses are expressed as the difference between successive conversion stages (represented as bars, from left to right)*

6.6 GHG emission analysis

The GHG emissions attributed to the respective synthetic fuels designed for transport is analysed in this section. The evaluation captures process emissions limited to the carbon capture process, fuel production process, gas conditioning and end-use combustion. The analysis does not extend to the life-cycle of the vehicles (production and end-of-life), nor does it include the environmental impact and land use change related to the construction of process units and energy generation plants. The system boundary also considers the effluent from the carbon point sources as initial feedstock rather than a byproduct of an additional process, as shown in (Figure 6.11).

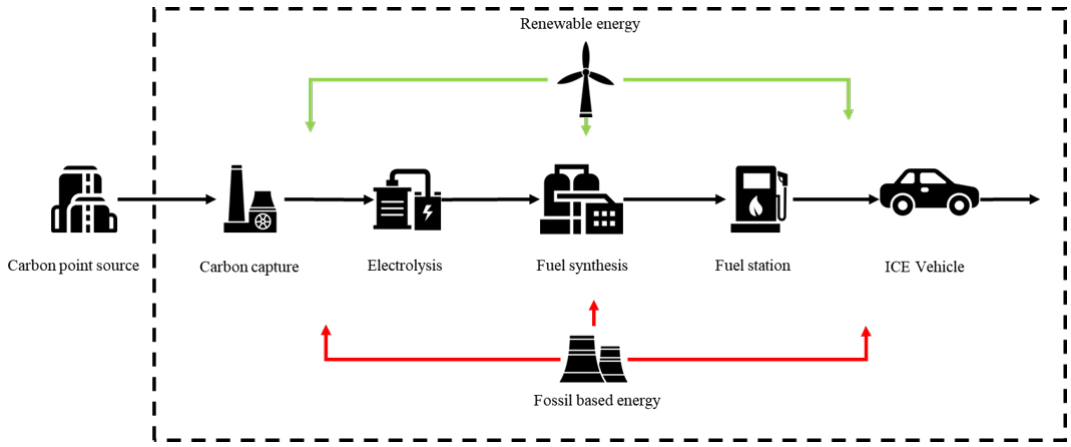

Figure 6.11: *System boundary of the GHG evaluation in this study.*

Equation (6.19) is used to estimate the GHG emissions in the defined system boundary.

$$\text{WTW GHG (g-CO}_{2\text{eq}}\text{/km)} = \text{WTT GHG (g-CO}_{2\text{eq}}\text{/MJ)} \times \text{TTW Energy (MJ/km)} + \text{TTW GHG (g-CO}_{2\text{eq}}\text{/km)} \quad (6.19)$$

The WTT GHG emissions data will account for emissions associated with

the production of 1 MJ of synthetic fuel. The data of GHG emissions for the WTT analysis is obtained from the latest BEIS report in Table 6.4.

Table 6.4: *Emission factors of energy use in the UK 2022 [338].*

Activity	CO_{2e} of CO_2	CO_{2e} of CH_4	CO_{2e} of N_2O
		g/MJ	
District heat and steam	46.96	0.30	0.16
Electricity UK	53.11	0.22	0.38
Electricity UK - T & D[1]	4.86	0.02	0.03

[1] transmission & distribution

In addition to the production phase, the obtainable carbon credit benefit - depending on the initial sources of carbon (as described in Chapter 4), during the use phase of the fuel is considered in this analysis. In the case of biogenic CO_2, the amount of CO_2 that is liberated during combustion is assumed to be equal to the amount of CO_2 sequestered during the plant's growing phase (Table 6.5).

Table 6.5: *Emission factors of synthetic fuels in g-CO_2/MJ*

Methane	Methanol	DME	FT-L
56.1	68.9	67.3	70.8

The TTW GHG emissions were calculated based on the EURO VI limits for total hydrocarbon (THC) and NOx, valid until 2025.

$$\mathrm{CO}_{2,\mathrm{eq}(\mathrm{CH}_4)} = \frac{THC}{1000} \cdot \frac{\mathrm{CH}_4}{THC} \cdot GWP_{(\mathrm{CH}_4)} \tag{6.20}$$

$$\mathrm{CO}_{2,\mathrm{eq}(\mathrm{N_2O})} = \frac{\mathrm{NOx}}{1000} \cdot \frac{\mathrm{N_2O}}{NOx} \cdot GWP_{(\mathrm{N_2O})} \tag{6.21}$$

Where THC, NOx is the legislation limit in mg/km in terms of THC or NOx emission, CH_4/THC is the percentage of the CH_4 over the total THC emission limit, N_2O/NOx is percentage of N_2O over the total NOx emission limit, and GWP is the global warming potential factor defined for CH_4 and N_2O as $25\,\mathrm{g} - CO_{2eq}$ and $298\,\mathrm{g} - CO_{2eq}$ respectively.

Table 6.6: *GHG Emissions in g-CO_2/km.*

Fuel	**as CO_2**[1]	**as CH_4**	**as N_2O**
Methane	77.71	1.50	0.54
Methanol[2]	100.13	0.13	0.54
DME	87.92	0.23	1.19
FT-L	91.31	0.23	1.19

[1] A. Huss [336]

[2] Due to lack of available data, E100 is used as a representative due to the similarity in density, octane rating and heating value.

Some assumptions were made due to the additional complexity in deriving the CO_2 emissions for the models. Thus, data from the work of A. Huss [336], which used the AVL CRUISE simulation software to calculate the CO_2 emissions based on the WLTP drive cycle, has been used in this analysis (Table 6.6).

Figure 6.12 shows the result of calculated GHG emissions as described by Equation (6.19). The results show the difference in the WTW GHG emissions for the studied synthetic fuels, based on the different sources of carbon as described in Chapter 4. The result shows that the WTW GHG for synthetic diesel produced from 'black' carbon is slightly higher than that of conventional transport diesel ($258\,\mathrm{g_{CO_2}}$/km). This offset can be attributed to the additional parasitic emissions from the distribution of the associated feedstock and product. The anomalous shape in the 'green' synthetic fuel is due to the significant change in energy requirement for carbon capture as a function of the useful energy produced during the fuel synthesis;

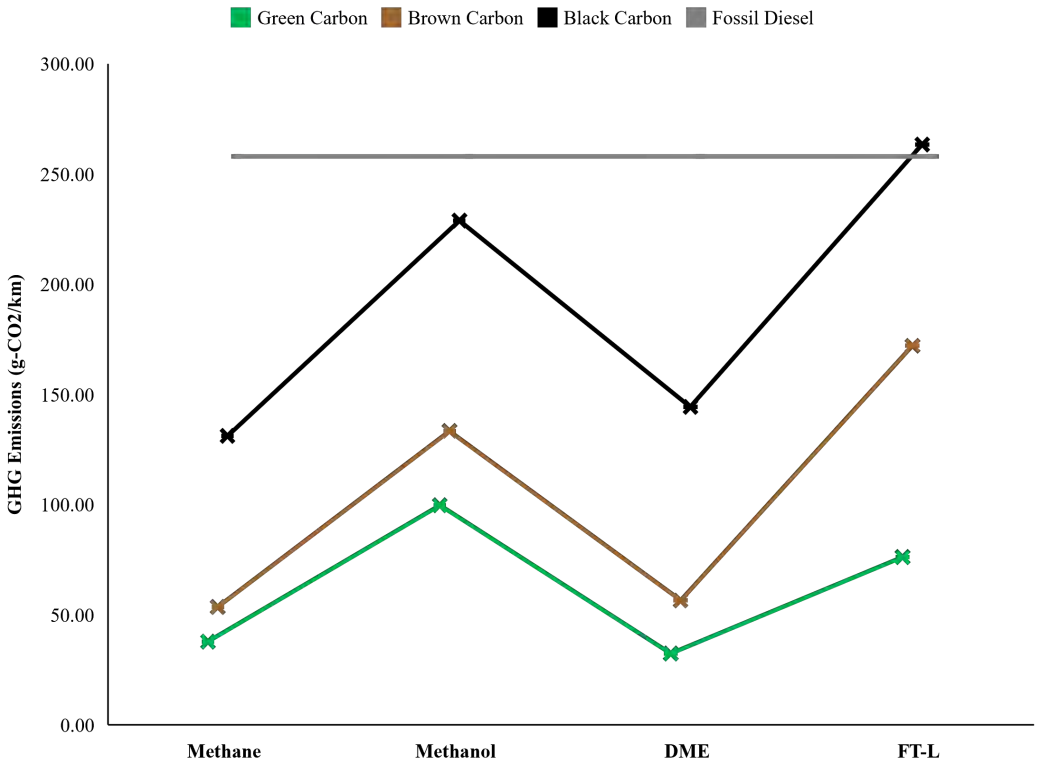

Figure 6.12: *Results of the WTW GHG emissions for the modelled synthetic fuels based on different point sources of carbon. The evaluation is based on a passenger car and the WLTP drive cycle in a 2025 and beyond scenario. The value for conventional diesel fuel [336] has been applied for comparative reference.*

compared to the other fuels.

6.7 Chapter Discussion

This chapter seeks to assess the degree of fossil fuel substitution that could be achieved based on the analysis carried out in the previous sections. In view of road transport demand, the forecast of newly registered road vehicles is considered due to the higher potential of engine re-modification at the point of production.

Preliminary results show that the conversion of high purity CO_2 from biogenic sources is only capable of meeting a limited proportion (27% from methane production) of the transport demand in the United Kingdom. Scotland and its regions are highlighted as the preferred coverage scope due to the smaller proportional demand and the close proximity to the point source of CO_2 and electricity.

In addition, it should be noted that this analysis does not fail to acknowledge the growing rate of electric vehicles in the United Kingdom in view of the proposed ban on the sales of internal combustion engine vehicles.

Technology learning curves are applied to project the investment costs that will be required to utilise the remainder of the assessed CO_2 from Chapter 4. The costs of carbon capture and compression are accounted for due to the lower CO_2 purity from the remaining sources (brown and black as in Chapter 4). The results show that capital costs for purchasing electrolyser units significantly dominate the overall investment costs, despite the author's optimistic base values.

This chapter also aimed to present a comparative analysis from an energetic and emission perspective. The assessment used a well-to-wheel analysis which considered the analysis from the production of the fuel to the use of the fuel upon vehicular combustion. The well-to-wheel analysis combines an assesment of the energy flow in the well-to-tank and vehicular operation with respect to distance driven and drive cycle.

In addition to the energetic values, the results gave an indication of the efficiency *'hot spots'* where savings could be made. Based on the model assumptions, methane and DME showed the most promise energetically and emission-wise.

Chapter 7

PROSPECTS TO DEPLOYMENT AND CONCLUSION

7.1 Goal of this section

Following the methodological assessments undertaken in this study, this section will highlight other significant elements that must be considered in the overall context of the research study. The section will emphasise the limitations to deploying PtX technologies as part of the climate mitigation strategies within the United Kingdom context. This section will also attempt to address the question of "what needs to happen to make it work?"[1]. This section will be limited to road transport.

This section of the study also brings the whole analysis to a close by presenting the concluding remarks, future outlooks of the study and future research recommendations.

[1] i.e., to keep affordable ICE vehicles on the roads

7.2 Infrastructure for the deployment of PtX technologies

As stated in the latest edition of the UK's report on the Statutory Security of Supply, the Government has committed £68 million towards deploying longer duration energy storage (LODES), illustrating an interest in this option. This is in view of the commercialisation of FOAK storage technologies such as PtX for the UK energy system. This section provides an overview and discusses the supply chain infrastructure required to further establish PtX as a bridging[2] technology in the UK climate strategy.

7.2.1 Infrastructure for Gas transport

Chapter 4 briefly discussed the means required for the transport of CO_2 in the UK and mapping in relation to the existing natural gas grid. Due to the volume of CO_2 discussed in this study, transportation via pipeline is considered the most feasible compared to railway, road and marine. Pipeline transport provides higher guarantees of supply security, connectivity and economical operation [339].

Flow assurance is one of the technical challenges that must be overcome in transporting CO_2 via pipelines due to the thermodynamic properties discussed in the aforementioned chapter. If natural gas pipelines are to be re-purposed for the transport of CO_2, booster pump stations will be required instead of compression stations to compensate for the propensity of two-phase flows being formed. At the time of this study, there is no fully commercialised repurpose of natural gas pipelines for transporting CO_2.

Uncertainties are also associated with the cost of CO_2 transport infras-

[2]This describes technologies that facilitate the transition between energy systems whilst still being viable in the proposed strategy.

tructure. According to a techno-economic study by Skaugen et al. [340] on the transport of CO_2 with varying impurities, the optimal investment and operating cost for laying 24" CO_2 pipes in Europe is 14.47 $£_{2014}/t_{CO_2}$ to 21.36 $£_{2014}/t_{CO_2}$ over a 500 km distance.

Hydrogen can be transported as gas (pipeline), liquid (by trucks), via liquid organic hydrogen carriers (LOHC) or as NH_3 (both by ship). A study by Collis and Schomaecker [341] concluded that hydrogen transport via LOHC and NH_3 are the most cost-effective due to the ease of transport and storage. However, investment costs for the dehydrogenation processes offset these low costs. Furthermore, the incurred energy losses (shown as round trip efficiencies) for LOHC (26 - 43% [342]) and NH_3 (11 - 19% [343]) are higher than liquefied hydrogen (9 - 22% [344]) and compressed hydrogen gas (5 - 15% [345]). Given the scope of this study, transportation of compressed hydrogen is preferred despite the higher capital costs for new pipelines. BloombergNEF [346] estimates that the cost of distributing hydrogen via a pipeline over a distance of 100 km will not exceed £0.19/kg.

Much like for CO_2, pipelines from the existing natural gas networks may be repurposed for distributing hydrogen to achieve up to 33% cost savings [347]. Projects such as FutureGrid and H21 are currently undertaking feasibility assessments on repurposing the UK's gas distribution networks for hydrogen. As of December 2022, the project completion has been delayed till November 2023 due to issues with compression units.

7.2.2 Status of e-fuel compatible vehicles

The availability of Natural Gas Vehicles (NGV) has increased in recent decades. By the end of 2021, there were more than 30 million NGV (the majority of which are light-duty fleets) in operation globally, with the Asia-Pacific region accounting for the largest share with 71.7% and Europe with 7.2% [348]. A key barrier to the penetration of NGVs is the profitability and density of methane refuelling

stations in any region, with the ratio of vehicles to stations just over 400:1 in Europe [348].

The volumetric energy density of methane is significantly lower than petrol and diesel. To increase the driving range of NGVs, methane requires compression (at 200 bars) or liquefaction (CNG to $-162\,^{\circ}\mathrm{C}$ at atmospheric pressure), stored in high-pressure tanks and insulated cooling tanks, respectively. Owing to its higher H/C ratio, the carbon intensity of methane is better than petrol and diesel, reflected in relatively less CO_2 emissions and other large-sized particulate matter, depending on the engine efficiency [349]. However, methane slippage remains a concern during automotive use, especially in idling conditions. Studies have shown that hydrogen enrichment can reduce total hydrocarbon levels by up to 30% [350].

While typically utilised in spark ignition (SI) engines, efforts have been made to retrofit compression ignition (CI) engines with methane systems in a duel-fuel mode. Trade-offs in efficiencies and emissions of dual-fuelled NGVs are discussed in a study by Chen et al. [351]. According to Ford's Qualified Vehicle Modifier programme, the cost of retrofitting a compressed methane fuel system to a vehicle is around $8,000 (as of 2015) [352].

Methanol as an alternative transport fuel is a concept that was first implemented as a response to the crude oil crises in the 1970s. However, the incompatibility of carbureted fuel systems to handle fuels with high oxygen content meant that methanol blends were limited to 3 to 5% (M3 - M5) by volume with petrol [353]. China largely dominates the market share for methanol as an automotive fuel; the annual production accounts to up to 500,000 vehicle engines compatible with lean methanol (M100) [353].

Methanol has a low air-to-fuel ratio due to the high oxygen content compared to petrol/diesel. This results in improved combustion efficiency, reduced CO emissions, and reduced formation of soot [354]. Conversely, the energy content of methanol is

lower, and the production of NOx emissions is increased due to the oxygen content.

Methanol has a high octane number and thus lends itself to use in SI engines. It can be used directly or in varying blends, including CH_3OH/H_2O and GEM (gasoline, ethanol and methanol). For compatibility with CI, which requires fuels with high auto-ignition, methanol blended with a high CN (cetane number) fuel can be premixed with the intake air [355]. The addition of an ignition enhancer is another option. A facility to inject methanol into the engine through the intake port is considered an easy retrofit option for existing CI engines [356].

The global commercialisation of DME as an automotive vehicle fuel is not as advanced as the previous fuels, with production and utilisation facilities concentrated mainly in China. However, it has begun to feature prominently as one of the fuels for the future, with companies like Volvo developing long-haul vehicle engines that run on DME [357].

DME is comparable to diesel fuel due to its high CN, which is suitable for CI engines. DME exists in a gaseous phase under normal conditions but can be liquefied for easy storage upon mild pressurisation (6 bars). Because DME shares similar physical properties with liquefied petroleum gas (LPG), pre-existing tank designs can be used for DME.

The emission characteristics of DME combustion have been studied in the works of Park and Lee [358] and Wang et al. [359]. Compared to diesel fuels, the formation of soot and HC emissions are significantly reduced during the combustion of DME due to the oxygen content and shorter ignition delay, respectively. However, higher CO emissions are associated with DME combustion because of the configuration of DME engines requiring a long injection duration and large spray holes. To further reduce emissions, especially NOx from the combustion of DME, DME can be blended with two or more fuels, including LPG, diesel and biodiesel, without solubility issues [358].

Due to the gaseous nature of DME, coupled with its low viscosity and lubricity - resulting in high leakage rates and surface wear in fuel injectors and fuel feed pumps; additives and lubricants are required for use in pre-existing diesel engines [359]. The development of DME fuelled engines is currently not as established as the other electrofuels in this study.

7.2.3 E-fuels for e-vehicles?

There is a growing interest in the promotion of zero-emission vehicles (ZEV) which include full battery electric vehicles (BEV) and fuel cell electric vehicles (FCEV). However, establishing ZEVs is heavily contingent upon successfully deploying the infrastructure required for fleet operation. This is particularly of great relevance, especially in the case of fuel cell-powered vehicles that are predominantly designed to operate on hydrogen. The onboard storage of hydrogen and the pervasiveness of fuelling infrastructure are still some of the social and economic barriers that hinder the deployment of hydrogen technologies for road transport [360].

Adopting electrofuels as alternative fuels to hydrogen in fuel cells provides an opportunity to ease the transition and enablement of a hydrogen-dominant energy economy. While the conventional use of hydrocarbon in fuel cell systems requires a reforming step before injection, the direct injection of methane [361], methanol [362], and DME [363] are currently under development.

This presents an opportunity to introduce high-temperature fuel cells that will use synthetic fuels more efficiently without needing new infrastructure, at an additional cost.

7.2.4 Additional Infrastructure for e-fuels supply

An essential feature of the deployment of transition technologies is their compatibility with existing infrastructure and the low degree of modification required.

The electrofuels in this study share physical properties with their conventional and fully commercialised counterparts, enabling them to use existing storage and refuelling technologies in their normal phases. The storability and supply of pressurised electrofuels (methane and DME) for onboard vehicular utilisation is technically challenging and will require further development. This feature is more important for private fleets where fast fuelling is critical, and filling stations may be very dispersed in remote locations at the onset of their deployment.

Table 7.1 shows an overview of the parameters that are required for further deployment of synthetic e-fuels in comparison with other fuels (hydrogen included). The concluding assessment was derived from an aggregate of opinions from academic and industrial stakeholders via private conversations and interviews. The molecular structures of e-fuels fuels lend them to share comparative features with fossil fuels as direct substitutions or drop-in fuels, with already existing infrastructure. While hydrogen-fuelled vehicles and BEVs may present the highest emission reduction potential at the tail-pipe of the vehicle, the technical challenges about storage and infrastructures, still need to be overcome to achieve full commercialisation. E-fuels have an edge in this regard and, and can support the development of the other fuels.

Table 7.1: *Overview of selected parameters for deploying different fuel types for road transport.*

Fuel type	**Investment**	**Storage**	**Additional Infrastruture**	**Vehicle Development**	**Fuel Stock[1]**
Fossil	Low	Easy	No	Easy	Medium
Electric	High	Dificult	Yes	Medium	High
E-fuels	High	Easy	No	Easy	Low
Hydrogen[2]	High	Difficult	Yes	Difficult	Low

The assessments are based on the author's estimation.

[1] Fuel stock is based on immediate availability.

[2] For use in fuel cell vehicles.

7.3 Scenarios for Deployment

In addition to the identified benefits of electrofuels, the successful deployment of PtX may also be contingent on some exogenous factors to be briefly discussed in this section.

- **The large-scale deployment of battery electric vehicles**

  Despite the upward trend in purchasing BEV, some technical (and economic) barriers still hinder their wider adoption. The increased penetration of BEV will require grid-related challenges to be overcome, such as the congestion of lines and transformers in highly populated areas, decreased resilience [364], poor load factor and thermal stress [365]. Battery degradation issues during fast charging and discharge in bidirectional power flow still have high economic implications that need to be resolved [366].

  The direct costs of BEV are still significantly higher than their ICE counterparts, with the battery component accounting for up to a third of the overall car cost. Despite dropping costs, BEVs are still expected to have higher total ownership costs by up to 10% over ICEs, by 2026 [367]. Policy development and incentives are therefore expedient to increase the uptake of BEVs and prevent a transport underclass amongst the population [368].

  The current ratio of vehicle recharging infrastructure to BEV is still insufficient for the proposed market uptake of BEV. The work by Tsiropoulos et al. [369] estimates that significant investments of up to 4 €bn are required annually from 2030 to 2050 in Europe.

- **The requirement of sufficient energy storage capacities**

  There is a greater interest in the increased penetration of renewables in global energy systems. The existing grid infrastructure of many energy systems currently lacks the robustness to deal with the flux of the proposed capacities

[370]. The United Kingdom is falling short of its target of installing more renewable capacity due to a delayed upgrade of the transmission grid [371]. The fluctuating nature of many renewable energy sources hampers the large-scale deployment of these technologies.

Increased renewable penetration is, therefore, contingent upon the availability of reliable and cost-effective energy storage technologies. While the overall costs of grid-scale energy storage are expected to decrease, a study by NREL showed that costs of conventional energy storage technologies like batteries increased by 13% from Q1 2021 to Q1 2022 [372]. This presents an opportunity for PtX to act as a means to store electrical energy with less dependence on expensive grid upgrades and novel storage technologies.

- **Long-term carbon storage**

  The capture of carbon is fundamental in any climate mitigation scenario. After capturing and transportation, storing CO_2 is the only option (other than utilisation). Carbon storage aims to sequester carbon and avoid re-emission, typically in geological formations. The main barriers towards the large-scale deployment of carbon storage generally relate to the reliability of storage options. Carbon leakages and the related economic burdens have been studied in various works, including [373, 374]. While the uncertainty of leakages of large amounts of carbon persists, the deployment of carbon storage will need to overcome the negative public perception and rely on incentivised policy regulation.

  The carbon mineralisation of CO_2 is a pathway to stori g carbon. This process is achieved either by circulating CO_2-rich fluids through suitable geological formations below the ground surface or above the ground under pressurised conditions [375]. The main barriers to commercialisation are related to its early stage of development and limited geological capacity [376].

There are still uncertainties surrounding the deployment of these climate

change mitigation strategies. This gives rise to the further consideration of PtX as an enabling technology, towards the achievement of the proposed net-zero targets.

7.4 Conclusion

This thesis addresses some questions about the various climate mitigation measures widely proposed in light of low-carbon economies. The ban on new petrol and diesel cars by 2030 in the United Kingdom is of particular interest due to the inherent difficulty in eradicating fossil fuels and the uncertainty relating to the complete establishment of a substitute technology. Consequently, original equipment manufacturers (OEMs) of major automobile companies have begun to resist the proposal of the ban, owing to and including the aforementioned issues [377].

The production of synthetic fuels via power-to-fuel (X) (methane, methanol, DME, synthetic diesel) for road transport is considered a proposal for climate change mitigation. PtX technology is transitionary in nature so that it does not hinder the prospect of a fully electrified or hydrogen economy, nor does it intend to bear the adverse burden of technology lock-ins. An added benefit is the circular utilisation of captured carbon and curtailed renewable electricity, resources that could be otherwise 'wasted' under current circumstances.

The feasibility of deploying these synthetic fuels was assessed via a comparative techno-economic analysis and emission analysis. The case study was based on the CO_2 resource availability in the United Kingdom (current to the duration of the research). The aim of the result of the assessment was not to offer an objective solution but to present the range of likelihood based on the assumptions made in the study.

Synthetic methane shows the most promise out of all the fuels. This is primarily due to the relatively highly efficient process and the potential for a high recovery potential. Methane performs favourably in the economic analysis, making it a viable option for long-term investment. The primary limitation of methane as a transport fuel relates to the limited availability of fleet refuelling infrastructure and engine modification facilities across Europe.

Producing methanol has the lowest techno-economic performance of the other fuels in this study. This can be potentially attributed to the process configuration used in the model simulation. This is further reflected in the high capital costs of the process equipment. Notwithstanding, methanol has the highest potential for road transport due to its long consideration and history as an alternative to conventional road transport fuels.

The dimethyl ether route may provide the most environmentally competitive option for methane, based on the analysis. The sootless emissions due to the lack of carbon-carbon bonds offer an excellent opportunity to reduce particulate matter emissions in diesel fuel combustion. The thermophysical properties of DME present the most significant challenge as a road transport fuel. Combustion engines fuelled by DME are the least advanced of the assessed fuels, thus hindering the immediate applicability of DME as a direct-injection fuel. Blending DME fuel with diesel is currently the most probable method to benefit from DME fuels' relative environmental advantage without the advanced conversion of existing IC engines.

Synthetic diesel has the most significant advantage in terms of its interchangeability with existing fuels (diesel in this case) compared with the other fuels in this study. Its compatibility with preexisting refuelling infrastructure further augments this. However, its deployment is hindered by the process's high energy intensity and production costs. While the economic analysis in this study indicates high profitability, this is primarily due to diesel's relatively high selling costs applied in the models at the time of the study.

7.5 Future Outlook PtX as a Transitionary Technology

While this study primarily focuses on deploying PtX technologies for road transportation, it also seeks to present it as a transitionary technology towards a near or fully-decarbonised energy system. PtX technology, as described in this study, couples carbon capture and the production of renewable hydrogen; based on an increased renewable electricity capacity. The two independent technologies are critical to achieving the Net Zero strategy laid out by the United Kingdom government. Therefore, this study presents PtX technology as a viable mitigation option rather than a proverbial "silver bullet".

A recent independent review of the Net Zero Strategy undertaken on behalf of the United Kingdom emphasised the need for synthetic fuels in its climate mitigation agenda [378].

> "*Not all our energy needs can be met with electricity and so we will continue to need liquid, gaseous and solid fuels. Government has therefore set ambitious targets for greener fuels, including hydrogen, low carbon fuels produced from biomass and other waste resources for use in different sectors such as transport, heating, power and wider industrial applications*" [378].
>
> "*This Review recommends developing by 2025 a long-term cross-sectoral infrastructure strategy to adapt and build respectively the distribution of liquid and gaseous fuels, electricity and CO_2 networks over the next decade*" [378].

Furthermore, the United Kingdom Government reiterated its commitment to a cleaner and constant energy supply in the latest edition of the Energy Security Plan (2023). The continued invasion of Ukraine (at the time of writing) confirms

the challenge of ensuring an independent, secure and resilient energy supply [379]. The report also recognised the importance of CCUS in transitioning the United Kingdom's energy landscape.

The deployment of PtX may provide a viable pathway to meet the aforementioned fuel demand for the United Kingdom within the context of the Net Zero Strategy. Studies have examined the application of PtX technologies in sectors beyond road transport, including the production of chemicals [380], decarbonisation of industrial processes [132], energy storage applications [381], and re-electrification [382].

7.6 Outlook on Future Work

The deployment of PtX in electrofuel production is a composite of independent processes and systems. A better understanding of the individual processes could guide research to build upon the work done in this thesis to meet the objectives set therein. Upon the completion of this study, the following recommendations are suggested for future research in this work:

- **Investigation of process model configurations**

  The study's final unit and process configurations are contingent upon the author's subjectivity in the process models. Multiple configurations should be chosen based on the process descriptions illustrated in Chapter 2. The results may indicate the relationship between process configurations and their respective process efficiencies, investment and operating costs.

- **Dynamic electrolyser performance**

  This study implies a steady-state operation of the electrolyser. However, a dynamic analysis will give a deeper understanding of real-life operations. This is important because the study assumes that a significant proportion of electricity is derived from renewable (wind) energy. While there is no intermediate electricity storage between the source and end use, the variabilities in renewable electricity supply should be considered.

- **SOE degradation analysis**

  The SOE units account for a large proportion of the investment costs in this study. However, the degradation of SOE is currently a technical challenge that needs to be overcome to make it more commercially viable [383]. Therefore, assessing the impact of the degradation rates of the SOE units and techno-economic implications is essential.

- **Life cycle analysis**

  Conducting a comprehensive life cycle analysis will shed more light on the related emissions and highlight environmental 'hot spots' along the production cycles. The results could feed into a comparative study of different CCUS and climate mitigation technologies.

- **Socio-economic analysis**

  The scope of the impacts of climate change is global, affecting the entire population with economic implications. A socioeconomic analysis is therefore important to present a well-rounded analysis of the study (as seen in Figure 1.3).

Bibliography

[1]P. Division, *World population prospects 2022: summary of results.* Tech. rep. UN DESA/POP/2022/TR/NO. 3. (United Nations Department of Economic and Social Affairs, 2022).

[2]B. Zohuri, "Nuclear fuel cycle and decommissioning", in *Nuclear reactor technology development and utilization* (Elsevier, 2020), pp. 61–120.

[3]IPCC, *Climate change 2014: synthesis report*, tech. rep. (Contribution of Working Groups I, II and III to the Fifth Assessment Report of the Intergovernmental Panel on Climate Change, Geneva, Switzerland, 2014).

[4]A. Nourian, M. K. Abba, and G. G. Nasr, "Measurements and analysis of non-methane voc (nmvoc) emissions from major domestic aerosol sprays at "source"", Environment International **146**, 106152 (2021).

[5]C. L. Lim, "Fundamental concepts of human thermoregulation and adaptation to heat: a review in the context of global warming", International Journal of Environmental Research and Public Health **17**, 7795 (2020).

[6]D. J. Arent, R. S. Tol, E. Faust, J. P. Hella, S. Kumar, K. M. Strzepek, F. L. Tóth, and D. Yan, "Key economic sectors and services", in *Climate change 2014 – impacts, adaptation and vulnerability: part a: global and sectoral aspects: working group ii contribution to the ipcc fifth assessment report: volume 1: global and sectoral aspects*, Vol. 1, edited by C. Intergovernmental Panel on Climate (Cambridge University Press, Cambridge, 2014), pp. 659–708.

[7]S. Hsiang, R. Kopp, A. Jina, J. Rising, M. Delgado, S. Mohan, D. J. Rasmussen, R. Muir-Wood, P. Wilson, M. Oppenheimer, K. Larsen, and T. Houser, "Estimating economic damage from climate change in the united states", Science **356**, 1362 (2017).

[8]U. N. F. C. on Climate Change, "Report of the conference of the parties on its twenty-first session, held in paris from 30 november to 13 december 2015", in Fccc/cp/2015/10/add.1 (UNFCCC, 2016).

[9]J.-F. Bastin, Y. Finegold, C. Garcia, D. Mollicone, M. Rezende, D. Routh, C. M. Zohner, and T. W. Crowther, "The global tree restoration potential", Science **365**, 76–79 (2019).

[10]T. D. N. Le, "Climate change adaptation in coastal cities of developing countries: characterizing types of vulnerability and adaptation options", Mitigation and Adaptation Strategies for Global Change **25**, 739–761 (2020).

[11]A. Otto, C. Göpfert, and A. H. Thieken, "Are cities prepared for climate change? an analysis of adaptation readiness in 104 german cities", Mitigation and Adaptation Strategies for Global Change **26**, 1–25 (2021).

[12]L. Messmer, B. Thom, P. Kruetli, E. Dawoe, K. Assefa, J. Six, and J. Joerin, "Beyond feasibility—the role of motivation to implement measures to enhance resilience", Mitigation and Adaptation Strategies for Global Change **26**, 1–24 (2021).

[13]IEA, *Key world energy statistics*, Dataset, 2018.

[14]IEA, *Net zero by 2050*, tech. rep. (International Energy Agency, Paris, 2021).

[15]IEA, *Energy efficiency 2018: analysis and outlooks to 2040* (International Energy Agency, Paris, 2018), p. 170.

[16]P. Larkin, R. Gracie, A. Shafiei, M. Dusseault, M. Sarkarfarshi, W. Aspinall, and D. Krewski, "Uncertainty in risk issues for carbon capture and geological storage: findings from a structured expert elicitation", International Journal of Risk Assessment and Management **22**, 429–463 (2019).

[17]J. B. S. Haldane, *Daedalus: or, science and the future; a paper read to the heretics, cambridge, on february 4th, 1923* (New York: Dutton, 1924).

[18]S. Appl-Scorza, J. Lippelt, and C. Littlejohn, "Challenges of electrification of heavy and long-haul traffic", in Cesifo forum, Vol. 19, 4 (München: ifo Institut–Leibniz-Institut für Wirtschaftsforschung an der ..., 2018), pp. 46–59.

[19]D. S. Mallapragada, D. Diaz Pilas, P. Gonzalez Fernandez, and A. Delgado Martín, "System implications of continued cost declines for wind and solar on driving power sector decarbonization", (2020).

[20]R. Hull and A. Jones, "Development of decentralised energy and storage systems in the uk", A Report for the Renewable Energy Association (2016).

[21]X. Liang, "Emerging power quality challenges due to integration of renewable energy sources", IEEE Transactions on Industry Applications **53**, 855–866 (2016).

[22]S. R. Sinsel, R. L. Riemke, and V. H. Hoffmann, "Challenges and solution technologies for the integration of variable renewable energy sources—a review", renewable energy (2019).

[23]Z. Cesaro, R. Nayak-Luke, and R. Bañares-Alcántara, "Energy storage technologies: power-to-x", in *Techno-economic challenges of green ammonia as an energy vector* (Elsevier, 2021), pp. 15–26.

[24]A. Dehghani-Sanij, E. Tharumalingam, M. Dusseault, and R. Fraser, "Study of energy storage systems and environmental challenges of batteries", Renewable and Sustainable Energy Reviews **104**, 192–208 (2019).

[25]J. Burre, D. Bongartz, L. Brée, K. Roh, and A. Mitsos, "Power-to-x: between electricity storage, e-production, and demand side management", Chemie Ingenieur Technik **92**, 74–84 (2020).

[26]R. M. Dolf Gielen Emanuele Taibi, *Hydrogen: a renewable energy perspective*, tech. rep. (International Renewable Energy Agency, 2019).

[27]P. Peltoniemi, J. Savolainen, R. Weiss, and O. Pyrhönen, "Frequency regulation possibilities of power-to-gas plants in grids including high shares of renewable energy production", in 10th international renewable energy storage, ires 2016 (EUROSOLAR The European Association for Renewable Energy, 2016).

[28]A. K. Sethi and S. P. Sethi, "Flexibility in manufacturing: a survey", International journal of flexible manufacturing systems **2**, 289–328 (1990).

[29]K. R. Khalilpour, "Chapter 1 - moving forward to the past, with adaptation and flexibility: the special role of resource storage", in *Polygeneration with polystorage for chemical and energy hubs*, edited by K. R. Khalilpour (Academic Press, 2019), pp. 1–25.

[30]I. Stadler and M. Sterner, "Urban energy storage and sector coupling", in *Urban energy transition* (Elsevier, 2018), pp. 225–244.

[31]F. Wagner, "Surplus from and storage of electricity generated by intermittent sources", The European Physical Journal Plus **131**, 1–21 (2016).

[32]S. Santhanam, M. Heddrich, M. Riedel, and K. A. Friedrich, "Process design study of reversible solid oxide cell (r-soc) system for coupling energy storage and hydrogen economy supply chain", ECS Transactions **78**, 2925 (2017).

[33]A. Baldinelli, L. Barelli, G. Bidini, G. Cinti, A. Di Michele, and F. Mondi, "How to power the energy–water nexus: coupling desalination and hydrogen energy storage in mini-grids with reversible solid oxide cells", Processes **8**, 1494 (2020).

[34]D. Connolly and B. V. Mathiesen, "A technical and economic analysis of one potential pathway to a 100% renewable energy system", International Journal of Sustainable Energy Planning and Management **1**, 7–28 (2014).

[35]F. Bouffard and D. S. Kirschen, "Centralised and distributed electricity systems", Energy policy **36**, 4504–4508 (2008).

[36]K. R. Khalilpour, "The nexus era: toward an integrated, interconnected, decentralized, and prosumer future", in *Polygeneration with polystorage for chemical and energy hubs* (Elsevier, 2019), pp. 27–52.

[37]P. Murray, A. Omu, K. Orehounig, and J. Carmeliet, "Power-to-gas for decentralized energy systems: development of an energy hub model for hydrogen storage", in Proceedings of the 15th ibpsa conference. san francisco, ca< http://dx. doi. org/10.26868/25222708.2017, Vol. 460 (2017), pp. 7–9.

[38]Q. Zeng, J. Fang, J. Li, and Z. Chen, "Steady-state analysis of the integrated natural gas and electric power system with bi-directional energy conversion", Applied Energy **184**, 1483–1492 (2016).

[39]S. Abanades, P. Charvin, F. Lemont, and G. Flamant, "Novel two-step SnO_2/SnO water-splitting cycle for solar thermochemical production of hydrogen", International Journal of Hydrogen Energy **33**, 6021–6030 (2008).

[40]J. d. Bucy, O. Lacroix, and L. Jammes, "The potential of power-to-gas. technology review and economic potential assessment", (2016).

[41]M. Götz, J. Lefebvre, F. Mörs, A. M. Koch, F. Graf, S. Bajohr, R. Reimert, and T. Kolb, "Renewable power-to-gas: A technological and economic review", Renewable energy **85**, 1371–1390 (2016).

[42]Ø. Ulleberg, T. Nakken, and A. Ete, "The wind/hydrogen demonstration system at Utsira in Norway: Evaluation of system performance using operational data and updated hydrogen energy system modeling tools", International Journal of Hydrogen Energy **35**, 1841–1852 (2010).

[43]M. Ozturk and I. Dincer, "A comprehensive review on power-to-gas with hydrogen options for cleaner applications", International Journal of Hydrogen Energy **46**, 31511–31522 (2021).

[44]C. Chen, W. Guo, H. H. Ngo, D.-J. Lee, K.-L. Tung, P. Jin, J. Wang, and Y. Wu, "Challenges in biogas production from anaerobic membrane bioreactors", Renewable Energy **98**, 120–134 (2016).

[45]I. Angelidaki, L. Treu, P. Tsapekos, G. Luo, S. Campanaro, H. Wenzel, and P. G. Kougias, "Biogas upgrading and utilization: current status and perspectives", Biotechnology advances **36**, 452–466 (2018).

[46]A. I. Adnan, M. Y. Ong, S. Nomanbhay, K. W. Chew, and P. L. Show, "Technologies for biogas upgrading to biomethane: A review", Bioengineering **6**, 92 (2019).

[47]Q. Sun, H. Li, J. Yan, L. Liu, Z. Yu, and X. Yu, "Selection of appropriate biogas upgrading technology - A review of biogas cleaning, upgrading and utilisation", Renewable and Sustainable Energy Reviews **51**, 521–532 (2015).

[48]L. Yang, X. Ge, C. Wan, F. Yu, and Y. Li, "Progress and perspectives in converting biogas to transportation fuels", Renewable and Sustainable Energy Reviews **40**, 1133–1152 (2014).

[49]R.-S. Taubner, C. Schleper, M. G. Firneis, and S. K.-M. Rittmann, "Assessing the ecophysiology of methanogens in the context of recent astrobiological and planetological studies", Life **5**, 1652–1686 (2015).

[50]T. T. Q. Vo, A. Xia, D. M. Wall, and J. D. Murphy, "Use of surplus wind electricity in ireland to produce compressed renewable gaseous transport fuel through biological power to gas systems", Renewable Energy **105**, 495–504 (2017).

[51]W.-H. Chen and S.-C. Lin, "Biogas partial oxidation in a heat recirculation reactor for syngas production and CO_2 utilization", Applied Energy **217**, 113–125 (2018).

[52]S. Dharma, H. Masjuki, H. C. Ong, A. Sebayang, A. Silitonga, F. Kusumo, and T. Mahlia, "Optimization of biodiesel production process for mixed jatropha curcas–ceiba pentandra biodiesel using response surface methodology", Energy Conversion and Management **115**, 178–190 (2016).

[53]P. Sabatier and J. B. Senderens, "Nouvelles synth'eses du m'ethane", Comptes Rendus Hebdomadaires des Séances de l'Académie des Sciences **134**, in French, 514–516 (1902).

[54]W. Wang, S. Wang, X. Ma, and J. Gong, "Recent advances in catalytic hydrogenation of carbon dioxide", Chemical Society Reviews **40**, 3703–3727 (2011).

[55]M. Vannice, "The catalytic synthesis of hydrocarbons from carbon monoxide and hydrogen", Catalysis Reviews—Science and Engineering **14**, 153–191 (1976).

[56]C. Mebrahtu, F. Krebs, S. Abate, S. Perathoner, G. Centi, and R. Palkovits, "CO_2 Methanation: principles and challenges", in *Horizons in sustainable industrial chemistry and catalysis*, Studies in Surface Science and Catalysis (2019), pp. 85–103.

[57]InfoMine, *Mining intelligence and technology*, (July 2020) `http://www.infomine.com/investment/`.

[58]J. Kirchner, J. K. Anolleck, H. Lösch, and S. Kureti, "Methanation of CO_2 on iron based catalysts", Applied Catalysis B: Environmental **223**, 47–59 (2018).

[59]Z. Baysal and S. Kureti, "CO_2 methanation on Mg-promoted Fe catalysts", Applied Catalysis B: Environmental **262**, 118300 (2020).

[60]T. Franken and A. Heel, "Are Fe based catalysts an upcoming alternative to Ni in CO_2 methanation at elevated pressure?", Journal of CO_2 Utilization **39**, `10.1016/j.jcou.2020.101175` (2020).

[61]C. Liang, L. Zhang, Y. Zheng, S. Zhang, Q. Liu, G. Gao, D. Dong, Y. Wang, L. Xu, and X. Hu, "Methanation of CO_2 over nickel catalysts: impacts of acidic/basic sites on formation of the reaction intermediates", Fuel **262**, `10.1016/j.fuel.2019.116521` (2020).

[62]A. Loder, M. Siebenhofer, and S. Lux, "The reaction kinetics of CO_2 methanation on a bifunctional Ni/MgO catalyst", Journal of Industrial and Engineering Chemistry **85**, 196–207 (2020).

[63]F. Ocampo, B. Louis, L. Kiwi-Minsker, and A.-C. Roger, "Effect of Ce/Zr composition and noble metal promotion on nickel based $CexZr_1{}^- xO_2$ catalysts for carbon dioxide methanation", Applied Catalysis A: General **392**, 36–44 (2011).

[64]D. L. Kurta, B. S. Dean, and E. P. Krenzelok, "Acute nickel carbonyl poisoning", The American journal of emergency medicine **11**, 64–66 (1993).

[65]W. J. Lee, C. Li, H. Prajitno, J. Yoo, J. Patel, Y. Yang, and S. Lim, "Recent trend in thermal catalytic low temperature CO_2 methanation: A critical review", Catalysis Today, `10.1016/j.cattod.2020.02.017` (2020).

[66]P. U. Aldana, F. Ocampo, K. Kobl, B. Louis, F. Thibault-Starzyk, M. Daturi, P. Bazin, S. Thomas, and A. Roger, "Catalytic CO_2 valorization into CH_4 on Ni-based ceria-zirconia. reaction mechanism by operando ir spectroscopy", Catalysis Today **215**, 201–207 (2013).

[67]B. Miao, S. S. K. Ma, X. Wang, H. Su, and S. H. Chan, "Catalysis mechanisms of CO_2 and CO methanation", Catalysis Science & Technology **6**, 4048–4058 (2016).

[68]F. Massa, A. Coppola, and F. Scala, "A thermodynamic study of sorption-enhanced CO_2 methanation at low pressure", Journal of CO_2 Utilization **35**, 176–184 (2020).

[69]L. Kiewidt and J. Thöming, "Predicting optimal temperature profiles in single-stage fixed-bed reactors for CO_2-methanation", Chemical Engineering Science **132**, 59–71 (2015).

[70]J. Lefebvre, M. Götz, S. Bajohr, R. Reimert, and T. Kolb, "Improvement of three-phase methanation reactor performance for steady-state and transient operation", Fuel Processing Technology **132**, 83–90 (2015).

[71]S. Rönsch, J. Schneider, S. Matthischke, M. Schlüter, M. Götz, J. Lefebvre, P. Prabhakaran, and S. Bajohr, "Review on methanation – from fundamentals to current projects", Fuel **166**, 276–296 (2016).

[72]I. Wender, "Reactions of synthesis gas", Fuel processing technology **48**, 189–297 (1996).

[73]T. Fujitani and J. Nakamura, "The effect of ZnO in methanol synthesis catalysts on Cu dispersion and the specific activity", Catalysis letters **56**, 119–124 (1998).

[74]T. Fujitani and J. Nakamura, "The chemical modification seen in the Cu/ZnO methanol synthesis catalysts", Applied Catalysis A: General **191**, 111–129 (2000).

[75]L. Grabow and M. Mavrikakis, "Mechanism of methanol synthesis on Cu through CO_2 and CO hydrogenation", Acs Catalysis **1**, 365–384 (2011).

[76]Y.-F. Zhao, Y. Yang, C. Mims, C. H. Peden, J. Li, and D. Mei, "Insight into methanol synthesis from CO_2 hydrogenation on Cu (1 1 1): complex reaction network and the effects of H_2O", Journal of Catalysis **281**, 199–211 (2011).

[77]Y. Yang, C. A. Mims, D. Mei, C. H. Peden, and C. T. Campbell, "Mechanistic studies of methanol synthesis over Cu from $CO/CO_2/H_2/H_2O$ mixtures: the source of C in methanol and the role of water", Journal of catalysis **298**, 10–17 (2013).

[78]J. Słoczyński, R. Grabowski, A. Kozłowska, P. Olszewski, M. Lachowska, J. Skrzypek, and J. Stoch, "Effect of Mg and Mn oxide additions on structural and adsorptive properties of $Cu/ZnO/ZrO_2$ catalysts for the methanol synthesis from CO_2", Applied Catalysis A: General **249**, 129–138 (2003).

[79]I. Melián-Cabrera, M. L. Granados, and J. Fierro, "Pd-modified $Cu--Zn$ catalysts for methanol synthesis from CO_2/H_2 mixtures: Catalytic structures and performance", Journal of Catalysis **210**, 285–294 (2002).

[80]J. Toyir, P. R. de la Piscina, J. L. G. Fierro, and N. Homs, "Highly effective conversion of CO_2 to methanol over supported and promoted copper-based catalysts: influence of support and promoter", Applied Catalysis B: Environmental **29**, 207–215 (2001).

[81]M. Saito, T. Fujitani, M. Takeuchi, and T. Watanabe, "Development of copper/zinc oxide-based multicomponent catalysts for methanol synthesis from carbon dioxide and hydrogen", Applied Catalysis A: General **138**, 311–318 (1996).

[82]L. Angelo, K. Kobl, L. M. M. Tejada, Y. Zimmermann, K. Parkhomenko, and A.-C. Roger, "Study of CuZnMOx oxides (m= Al, Zr, Ce, CeZr) for the catalytic hydrogenation of CO_2 into methanol", Comptes Rendus Chimie **18**, 250–260 (2015).

[83]J. Diez-Ramirez, F. Dorado, A. R. de la Osa, J. L. Valverde, and P. Sánchez, "Hydrogenation of CO_2 to methanol at atmospheric pressure over Cu/ZnO catalysts: influence of the calcination, reduction, and metal loading", Industrial & Engineering Chemistry Research **56**, 1979–1987 (2017).

[84]Z.-j. Wang, H. Song, H. Pang, Y. Ning, T. D. Dao, Z. Wang, H. Chen, Y. Weng, Q. Fu, T. Nagao, et al., "Photo-assisted methanol synthesis via CO_2 reduction under ambient pressure over plasmonic Cu/ZnO catalysts", Applied Catalysis B: Environmental **250**, 10–16 (2019).

[85]L. Wang, Y. Yi, H. Guo, and X. Tu, "Atmospheric pressure and room temperature synthesis of methanol through plasma-catalytic hydrogenation of CO_2", ACS Catalysis **8**, 90–100 (2018).

[86]V. Dieterich, A. Buttler, A. Hanel, H. Spliethoff, and S. Fendt, "Power-to-liquid via synthesis of methanol, DME or Fischer-Tropsch-fuels: a review", Energy & Environmental Science **13**, 3207–3252 (2020).

[87]P. Tijm, F. Waller, and D. Brown, "Methanol technology developments for the new millennium", Applied Catalysis A: General **221**, 275–282 (2001).

[88]G. Bozzano and F. Manenti, "Efficient methanol synthesis: perspectives, technologies and optimization strategies", Progress in Energy and Combustion Science **56**, 71–105 (2016).

[89]J. Sun, G. Yang, Y. Yoneyama, and N. Tsubaki, "Catalysis chemistry of dimethyl ether synthesis", ACS Catalysis **4**, 3346–3356 (2014).

[90]J. Park, J. Cho, M.-J. Park, and W. B. Lee, "Microkinetic modeling of DME synthesis from methanol over H-zeolite catalyst: associative vs. dissociative pathways", Catalysis Today (2020).

[91]Z. Azizi, M. Rezaeimanesh, T. Tohidian, and M. R. Rahimpour, "Dimethyl ether: a review of technologies and production challenges", Chemical Engineering and Processing: Process Intensification **82**, 150–172 (2014).

[92]W. Yan, W.-l. WANG, Y.-x. CHEN, J.-j. ZHENG, and R.-f. LI, "Synthesis of dimethyl ether from syngas using a hierarchically porous composite zeolite as the methanol dehydration catalyst", Journal of Fuel Chemistry and Technology **41**, 873–880 (2013).

[93]M. Rafati, L. Wang, D. C. Dayton, K. Schimmel, V. Kabadi, and A. Shahbazi, "Techno-economic analysis of production of Fischer-Tropsch liquids via biomass gasification: the effects of Fischer-Tropsch catalysts and natural gas co-feeding", Energy Conversion and Management **133**, 153–166 (2017).

[94]A. d. Klerk, *Fischer–Tropsch Process*, Kirk-Othmer Encyclopedia of Chemical Technology (John Wiley and Sons, 2013).

[95]H. Mahmoudi, M. Mahmoudi, O. Doustdar, H. Jahangiri, A. Tsolakis, S. Gu, and M. LechWyszynski, "A review of Fischer-Tropsch synthesis process, mechanism, surface chemistry and catalyst formulation", Biofuels Engineering **2**, 11–31 (2017).

[96]R. A. van Santen, A. J. Markvoort, I. A. Filot, M. M. Ghouri, and E. J. Hensen, "Mechanism and microkinetics of the Fischer-Tropsch reaction", Phys Chem Chem Phys **15**, 17038–63 (2013).

[97]R. Guettel, U. Kunz, and T. Turek, "Reactors for Fischer-Tropsch synthesis", Chemical Engineering & Technology: Industrial Chemistry-Plant Equipment-Process Engineering-Biotechnology **31**, 746–754 (2008).

[98]A. de Klerk, "Fischer–Tropsch refining: technology selection to match molecules", Green Chemistry **10**, 10.1039/b813233j (2008).

[99]E. van Steen and M. Claeys, "Fischer-Tropsch Catalysts for the Biomass-to-Liquid (BTL)-Process", Chemical Engineering & Technology: Industrial Chemistry-Plant Equipment-Process Engineering-Biotechnology **31**, 655–666 (2008).

[100]D. F. Rodríguez Vallejo and A. de Klerk, "Improving the interface between Fischer–Tropsch synthesis and refining", Energy & Fuels **27**, 3137–3147 (2013).

[101]T. Schaaf, J. Grünig, M. R. Schuster, T. Rothenfluh, and A. Orth, "Methanation of co2-storage of renewable energy in a gas distribution system", Energy, Sustainability and Society **4**, 1–14 (2014).

[102]J. Matthey, *World's largest single train methanol plants to use johnson matthey technology*, (Dec. 2020) https://matthey.com/news/2020/worlds-largest-single-train-methanol-plants-to-use-johnson-matthey-technology.

[103]T. E. Corporation, *Dme (dimethyl ether)*, (Aug. 2022) www.toyo-eng.com.

[104]Sasol, *Production and sales metrics*, tech. rep. (Sasol Limited, 2022).

[105]C. Wulf, A. Schreiber, and P. Zapp, "Review of power-to-gas projects in Europe", Frontiers in Energy Research **8**, 77–89 (2020).

[106]XE, *Historical rate tables*, (Oct. 2021) https://www.xe.com/currencytables/.

[107]D. Parra and M. K. Patel, "Techno-economic implications of the electrolyser technology and size for power-to-gas systems", International Journal of Hydrogen Energy **41**, 3748–3761 (2016).

[108]D. Parra, X. Zhang, C. Bauer, and M. K. Patel, "An integrated techno-economic and life cycle environmental assessment of power-to-gas systems", Applied energy **193**, 440–454 (2017).

[109]E. Giglio, A. Lanzini, M. Santarelli, and P. Leone, "Synthetic natural gas via integrated high-temperature electrolysis and methanation: Part I — Energy performance", Journal of Energy Storage **1**, 22–37 (2015).

[110]E. Giglio, A. Lanzini, M. Santarelli, and P. Leone, "Synthetic natural gas via integrated high-temperature electrolysis and methanation: Part II — Economic analysis", Journal of Energy Storage **2**, 64–79 (2015).

[111]D. Parigi, E. Giglio, A. Soto, and M. Santarelli, "Power-to-fuels through carbon dioxide re-utilization and high-temperature electrolysis: a technical and economical comparison between synthetic methanol and methane", Journal of cleaner production **226**, 679–691 (2019).

[112]S. McDonagh, R. O'Shea, D. M. Wall, J. P. Deane, and J. D. Murphy, "Modelling of a power-to-gas system to predict the levelised cost of energy of an advanced renewable gaseous transport fuel", Applied Energy **215**, 444–456 (2018).

[113]S. McDonagh, D. M. Wall, P. Deane, and J. D. Murphy, "The effect of electricity markets, and renewable electricity penetration, on the levelised cost of energy of an advanced electro-fuel system incorporating carbon capture and utilisation", Renewable Energy **131**, 364–371 (2019).

[114]C. Van Leeuwen and M. Mulder, "Power-to-gas in electricity markets dominated by renewables", Applied Energy **232**, 258–272 (2018).

[115]F. Salomone, E. Giglio, D. Ferrero, M. Santarelli, R. Pirone, and S. Bensaid, "Techno-economic modelling of a power-to-gas system based on soec electrolysis and CO_2 methanation in a RES-based electric grid", Chemical Engineering Journal **377**, 120233 (2019).

[116]G. Leonzio, "Design and feasibility analysis of a power-to-gas plant in germany", Journal of Cleaner Production **162**, 609–623 (2017).

[117]M. Van Dael, S. Kreps, A. Virag, K. Kessels, K. Remans, D. Thomas, and F. De Wilde, "Techno-economic assessment of a microbial power-to-gas plant–case study in belgium", Applied energy **215**, 416–425 (2018).

[118]J. Witte, J. Settino, S. M. Biollaz, and T. J. Schildhauer, "Direct catalytic methanation of biogas – Part I: New insights into biomethane production using rate-based modelling and detailed process analysis", Energy Conversion and Management **171**, 750–768 (2018).

[119]J. Witte, A. Kunz, S. M. Biollaz, and T. J. Schildhauer, "Direct catalytic methanation of biogas – Part II: Techno-economic process assessment and feasibility reflections", Energy conversion and management **178**, 26–43 (2018).

[120]D. H. König, M. Freiberg, R.-U. Dietrich, and A. Wörner, "Techno-economic study of the storage of fluctuating renewable energy in liquid hydrocarbons", Fuel **159**, 289–297 (2015).

[121]F. G. Albrecht, D. H. König, N. Baucks, and R.-U. Dietrich, "A standardized methodology for the techno-economic evaluation of alternative fuels – A case study", Fuel **194**, 511–526 (2017).

[122]R.-U. Dietrich, F. G. Albrecht, S. Maier, D. H. König, S. Estelmann, S. Adelung, Z. Bealu, and A. Seitz, "Cost calculations for three different approaches of biofuel production using biomass, electricity and CO_2", Biomass and Bioenergy **111**, 165–173 (2018).

[123]F. G. Albrecht and T.-V. Nguyen, "Prospects of electrofuels to defossilize transportation in Denmark – A techno-economic and ecological analysis", Energy **192**, 116511 (2020).

[124]E. Peduzzi, G. Boissonnet, G. Haarlemmer, and F. Maréchal, "Thermo-economic analysis and multi-objective optimisation of lignocellulosic biomass conversion to Fischer–Tropsch fuels", Sustainable Energy & Fuels **2**, 1069–1084 (2018).

[125]S. Schemme, J. L. Breuer, M. Köller, S. Meschede, F. Walman, R. C. Samsun, R. Peters, and D. Stolten, "H_2-based synthetic fuels: a techno-economic comparison of alcohol, ether and hydrocarbon production", International journal of hydrogen energy **45**, 5395–5414 (2020).

[126]P. Schmidt, V. Batteiger, A. Roth, W. Weindorf, and T. Raksha, "Power-to-liquids as renewable fuel option for aviation: A review", Chemie Ingenieur Technik **90**, 127–140 (2018).

[127]P. Schmidt, W. Weindorf, A. Roth, V. Batteiger, and F. Riegel, "Power-to-liquids — potentials and perspectives for the future supply of renewable aviation fuel", German Environment Agency, 1–32 (2016).

[128]J. Nyári, M. Magdeldin, M. Larmi, M. Järvinen, and A. Santasalo-Aarnio, "Techno-economic barriers of an industrial-scale methanol CCU-plant", Journal of CO_2 utilization **39**, 101166 (2020).

[129]D. Bellotti, A. Sorce, M. Rivarolo, and L. Magistri, "Techno-economic analysis for the integration of a power to fuel system with a CCS coal power plant", Journal of CO_2 Utilization **33**, 262–272 (2019).

[130]M. Bos, S. Kersten, and D. Brilman, "Wind power to methanol: Renewable methanol production using electricity, electrolysis of water and CO_2 air capture", Applied Energy **264**, 114672 (2020).

[131]C. Hank, S. Gelpke, A. Schnabl, R. J. White, J. Full, N. Wiebe, T. Smolinka, A. Schaadt, H.-M. Henning, and C. Hebling, "Economics & carbon dioxide avoidance cost of methanol production based on renewable hydrogen and recycled carbon dioxide–power-to-methanol", Sustainable Energy & Fuels **2**, 1244–1261 (2018).

[132]M. Bailera, P. Lisbona, B. Peña, and L. M. Romeo, "A review on CO_2 mitigation in the iron and steel industry through power to X processes", Journal of CO_2 Utilization **46**, 101456 (2021).

[133]H. Zhang, L. Wang, F. Maréchal, U. Desideri, et al., "Techno-economic evaluation of biomass-to-fuels with solid-oxide electrolyzer", Applied Energy **270**, 115113 (2020).

[134]N. Kassem, J. Hockey, C. Lopez, L. Lardon, L. T. Angenent, and J. W. Tester, "Integrating anaerobic digestion, hydrothermal liquefaction, and biomethanation within a power-to-gas framework for dairy waste management and grid decarbonization: A techno-economic assessment", Sustainable Energy & Fuels **4**, 4644–4661 (2020).

[135]M. Di Salvo and M. Wei, "Synthesis of natural gas from thermochemical and power-to-gas pathways for industrial sector decarbonization in California", Energy **182**, 1250–1264 (2019).

[136]S. Hienuki, H. Mitoma, M. Ogata, I. Uchida, and S. Kagawa, "Environmental and energy life cycle analyses of passenger vehicle systems using fossil fuel-derived hydrogen", International Journal of Hydrogen Energy (2021).

[137]Y. Li, W. Gao, and Y. Ruan, "Potential and sensitivity analysis of long-term hydrogen production in resolving surplus RES generation — a case study in Japan", Energy **171**, 1164–1172 (2019).

[138]Z. Chehade, C. Mansilla, P. Lucchese, S. Hilliard, and J. Proost, "Review and analysis of demonstration projects on power-to-X pathways in the world", International Journal of Hydrogen Energy **44**, 27637–27655 (2019).

[139]M. Thema, F. Bauer, and M. Sterner, "Power-to-gas: Electrolysis and methanation status review", Renewable and Sustainable Energy Reviews **112**, 775–787 (2019).

[140]M. Bailera, P. Lisbona, L. M. Romeo, and S. Espatolero, "Power to gas projects review: lab, pilot and demo plants for storing renewable energy and co2", Renewable and Sustainable Energy Reviews **69**, 292–312 (2017).

[141]R. Otten, "The first industrial ptg plant-audi e-gas as driver for the energy turnaround", CEDEC Gas Day (2014).

[142]EU, *Delfzijl joint development of green water electrolysis at large scale*, (Oct. 2021) `https://cordis.europa.eu/project/id/826089`.

[143]M. Samavati, "Design and analysis of solid oxide electrolysis-based systems for synthetic liquid fuels production", PhD thesis (KTH Royal Institute of Technology, 2018).

[144]S.-H. Lee, J.-W. Lee, S.-B. Lee, S.-J. Park, R.-H. Song, U.-J. Yun, and T.-H. Lim, "Electrochemical performance of H_2O-CO_2 coelectrolysis with a tubular solid oxide coelectrolysis (SOC) cell", International Journal of Hydrogen Energy **41**, 7530–7537 (2016).

[145]B. Chen, H. Xu, and M. Ni, "Modelling of SOEC-FT reactor: pressure effects on methanation process", Applied energy **185**, 814–824 (2017).

[146]M. Samavati, M. Santarelli, A. Martin, and V. Nemanova, "Thermodynamic and economy analysis of solid oxide electrolyser system for syngas production", Energy **122**, 37–49 (2017).

[147]L. Wang, M. Rao, S. Diethelm, T.-E. Lin, H. Zhang, A. Hagen, F. Maréchal, et al., "Power-to-methane via co-electrolysis of H_2O and CO_2: the effects of pressurized operation and internal methanation", Applied Energy **250**, 1432–1445 (2019).

[148]Q. Fu, C. Mabilat, M. Zahid, A. Brisse, and L. Gautier, "Syngas production via high-temperature steam/CO_2 co-electrolysis: an economic assessment", Energy & Environmental Science **3**, 1382–1397 (2010).

[149]M. Ni, "An electrochemical model for syngas production by co-electrolysis of H_2O and CO_2", Journal of power sources **202**, 209–216 (2012).

[150]J. P. Stempien, O. L. Ding, Q. Sun, and S. H. Chan, "Energy and exergy analysis of solid oxide electrolyser cell (SOEC) working as a CO_2 mitigation device", International Journal of Hydrogen Energy **37**, 14518–14527 (2012).

[151]V. Menon, Q. Fu, V. M. Janardhanan, and O. Deutschmann, "A model-based understanding of solid-oxide electrolysis cells (SOECs) for syngas production by H_2O/CO_2 co-electrolysis", Journal of Power Sources **274**, 768–781 (2015).

[152]Z. Zhan, W. Kobsiriphat, J. R. Wilson, M. Pillai, I. Kim, and S. A. Barnett, "Syngas production by coelectrolysis of CO_2/H_2O: the basis for a renewable energy cycle", Energy & Fuels **23**, 3089–3096 (2009).

[153]A. Zaccara, A. Petrucciani, I. Matino, T. A. Branca, S. Dettori, V. Iannino, V. Colla, M. Bampaou, and K. Panopoulos, "Renewable hydrogen production processes for the off-gas valorization in integrated steelworks through hydrogen intensified methane and methanol syntheses", Metals **10**, 1535 (2020).

[154]M. Hauck, S. Herrmann, and H. Spliethoff, "Simulation of a reversible SOFC with aspen plus", International Journal of Hydrogen Energy **42**, 10329–10340 (2017).

[155]S. Ali, K. Sørensen, and M. P. Nielsen, "Modeling a novel combined solid oxide electrolysis cell (SOEC)-biomass gasification renewable methanol production system", Renewable Energy **154**, 1025–1034 (2020).

[156]G. Léonard, D. Giulini, and D. Villarreal-Singer, "Design and evaluation of a high-density energy storage route with CO_2 re-use, water electrolysis and methanol synthesis", in *Computer aided chemical engineering*, Vol. 38 (Elsevier, 2016), pp. 1797–1802.

[157]E. Giglio, A. Lanzini, M. Santarelli, and P. Leone, "Synthetic natural gas via integrated high-temperature electrolysis and methanation: Part I — Energy performance", Journal of Energy Storage **1**, 22–37 (2015).

[158]R. Chauvy, L. Dubois, P. Lybaert, D. Thomas, and G. De Weireld, "Production of synthetic natural gas from industrial carbon dioxide", Applied Energy **260**, 114249 (2020).

[159]L. ErikØi, "Comparison of aspen HYSYS and aspen plus simulation of CO_2 absorption into MEA from atmospheric gas", Energy Procedia **23**, 360–369 (2012).

[160]W. K. Lewis and W. G. Whitman, "Principles of gas absorption.", Industrial & Engineering Chemistry **16**, 1215–1220 (1924).

[161]C. Madeddu, M. Errico, and R. Baratti, *CO_2 capture by reactive absorption-stripping modelling, analysis and design* (Feb. 2019).

[162]†. Kvamsdal and G. Rochelle, "Effects of the temperature bulge in CO_2 absorption from flue gas by aqueous monoethanolamine", Industrial and Engineering Chemistry Research **47**, `10.1021/ie061651s` (2008).

[163]P. Tontiwachwuthikul, A. Meisen, and C. J. Lim, "CO_2 absorption by NaOH, monoethanolamine and 2-amino-2-methyl-1-propanol solutions in a packed column", Chemical engineering science **47**, 381–390 (1992).

[164]N. Razi, H. F. Svendsen, and O. Bolland, "Validation of mass transfer correlations for CO_2 absorption with MEA using pilot data", International Journal of Greenhouse Gas Control **19**, 478–491 (2013).

[165]C. Madeddu, M. Errico, and R. Baratti, "Process analysis for the carbon dioxide chemical absorption–regeneration system", Applied energy **215**, 532–542 (2018).

[166]R. E. Dugas, "Pilot plant study of carbon dioxide capture by aqueous monoethanolamine", MSE Thesis, University of Texas at Austin (2006).

[167]A. Kiani, K. Jiang, and P. Feron, "Techno-economic assessment for CO_2 capture from air using a conventional liquid-based absorption process", Frontiers in Energy Research **8**, 92 (2020).

[168]A. Kothandaraman, L. Nord, O. Bolland, H. J. Herzog, and G. J. McRae, "Comparison of solvents for post-combustion capture of CO_2 by chemical absorption", Energy procedia **1**, 1373–1380 (2009).

[169]J. M. Douglas, *Conceptual design of chemical processes*, Vol. 1110 (McGraw-Hill New York, 1988).

[170]J. Gao, Y. Wang, Y. Ping, D. Hu, G. Xu, F. Gu, and F. Su, "A thermodynamic analysis of methanation reactions of carbon oxides for the production of synthetic natural gas", RSC advances **2**, 2358–2368 (2012).

[171]D.-Y. Peng and D. B. Robinson, "A new two-constant equation of state", Industrial & Engineering Chemistry Fundamentals **15**, 59–64 (1976).

[172]J. Kopyscinski, T. J. Schildhauer, F. Vogel, S. M. A. Biollaz, and A. Wokaun, "Applying spatially resolved concentration and temperature measurements in a catalytic plate reactor for the kinetic study of CO methanation", Journal of Catalysis **271**, 262–279 (2010).

[173]X. Bai, S. Wang, T. Sun, and S. Wang, "The sintering of Ni/Al_2O_3 methanation catalyst for substitute natural gas production", Reaction Kinetics, Mechanisms and Catalysis **112**, 437–451 (2014).

[174]G. Graaf, E. Stamhuis, and A. Beenackers, "Kinetics of low-pressure methanol synthesis", Chemical Engineering Science **43**, 3185–3195 (1988).

[175]G. Graaf and A. Beenackers, "Comparison of two-phase and three-phase methanol synthesis processes", Chemical Engineering and Processing: Process Intensification **35**, 413–427 (1996).

[176]G. Bercic and J. Levec, "Catalytic dehydration of methanol to dimethyl ether. kinetic investigation and reactor simulation", Industrial & engineering chemistry research **32**, 2478–2484 (1993).

[177]S. Al-Dawery, "Methanol removal from methanol-water mixture using municipal activated sludge", Journal of Engineering Science and Technology **8**, 578–587 (2013).

[178]D. Takaiwa, E. Yamamoto, K. Yasuoka, et al., "Water–methanol separation with carbon nanotubes and electric fields", Nanoscale **7**, 12659–12665 (2015).

[179]O. O. James, B. Chowdhury, M. A. Mesubi, and S. Maity, "Reflections on the chemistry of the Fischer–Tropsch synthesis", Rsc Advances **2**, 7347–7366 (2012).

[180]B. Todic, T. Bhatelia, G. F. Froment, W. Ma, G. Jacobs, B. H. Davis, and D. B. Bukur, "Kinetic model of Fischer–Tropsch synthesis in a slurry reactor on $Co--Re/Al_2O_3$ catalyst", Industrial & Engineering Chemistry Research **52**, 669–679 (2013).

[181]M. Hillestad, "Modeling the Fischer–Tropsch product distribution and model implementation", Chemical Product and Process Modeling **10**, 147–159 (2015).

[182]B. Todic, W. Ma, G. Jacobs, B. H. Davis, and D. B. Bukur, "CO-insertion mechanism based kinetic model of the Fischer–Tropsch synthesis reaction over Re-promoted Co catalyst", Catalysis Today **228**, 32–39 (2014).

[183]W. D. Shafer, M. K. Gnanamani, U. M. Graham, J. Yang, C. M. Masuku, G. Jacobs, and B. H. Davis, "Fischer–Tropsch: product selectivity–the fingerprint of synthetic fuels", Catalysts **9**, 259 (2019).

[184]I. J. Okeke and S. Mani, "Techno-economic assessment of biogas to liquid fuels conversion technology via Fischer-Tropsch synthesis", Biofuels, Bioproducts and Biorefining **11**, 472–487 (2017).

[185]F. Campanario and F. G. Ortiz, "Techno-economic assessment of bio-oil aqueous phase-to-liquids via Fischer-Tropsch synthesis and based on supercritical water reforming", Energy Conversion and Management **154**, 591–602 (2017).

[186]U. Pandey, A. Runningen, L. Gavrilović, E. A. Jørgensen, K. R. Putta, K. R. Rout, E. Rytter, E. A. Blekkan, and M. Hillestad, "Modeling Fischer–Tropsch kinetics and product distribution over a cobalt catalyst", AIChE Journal, e17234 (2021).

[187]M. A. Baltanas, H. Vansina, and G. F. Froment, "Hydroisomerization and hydrocracking. 5. kinetic analysis of rate data for n-octane", Industrial & engineering chemistry product research and development **22**, 531–539 (1983).

[188]L. A. Pellegrini, S. Gamba, V. Calemma, and S. Bonomi, "Modelling of hydrocracking with vapour–liquid equilibrium", Chemical engineering science **63**, 4285–4291 (2008).

[189]H. Monzón and M. A. Laguna-Bercero, "Co2 and steam electrolysis using a microtubular solid oxide cell", Journal of Physics: Energy **2**, 014005 (2019).

[190]Y. İçıngür and D. Altiparmak, "Effect of fuel cetane number and injection pressure on a di diesel engine performance and emissions", Energy conversion and management **44**, 389–397 (2003).

[191]Z. Zhu, H. Guo, A. Zhou, D. Li, and S. Liu, "One way to reduce the no x emission of biodiesels: the increase of cetane number", International journal of green energy **13**, 957–962 (2016).

[192]J. Jenčík, V. Hönig, M. Obergruber, J. Hájek, A. Vráblík, R. Černy, D. Schlehöfer, and T. Herink, "Advanced biofuels based on fischer–tropsch synthesis for applications in diesel engines", Materials **14**, 3077 (2021).

[193]A. Lappas and E. Heracleous, "Production of biofuels via fischer–tropsch synthesis: biomass-to-liquids", in *Handbook of biofuels production* (Elsevier, 2016), pp. 549–593.

[194]F. Andrade Torres, O. Doustdar, J. M. Herreros, R. Li, R. Poku, A. Tsolakis, J. Martins, and S. A. Vieira de Melo, "A comparative study of biofuels and fischer–tropsch diesel blends on the engine combustion performance for reducing exhaust gaseous and particulate emissions", Energies **14**, 1538 (2021).

[195]Worldwide Fuel Charter, *Gasoline and diesel fuel*.

[196]K. Winans, A. Kendall, and H. Deng, "The history and current applications of the circular economy concept", Renewable and Sustainable Energy Reviews **68**, 825–833 (2017).

[197]IEA, *CO_2 emissions from fuel combustion: overview (2019 edition)*, Report, All rights reserved (International Energy Agency, 2019).

[198]H. Naims, "Economics of carbon dioxide capture and utilization-a supply and demand perspective", Environ Sci Pollut Res Int **23**, 22226–22241 (2016).

[199]C. Brief, *Global coal power*, Web Page, 2019.

[200]N. von der Assen, L. J. Muller, A. Steingrube, P. Voll, and A. Bardow, "Selecting CO_2 sources for CO_2 utilization by environmental-merit-order curves", Environ Sci Technol **50**, 1093–101 (2016).

[201]IEA, *Transforming industry through CCUS*, Web Page, 2019.

[202]D. L. Sanchez, N. Johnson, S. T. McCoy, P. A. Turner, and K. J. Mach, "Near-term deployment of carbon capture and sequestration from biorefineries in the United States", Proceedings of the National Academy of Sciences **115**, 4875 (2018).

[203]S. Aryana, M. Ahmadi, G. Gomes Vincent, A. Romagnoli Jose, and K. Ngian, *Modelling and optimisation of an industrial ethylene oxide reactor*, Generic, 2009.

[204]I. Sreedhar, T. Nahar, A. Venugopal, and B. Srinivas, "Carbon capture by absorption – path covered and ahead", Renewable and Sustainable Energy Reviews **76**, 1080–1107 (2017).

[205]T. N.Borhani and M. Wang, "Role of solvents in CO_2 capture processes: the review of selection and design methods", Renewable and Sustainable Energy Reviews **114**, 10.1016/j.rser.2019.109299 (2019).

[206]D. A. Glasscock, J. E. Critchfield, and G. T. Rochelle, "CO_2 absorption/desorption in mixtures of methyldiethanolamine with monoethanolamine or diethanolamine", Chemical Engineering Science **46**, 2829–2845 (1991).

[207]T. N. Borhani, E. Oko, and M. Wang, "Process modelling, validation and analysis of rotating packed bed stripper in the context of intensified CO_2 capture with MEA", Journal of Industrial and Engineering Chemistry **75**, 285–295 (2019).

[208]T. Li and T. C. Keener, "A review: desorption of CO_2 from rich solutions in chemical absorption processes", International Journal of Greenhouse Gas Control **51**, 290–304 (2016).

[209]F. Vega, F. M. Baena-Moreno, L. M. Gallego Fernández, E. Portillo, B. Navarrete, and Z. Zhang, "Current status of CO_2 chemical absorption research applied to CCS: towards full deployment at industrial scale", Applied Energy **260**, 10.1016/j.apenergy.2019.114313 (2020).

[210]U. H. Bhatti, A. K. Shah, J. N. Kim, J. K. You, S. H. Choi, D. H. Lim, S. Nam, Y. H. Park, and I. H. Baek, "Effects of transition metal oxide catalysts on MEA solvent regeneration for the post-combustion carbon capture process", ACS Sustainable Chemistry & Engineering **5**, 5862–5868 (2017).

[211]A. H. Alami, A. Abu Hawili, M. Tawalbeh, R. Hasan, L. Al Mahmoud, S. Chibib, A. Mahmood, K. Aokal, and P. Rattanapanya, "Materials and logistics for carbon dioxide capture, storage and utilization", Sci Total Environ **717**, 137221 (2020).

[212]M. Innovation, "Accelerating breakthrough innovation in carbon capture, utilization, and storage", in Report of the mission innovation carbon capture, utilization, and storage experts' workshop. available online at: https://www. energy. gov/fe/downloads/accelerating-breakthrough-innovationcarbon-capture-utilization-and-storage (accessed march 01, 2019) (2017).

[213]N. Jiang, Y. Shen, B. Liu, D. Zhang, Z. Tang, G. Li, and B. Fu, "CO_2 capture from dry flue gas by means of VPSA, TSA and TVSA", Journal of CO_2 Utilization, 10.1016/j.jcou.2019.09.012 (2019).

[214]X. Zhu, S. Li, Y. Shi, and N. Cai, "Recent advances in elevated-temperature pressure swing adsorption for carbon capture and hydrogen production", Progress in Energy and Combustion Science **75**, 10.1016/j.pecs.2019.100784 (2019).

[215]L. Jiang, A. P. Roskilly, and R. Z. Wang, "Performance exploration of temperature swing adsorption technology for carbon dioxide capture", Energy Conversion and Management **165**, 396–404 (2018).

[216]Q. Zhao, F. Wu, Y. He, P. Xiao, and P. A. Webley, "Impact of operating parameters on CO_2 capture using carbon monolith by electrical swing adsorption technology (ESA)", Chemical Engineering Journal **327**, 441–453 (2017).

[217]D. P. Hanak, S. Michalski, and V. Manovic, "From post-combustion carbon capture to sorption-enhanced hydrogen production: a state-of-the-art review of carbonate looping process feasibility", Energy Conversion and Management **177**, 428–452 (2018).

[218]A. Rolfe, Y. Huang, M. Haaf, S. Rezvani, D. McLIveen-Wright, and N. J. Hewitt, "Integration of the calcium carbonate looping process into an existing pulverized coal-fired power plant for CO_2 capture: techno-economic and environmental evaluation", Applied Energy **222**, 169–179 (2018).

[219]F. E. Furcas, W. Pragot, R. Chacartegui, and W. Afzal, "Sodium carbonate-based post combustion carbon capture utilising trona as main sorbent feed stock", Energy Conversion and Management **208**, 10.1016/j.enconman.2020.112484 (2020).

[220]M. Matzen, J. Pinkerton, X. Wang, and Y. Demirel, "Use of natural ores as oxygen carriers in chemical looping combustion: a review", International Journal of Greenhouse Gas Control **65**, 1–14 (2017).

[221]T. Mattisson, M. Keller, C. Linderholm, P. Moldenhauer, M. Rydén, H. Leion, and A. Lyngfelt, "Chemical-looping technologies using circulating fluidized bed systems: status of development", Fuel Processing Technology **172**, 1–12 (2018).

[222]I. Adánez-Rubio, A. Pérez-Astray, A. Abad, P. Gayán, L. F. De Diego, and J. Adánez, "Chemical looping with oxygen uncoupling: an advanced biomass combustion technology to avoid CO_2 emissions", Mitigation and Adaptation Strategies for Global Change **24**, 1293–1306 (2019).

[223]S. N. Shoghl, A. Raisi, and A. Aroujalian, "Modeling of gas solubility and permeability in glassy and rubbery membranes using lattice fluid theory", Polymer **115**, 184–196 (2017).

[224]I. Sreedhar, R. Vaidhiswaran, B. M. Kamani, and A. Venugopal, "Process and engineering trends in membrane based carbon capture", Renewable and Sustainable Energy Reviews **68**, 659–684 (2017).

[225]Y. Han, D. Wu, and W. W. Ho, "Nanotube-reinforced facilitated transport membrane for CO_2/N_2 separation with vacuum operation", Journal of membrane science **567**, 261–271 (2018).

[226]X. Li, L. Ma, H. Zhang, S. Wang, Z. Jiang, R. Guo, H. Wu, X. Cao, J. Yang, and B. Wang, "Synergistic effect of combining carbon nanotubes and graphene oxide in mixed matrix membranes for efficient CO_2 separation", Journal of Membrane Science **479**, 1–10 (2015).

[227]S. Roussanaly, M. Vitvarova, R. Anantharaman, D. Berstad, B. Hagen, J. Jakobsen, V. Novotny, and G. Skaugen, "Techno-economic comparison of three technologies for precombustion CO_2 capture from a lignite-fired IGCC", Frontiers of Chemical Science and Engineering, `10.1007/s11705-019-1870-8` (2019).

[228]A.-M. Cormos and C.-C. Cormos, "Techno-economic assessment of combined hydrogen & power co-generation with carbon capture: the case of coal gasification", Applied Thermal Engineering **147**, 29–39 (2019).

[229]M. Gazzani, E. Macchi, and G. Manzolini, "CO_2 capture in natural gas combined cycle with SEWGS. Part A: thermodynamic performances", International journal of greenhouse gas control **12**, 493–501 (2013).

[230]K. Smith, G. Xiao, K. Mumford, J. Gouw, I. Indrawan, N. Thanumurthy, D. Quyn, R. Cuthbertson, A. Rayer, N. Nicholas, et al., "Demonstration of a concentrated potassium carbonate process for CO_2 capture", Energy & fuels **28**, 299–306 (2014).

[231]M. Stec, A. Tatarczuk, L. Więcław-Solny, A. Krótki, T. Spietz, A. Wilk, and D. Śpiewak, "Demonstration of a post-combustion carbon capture pilot plant using amine-based solvents at the Łaziska power plant in Poland", Clean Technologies and Environmental Policy **18**, 151–160 (2016).

[232]S. Krishnamurthy, V. R. Rao, S. Guntuka, P. Sharratt, R. Haghpanah, A. Rajendran, M. Amanullah, I. A. Karimi, and S. Farooq, "CO_2 capture from dry flue gas by vacuum swing adsorption: a pilot plant study", AIChE Journal **60**, 1830–1842 (2014).

[233]E. Osagie, C. Biliyok, G. Di Lorenzo, D. P. Hanak, and V. Manovic, "Techno-economic evaluation of the 2-amino-2-methyl-1-propanol (AMP) process for CO_2 capture from natural gas combined cycle power plant", International Journal of Greenhouse Gas Control **70**, 45–56 (2018).

[234]S. Seddighi, D. Pallares, F. Normann, and F. Johnsson, "Heat extraction from a utility-scale oxy-fuel-fired CFB boiler", Chemical Engineering Science **130**, 144–150 (2015).

[235]S. Seddighi, P. T. Clough, E. J. Anthony, R. W. Hughes, and P. Lu, "Scale-up challenges and opportunities for carbon capture by oxy-fuel circulating fluidized beds", Applied energy **232**, 527–542 (2018).

[236]F. Carrasco-Maldonado, R. Spörl, K. Fleiger, V. Hoenig, J. Maier, and G. Scheffknecht, "Oxy-fuel combustion technology for cement production–state of the art research and technology development", International Journal of Greenhouse Gas Control **45**, 189–199 (2016).

[237]Y. Tang and F. You, "Life cycle environmental and economic analysis of pulverized coal oxy-fuel combustion combining with calcium looping process or chemical looping air separation", Journal of Cleaner Production **181**, 271–292 (2018).

[238]Global CCS Institute, *Global status of CCS 2021: CCS accelerating to net zero* (Australia, 2021), p. 44.

[239]IEA, *Ccus around the world* (Paris, 2021).

[240]Carbon Engineering, *Our technology*, (2021) `https://carbonengineering.com/our-technology/` (visited on 10/25/2021).

[241]D. W. Keith, G. Holmes, D. St. Angelo, and K. Heidel, "A process for capturing CO_2 from the atmosphere", Joule **2**, 1573–1594 (2018).

[242]P. Bains, P. Psarras, and J. Wilcox, "CO_2 capture from the industry sector", Progress in Energy and Combustion Science **63**, 146–172 (2017).

[243]S. Budinis, S. Krevor, N. M. Dowell, N. Brandon, and A. Hawkes, "An assessment of CCS costs, barriers and potential", Energy Strategy Reviews **22**, 61–81 (2018).

[244]IEAGHG, *Proceedings: CCS cost network, 2017 workshop*, tech. rep. (IEAGHG, Mar. 2018).

[245]T. Fleiter, A. Herbst, M. Rehfeldt, and M. Arens, "Industrial innovation: pathways to deep decarbonisation of industry. part 2: scenario analysis and pathways to deep decarbonisation", (2019).

[246]H. Gerbelová, M. van der Spek, and W. Schakel, "Feasibility assessment of CO_2 capture retrofitted to an existing cement plant: post-combustion vs. oxy-fuel combustion technology", Energy Procedia **114**, 6141–6149 (2017).

[247]C. Nwaoha and P. Tontiwachwuthikul, "Carbon dioxide capture from pulp mill using 2-amino-2-methyl-1-propanol and monoethanolamine blend: techno-economic assessment of advanced process configuration", Applied Energy **250**, 1202–1216 (2019).

[248]A. Mathisen, H. Sørensen, N. Eldrup, R. Skagestad, M. Melaaen, and G. I. Müller, "Cost optimised CO_2 capture from aluminium production", Energy Procedia **51**, 184–190 (2014).

[249]H. Jilvero, A. Mathisen, N.-H. Eldrup, F. Normann, F. Johnsson, G. I. Müller, and M. C. Melaaen, "Techno-economic analysis of carbon capture at an aluminum production plant – comparison of post-combustion capture using MEA and ammonia", Energy Procedia **63**, 6590–6601 (2014).

[250]F. T. F. da Silva, F. M. Carvalho, J. L. G. Corrêa, P. R. d. C. Merschmann, I. S. Tagomori, A. Szklo, and R. Schaeffer, "CO_2 capture in ethanol distilleries in brazil: designing the optimum carbon transportation network by integrating hubs, pipelines and trucks", International Journal of Greenhouse Gas Control **71**, 168–183 (2018).

[251]IEAGHG, *CO_2 capture in natural gas production by adsorption processes for CO_2 storage, eor and egr*, tech. rep. (IEAGHG, Feb. 2017).

[252]R. S. Middleton, A. F. Clarens, X. Liu, J. M. Bielicki, and J. S. Levine, "CO_2 deserts: implications of existing CO_2 supply limitations for carbon management", Environmental science & technology **48**, 11713–11720 (2014).

[253]M. Mazzotti, R. Baciocchi, M. J. Desmond, and R. H. Socolow, "Direct air capture of CO_2 with chemicals: optimization of a two-loop hydroxide carbonate system using a countercurrent air-liquid contactor", Climatic change **118**, 119–135 (2013).

[254]G. Reiter and J. Lindorfer, "Evaluating CO_2 sources for power-to-gas applications – a case study for austria", Journal of CO2 Utilization **10**, 40–49 (2015).

[255]I. GHG, "Iron and steel CCS study (techno-economics integrated steel mill)", Paris, France: IEA (2013).

[256]K. Koring, V. Hoenig, H. Hoppe, J. Horsh, C. Suchak, V. Llevenz, and B. Emberger, "Deployment of CCS in the cement industry", IEA Report 2013 **19** (2013).

[257]S. Herron, A. Zoelle, and W. M. Summers, *Cost of capturing CO_2 from industrial sources*, tech. rep. (NETL, 2014).

[258]K. Onarheim, S. Santos, P. Kangas, and V. Hankalin, "Performance and costs of CCS in the pulp and paper industry Part 1: performance of amine-based post-combustion CO_2 capture", International Journal of Greenhouse Gas Control **59**, 58–73 (2017).

[259]BEIS, *2020 UK greenhouse gas emissions, provisional figures*, National Statistics (Department for Business, Energy & Industrial Strategy, 2021).

[260]BEIS, *UK energy statistics, Q1 2020*, National Statistics (Department for Business, Energy & Industrial Strategy, June 2020).

[261]S. Evans, "Analysis: Coronavirus set to cause largest ever annual fall in CO_2 emissions", Carbon Brief **9** (2020).

[262]IEA, *Material efficiency in clean energy transitions*, 2019.

[263]BEIS, *UK enshrines new target in law to slash emissions by 78% by 2035*, Press Release (Department for Business, Energy & Industrial Strategy, Apr. 2021).

[264]*BS 4105:1990 : specification for liquid carbon dioxide, industrial*, tech. rep. (British Standards Institution, 1991).

[265]EIGA WG-8, *Doc 70/17 - carbon dioxide food and beverages grade, source qualification, quality standards and verification*, tech. rep. (European Industrial Gases Association AISBL, 2016).

[266]B. Wetenhall, J. Race, and M. Downie, "The effect of CO_2 purity on the development of pipeline networks for carbon capture and storage schemes", International Journal of Greenhouse Gas Control **30**, 197–211 (2014).

[267]P. A. Brownsort, "Briefing on carbon dioxide specifications for transport", (2019).

[268]BEIS, *Consultation on the early phase out of unabated coal generation in great britain*, Consultation (BEIS, 2021).

[269]Mauna Loa Observatory, *Monthly co2*, (2021) `https://www.co2.earth/monthly-co2`.

[270]M. Fernández-Martínez, J. Sardans, F. Chevallier, P. Ciais, M. Obersteiner, S. Vicca, J. Canadell, A. Bastos, P. Friedlingstein, S. Sitch, et al., "Global trends in carbon sinks and their relationships with CO_2 and temperature", Nature Climate Change **9**, 73–79 (2019).

[271]T. DeVries, C. Le Quéré, O. Andrews, S. Berthet, J. Hauck, T. Ilyina, P. Landschützer, A. Lenton, I. D. Lima, M. Nowicki, et al., "Decadal trends in the ocean carbon sink", Proceedings of the National Academy of Sciences **116**, 11646–11651 (2019).

[272]P. P. Tans, "Nurturing natural carbon sinks", Climate 2020 (2016).

[273]W. Foster, U. Azimov, P. Gauthier-Maradei, L. C. Molano, M. Combrinck, J. Munoz, J. J. Esteves, and L. Patino, "Waste-to-energy conversion technologies in the UK: processes and barriers–a review", Renewable and Sustainable Energy Reviews **135**, 110226 (2021).

[274]N. N.-F. C. Centre, *Official Biogas Map*, (Apr. 2021) `https://www.biogas-info.co.uk/biogas_map_2020_site_list_external/`.

[275]D. M. Riley, J. Tian, G. Güngör-Demirci, P. Phelan, J. R. Villalobos, and R. J. Milcarek, "Techno-economic assessment of CHP systems in wastewater treatment plants", Environments **7**, 74 (2020).

[276]T. Pröll and F. Zerobin, "Biomass-based negative emission technology options with combined heat and power generation", Mitigation and Adaptation Strategies for Global Change **24**, 1307–1324 (2019).

[277]IEAGHG, *Towards zero emissions CCS from power stations using higher capture rates or biomass*, tech. rep. 2 (IEAGHG, Mar. 2019).

[278]BEIS, *Digest of united kingdom energy statistics 2020*, National Statistics (BEIS, 2020).

[279]NGN, *Biomethane: a producer's handbook*, Oniline, https://biomethane.northerngasnetworks.co.uk/do library/, 2021.

[280]AVR, *Biogas*, (2021) `https://www.avkuk.co.uk/en-gb/gas-supply/biogas`.

[281]GENECO, *Biomethane*, (2019) `https://www.geneco.uk.com/Biomethane/`.

[282]C. Kavuma, *Variation of methane and carbon dioxide yield in a biogas plant*, 2013.

[283]W. Köppel, M. Götz, and F. Graf, "Biogas upgrading for injection into the gas grid", Gwf-Gas Erdgas **150**, 26–35 (2009).

[284]Y. Li, C. P. Alaimo, M. Kim, N. Y. Kado, J. Peppers, J. Xue, C. Wan, P. G. Green, R. Zhang, B. M. Jenkins, et al., "Composition and toxicity of biogas produced from different feedstocks in California", Environmental science & technology **53**, 11569–11579 (2019).

[285]U. Onthong and N. Juntarachat, "Evaluation of biogas production potential from raw and processed agricultural wastes", Energy Procedia **138**, 205–210 (2017).

[286]A. M. Enitan, J. Adeyemo, F. M. Swalaha, and F. Bux, "Anaerobic digestion model to enhance treatment of brewery wastewater for biogas production using UASB reactor", Environmental Modeling & Assessment **20**, 673–685 (2015).

[287]S. Rasi, *Biogas composition and upgrading to biomethane*, 202 (University of Jyväskylä, 2009).

[288]C. Rashama, G. Ijoma, and T. Matambo, "Biogas generation from by-products of edible oil processing: a review of opportunities, challenges and strategies", Biomass Conversion and Biorefinery, 1–24 (2019).

[289]t. E4Tech (UK) Ltd report for department of transport in partnership with TRL and scarlett research, *Advanced drop in biofuels - UK production capacity outlook to 2030*, (Feb. 2017) `https://www.gov.uk/government/publications/advanced-drop-in-biofuels-uk-production-capacity-outlook-to-2030`.

[290]A. Molino, V. Larocca, S. Chianese, and D. Musmarra, "Biofuels production by biomass gasification: a review", Energies **11**, 811 (2018).

[291]WRA, *What is the Wood Recyclers Association?*, (2021) `https://woodrecyclers.org/`.

[292]CoGen, *Projects*, (2018) `https://www.cogenuk.com/projects`.

[293]C. Dinca, N. Slavu, C.-C. Cormoş, and A. Badea, "CO_2 capture from syngas generated by a biomass gasification power plant with chemical absorption process", Energy **149**, 925–936 (2018).

[294]P. French, *England overtakes scotland in distillery numbers for the first time*, (Jan. 2019) `https://www.thedrinksbusiness.com/2019/01/england-overtakes-scotland-in-distillery-numbers-for-the-first-time/`.

[295]R. C. Roland Arnison, *Circular economy evidence building programme: sector study on beer, whisky and fish*, tech. rep. (Ricardo-AEA, 2015).

[296]Whisky Invest Direct, *Grain whisky distilleries in Scotland*, (Apr. 2021) `https://www.whiskyinvestdirect.com/about-whisky/grain-whisky-distilleries-in-scotland`.

[297]Whisky Invest Direct, *Malt whisky distilleries in Scotland*, (Apr. 2021) `https://www.whiskyinvestdirect.com/about-whisky/malt-whisky-distilleries-in-scotland`.

[298]A. Kumar and S. R. Samadder, "A review on technological options of waste to energy for effective management of municipal solid waste", Waste Management **69**, 407–422 (2017).

[299]EC, *Council directive 2008/98/EC of the european parliament and of the council of 19 november 2008 on waste and repealing certain directives oj l 312*, Nov. 2008.

[300]DEFRA, *Statistics on waste managed by local authorities in england in 2019/20*, National Statistics (Department for Environment, Food & Rural Affairs, 2021).

[301]N. S. Louise Smith, *Waste incineration facilities*, Debate Pack (The House of Commons Library, 2020).

[302]Y. Tang, J. Dong, G. Li, Y. Zheng, Y. Chi, A. Nzihou, E. Weiss-Hortala, and C. Ye, "Environmental and exergetic life cycle assessment of incineration-and gasification-based waste to energy systems in China", Energy **205**, 118002 (2020).

[303]M. He, Z. Hu, B. Xiao, J. Li, X. Guo, S. Luo, F. Yang, Y. Feng, G. Yang, and S. Liu, "Hydrogen-rich gas from catalytic steam gasification of municipal solid waste (MSW): influence of catalyst and temperature on yield and product composition", International Journal of Hydrogen Energy **34**, 195–203 (2009).

[304]J. Li, S. Liao, W. Dan, K. Jia, and X. Zhou, "Experimental study on catalytic steam gasification of municipal solid waste for bioenergy production in a combined fixed bed reactor", Biomass and Bioenergy **46**, 174–180 (2012).

[305]M. Irfan, A. Li, L. Zhang, M. Wang, C. Chen, and S. Khushk, "Production of hydrogen enriched syngas from municipal solid waste gasification with waste marble powder as a catalyst", International Journal of Hydrogen Energy **44**, 8051–8061 (2019).

[306]C. Waite, *2019 UK greenhouse gas emissions, final figures*, tech. rep. (BEIS, Feb. 2021).

[307]P. W. Griffin and G. P. Hammond, "Analysis of the potential for energy demand and carbon emissions reduction in the iron and steel sector", Energy Procedia **158**, 3915–3922 (2019).

[308]S. Pamenter and R. J. Myers, "Decarbonizing the cementitious materials cycle: a whole-systems review of measures to decarbonize the cement supply chain in the uk and european contexts", Journal of Industrial Ecology **25**, 359–376 (2021).

[309]Element Energy, *Demonstrating CO_2 capture in the UK cement, chemicals, iron and steel and oil refining sectors by 2025: a techno-economic study*, tech. rep. (DECC and BIS, Apr. 2014).

[310]IEA, *Technology roadmap low-carbon transition in the cement industry*, tech. rep. (IEA, Mar. 2018).

[311]Office of Gas and Electricity Markets, *Feed-in tariff (fit) rates*, (2019) `https://www.ofgem.gov.uk/environmental-and-social-schemes/feed-tariffs-fit/feed-tariff-fit-rates` (visited on 08/30/2019).

[312]Element Energy, *Shipping CO_2 – UK cost estimation study*, tech. rep. (BEIS, Nov. 2018).

[313]P. Brownsort, K. Carruthers, R. S. Haszeldine, G. Johnson, R. Kapila, A. Kemp, C. Littlecott, L. Mabon, E. Mackay, R. Macrory, et al., *CO_2 storage and enhanced oil recovery in the North Sea: securing a low-carbon future for the UK*, tech. rep. (SCCS, 2015).

[314]J. Serpa, J. Morbee, and E. Tzimas, "Technical and economic characteristics of a CO_2 transmission pipeline infrastructure", JRC62502, 1–43 (2011).

[315]ACORN, *Act acorn pipeline re-use factsheet*, https://www.actacorn.eu/about-act-acorn/infrastructure-reuse-and-decommissioning (visited on 10/27/2021).

[316]S. Holloway, "Storage capacity and containment issues for carbon dioxide capture and geological storage on the UK continental shelf', Proceedings of the Institution of Mechanical Engineers, Part A: Journal of Power and Energy **223**, 239–248 (2009).

[317]REF, *Balancing mechanism wind farm constraint payments*, (May 2021) https://www.ref.org.uk/constraints/indexbymth.php?order=mth%5C&dir=asc%5C&start=.

[318]National Grid ESO, *Electricity ten year statement* (Warwick, Nov. 2019).

[319]N. Statistics, *2022 uk greenhouse gas emissions, provisional figures*, Statistics (Department for Energy Security & Net Zero, 2023).

[320]K. Li, W. Leigh, P. Feron, H. Yu, and M. Tade, "Systematic study of aqueous monoethanolamine (mea)-based co2 capture process: techno-economic assessment of the mea process and its improvements", Applied Energy **165**, 648–659 (2016).

[321]Eurostat, *Statistics on the production of manufactured goods value annual 2020*, (June 2022) https://ec.europa.eu/eurostat/web/prodcom/data/excel-files-nace-rev.2.

[322]N. Statistics, *Prices of fuels purchased by non-domestic consumers in the uk*, Statistics (Department for Energy Security & Net Zero, 2023).

[323]R. Peters, N. Wegener, R. C. Samsun, F. Schorn, J. Riese, M. Grünewald, and D. Stolten, "A techno-economic assessment of fischer–tropsch fuels based on syngas from co-electrolysis", Processes **10**, 699 (2022).

[324]A. Sainz, *A way out of the eu gas price crisis with biomethane*, (Feb. 2022) https://www.europeanbiogas.eu/a-way-out-of-the-eu-gas-price-crisis-with-biomethane/.

[325]MMSA, *Methanol supply/demand*, (Apr. 2022) https://www.methanol.org/methanol-price-supply-demand/.

[326]G. P. Prices, *Diesel prices, litre, 06-jun-2022*, (June 2022) https://www.globalpetrolprices.com/diesel_prices/.

[327]T. Economics, *Naphtha2022*, (June 2022) https://tradingeconomics.com/commodity/naphtha.

[328]S. Hawer, A. Schönmann, and G. Reinhart, "Guideline for the classification and modelling of uncertainty and fuzziness", Procedia Cirp **67**, 52–57 (2018).

[329]S. Roussanaly, J. A. Ouassou, R. Anantharaman, and M. Haaf, "Impact of uncertainties on the design and cost of ccs from a waste-to-energy plant", Frontiers in Energy Research **8**, 17 (2020).

[330]D. for Transport statistics, *Statistics at dft*, (Aug. 2022) https://www.gov.uk/government/organisations/department-for-transport/about/statistics.

[331]D. of Energy and C. Change, *Scotland analysis: energy*, tech. rep. (HM Government, 2014).

[332]S. Roussanaly, E. S. Rubin, M. W. Van Der Spek, G. Booras, N. Berghout, T. Fout, M. Garcia, S. O. Gardarsdottir, V. N. Kuncheekanna, M. Matuszewski, et al., "Towards improved guidelines for cost evaluation of carbon capture and storage-a white paper", (2021).

[333]S. Hänggi, P. Elbert, T. Bütler, U. Cabalzar, S. Teske, C. Bach, and C. Onder, "A review of synthetic fuels for passenger vehicles", Energy Reports **5**, 555–569 (2019).

[334]L. Guzzella, A. Sciarretta, et al., *Vehicle propulsion systems*, Vol. 1 (Springer, 2007).

[335]V. C. Agency, *The worldwide harmonised light vehicle test procedure (wltp)*, (Apr. 2021) https://www.vehicle-certification-agency.gov.uk/fuel-consumption-co2/the-worldwide-harmonised-light-vehicle-test-procedure/.

[336]P. W. A. Huss, *Jec tank-to-wheels report v5: passenger cars.* Tech. rep. EUR 30270 EN (Publications Office of the European Union, Luxembourg: 2020).

[337]M. Prussi, M. Yugo, M. De Prada L.and Padella, and R. L. Edwards, *Jec well-to-tank report v5*, tech. rep. 978-92-76-19926-7, doi:10.2760/959137 (Publications Office of the European Union, 2020).

[338]G. Thistlethwaite, E. Karagianni, A. Collins, J. MacCarthy, H. Thomas, P. Mullen, A. Kelsall, R. Bramwell, J. Wong, P. Quinn, C. Walkerd, and B. Harris, *2022 government greenhouse gas conversion factors for company reporting*, tech. rep. (Department for Business Energy & Industrial Strategy, June 2022).

[339]H. Lu, X. Ma, K. Huang, L. Fu, and M. Azimi, "Carbon dioxide transport via pipelines: a systematic review", Journal of Cleaner Production **266**, 121994 (2020).

[340]G. Skaugen, S. Roussanaly, J. Jakobsen, and A. Brunsvold, "Techno-economic evaluation of the effects of impurities on conditioning and transport of co2 by pipeline", International Journal of Greenhouse Gas Control **54**, 627–639 (2016).

[341]J. Collis and R. Schomaecker, "Determining the production and transport cost for h2 on a global scale", (2022).

[342]P. M. Modisha, C. N. Ouma, R. Garidzirai, P. Wasserscheid, and D. Bessarabov, "The prospect of hydrogen storage using liquid organic hydrogen carriers", Energy & fuels **33**, 2778–2796 (2019).

[343]S. Giddey, S. Badwal, C. Munnings, and M. Dolan, "Ammonia as a renewable energy transportation media", ACS Sustainable Chemistry & Engineering **5**, 10231–10239 (2017).

[344]C. Baker and R. Shaner, "A study of the efficiency of hydrogen liquefaction", International Journal of Hydrogen Energy **3**, 321–334 (1978).

[345]O. S. Bruno Lajoie Romain Debarre, *Hydrogen-based energy conversion.* (Energy Transition Institute, Feb. 2014).

[346]BloombergNEF, *Hydrogen economy outlook*, tech. rep. (Bloomberg Finance L.P, 2020).

[347]ACER, *Transporting pure hydrogen by repurposing existing gas infrastructure*, tech. rep. (European Union Agency for the Cooperation of Energy Regulators, 2021).

[348]N. Global, *Current natural gas vehicle statistics*, http://www.iangv.org/current-ngv-stats/.

[349]D. Rosenblatt, K. Winther, and D. Rosenblatt, *Real driving emissions and fuel consumption: a report from the advanced motor fuels technology collaboration programme. 2020.*

[350]A. Sanli, I. T. Yılmaz, and M. Gümüş, "Assessment of combustion and exhaust emissions in a common-rail diesel engine fueled with methane and hydrogen/methane mixtures under different compression ratio", International Journal of Hydrogen Energy **45**, 3263–3283 (2020).

[351]H. Chen, J. He, and X. Zhong, "Engine combustion and emission fuelled with natural gas: a review", Journal of the Energy Institute **92**, 1123–1136 (2019).

[352]Ford, *2016 f-150 with class-exclusive compressed natural gas, propane capability grows ford's alternative fuel leadership*, (2015) https://media.ford.com/content/fordmedia/fna/us/en/news/2015/05/04/2016-f150-alternative-fuel-leadership.html.

[353]T. Klein, *Methanol: a future-proof fuel*, tech. rep. (Future Fuel Strategies, 2020).

[354]M. R. Saxena, R. K. Maurya, and P. Mishra, "Assessment of performance, combustion and emissions characteristics of methanol-diesel dual-fuel compression ignition engine: a review", Journal of Traffic and Transportation Engineering (English Edition) **8**, 638–680 (2021).

[355]S. Verhelst, J. W. Turner, L. Sileghem, and J. Vancoillie, "Methanol as a fuel for internal combustion engines", Progress in Energy and Combustion Science **70**, 43–88 (2019).

[356]H.-W. Wu, C.-M. Fan, J.-Y. He, and T.-T. Hsu, "Optimal factors estimation for diesel/methanol engines changing methanol injection timing and inlet air temperature", Energy **141**, 1819–1828 (2017).

[357]B. Borgna, *Volvo trucks to bring its full heavy-duty range to the 2014 mid-america trucking show*, (Mar. 2014) https://www.volvogroup.com/en/news-and-media/news/2014/mar/news-146653.html.

[358]S. H. Park and C. S. Lee, "Applicability of dimethyl ether (dme) in a compression ignition engine as an alternative fuel", Energy Conversion and Management **86**, 848–863 (2014).

[359]Y. Wang, Y. Zhao, F. Xiao, and D. Li, "Combustion and emission characteristics of a diesel engine with dme as port premixing fuel under different injection timing", Energy Conversion and Management **77**, 52–60 (2014).

[360]A. Kovač, M. Paranos, and D. Marciuš, "Hydrogen in energy transition: a review", International Journal of Hydrogen Energy **46**, 10016–10035 (2021).

[361]M. Morales, M. Laguna-Bercero, and E. Jiménez-Piqué, "Direct-methane anode-supported solid oxide fuel cells fabricated by aqueous gel-casting", Journal of the European Ceramic Society (2022).

[362]Y. Zuo, W. Sheng, W. Tao, and Z. Li, "Direct methanol fuel cells system: a review of dual-role electrocatalysts for oxygen reduction and methanol oxidation", Journal of Materials Science & Technology (2022).

[363]D. Kashyap, H. Teller, P. Subramanian, P. Bělskỳ, M. G. Gebru, I. Pitussi, R. S. Yadav, H. Kornweitz, and A. Schechter, "Sn-based atokite alloy nanocatalyst for high-power dimethyl ether fueled low-temperature polymer electrolyte fuel cell", Journal of Power Sources **544**, 231882 (2022).

[364]M. Alizadeh, M. Jafari-Nokandi, and M. Shahabi, "Resiliency-oriented islanding of distribution network in the presence of charging stations for electric vehicles", International Transactions on Electrical Energy Systems **30**, e12670 (2020).

[365]Q. Hu, H. Li, and S. Bu, "The prediction of electric vehicles load profiles considering stochastic charging and discharging behavior and their impact assessment on a real uk distribution network", Energy Procedia **158**, 6458–6465 (2019).

[366]O. Sadeghian, A. Oshnoei, B. Mohammadi-Ivatloo, V. Vahidinasab, and A. Anvari-Moghaddam, "A comprehensive review on electric vehicles smart charging: solutions, strategies, technologies, and challenges", Journal of Energy Storage **54**, 105241 (2022).

[367]A. König, L. Nicoletti, D. Schröder, S. Wolff, A. Waclaw, and M. Lienkamp, "An overview of parameter and cost for battery electric vehicles", World Electric Vehicle Journal **12**, 21 (2021).

[368]Z. Liu, J. Song, J. Kubal, N. Susarla, K. W. Knehr, E. Islam, P. Nelson, and S. Ahmed, "Comparing total cost of ownership of battery electric vehicles and internal combustion engine vehicles", Energy Policy **158**, 112564 (2021).

[369]I. Tsiropoulos, P. Siskos, and P. Capros, "The cost of recharging infrastructure for electric vehicles in the eu in a climate neutrality context: factors influencing investments in 2030 and 2050", Applied Energy **322**, 119446 (2022).

[370]T. M. Gür, "Review of electrical energy storage technologies, materials and systems: challenges and prospects for large-scale grid storage", Energy & Environmental Science **11**, 2696–2767 (2018).

[371]H. Thomas-Peter, *'damning' report calls for major national grid changes to prevent uk missing key wind power targets*, (Apr. 2023) `https://news.sky.com/story/damning-report-calls-for-major-national-grid-changes-to-prevent-uk-missing-key-wind-power-targets-12850663`.

[372]V. Ramasamy, J. Zuboy, E. O'Shaughnessy, D. Feldman, J. Desai, M. Woodhouse, P. Basore, and R. Margolis, *Us solar photovoltaic system and energy storage cost benchmarks, with minimum sustainable price analysis: q1 2022*, tech. rep. (National Renewable Energy Lab.(NREL), Golden, CO (United States), 2022).

[373]H. Deng, J. M. Bielicki, M. Oppenheimer, J. P. Fitts, and C. A. Peters, "Leakage risks of geologic co 2 storage and the impacts on the global energy system and climate change mitigation", Climatic Change **144**, 151–163 (2017).

[374]A. Vinca, J. Emmerling, and M. Tavoni, "Bearing the cost of stored carbon leakage", Frontiers in Energy Research **6**, 40 (2018).

[375]F. Kazemifar, "A review of technologies for carbon capture, sequestration, and utilization: cost, capacity, and technology readiness", Greenhouse Gases: Science and Technology **12**, 200–230 (2022).

[376]P. Kelemen, S. M. Benson, H. Pilorgé, P. Psarras, and J. Wilcox, "An overview of the status and challenges of co2 storage in minerals and geological formations", Frontiers in Climate **1**, 9 (2019).

[377]S. Gallagher, *Uk ban of petrol engined cars from 2030 – oems react*, (Aug. 2022) https://www.evo.co.uk/electric-cars/19743/uk-ban-of-petrol-engined-cars-from-2030-oems-react.

[378]N. Z. Review, *Mission zero - independent review of net zero*, Independent Review (Net Zero Review, 2023).

[379]H. Government, *Powering up britain: energy security plan*, tech. rep. 978-1-5286-4018-3 (HM Government, 2023).

[380]M. Mostafa, C. Varela, and E. Zondervan, "Optimization of electrolysis and carbon capture processes for sustainable production of chemicals through power-to-x", Physical Sciences Reviews (2022).

[381]M. Sterner and M. Specht, "Power-to-gas and power-to-x—the history and results of developing a new storage concept", Energies **14**, 6594 (2021).

[382]V. Venkataraman, M. Pérez-Fortes, L. Wang, Y. S. Hajimolana, C. Boigues-Muñoz, A. Agostini, S. J. McPhail, F. Maréchal, J. Van Herle, and P. Aravind, "Reversible solid oxide systems for energy and chemical applications–review & perspectives", Journal of Energy Storage **24**, 100782 (2019).

[383]M. Lang, S. Raab, M. S. Lemcke, C. Bohn, and M. Pysik, "Long-term behavior of a solid oxide electrolyzer (soec) stack", Fuel Cells **20**, 690–700 (2020).